Locally Doped Nanorods: Introducing Distance-Dependence in Excitonic Nanostructures

Doctoral thesis
for obtaining the degree
Doctor of Natural Sciences (Dr. rer. nat.)

submitted by
Fischli, Danja

at the

Universität
Konstanz

Faculty of Science
Department of Chemistry

Konstanz, 2022

Date of the oral examination: 30.05.2023
1. Reviewer: Prof. Dr. Klaus Boldt
2. Reviewer: Prof. Dr. Helmut Cölfen
3. Reviewer: Prof. Dr. Alf Mews

Danksagung

Als erstes möchte ich Professor Dr. Klaus Boldt danken, der mich in die Arbeitsgruppe aufgenommen hat, und mir ein anspruchsvolles Thema anvertraut hat, an dem ich viel lernen konnte. Ich konnte jederzeit mit Fragen und Anliegen auf dich zukommen, und habe die Freiheit oder Unterstützung bekommen, die ich zum jeweiligen Zeitpunkt brauchte. Danke für die angeregten und respektvollen fachlichen Diskussionen! Besonders aus den Schreibprozesse an den gemeinsamen Publikationen habe ich viel mitgenommen. Eine bessere Betreuung kann man sich während der Promotion kaum wünschen.

Ich danke Professor Dr. Helmut Cölfen für die Übernahme des Zweitgutachtens, sowie die wertvollen Anregungen bei der Besprechung der Zwischenberichte. Vielen Dank an Professor Dr. Alf Mews für die Übernahme des Drittgutachtens. Professorin Dr. Miriam Unterlass danke ich für die Übernahme des Vorsitzes der Prüfungskommission.

Allen aktuellen und vorherigen Mitgliedern der AG Boldt, Michi, Jessi, Eva, Eva, Flo, Daniel und Sebastian danke ich für die KameradInnenschaft, die gute Zusammenarbeit, und die anregende Gespräche in den Mittags- und Kaffeepausen. Besonders danke ich Michi und Jessi dafür, dass sie sich geduldig ein Labor mit mir geteilt haben.

Ich danke allen Studierenden, die im Rahmen von Praktika und als HiWis zum Gelingen des Projektes beigetragen haben. Patricia, Veit, Eva, Jessi, Berk, Luisa und Celine: Vielen Dank für euren Einsatz!

Ein großes Danke an Jochen, Sebi, Kathi, Jessi und Eva, die meine Arbeit Korrektur gelesen und angemessen zerpflückt haben. Vielen Dank, dass ihr euch die Zeit genommen habt!

Dr. Marina Krumova danke ich für die Unterstützung bei TEM Messungen. Danke ebenfalls an Andreas Kornowski an der Uni Hamburg für die Aufnahme der EDX mappings. Der AG Winter danke ich dafür, dass ich ihr EPR-Gerät nutzen durfte, sowie für Rat und Tat bei PL-Messungen.

Ein großes Dankeschön gilt den Mitarbeiterinnen im Fachbereichssekretariat, Dagmar Talke, Christiane Weber und Susanna Schnell. Den Mitarbeiterinnen im Büro der Graduiertenschule, Tanja, Dagmar, und vor allem Tina danke ich für das offene Ohr, die Hilfe beim Papierkram, und die Schokolade.

Ich danke all meinen Freunden, in Konstanz und in der Ferne, für schöne Stunden und Unternehmungen. Besonders möchte ich Yvonne danken, die immer ein offenes Ohr hat und stets für einen Schwatz bereit war, wenn mir die Chemie ab und an zu den Ohren herauskam. Ohne M.B. und N.K. wäre diese Dissertation niemals fertig geworden. Vielen Dank für die Unterstützung!

Meiner Familie danke ich für die Unterstützung während des Studiums. Besonders möchte ich meiner Schwester danken, die mir geholfen hat, auch die letzten Wochen der Schreibphase noch zu meistern.

Mein größter Dank gilt Julian. Dafür, dass du mich unterstützt, mir den Rücken freihältst, und, gerade in der Endphase der Dissertation, mit Essen, Tee, Wärmflaschen, und moralischer Unterstützung für mein leibliches und seelisches Wohl gesorgt hast. Es gibt niemanden auf der Welt, mit dem ich mein Leben lieber verbringen möchte.

Table of Contents

I List of Abbreviations

a.u.	Arbitrary units
CB	Conduction band
CP	Coordination polymer
EDX	Energy-dispersive X-ray spectroscopy
EFTEM	Energy-filtered transmission electron microscopy
EPR	Electron paramagnetic resonance spectroscopy
EXAFS	Extended X-ray absorption fine structure
FFT	Fast Fourier transform
HAADF	High-angle annular dark field imaging
HPA	Hexylphosphonic acid
HR-TEM	High-resolution transmission electron microscopy
ICP-OES	Inductively coupled plasma optical emission spectroscopy
ML	Monolayer
MSC	Magic-sized clusters
NC	Nanocrystal
NMR	Nuclear magnetic resonance
OA	Oleic acid
ODE	1-Octadecene
ODPA	Octadecylphosphonic acid
OlAm	Oleylamine
PL	Photoluminescence
QD	Quantum dot
QY	Quantum yield
TCSPC	Time-correlated single photon counting
TBP	Tributylphosphine
TOP	Trioctylphosphine
TOPO	Trioctylphosphine oxide
TOP-S	Trioctylphosphine sulfide
TOP-Se	Trioctylphosphine selenide
TOP-Te	Trioctylphosphine telluride
UV	Ultraviolet
VB	Valence band
Vis	Visible
XRD	X-Ray diffraction

II List of Figures

1 Introduction

While in some aspects of life (cars, TV screens, houses) society generally seems to adhere to the motto "the bigger, the better", the technology behind those amenities heads in the opposite direction: Computers turned from machines that fill up rooms to tiny gadgets that fit into the dimensions of a wristwatch, while at the same time multiplying their calculation power. This development was predicted by Gordon Moore, former CEO of Intel. He stated in 1975 that the number of transistors on an integrated circuit will double every year, which he later revised to every two years.[1] This rule of thumb, known as Moore's law, has become a self-fulfilling prophecy that guides long-term planning in the semiconductor industry, and sets targets for research and development. As simply doubling the amount of transistors on an integrated circuit without downsizing them would lead to bigger and bigger devices minimizing the transistors' size in necessary.

Figure 1.1: Nanoscale gold as an example for the fundamental changes of a materials appearance at different sizes. Adapted from Sustainable-nano.com.[2]

This is where nanotechnology comes into play. Scaling a system down leads to more than just a smaller size. At a sufficiently small scale additional size dependent properties set in. The most famous of these are the quantum size effect in semiconductors and surface plasmon resonance in metals. These effects can change the properties and appearance of a material so drastically that an unsuspecting onlooker would never think that they are made of the same atoms. An example is shown in Figure 1.1: The red to violet color of colloidal gold in solution significantly differs in appearance from bulk gold, all due to size dependent properties.

These properties are not always advantageous. The toxicology of nanoparticles comes increasingly into focus. Recently, the use of titanium dioxide as a food additive, as its nanoparticles can

---

[1] Gordon E Moore. , **86**: 82–85, 1965.

[2] mengwu4 *aunps-stephmitchell* https://sustainable-nano.com/2019/11/12/gold-nanoparticles-color/ accessed Sep 02, 2022 Nov. 2019

enter cells and promote inflammation.[3] In technical applications the increasing surface-to-volume ratio that results from the decreasing size poses specialized challenges regarding conductivity.[4]

Despite these drawbacks, nanoscale materials offer unique possibilities in the field of optics, catalysis, and surface science, with practical implications for everyday life: Products such as sunscreen, various pigments, self-cleaning coatings, and high quality TV screens rely on the use of nanoparticles. Some are used to treat diseases including cancer, all on the basis of properties that are linked to their size.

A main reason behind this is that unique challenges which arise alongside the unique opportunities have to be dealt with in research. A major issue for instance is the fact that processes which require little effort on the macroscale become increasingly difficult when scaled down to dimensions that are smaller than the wavelength of light. That includes seemingly basic tasks such as imaging a material, or combining two materials. Dilute Magnetic Semiconductors (DMS) are a popular example for such a combination. They combine the conductive properties of semiconductors with magnetic ones of *via* transition metal ions with unpaired electrons. This combination makes them ideally suited for spintronics applications, in which electric charges and magnetic spins interact, e.g., to create spin-based transistors.[5] Sizing these materials down would make it possible to use size dependent properties as an additional tool to optimize their electronic structure for their specific applications. Doping transition metal ions into nanostructures is a baseline requirement to achieve this goal, but has proven to be a challenge due to the small size of the host structures.[6] Once the dopant is introduced, self-purification processes are strongly favored, which makes the particles difficult to process. Additional effects such as intra-particle diffusion oppose localization of the dopant within the particle.

This thesis aims to control the composition of a nanoparticle with nanometer precision by locally introducing transition metal dopants into an excitonic structure. While the bulk equivalent of transition metal doped semiconductor materials is mainly interesting for spintronic applications, the added benefit of size dependent properties comes into play at the nanoscale. Additionally, locally introducing dopants into nanoparticles requires an unprecedented level of control over reaction kinetics. The resulting structures can provide help to uncover the fundamental processes that govern exciton dynamics.

---

[3] European Food Safety Authority *Titanium dioxide: E171 no longer considered safe when used as a food additive* https://www.efsa.europa.eu/de/news/titanium-dioxide-e171-https://www.efsa.europa.eu/en/news/titanium-dioxide-e171-no-longer-considered-safe-when-used-food-additive Accessed Sep 20, 2022 May 2021

[4] Daniel Josell, Sywert H. Brongersma, and Zsolt Tőkei. *Ann. Rev. Mater. Res.*, **39**: 231–254, 2009.

[5] Sebastiaan van Dijken, Xin Jiang, and Stuart S. P. Parkin. *Appl. Phys. Lett.*, **80**: 3364–3366, 2002.

[6] Steven C. Erwin et al. *Nature*, **436**: 91, 2005.

2 Theoretical Background

2.1 Electronic band structure of semiconductor nanocrystals

2.1.1 Band structure of bulk solids

Crystalline solids in the classical sense are defined by their periodicity: Their 3D structure consists of periodically repeating subunits, e.g., an elemental cell of atoms, forming a lattice that extends in all directions. The atomic orbitals of these atoms combine to form molecular orbitals (Linear combination of atomic orbitals, or LCAO). For a number of atoms $N \to \infty$ in the lattice, the density of molecular orbitals increases to a degree that they can no longer be regarded as distinct energy levels. Instead, continuous bands form which are occupied by electrons. As electrons are fermions, they follow the Pauli principle: Two or more identical fermions can't occupy the same quantum state within a quantum system at the same time. The probability of an energy level E to be occupied by an electron is described by the Fermi-Dirac distribution (Equation 2.1).

$$F(T) = \frac{1}{\exp(E - E_F)/k_B T + 1} \tag{2.1}$$

T is the absolute temperature, k_B the Boltzmann constant, and E_F is the Fermi level, which is the energy at which a hypothetical state would have a 50% probability of being occupied at thermal equilibrium. The Fermi level is independent of temperature and an important material constant as the conductive properties of a given material largely rely on the degree to which its states are occupied by electrons. Only electrons above the Fermi level will contribute towards electric conductivity.

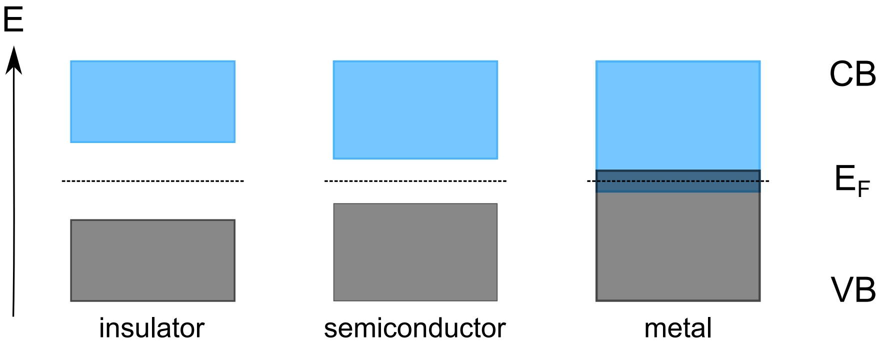

Figure 2.1: Schematic band structures of insulators, semiconductors, and metals. The different material classes are characterized by the relative energetic position of the valence band (VB) and conduction band (CB). The Fermi level E_F characterizes the energetic position of a level with a 50 % probability of being occupied.

Crystalline solids can be classified by their electronic band structures, as shown in Figure 2.1. Metallic conductors have overlapping conduction and valence bands (CB and VB, respectively), so electrons can freely enter the CB: The material is conductive regardless of temperature. In the case of semiconductors and insulators, CB and VB do not overlap, but are separated by a band gap of a specific energy E_g. This gap has to be overcome by an electron to enter the CB and make conduction possible. Within the band gap lies the Fermi level. If there is a state at the Fermi level that state will have a 50% chance of being occupied. For an insulator, the Fermi level is far from states that are able to carry current, within a large band gap (typically larger than 3 eV). For semiconductors, the band gap is smaller, the Fermi level is closer to the band edges, so that a number of thermally excited carriers resides near the band edge. If the electron is supplied with the necessary energy it can overcome the band gap and reach the CB. This requires e.g., a photon with $E_{\text{photon}} \geq E_{\text{gap}}$.

When an electron is excited from the VB into the CB by absorption of a photon, it leaves behind a positively charged hole. The arising electron-hole pair (exciton) can be described like a hydrogen atom and can be assigned a Bohr radius. This material specific quantity describes the mean distance between the charge carriers. Both the positively charged hole and the negatively charged electron are subject to Coulomb interactions, can move within the crystal as quasi-particles, and are described by a wave function.

Semiconductors can be further subdivided with regard to their band structure in momentum space, or k-space. Particles such as charge carriers can be interpreted as matter waves with a crystal momentum (k-vector). Interactions between those particles follow momentum conservation, so the value of the k-vector must be preserved during those interactions. In a direct semiconductor, an electron occupying the lowest energetic state of the CB and a hole occupying the highest state of the VB will have the same crystal momentum, so they can freely interact with one another, and recombine under release of a photon of the band gap energy. In an indirect semiconductor, the momenta of the VB maximum and the CB minimum differ. Particles such as a hole and electron occupying those states cannot simply recombine, as this would violate momentum conservation. Recombination under emission of a photon in thus only possible, if a phonon is involved, where the phonon momentum equals the difference in electron and hole momentum. As this process involves three particles instead of two, its probability is significantly reduced. Direct semiconductors are thus ideal candidates for optical applications, such as LEDs, while the properties of indirect semiconductors lend themselves to applications such as photovoltaics. Typical examples for direct semiconductors are II-IV semiconductors, while indirect semiconductors are mainly elemental semiconductors such as silicon and germanium.

2.1.2 Quantum size effect

Semiconductor nanocrystals (NC) are a nanometer-scale particles that contain approximately 100 to 10,000 atoms. Their optoelectronic properties differ from the bulk material, the most significant difference being the dependence of the band gap on the size of the particle (quantum size effect, QSE). This is an effect of the particle radius being smaller the exciton Bohr radius which means that the exciton can no longer move freely across the material, but experiences the particle boundaries as potential barriers. This confinement leads to quantization of the energy levels that the electron and hole, the two components of the exciton, can occupy. The quantum chemical model of the particle

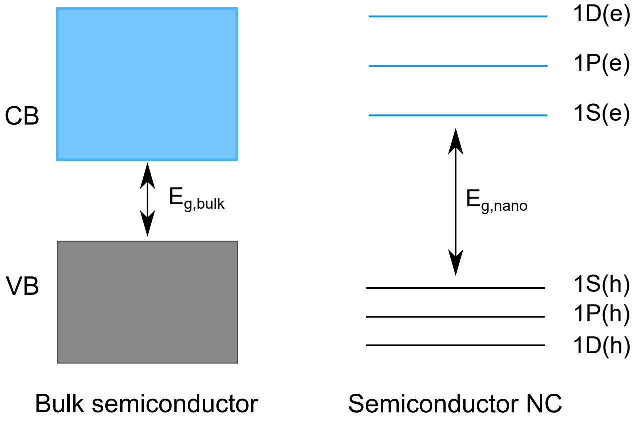

Figure 2.2: Schematic representation of the change in electronic structure band gap energy in a nanocrystal compared to the bulk structure. The NC electronic structure is simplified to the model case of a two band semiconductor.

in a box describes this behavior, and assigns discrete energy levels E_n for the one dimensional case as shown by Equation 2.2 A schematic representation can be found in Figure 2.2.

$$E_n = \frac{h^2}{8mL^2}n^2 \tag{2.2}$$

h is the Planck constant, m the mass of the particle (the electron/hole), L the size of the box, and n the quantum number. From the equation follows that $E_n \propto L^{-2}$ which in turn leads to a bigger gap between the energy levels $\Delta E = E_{n+1} - E_n$ the smaller the box, or the particle. The relationship between the particle size and the energy of the band gap was first described by Henglein in 1982, followed by the first mathematical description by Louis E. Brus in 1984.[7]

$$E_{g,\text{nano}} = E_{g,\text{bulk}} + \frac{\hbar^2\pi^2}{2R^2}\left(\frac{1}{m_e^*} + \frac{1}{m_h^*}\right) - \frac{1.8e^2}{\epsilon R} + \text{smaller terms} \tag{2.3}$$

$E_{g,\text{nano}}$ and $E_{g,\text{bulk}}$ are the band gaps of the bulk and the nanoparticle, $\hbar = h/2\pi$ with the Planck constant h, R is the particle radius, m_e^* and m_h^* are the effective mass of the electron and the hole, respectively. e is the elementary charge, ϵ the relative permittivity. The first term describes confinement effects on the exciton, the second the Coulomb interactions, the smaller terms are due to effects such as solvation energy loss. The Brus equation relies heavily on empirical quantities, namely the band gap, effective mass, and the relative permittivity, and can qualitatively describe the effects of size quantization.

Alternatively, the LCAO method can be used to explain this behavior. As the number of atoms in the crystal is no longer infinite, the number of molecular orbitals isn't either. Consequently, discrete states are formed instead of bands. The density of these discrete states is reduced at the edges of the former bands, so the band gap is bigger the fewer atoms are involved, or the smaller the particle.

---

[7] Louis E. Brus. *J. Chem. Phys.*, **80**: 4403–4409, 1984.

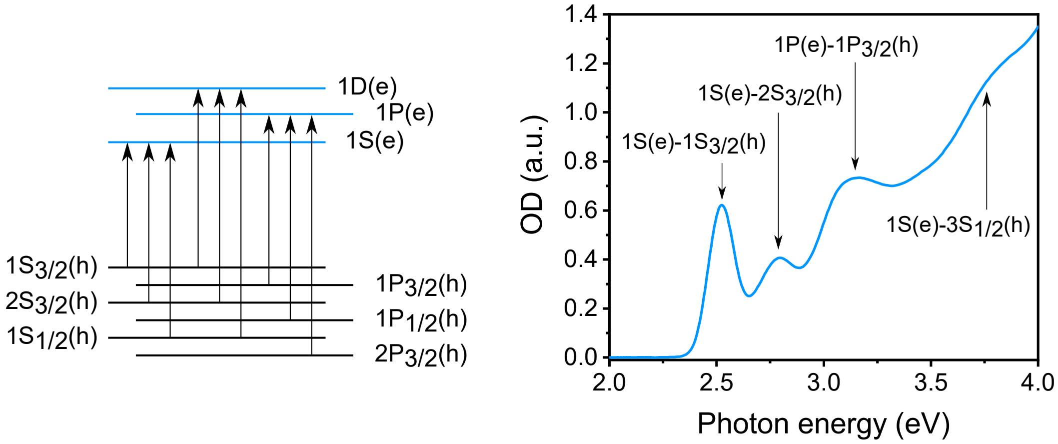

Figure 2.3: Allowed optical transitions in CdSe quantum dots (left), and UV/vis absorption spectrum of CdSe QDs with four well resolved transitions (right).

2.1.3 Absorption spectra of semiconductor nanocrystals

Figure 2.3 shows a more detailed look at the optical transitions in NCs, in this case CdSe quantum dots. Due to quantum confinement, different valence subbands mix, leading to a more complex structure of hole quantized states. Using the absorption spectrum in combination with a secondary means of size calculation it was possible in recent years to obtain material dependent, empirical equations that allow for the fast evaluation of particle sizes as well as concentrations. A commonly used example is the equation for spherical CdSe nanoparticles developed by Jasieniak et al.,[8] while other works provide similar equations for additional materials.

2.1.4 Exciton decay pathways

Excited states in semiconductors have a limited lifetime. Consequently, the system will at some point relax to the ground state and the stored energy is transferred to the environment. This relaxation can occur over different pathways, often in the form of emission of a photon, i.e., radiative decay. This photon typically has a lower energy than was absorbed previously, the emission is shifted to longer wavelengths/lower energies compared to the absorption edge. The observed phenomenon (Stokes shift) is due to the fact that electronic transitions usually don't occur between the vibrational ground states of the involved electronic states but higher vibrational states, and was first described for fluorescence processes in molecules: The excitation of the electron in a higher state is very fast due to its small mass, so that the position of the core can be assumed as fixed on this timescale (Born-Oppenheimer approximation). Consequently, the ground state and the excited state have to be immediately compatible. The transition is more likely, the bigger the overlap of the vibronic wave functions of the involved states, explaining the differences in intensity for different vibrational transitions. This is called the Frank-Condon principle. The thus formed "hot" exciton will then relax non-radiatively to the vibrational ground state of the excited electronic

---

[8] Jacek Jasieniak et al. *J. Phys. Chem. C*, **113**: 19468–19474, 2009.

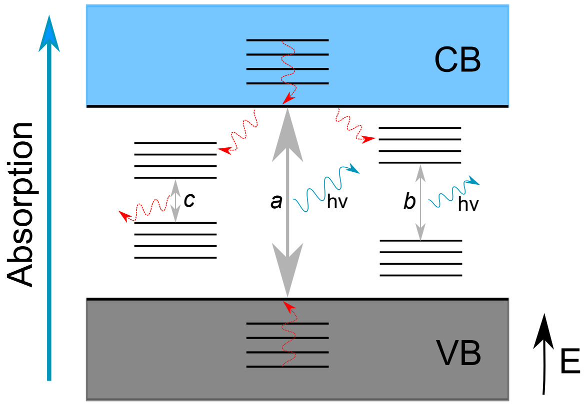

Figure 2.4: Exciton relaxation pathways. Band edge emission (a): The exciton relaxes non-radiatively towards the band edge, and then radiatively, emitting a photon with band gap energy. Trap emission (b): the exciton is transferred to an intra-gap trap state, and relaxes radiatively from there. The photon energy is lower than for band gap emission. Non-radiative trap relaxation (c): the exciton is transferred to an intra-gap trap state from which radiative relaxation is not possible. The exciton energy dissipates e.g., in the form of a lattice phonon.

state, releasing the excess energy i.e., in the form of lattice vibrations to the crystal lattice. This accounts for the energy difference between the absorbed and the emitted exciton.

Band edge relaxation in nanoparticles can occur over different pathways, as shown in Figure 2.4. The most straight-forward is the recombination of electron and hole under emission of radiation: This is the radiative relaxation pathway (a). Nanoparticles have a high surface-to-volume ratio. As surfaces typically have a higher defect density than the bulk material due to unsaturated bonds and surface reconstruction, this can lead to additional trap states within the band gap of the material. Additional sources of trap states can arise due to lattice strain at heterojunctions or the introduction of dopants, e.g., transition metal dopants with unsaturated d-orbitals. Charge carriers occupying trap states can relax radiatively or non-radiatively. In the case of radiative relaxation of surface trap states (b), the emission is typically red shifted and has considerably longer lifetimes than the band edge-emission. For trap states due to transition metal dopants, the recombination can occur radiatively or non-radiatively (c), depending on whether the transition from the trap states are allowed. Trap states often lead to a reduction of the band edge lifetime and the quantum yield, i.e., the ratio of the emitted photons and the absorbed photons. The lifetime reduction is a result of the fast depletion of the excited state by energy transfer to the trap state.

2.1.5 Heterostructures

In order to tune the emission characteristics of nanoparticles, it is possible to combine different semiconductor materials in order to form a heterostructure. The simplest example of such a structure is a core-shell particle. Heterostructures can be subdivided into different types depending on the relative positions of the band gap of the used materials, see Figure 2.5.

In a type I structure, the core material has a smaller bandgap than the shell material. The CB and VB of the shell material are significantly higher and lower in energy, respectively, than CB and VB of the core material. That leads to the localization of both electron and hole in the core,

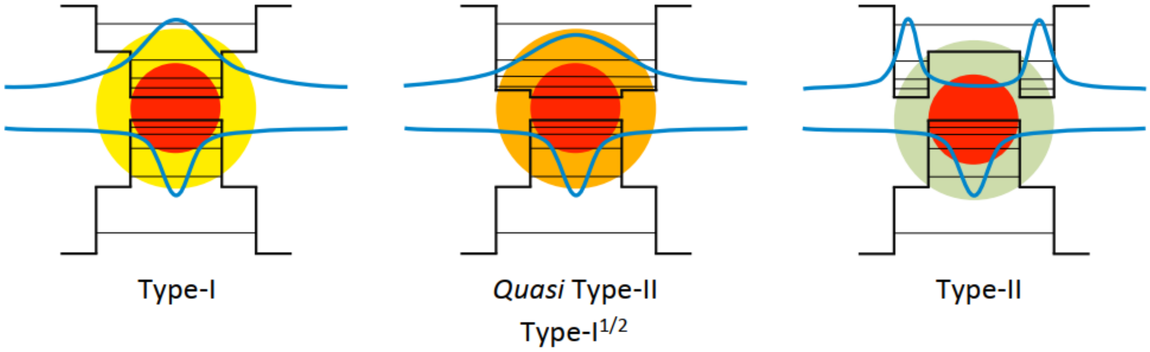

Figure 2.5: Classification of nanoheterostructures according to their band alignment.

increasing the likelihood of recombination and separating the charge carriers from the particle surface, which in turn increases the quantum yield.

In a type II structure, the charge carriers are effectively separated from each other by a staggered alignment of the band edges of the core and the shell material. Recombination is less likely due to the smaller overlap of the wave functions, increasing exciton lifetimes while reducing the quantum yield. The emission is strongly shifted towards lower energies because the effective band gap is characterized by the transition between the highest VB and the lowest CB state in the system, significantly reducing the band gap energy compared to that of the materials making up the structure.

The third type, type I$^{1/2}$, describes a structure in between; one charge carrier, in this case the hole, is localized within the core, while the electron extends into the shell. This decreases confinement, leading to a shift of the emission to lower energies and high quantum yields. A common example for this structure is the system CdSe/CdS, which is the main focus of this thesis.

2.2 Semiconductor nanocrystal synthesis: LaMer model and Ostwald ripening

Nanocrystals have a high surface-to-volume ratio, which makes them thermodynamically unfavorable. This leads to special requirements regarding particle synthesis and stabilization. As characteristics depend heavily on particle size, a narrow size distribution is a main criterion for successful particle synthesis which requires good control over the reaction conditions.

According to the classical nucleation theory as shown in Figure 2.6 (left), a nucleus is formed when the negative contribution of the bulk free energy $\Delta G_{\text{volume}} \propto r^3$ becomes large enough to compensate for the positive contribution of the surface energy $\Delta G_{\text{surface}} \propto r^2$, forming a nucleus of the radius r_c. It is thermodynamically favorable for this nucleus to grow, as ΔG continues to decrease with increasing particle size. A thermodynamically governed reaction regime would thus lead to few, big particles. In order to obtain particles on the nanoscale instead, a kinetic approach is favorable.

A qualitative description of the conditions necessary for the formation of monodisperse nanopar-

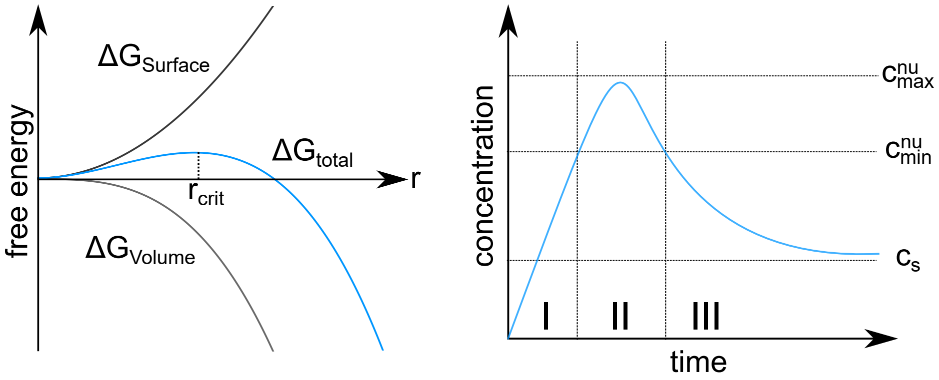

Figure 2.6: The Lamer model of nucleation describes the nucleation process according to classical nucleation theory. Nucleation only becomes energetically favorable when a critical particle radius is surpassed (left). The nucleation itself can be divided into stages. Monomer build-up (I), nucleation (II), and growth (III).

ticles was provided by Lamer and Dinegar in 1950[9] and is presented in Figure 2.6 (right). Monomer is dissolved in the reaction medium until its concentration exceeds the solubility creating an oversaturated solution (stage I). The system is metastable until it exceeds the critical oversaturation which leads to the formation of nuclei (stage II). Nucleation of more and more particles lowers the monomer concentration until it is below the critical oversaturation. At this point, no new nuclei are formed, but the existing particles grow (stage III), which has a negative net energy as the volume increase overcompensates for the slight increase in particle surface.

In order to obtain a narrow size distribution the key step is to separate the nucleation from the growth phase, so no new nuclei are formed while other nuclei are already growing. In classical semiconductor nanoparticle synthesis, first described by Murray, Norris, and Bawendi in 1993 ,[10] this is done via the so called hot-injection method. Highly reactive precursors are added to a hot solution of stabilizing agents which results in a rapid increase in monomer concentration and a burst of nucleation. A high number of nuclei is formed within a short amount of time, lowering the oversaturation below the threshold for homogeneous nucleation. Subsequently, the nuclei grow until the desired particle size is achieved. This principle can be adapted to form heterostructures as well: If a seed particle is introduced to a system with a momomer concentration below the critical nucleation threshold but above the oversaturation, new material will deposit on the preexisting particles, given the material lattices are compatible. That way, core-shell particles and other heterostructures are available.[11–14]

In addition to the separation of nucleation and growth the suppression of ripening effects is mandatory to achieve high quality nanoparticles. The most commonly used model for these effects was described by Ostwald in 1900.[15] Ostwald ripening is based on the curvature-dependence of the solubility of particles. Small particles can dissolve more easily than larger particles. The released

---

[9] Victor K. Lamer and Robert H. Dinegar. *J. Am. Chem. Soc.*, **72**: 4847–4854, 1950.

[10] C. B. Murray, D. J. Norris, and M. G. Bawendi. *J. Am. Chem. Soc.*, **115**: 8706–8715, 1993.

[11] Luigi Carbone et al. *Nano Lett.*, **7**: 2942–2950, 2007.

[12] Simon M. Fairclough et al. *J. Phys. Chem. C*, **116**: 26898–26907, 2012.

[13] Klaus Boldt et al. *Chem. Mater.*, **25**: 4731–4738, 2013.

[14] Florian Enders et al. *Chem. Mater.*, **32**: 10566–10574, 2020.

[15] W. Ostwald. *Z. Phys. Chem.*, **34U**: 495–503, 1900.

monomer deposits onto bigger particles, leading to a net flux of material from smaller to larger particles. The system tends towards the formation of few large particles which is unfavorable for nanoparticle applications. This effect can be suppressed by a high degree of particle stabilization and avoiding prolonged heating of the particles after the synthesis.

2.3 State of the art

2.3.1 Shape anisotropy

Semiconductor nanoparticle research as it is today is largely founded on a paper by Murray, Norris, and Bawendi in 1993.[10] This was the first paper to present the hot-injection synthesis, a robust method to obtain size tunable, monodisperse II-VI semiconductor nanoparticles. This first iteration of the method still used highly reactive, pyrophoric precursors, which were later dropped in favor of less hazardous systems. Additionally, the approach was widened to more materials: zinc chalcogenides, cadmium chalcogenides, and lead chalcogenides are all synthetically available.[16,17]

Along with particle materials, the number of available particle morphologies was expanded considerably. 1D structures such as wires and nanorods[18] are available as well as 2D nanopaletets, which were first reported in 2008 by Ithurria and Dubertret.[19] Additionally, 3D structures can be synthesized, often on the basis of a seeded growth regime. Among those are CdSe/CdS and seeded rods,[11] anisotropically functionalized CdSe@CdSe/CdS tipped rods,[20] and tetrapods.[21]

The characteristics of nanostructures are governed by their smallest dimension, due to the quantum size effect. For instance, an exciton in a nanorod experiences quantization only along the width of the particle, but can travel relatively freely along its length.[22] In contrast, nanoplatelets can be synthesized with atomic precision over their thickness, enabling narrow emission peaks due to the strong confinement in this dimension, while excitons can travel freely on the 2D surface. Thus, studying different particle morphologies can provide deeper insight into light-matter interactions. Each has unique potential applications as well, such as catalysis, e.g., in the case of CdTe@CdSe/CdS rods,[23,24] lasing, e.g., in CdSe/CdS seeded rods,[25] or as emitters, as for $Cd_xHg_{1-x}Se$ based core/shell particles.[26] Despite this wide synthetic range, precise knowledge of the synthetic requirements and mechanisms of anisotropic growth is still incomplete and a topic of ongoing research. A recent example are the differing theories regarding the formation of nanoplatelets.[27–31]

---

[16] Jin Joo et al. *J. Am. Chem. Soc.*, **125**: 11100–11105, 2003.

[17] Z. Adam Peng and Xiaogang Peng. *J. Am. Chem. Soc.*, **124**: 3343–3353, 2002.

[18] Felice Shieh, Aaron E Saunders, and Brian A Korgel. *J. Phys. Chem. B*, **109**: 8538–8542, 2005.

[19] Sandrine Ithurria and Benoit Dubertret. *J. Am. Chem. Soc.*, **130**: 16504–16505, 2008.

[20] Zvicka Deutsch, Lior Neeman, and Dan Oron. *Nat. Nanotechnol.*, **8**: 649–653, 2013.

[21] Dmitri V. Talapin et al. *Nano Lett.*, **7**: 2951–2959, 2007.

[22] James K. Utterback et al. *Nat. Chem.*, **8**: 1061–1066, 2016.

[23] Florian Enders et al. *Nanoscale*, **10**: 22362–22373, 2018.

[24] Maria Wächtler. *Nachr. Chem.*, **67**: 44–50, 2019.

[25] Guichuan Xing et al. *ACS Nano*, **6**: 10835–10844, 2012.

[26] Andrei Mitrofanov et al. *Chem. Mater.*, **33**: 7693–7702, 2021.

[27] Florian D. Ott et al. *Nano Lett.*, **17**: 6870–6877, 2017.

[28] Ye Jiang et al. *ACS Omega*, **3**: 6199–6205, 2018.

[29] Nicolo Castro et al. *Nano Lett.*, **19**: 6466–6474, 2019.

[30] Chenqi Zhu et al. *Angew. Chem. Int. Ed.*, **58**: 17764–17770, 2019.

[31] Patrick D. Cunningham et al. *ACS Nano*, **14**: 3847–3857, 2020.

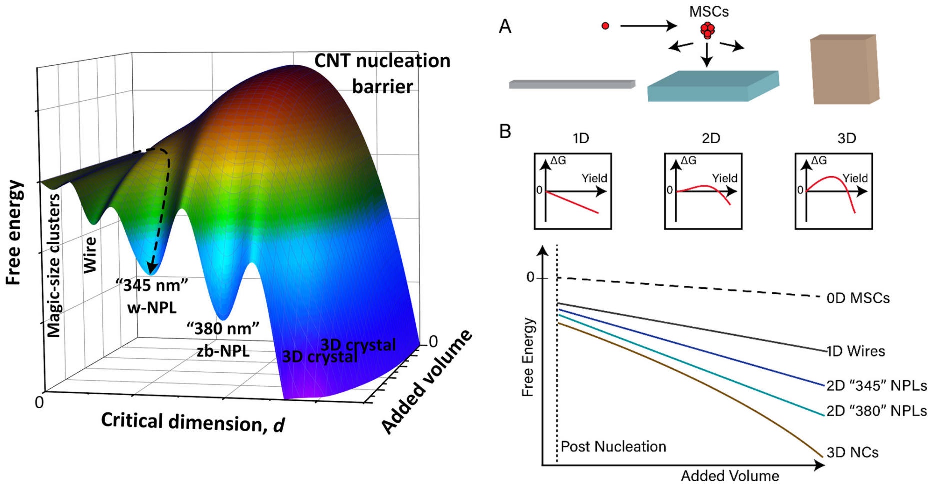

Figure 2.7: Unified reaction pathway for ZnSe MSCs, wires, platelets, and 3D crystals. Potential energy landscape for the formation of structures of different dimensionality from the same precursors (left). Comparison of the free energy change associated with nucleation of 1D, 2D, and 3D structures, and change in chemical potential associated with post nucleation growth for nanostrucures of different dimensionalities. Reprinted with permission from Cunningham et al.[31] Copyright 2020 American Chemical Society.

One growth model is provided by Ott et al. They find that for CdSe nanoplatelets, the distribution of nanoparticle thickness upon ripening does not defocus, but that the thickness jumps sequentially from m to $m+1$ monolayers.[27] The formation of another monolayer of material on an existing platelet is energetically less favorable than lateral growth, since the former requires the nucleation of an island on the nanoplatelet plane, which amounts to the creation of more surface. Nanoplatelets thus grow primarily in the lateral direction, with growth of narrow platelets being kinetically favored. This is why, at first, only species of the smallest thickness form. They grow from their critical seeds, until the monomer concentration is reduced to a level at which Oswald ripening sets in. These ripening effects occur only in the lateral direction as well, i.e., platelets loose material at their edges, dissolving to form monomer. When the monomer concentration in solution becomes high enough, and the next thicker species starts to form, as each thickness is thermodynamically more stable than the one before. That is why the growth steps take longer, for each consecutive species.

Cunningham et al. found that different dimensionalities of ZnSe particles, from magic size clusters (MSCs) over wires, platelets, to 3D crystals, can be synthesized from the same reagents, depending on the reaction temperature.[31] They thus propose a unified reaction pathway that is governed by two critical dimensions: the smallest critical nucleation volume for a given population V_{add}, and the smallest dimension for a given shape diameter d. As the nucleation barrier for MSCs is the lowest, they form first, followed by 1D wires, 2D platelets, and 3D nanocrystals. According to this theory, 0D, 1D, and 2D species are thus local minima in a reaction landscape that heads towards the formation of 3D nanocrystals, as shown in Figure 2.7. The outcome in a given amount of time can then be controlled by the reaction temperature. This is a particularly interesting model, as it encompasses a wide variety of particle morphologies, which so far have been regarded separately. Also, it connects both 0D reaction intermediates and as 1D wires with the growth of bigger nanoparticle species.

2.3.2 Non-classical reaction intermediates

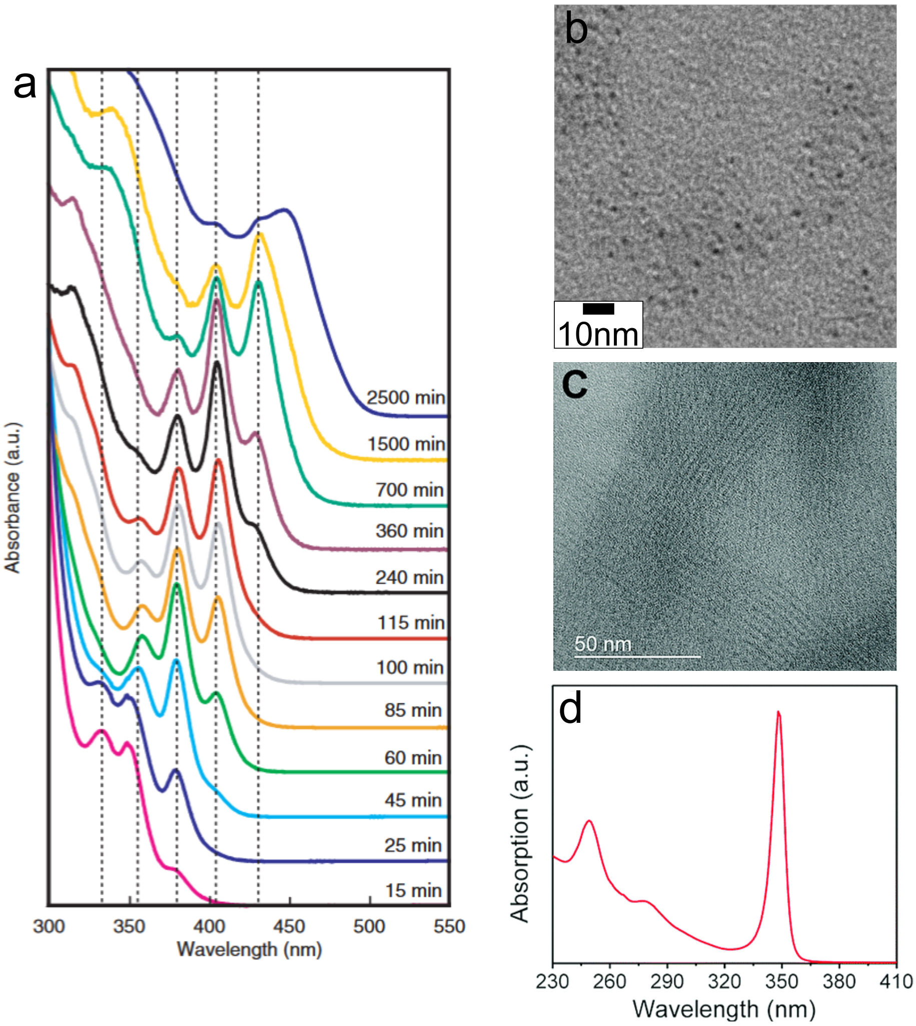

Figure 2.8: Magic size clusters (MSCs) and coordination polymers (CPs) as the two classes of reaction intermediates. UV/vis absorption kinetics of the sequential growth of CdSe MSCs (a). TEM micrograph of a CdSe MSC sample with the first absorption feature centered at 447 nm (b) and CdSe CP-350 (c). UV/vis absorption spectra of CdSe CP-350 (d). (a,b) Reprinted with permission from Kudera et al.[32] Copyright 2007 Wiley VCH. (c,d) Reprinted with permission from Wurmbrand et al.[33] Copyright 2018 Royal Chemical Society.

The connection between small intermediate species and the growth of nanocrystals, which suggests complex mechanisms of particle formation beyond the classical nucleation theory, have come into focus in recent years. A key discovery was the existence of stable prenucleation clusters that form with a neglible activation barrier.[34] Similar reaction intermediates were identified during II-VI semiconductor NP synthesis.

MSCs and nanowire-like, fibrillar 1D intermediates are the two main classes of reaction intermediates are discussed in literature. Magic size clusters (MSCs) are the more well known of the two. They are described as ultrasmall nanocrystals with defined structure and stoichiometry that occupy deep, local minima along the reaction coordinate.[35] They have been observed in early stages of nucleation and growth since the development of the hot injection synthesis, and appear to act as critical sized nuclei.[17] Kudera et al. identified several persistent cluster families that occur during CdSe nanoparticle growth, and developed a model for their growth.[32] They are mostly observed by UV/vis spectroscopy as narrow lines that do not shift with growth, but follow a quantized growth to the next larger size of MSC or to regular NCs, as shown in Figure 2.8 (a). In TEM micrographs, they appear as isotropic structures (see Figure 2.8 (b)). Recent findings suggest that instead of constituting a long-lived step of NC growth they appear and disappear following a nucleation/dissolution mechanism,[36] similar to the proposed formation mechanism of atomically flat nanoplatelets and nanowires.[27,31]

The first description of 1D coordination polymers (CPs) was a byproduct of MSC research. Jiang and Kelley first reported a link between the presence of MSCs and nanorod formation.[37] They observed the formation of a transient species with a narrow absorption at 350 nm during the formation of CdSe nanorods with n-octadecylphosphonic acid as surface ligands. In their model the available monomer is limited by formation of MSCs above a concentration threshold. The MSCs apparently regulate the monomer feed by acting as a reservoir.[37] A later study shows that this reaction intermediate has the form of thin and highly anisotropic fibrils (see Figure 2.8 (c)) that aggregate into a colorless gel below 50 °C. The species was identified to be a coordination polymer of the composition $[\mathrm{Cd_2Se(ODPA)_n}]_\mathrm{m}$, most likely made up of individual MSCs linked by phosphonic anhydride bridging ligands,[33] or thin nanowires grown from an MSC seed. This species of coordination polymer is referred to as CP-350, due to its characteristic absorption peak at 350 nm (see Figure 2.8 (d)), and has morphology directing properties that favor anisotropic growth into nanorods. Their presence in the reaction is strongly dependent on the absence of water and other protic additives, as even traces of these molecules break up the coordination polymer, leading to a rapid dissolution and release of monomer.[38]

2.3.3 Transition metal doping of II-VI semiconductor nanoparticles

In bulk semiconductors, doping with transition metal ions (TM) is a fundamentally important approach to tune their electronic structures. Consequently, doping methods were applied to semi-

---

[34] Denis Gebauer, Antje Völkel, and Helmut Cölfen. *Science*, **322**: 1819–1822, 2008.

[35] Cristina Palencia, Kui Yu, and Klaus Boldt. *ACS Nano*, **14**: 1227–1235, 2020.

[32] Stefan Kudera et al. *Adv. Mater.*, **19**: 548–552, 2007.

[36] Christopher M. Evans, Alyssa M. Love, and Emily A. Weiss. *J. Am. Chem. Soc.*, **134**: 17298–17305, 2012.

[37] Zhong Jie Jiang and David F. Kelley. *ACS Nano*, **4**: 1561–1572, 2010.

[33] Daniel Wurmbrand et al. *Chem. Commun.*, **54**: 7358–7361, 2018.

[38] Nicholas Kirkwood and Klaus Boldt. *Nanoscale*, **10**: 18238–18248, 2018.

conductor nanocrystals as well, but the success was limited at first. While some materials, such as CdS and ZnSe,[39–41], could be doped with Mn^{2+} early on, doping of CdSe proved to be a challenge.

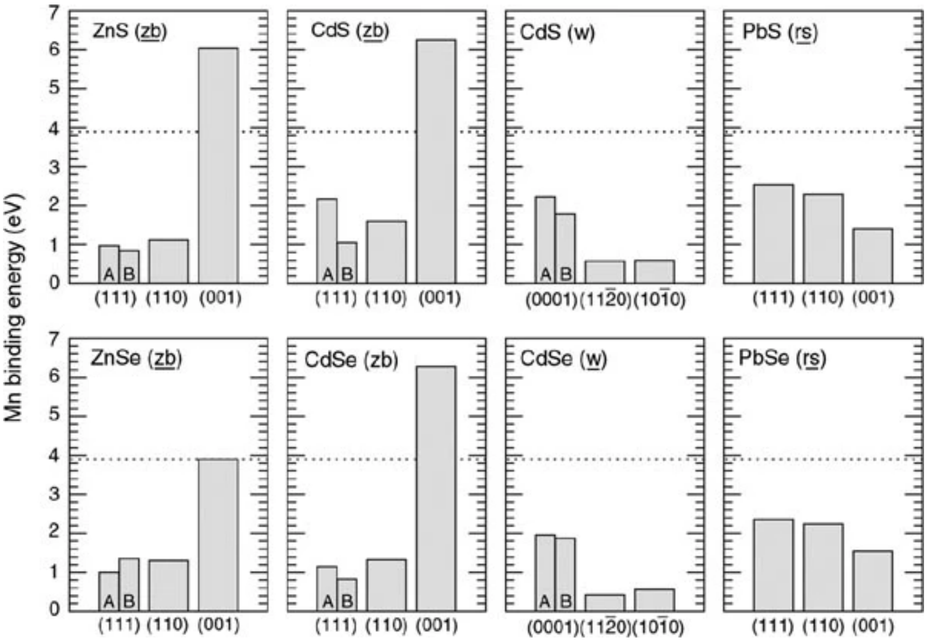

Figure 2.9: Binding energies of Mn adsorbates to semiconductor surfaces. The crystal structure of these semiconductors is either zinc blende (zb), wurtzite (w) or rock salt (rs); the most commonly occurring structure in nanocrystal form is underlined. Calculated binding energies of the three most common crystallographic orientations; 'A' and 'B' denote inequivalent terminations of surfaces having the same orientation. Dotted line indicates the the binding energy per atom of bulk crystalline Mn. Reprinted with permission from Erwin et al. [6]. Copyright 2005 Springer Nature.

Intuitively, the three materials should be equally easy to dope, as Mn dopants have similarly high bulk solubilitites in them. Further research showed, though, that for doping on the nanoscale, additional requirements have to be met. An essential factor is that doping usually occurs during the formation of the particles, i.e., during nucleation and growth. Both Schwartz et al. and Norberg et al. observed that dopants are excluded from nuclei during the synthesis.[42,43] The reason for this is that very small nanocrystals cannot compensate for the lattice distortion due to the incorporation of a guest ion. When the nucleus reaches a critical size the dopant can then be are reabsorbed. This implies that at some point, the dopant must be adsorbed to the particle surface, which Erwin et al. identified as the crux in the synthesis of Mn:CdSe: The binding energies of Mn adsorbates on semiconductor surfaces vary strongly both by facet and by material, with adsorption on wurtzite CdSe being the least favorable case (see Figure 2.9).[6] This explains why ZnS and CdS in sphalerit

---

[39] L. Levy, J. F. Hochepied, and M. P. Pileni. *J. Phys. Chem.*, **100**: 18322–18326, 1996.

[40] J. F. Suyver et al. *Phys. Chem. Chem. Phys.*, **2**: 5445–5448, 2000.

[41] D. J. Norris et al. *Nano Lett.*, **1**: 3–7, 2001.

[42] Dana A. Schwartz et al. *J. Am. Chem. Soc.*, **125**: 13205–13218, 2003.

[43] Nick S. Norberg et al. *J. Am. Chem. Soc.*, **128**: 13195–13203, 2006.

[6] Steven C. Erwin et al. *Nature*, **436**: 91, 2005.

structure are relatively easy to dope with Mn^{2+} compared to wurtzite CdSe. Another factor that is commonly cited as opposing dopant incorporation are self-purification effects, as the formation of defects becomes energetically less favorable, the smaller the particle.[44] Dopant ions thus tend to be excluded from the particle quickly.

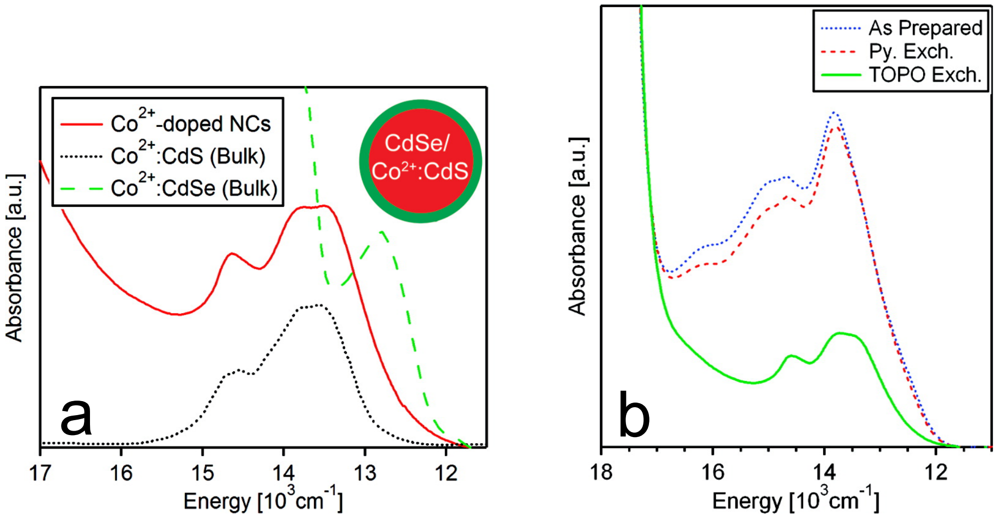

Figure 2.10: Synthesis of Co^{2+} doped NCs by cluster decomposition. UV/vis absorption analysis shows the unintentional formation of a CdSe/Co:CdS core shell particle if sulfur-conaining clusters are used in the synthesis (a). UV/vis spectra of Co^{2+}-doped nanoparticles in the energy range of Co^{2+} absorption before purification, as well as after TOPO and pyridine ligand exchange (b). Pyridine exchange is inefficient at removing adsorbed dopant ions, while TOPO significantly reduces their signal. Reprinted with permission from Archer, Santangelo, and Gamelin [45]. Copyright 2007 American Chemical Society.

While the lack of adsorption of Mn^{2+} ions prevented doping with them, Co^{2+} ions' tendency to effectively bind to surfaces leads to complications as well. Co^{2+} can be doped relatively easily into sulfide materials. One method to do so was developed in the Strouse group.[46] They used a cluster containing Cd^{2+} and chalcogenides (S^{2-}, Se^{2-}), as well as an analogue containing Co^{2+} as precursors for Co:CdSe nanoparticles. They found that the resulting particles had a dopant level equal to the molar ratio in the precursor mixture, which was 0.3. Theoretically, that meant stochiometric incorporation of dopant, and thus, that the dopant level can be easily controlled by changing the precursor ratio. However, later studies by the Gamelin group revealed that in order to synthesize Co:CdSe QDs, it is imperative to not have S^{2-} present in the reaction, as otherwise, a CdSe/Co:CdS core/shell structure will form (see Figure 2.10, (a)).[45] Additionally, they showed that Co^{2+} binds so effectively to the particle surface that it cannot be removed by the standard purification method at the time, a ligand exchange procedure with pyridine, resulting in an overestimation of the dopant level. They showed that ligand exchange with TOPO is significantly more effective, removing a high amount of dopant adsorbates from the particle surface (see Figure 2.10, (b)). These results

---

[44] Gustavo M. Dalpian and James R. Chelikowsky. *Phys. Rev. Lett.*, **96**: 226802, 2006.

[46] Khalid M. Hanif, Robert W. Meulenberg, and Geoffrey F. Strouse. *J. Am. Chem. Soc.*, **124**: 11495–11502, 2002.

[45] Paul I. Archer, Steven A. Santangelo, and Daniel R. Gamelin. *J. Am. Chem. Soc.*, **129**: 9808–9818, 2007.

put a focus on the importance of controlling for false negative reports of doping, as adsorbed ions can easily be mistaken for incorporated ions.

Archer, Santangelo, and Gamelin provided an explanation for this unintentional formation of a doped shell in CdSe/Co:CdS QDs. They argued that according to the hard and soft acids and bases principle (HSAB), Co^{2+} as an intermediate acid favors interaction with the harder S^{2-} over the soft Se^{2-}. The HSAB theory was originally developed by Pearson to explain empirical observations regarding binding preferences between Lewis acids and bases.[47,48] According to his theory, acids and bases can be categorized by their polarizability into soft (polarizable) and hard (nonpolarizable). Soft acids preferentially interact with soft bases, and vice versa. While this provides an empirical explanation for the formation of the doped shell, HSAB theory has its limits, as Pearson himself points out: a preference is by no means a hard rule, and the hardness does not differ significantly between S^{2-} and Se^{2-}, making it difficult to explain the high preferentiality of dopant incorporation by hard numbers.[49] It has, however, proven to be a good rule of thumb for which material combinations work, e.g., for doping, and is thus widely used in research. The HSAB principle provides a qualitative reason for why Mn:CdSe doping proved such a challenge as well.[50] Mn^{2+} ions are hard acids, due to their half filled d^5 shell, and thus cannot outcompete the soft Cd^{2+} ions for the soft Se^{2-} base.

Mn^{2+}-doping of CdSe nanoparticles was only solved in 2013, when the Gamelin group published their protocol for diffusion doping.[51] This synthesis utilizes pre-synthesized particles that are treated with TM oleate and an excess of chalcogenide. The chalcogenide excess tunes the chemical potentials in such a way that TM^{2+} adsorption is favorable, thus overcoming the main barrier towards Mn:CdSe particles, as presented in Figure 2.11. Mn-chalcogenide units are deposited on the particles. Then, the ion diffuses into the particle. This method results in very high doping levels (up to dopant cationic fractions of 0.4), and can be adapted for a variety of ions and host materials. Since dopant-chalcogenide units are deposited during the reaction, the particles increase slightly in size, but their overall morphology is retained. Still, dopant is easily lost: Subsequent treatment with host ions, such as Cd^{2+}, leads to partial cation exchange. This can be utilized to control the doping level.[52]

A wide variety of dopant/host systems has become available over the years, however, the question of the exact location of the dopant within the particle remains, including, but not limited to, the issue of incorporated vs. adsorbed ions: Robust methods are needed to tell the two apart. In addition to emission spectroscopy,[53], and, in the case of Co^{2+}-doping, UV/vis absorption spectroscopy, EPR is an easily available, versatile way to investigate that issue for doping with paramagnetic ions.[54]. The method's sensitivity allows for distinction between various dopants positions, e.g., within the particle, close to the surface, and adsorbed, and chemical environments, for example different host materials or differences in dopant concentration. Another well-suited method is magnetic circular dichroism spectroscopy, which is even more sensitive to the environment of a

---

[47] Ralph G. Pearson. *J. Am. Chem. Soc.*, **85**: 3533–3539, 1963.

[48] Ralph G. Pearson. *Inorg. Chem.*, **27**: 734–740, 1988.

[49] Ralph G. Pearson. *Inorg. Chim. Acta*, **240**: 93–98, 1995.

[50] Raffaella Buonsanti and Delia J. Milliron. *Chem. Mater.*, **25**: 1305–1317, 2013.

[51] Vladimir A. Vlaskin et al. *J. Am. Chem. Soc.*, **135**: 14380–14389, 2013.

[52] Charles J. Barrows et al. *ACS Nano*, **10**: 910–918, 2016.

[53] Payel Mondal et al. *J. Phys. Chem. C*, **125**: 11007–11013, 2021.

[54] Huijuan Zhou et al. *J. Appl. Phys.*, **99**: , 2006.

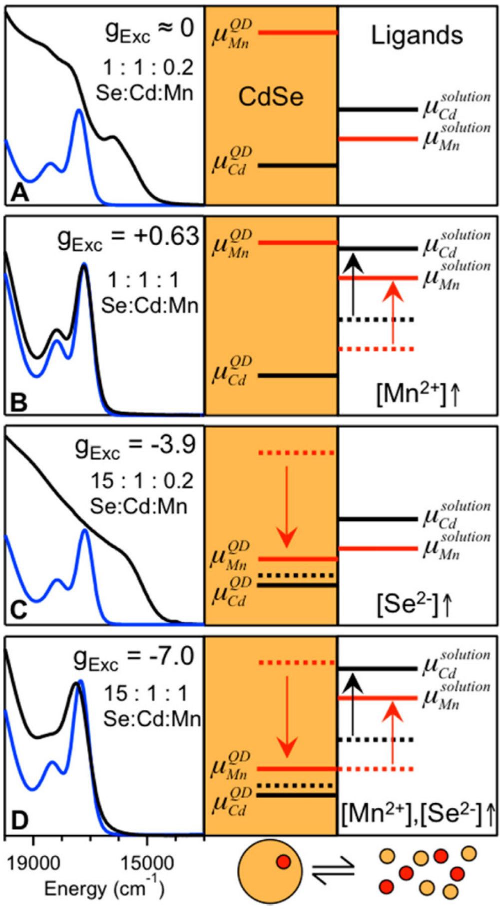

Figure 2.11: Mn^{2+}-diffusion doping of CdSe NCs. UV/vis spectra before (blue) and after doping (black). Changes in chemical potentials μ depending on the concentration of Mn^{2+} and Se^{2-} in the concentration. An excess of both Mn^{2+} and Se^{2-} suppresses ripening effects and enables the adsorption of Mn-Se units on the particle surface, which leads to doping. Reprinted with permission from Vlaskin et al. [51]. Copyright 2013 American Chemical Society.

magnetic ion, as well as its concentration.[55–57] This method is however very specialized and not widely available.

From a synthetical standpoint, the control of the dopant location is interesting in terms of investigating elementary processes, e.g., exciton transfer. So far, control over the dopant location has mainly been achieved in terms of the radial position, e.g., by adsorbing ions to the particle surface before adding a shell,[58] or doping the shell itself.[59] In terms of doping specific sites of a

---

[55] Charles J. Barrows, Vladimir A. Vlaskin, and Daniel R. Gamelin. *J. Phys. Chem. Lett.*, **6**: 3076–3081, 2015.

[56] Rachel Fainblat et al. *Nano Lett.*, **16**: 6371–6377, 2016.

[57] Joanna Dehnel et al. *ACS Nano*, **14**: 13478–13490, 2020.

[58] Yongan Yang et al. *Chem. Eur. J.*, **15**: 3186–3197, 2009.

[59] Elan Hofman et al. *J. Am. Chem. Soc.*, **139**: 8878–8885, 2017.

nanostructure, it is possible to introduce both Mn^{2+} ions,[60] as well as Co^{2+} ions[61] into nanoclusters with control over the exact atom to be exchanged.[62]

In terms of controlling the position beyond the radial distribution, the closest thing in literature is particle cation exchange. These processes allow for the exchange cation of certain domains of a particle.[63] However, this is only possible if the material/dopant combination is suitable.[64] Typically, in a cation exchange reaction, a bivalent cation is exchanged for two monovalent cations, such as Cu^{+} and Ag^{+}. Doping with these ions can thus be achieved by this method.[65,66] Bivalent TM^{2+} ions are harder to introduce. One of the few reports in this area are by Eilers et al., who reported doping of ZnTe MSCs with Mn^{2+}.[67] However, cation exchange is only available for a selection of dopant/host combinations, and no reports exist on the doping of CdSe or CdS nanoparticles with TM^{2+} ions *via* this route.

---

[60] J Yang et al. , **137**: 12776–12779, 2015.

[61] Jiwoong Yang et al. *Nano Lett.*, **18**: 7350–7357, 2018.

[62] Fumitoshi Kato and Kevin R. Kittilstved. *Chem. Mater.*, **30**: 4720–4727, 2018.

[63] Benjamin C. Steimle, Julie L. Fenton, and Raymond E. Schaak. *Science*, **367**: 418–424, 2020.

[64] Luca De Trizio and Liberato Manna. *Chem. Rev.*, **116**: 10852–10887, 2016.

[65] Shinjita Acharya and Narayan Pradhan. , **115**: 19513–19519, 2011.

[66] Ayaskanta Sahu et al. *Nano Lett.*, **12**: 2587–2594, 2012.

[67] Joren Eilers et al. *J. Phys. Chem. Lett.*, **3**: 1663–1667, 2012.

3 Scope

This thesis aims to achieve precise control over the location of TM^{2+} dopant, specifically Mn^{2+} and Co^{2+} ions, within II-VI semiconductor heterostructures. Up to now, only radial control over the dopant location has been achieved. Here, the concept will be expanded towards anisotropic control, achieving spatial separation of a reporter, e.g., a seed, and an alternative relaxation pathway, the dopant, within the same nanoparticle.

This requires enhanced knowledge of the mechanisms that lead to symmetry breaking and anisotropic growth. The first chapter will thus focus on the so far largely disregarded factor of the role of reaction intermediates in anisotropic growth. Fibrillar 1-dimensional intermediates have previously been reported in the context of nanorod growth. Their role will be further studied, as well as the factors that enhance or hinder their formation. This will lead to a better understanding of anisotropic growth mechanisms, and provide the opportunity so influence them. Reaction intermediates with a 0-dimensional structure (0D) will then be studied in the context of a different type of anisotropic reaction. Magic size clusters have been discussed in the context of tip growth on nanorods before, but their role in the reaction was not fully uncovered. In this section the question will be answered whether they have a shape-directing influence on the reaction. This will help clear up the role of MSCs in the reaction, answer whether their occurrence is the key factor deciding whether tips can be grown, and enable to find reaction conditions suitable to tip growth of a wider array of materials.

The second chapter will focus on finding the right doping approach for anisotropic introduction of dopants. As an intermediate goal, dopants will be selectively introduced into one domain of a nanoheterostucture, while other domains remain undoped. This approach will exploit the varying affinities of materials towards dopants. For instance the introduction of Co^{2+} ions into CdS is relatively easy, while Mn^{2+} into CdSe is more challenging and requires specific conditions to succeed. These reactivity differences will be utilized in order to only dope one material within a heterostructure, e.g., only the CdS rod shell, while the CdSe seed remains undoped. Different stages of the heterojunction formation can be targeted by different doping methods, i.e., doping can occur before, after, or during heterojunction formation. These will systematically be screened for the optimal point of dopant introduction, which will in turn lead to finding a method for localized doping.

In the third chapter, the focus will be on doping only part of a domain, e.g., the tip of a nanorod, while the rest of the rod (of the same material) remains undoped. Building on the findings of the previous two chapters the gained knowledge of anisotropic growth will be combined with the understanding of how dopant introduction into nanoparticles works. A focus will lie on understanding the diffusion processes that counteract dopant localization to be able to control them and their influence on the dopant locale.

In the long term introducing a distance between the dopants and the reporter seed will provide an additional option to further tune electronic characteristics and study relaxation dynamics. As these processes are the foundation for nanoparticle applications, e.g., in catalysis and optical applications, achieving localized doping has the potential to bring along new developments in these areas that might prove relevant to everyday life.

4 Understanding anisotropic growth: The role of reaction intermediates

Reaction intermediates have been reported in various nanoparticle syntheses. Mainly, these reactions were aimed towards isotropic particles, but recent studies point towards the role of intermediates for the growth of anisotropic particle: While Wurmbrand et al. found that fibrillar coordination polymers (CPs) show self-templating effects that lead to the formation of nanorods,[33] Florian Enders discovered in his thesis that the occurrence of magic size clusters (MSCs) during anisotropic tip growth is related to the growth of heteromaterial tips on preexisting nanorods.[68] A closer look at reaction intermediates is thus promising in order to gain deeper insight into the underlying principles that govern anisotropic growth as well as symmetry breaking. This will provide the groundwork necessary to tackle the challenge of anisotropically introducing dopants.

The first part of this chapter focuses on the role of CPs for anisotropic rod growth, a factor which is so far rarely discussed. Most studies concentrate on other aspects, such as ligand chain length.[69] Here, multiple factors that influence CP formation are investigated, as well as how influencing CP formation changes anisotropic growth. The results are summarized in a proposed reaction mechanism. Using this knowledge, better control over anisotropic growth is achievable. This will prove useful for the more complex systems that enable dopant introduction.

In the second part, the role of MSCs for tip growth is investigated. Building on the works of Deutsch, Neeman, and Oron[20] the tip growth synthesis was previously refined to reliably work for MTe ,[23] but the same was not possible for MSe tip growth (M=Cd,Zn).[68] The occurrence of MSCs appear to be related to successful growth of heteromaterial tips, but their specific role is unclear. This part of the thesis aims to answer whether MSCs have a specific function during the growth of heteromaterial tips, which makes them necessary for a successful reaction. If that is the case, doped MSCs could be used in order to grow doped tips on nanorods, which would fulfill the aim to introduce dopants in a localized fashion.

Parts of this chapter have been previously published and adapted from the following publication:

Danja Fischli, Florian Enders, and Klaus Boldt. Kinetically Driven Cadmium Chalcogenide Nanorod Growth Fed by Local Cluster Aggregates. *Journal of Physical Chemistry C*, **124**: 12774–12783, 2020. DOI: `10.1021/acs.jpcc.0c02730`

Additionally, the second part of this chapter provided groundwork for the following publication:

Florian Enders et al. Regioselective Growth Mechanism of Single Semiconductor Tips on CdS Nanorods. *Chemistry of Materials*, **32**: 10566–10574, 2020. DOI: `10.1021/acs.chemmater.0c03636`

---

[33] Daniel Wurmbrand et al. *Chem. Commun.*, **54**: 7358–7361, 2018.

[68] Florian Enders. *Tailoring the Charge Carrier Relaxation in Colloidal Semiconductor Nano-Heterostructures*. PhD thesis. Konstanz: University of Konstanz, 2019.

[69] Dahin Kim et al. *ACS Nano*, **11**: 12461–12472, 2016.

[20] Zvicka Deutsch, Lior Neeman, and Dan Oron. *Nat. Nanotechnol.*, **8**: 649–653, 2013.

[23] Florian Enders et al. *Nanoscale*, **10**: 22362–22373, 2018.

4.1 Coordination polymers in anisotropic rod growth

4.1.1 General considerations for nanorod growth

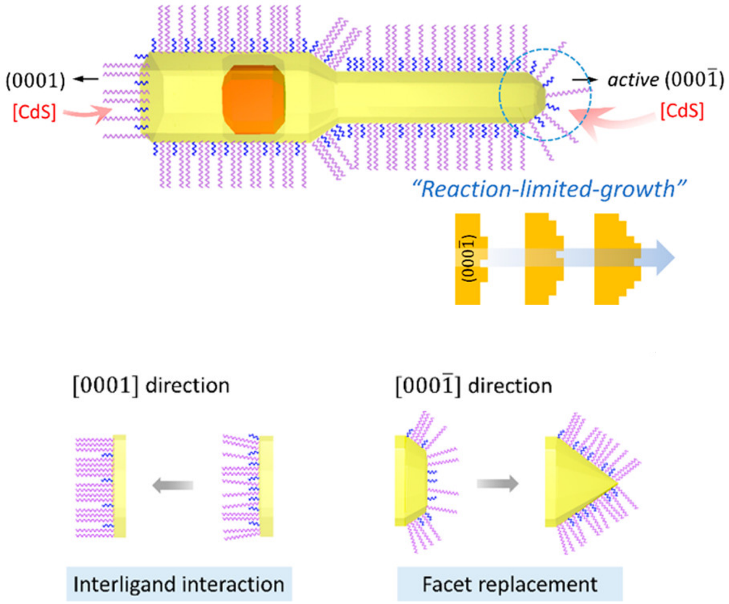

Scheme 4.1: Different shape of the crystal facets of a CdSe/CdS nanorod. The more strongly curved $(000\bar{1})$ facet is favored for deposition of monomer. Reprinted with permission from Kim et al.[69] Copyright 2016 American Chemical Society.

Generally, a limited number of factors for anisotropic seeded growth are discussed, mainly the monomer concentration, diffusion or reaction control of monomer deposition, facet reactivity, ligand chain length, and coverage. The correct range of the first of these factors, the monomer concentration, can be derived from the LaMer diagram (Figure 2.6): It has to be maintained between the critical oversaturation thresholds for heterogeneous and homogeneous nucleation. This suppresses the nucleation of new particles.

Additionally, growth needs to be reaction instead of diffusion limited. If the rate determining step is the deposition of material at the seeds' surface, particle growth proceeds rapidly and selectively in one dimension at the crystal facet with the highest energy. In contrast, in a diffusion controlled reaction the reactive facets disappear and isotropic growth towards the Wulff shape occurs. In CdSe and CdS nanorods this is indicated by different tip shapes along the elongated c-axis: while the (0001) facet appears flat the $(000\bar{1})$ facet is replaced by pyramidal growth,[23,69,71] as shown in Figure 4.1.

With regard to facet reactivity, the wurtzite crystal structure is ideally suited towards anisotropic growth: It is inherently anisotropic, with a chalcogenide terminated, negatively charged $(000\bar{1})$ end and a metal terminated, positively charged (0001) end. This leads to an intrinsic dipole of

---

[71] Giovanni Bertoni et al. *ACS Nano*, **6**: 6453–6461, 2012.

the nanorods due to the oppositely charged, polar facets,[72] as well as different reactivities and consequently, reaction rates, which can be further increased by selective passivation of the exposed facets.

For II-VI semiconductor rods this is usually achieved by employing a mixture of short and long chain alkylphosphonic acids.[11,21,73] Short chain ligands bind more efficiently to a nanocrystal surface than those with a longer chain. This is despite the fact that phosphonate groups have the same binding affinity, which is attributed to the reduced repulsive osmotic pressure between shorter chains.[74] As this effect is pronounced for the wurtzite $\{0001\}$ facets, the chain length can be used to direct the particle shape and crystal structure: facets that are more densely packed with ligands are less accessible to monomer. This leads to different relative growth rates, with faster material deposition on the anion-rich $(000\bar{1})$ facet than on the cation-rich (0001) facet. This difference in growth rate is easily observed in CdSe/CdS seeded nanorods, in which the CdSe seed is usually located at about two thirds along the c-axis.[71]

The rate of precursor decomposition and subsequent release of monomer as an important factor in anisotropic growth has played only a minor role in literature so far. A very fast decomposition reaction, e.g., when pyrophoric precursors are used, leads to reaction kinetics that are dominated by the diffusion of material to the seeds' surface. Slow monomer formation, however, leads to the disappearance of the unpassivated $(000\bar{1})$ facet and would mitigate the fast 1D growth regime. Ideally, the reaction is thus performed in a regime in-between the two extremes. This can be achieved by decoupling the formation of monomer from the precursors from its release at the reaction site. One possible means to do this is by using reaction intermediates as monomer reservoirs.

This chapter will expand the focus of anisotropic growth factors from ligand chain length and overall monomer concentration to the role of CPs as reaction intermediates. The hypothesis is that heterogeneously distributed aggregates of polymeric magic-sized cluster fibrils cause fast and regio-selective growth of seeded CdSe/CdS dual diameter nanorods under reaction-limited control. These intermediates decompose rapidly into monomer at the surface of the seeds and feed rapid 1D growth. Therefore, under conditions favoring CP nucleation the reaction proceeds under much higher local concentrations than what would be expected from a homogeneous distribution of nucleation monomer. The hypothesis will be tested by varying the S-Cd precursor and short to long chain ligand ratio, by adding zero-dimensional MSCs as precursors, and by addition of water. These strategies suppress the formation of coordination polymer and should lead to a more homogeneous distribution of monomer and reduced 1D growth rates of CdS.

4.1.2 Synthesis and characterization of CdSe/CdS dual rods

In order to be able to monitor the selectivity of particle growth along the c-axis, a suitable system is necessary. Kim et al. used spherical seed particles with more than 5 nm in diameter which made it possible to easily distinguish rod growth in $[0001]$ direction and $[000\bar{1}]$ direction from the width of the growing segments.[69] A similar approach was used for the experiments underlying this chapter: The standard rod synthesis by Carbone et al. was adapted for CdSe nanorod seeds with a diameter

---

[72] Liang-Shi Li and A. Paul Alivisatos. *Phys. Rev. Lett.*, **90**: 097402, 2003.

[11] Luigi Carbone et al. *Nano Lett.*, **7**: 2942–2950, 2007.

[21] Dmitri V. Talapin et al. *Nano Lett.*, **7**: 2951–2959, 2007.

[73] Dirk Dorfs et al. *Small*, **4**: 1319–1323, 2008.

[74] Jing Huang, Maksym V. Kovalenko, and Dmitri V. Talapin. *J. Am. Chem. Soc.*, **132**: 15866–15868, 2010.

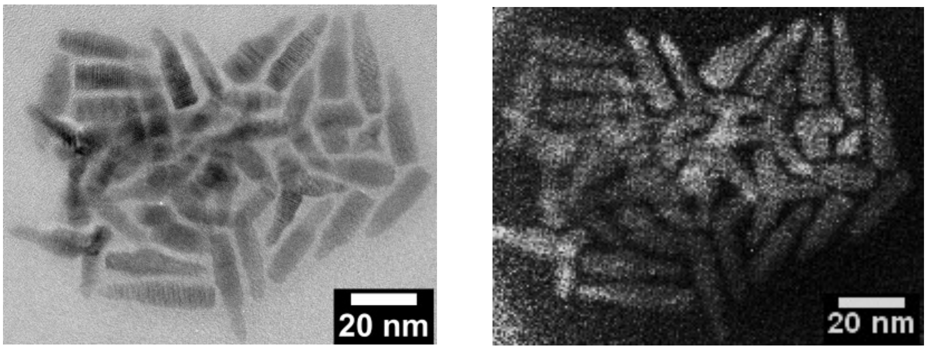

Figure 4.1: Selective growth of CdS domains on CdSe nanorod seeds during dual rods synthesis. Unfiltered TEM micrograph (left) and energy-filtered image obtained at the Sulfur $L_{2,3}$ edge (right).

of 6 nm. Under conditions that favor rapid, one-dimensional growth the reaction yields bottle-shaped dual-diameter nanorods in which the larger diameter CdSe part is easily distinguishable from the narrow CdS rod growing selectively from one end of the core particle. The experimental details can be found in Section 8.3.6. This selectivity was confirmed by energy filtered transmission electron microscopy (EFTEM) obtained at the sulfur $L_{2,3}$ edge as shown in Figure 4.1. Sulfur-rich regions in the particles appear brighter in the dark field and can be clearly assigned to the thin neck region, as well as to a small deposition at the opposing end of the seed.

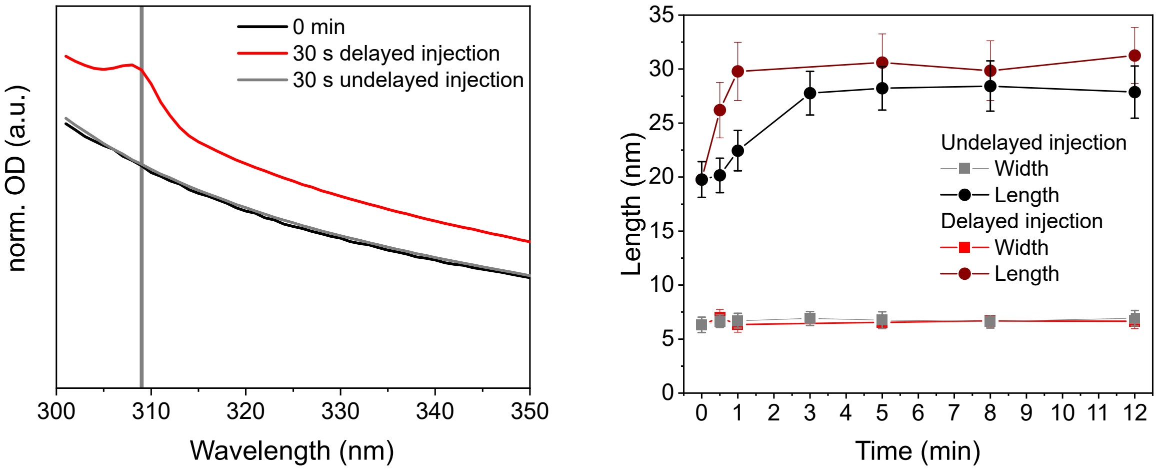

Figure 4.2: Absorption spectra of samples drawn during dual rod synthesis (left): At 0 s (black) and 30 s after undelayed (red) and undelayed injection (gray) of sulfur precursor addition. For the undelayed injection, seed particles and sulfur precursor were injected simulatneously, for the delayed, sulfur precursor was added 30 s after the seeds. Length (dots) and width evolution (squares) during particle growth with delayed (red) and undelayed sulfur precursor injection (black and gray). Lines are a guide to the eye.

Xia et al. report an increased selectivity of 1D growth at the $(000\bar{1})$ facet when the seed particles were injected with a 20 s delay after hot-injection of the precursor that starts the reaction.[75] As

---

[75] Chenghui Xia et al. *J. Am. Chem. Soc.*, **140**: 5755–5763, 2018.

a possible reason they propose that the conversion rate from precursors to monomer is the rate limiting step in the formation of binary semiconductors, and that the delay gives the system the necessary time to equilibrate at a higher concentration of monomer when the seeds are injected. If applied to the system at hand it is also found that a delayed seed injection leads to faster growth and yields higher aspect ratio nanorods, as shown in Figure 4.2 (right). The faster growth is correlated with the appearance of a sharp peak in the absorption spectrum at 309 nm, while no such signal appears when the sulfur precursor and the seeds are injected simultaneously (see Figure 4.2 (left)). The peak at 309 nm has been reported before as belonging to a reaction intermediate during CdS particle synthesis.[76] The selectivity of growth at the $(000\bar{1})$ over the (0001) facet, i.e., in length, is significantly more pronounced compared to the study by Kim et al. under similar conditions.[69] Analysis of the nanorod width using TEM shows that deposition at facets perpendicular to the growth direction, i.e., in the particle width, is negligible (see Figure 4.2 (right)).

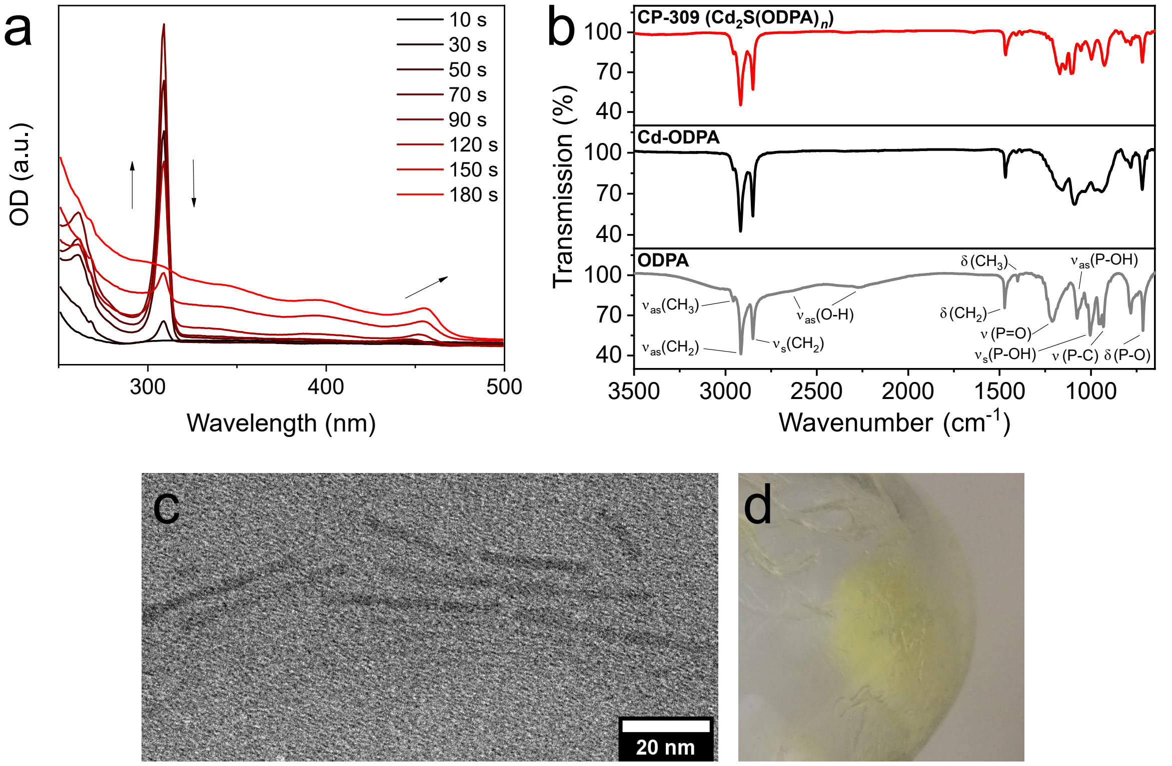

Figure 4.3: UV/vis spectra of CP-309 formation and subsequent formation of nanoparticles (a), IR chracterization of isolated CP-309 (b), TEM micrograph (c) and photograph (d) of the substance.

Figure 4.3 (a) shows UV/vis spectra taken during the early stages of a rod synthesis without any seeds. The signal at 309 nm appears after approximately 30 s of reaction time, and increases in intensity until approximately 90 s into the reaction, at which point it starts to decrease until it falls below the detection limit after 180 s. This signal does not shift, but remains stationary at the same energy. At 50 s a second signal appears at 450 nm. This peak slowly increases in intensity and

---

[76] Qiyu Yu and Chun-Yan Liu. *J. Phys. Chem. C*, **113**: 12766–12771, 2009.

shifts to longer wavelengths, which is attributed to particle growth and a simultaneous decrease of exciton energy. The biggest changes in this peak are observable from 90 s on, when the CP-309 signal starts to decrease. The energetic position and shape of this peak, along with the energy shift is characteristic for CdS nanorods.

The TEM micrograph of the sample taken at 150 s of reaction time confirms this. It shows rod-shaped particles, along with fibrillar 1D structures surrounding it (Figure 4.3 (c)). The isolated intermediate appears as a waxy solid that transforms into nanorods upon heating (Figure 4.3 (d)). Further analysis using IR spectroscopy shown in Figure 4.3 (b) allow the species to be identified as the sulfide analogue of the previously reported CdSe coordination polymer (CP-350).[33] Energy dispersive X-ray spectroscopy (EDX) analysis revealed a Cd:S ratio of 2.54:1 (see Appendix B, Table B.1), slightly above the expected value of 2:1 determined for the CdSe analogue. This discrepancy can be resolved by assuming co-precipitation of Cd phosphonates, which have a similar solubility and tendency to form extended networks.[77]

As the CdS reaction intermediate appears at 309 nm in the UV/vis spectra it will be referred to as CP-309 from now on. Additionally, a peak at 260 nm emerges and decreases together with the one at 309 nm. This peak has been reported before,[76] where it was attributed to a molecular species that can be separated from the 309 nm species by size-selective precipitation. This species is observable at short wavelengths that are only accessible by using appropriate solvents with a low absorption cut-off wavelength, e.g., *n*-octane, which was used for these experiments. These solvents in turn complicate particle isolation. Since it was only detected concurrently with the 309 nm peak it can be assumed that the two species are at equilibrium. The discussion will thus exclusively cover CP-309 and disregard the 260 nm species.

4.1.3 Influence of the sulfur concentration on CP-309 formation

The S:Cd ratio of CP-309 of approximately 1:2 from EDX analysis differs dramatically from the employed ratio in the typical reaction conditions during rod growth of 8:1.[11] This discrepancy appears counter-intuitive, and leads to whether a precursor ratio that resembles the final product more closely would result in more efficient formation of CP-309, and, in turn, anisotropic growth. In order to investigate this question, UV/vis kinetic measurements described above were repeated for S:Cd ratios of 20:1, 12:1, and 2:1. The amount of Cd precursor, which is the limiting factor for the maximal monomer concentration, was kept constant. As temperature has an impact of the formation kinetics of CP-309, precautions were taken in order to minimize fluctuations induced by the different injection volumes: the injection temperature was adjusted depending on the injection volume, to 335 °C for a 2-fold excess of TOP-S, to 360 °C for an 8-fold excess, and to 370 °C for a 12-fold and 20-fold excess. In all reactions except for the 20-fold excess this resulted in cooling to the target temperature of 320 °C upon injection. As the solvent boiled at 370 °C the temperature could not be raised further and injecting the large volume for the 20-fold TOP-S excess resulted in a brief temperature drop below 320 °C. The results of these experiments can be found in Figure 4.4.

Figure 4.4 (b) shows that decreasing the S:Cd ratio to 2:1 leads to no formation of CP-309 at all, but also no homogeneous nucleation of CdS NCs over the course of the monitored time frame. This is attributed to the fact that at the reduced chalcogenide concentration the solubility product $K_s = [\mathrm{Cd}^{2+}][\mathrm{S}^{2-}]$ does not exceed the critical value necessary for nucleation. In the

---

[77] Guang Cao, Vincent M. Lynch, and Leonard N. Yacullo. *Chem. Mater.*, **5**: 1000–1006, 1993.

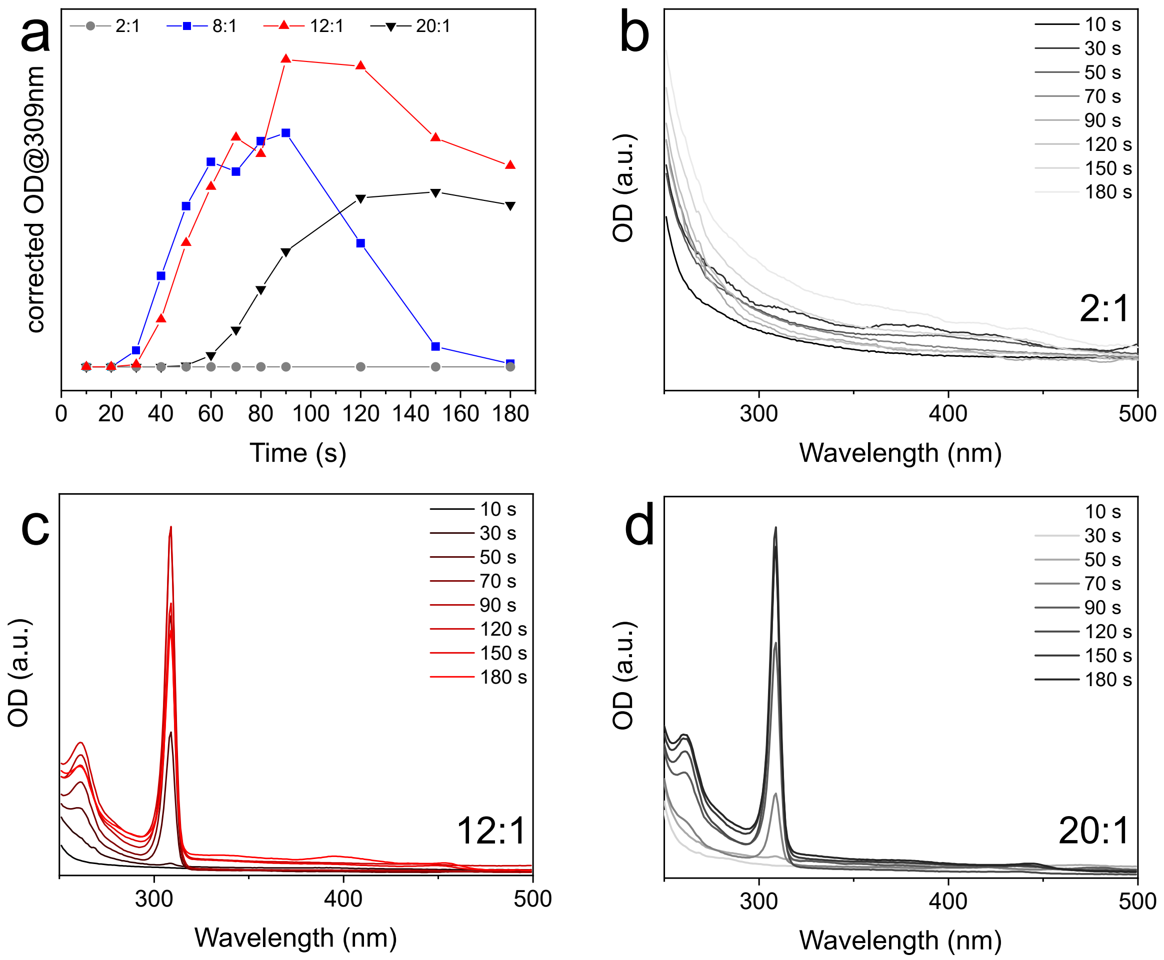

Figure 4.4: Influence of the sulfur concentration: Overview over CP-309 UV/vis kinetics at different S:Cd ratios (a). UV/vis kinetic primary data with S-Cd ratio of 2:1 (b), 12:1 (c), and 20:1 (d).

intermediate range (8- and 12-fold excess, Figure 4.3 (a) and Figure 4.4 (c)) CP-309 formation occurs at approximately the same rate, but its dissolution becomes slower with increasing S:Cd ratio. This can be due to either better kinetic stabilization of the reaction intermediate or by an equilibrium that is shifted in favor of CP-309 formation by the high sulfur excess.[33] When a 20-fold excess of chalcogenide precursor was used, the CP-309 signal reached intensities comparable to an 8-fold excess, but with a delay. CP-309 is first observed at 60 s into the reaction and reaches its maximum intensity at 150 s, as opposed to at 30 s and 90 s, respectively (Figure 4.4 (d)). It is also notable that the slope of the signal intensity as a function of the reaction time is less steep both during formation and depletion of CP-309, so the reaction intermediate forms and dissolves more slowly. This behavior is attributed to the slower temperature recovery due to the large injection volume.

Figure 4.5 shows the effect that the presence of CP-309 has on heterogeneous nucleation and anisotropic growth. The standard reaction scheme is shown in Scheme 4.2. The experiments were

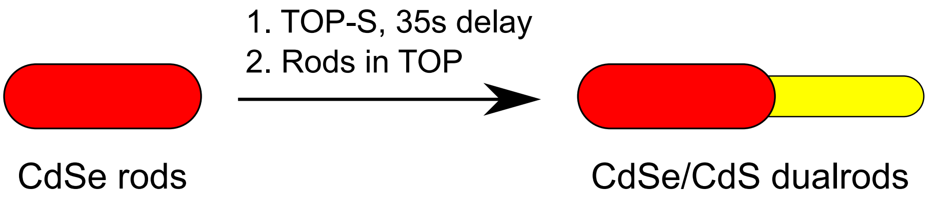

Scheme 4.2: Reaction scheme for dual rod growth via delayed injection.

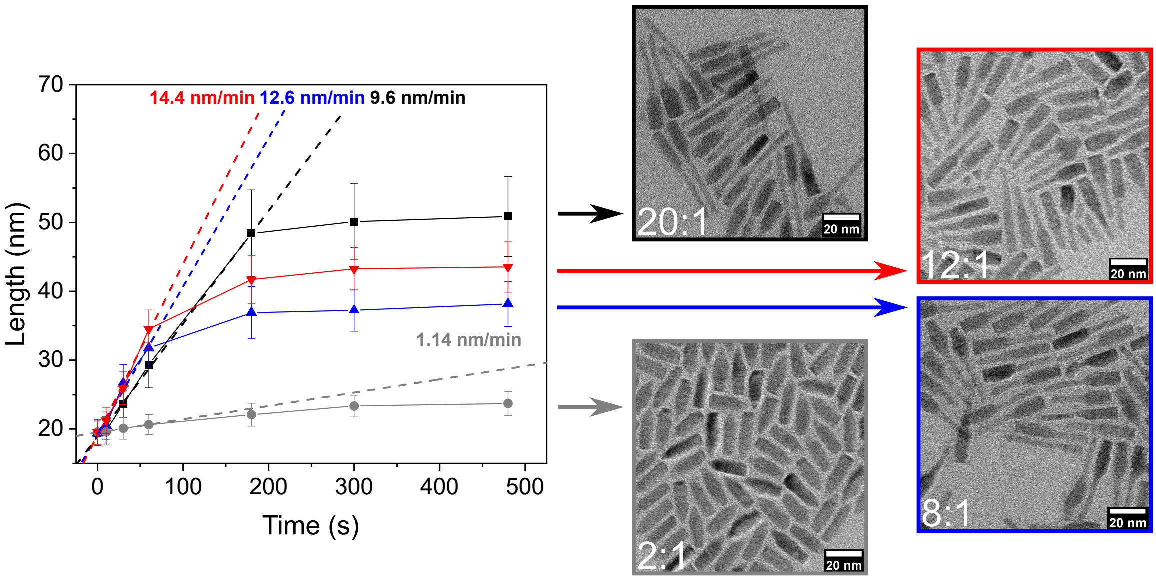

Figure 4.5: Influence of the sulfur concentration: TEM kinetics of dual rod growth at different S:Cd ratios (left). Solid lines are linear fits of the first 60 s of reaction, dashed lines are a guide to the eye. TEM micrographs of rods synthesized at different Cd:S ratios (right).

conducted as described before, but this time included the delayed injection of CdSe nanorod seeds, 35 s after TOP-S injection in the case of 2-, 8-, and 12-fold sulfur excess, and with a 60 s delay for the 20-fold excess to account for the longer recovery period. The time of seed injection was set to $t = 0$ s. Linear fits over the first 60 s (4 data points) were performed to compare the growth rates of the three reactions.

All kinetics follow the same trend: nanorods grow quickly at a constant rate for about 60 s, followed by a significant decrease in growth rate that indicates depletion of available monomer. The rods reach their final length after approximately 3 min. At 8-, 12-, and 20-fold TOP-S excess the initial growth rates were similar ($v_{8:1} = (12.6 \pm 1.3)$ nm/min, $v_{12:1} = (14.4 \pm 1.0)$ nm/min, $v_{20:1} = (9.6 \pm 1.2)$ nm/min) and closely follow the rates of formation for CP-309 observed without seeds present (1.60 min for a 8:1 ratio, 1.48 min for a 12:1 ratio, 0.89 min for a 20:1 ratio). The deviations between the measurements can be explained by fluctuations of the reaction temperature. For the 2-fold excess the growth rate is significantly slower, with $v_{2:1} = (1.14 \pm 0.11)$ nm/min.

This agrees with the observations by Kim et al., who report 1D growth with a rate of 19 nm/min.[69] The ∼ 1.6-fold higher growth rate is in accordance with the 30 K higher reaction temperature employed in the earlier study. The Arrhenius equation predicts an increase by a factor of 2 for an activation energy of $E_A = 86\,\mathrm{kJ\,mol^{-1}}$ for the decomposition of CP-309.[33,78] However, in addition to the shape-control from surface passivation by ligands this leads to the hypothesis that the presence of CP-309 is an important factor in the reaction mechanism, based on the strong correlation between the rates of formation of CP-309 and 1D growth. As the growth rate is significantly slower in the absence of CP-309 at a low S:Cd ratio it appears likely that dissolution of CP-309 into the active monomer species is the rate determining step. The thin CdS rods reach lengths of 4 nm, 19 nm, 24 nm and 31 nm for a sulfur excess of 2, 8, 12, and 20, respectively. The dependence of the final length on the S:Cd ratio follows the expected decrease of the effective solubility product according to the law of mass action when the activity of one ion is increased with respect to the other. However, the fact that the higher oversaturation does not lead to more homogeneous nucleation or isotropic growth, but to prolonged growth in the $[000\bar{1}]$ direction, supports the critical role that CP-309 plays for anisotropic growth.

4.1.4 Ligand influence on CP-309 formation

Kim et al. established the ratio between long and short chain phosphonate ligands as the main factor that contributes to anisotropic growth.[69] Therefore the influence of the fraction of *n*-octadecylphosphonic acid (ODPA) compared to *n*-hexylphosphonic acid (HPA), $f_{\mathrm{ODPA}} = n_{\mathrm{ODPA}}/(n_{\mathrm{ODPA}} + n_{\mathrm{HPA}})$, on the formation of CP-309 was investigated. f_{ODPA} was varied from 1 to 0.46 in the absence of seed particles while keeping the overall phosphonic acid concentration constant.

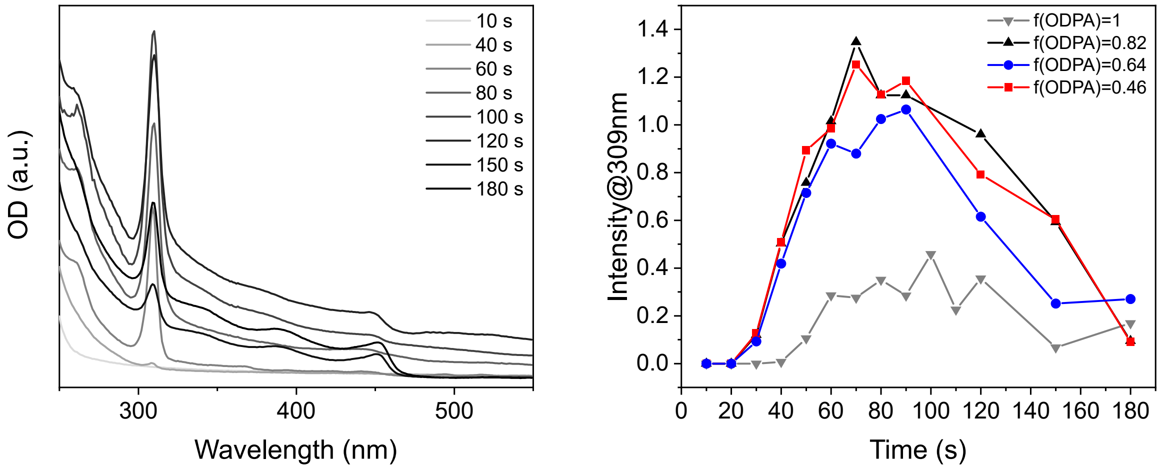

Figure 4.6: UV/vis spectra of CP-309 formation with pure ODPA (left) and formation of CP-309 depending on the fraction $f_{\mathrm{ODPA}} = n_{\mathrm{ODPA}}/(n_{\mathrm{ODPA}} + n_{\mathrm{HPA}})$ (right).

The results of this experiment are shown in Figure 4.6 (right). With no HPA present ($f_{\mathrm{ODPA}} = 1$, gray) CP-309 forms after 40 s and reaches the highest intensity after 100 s. Homogeneous nucleation occurs after 80 s and CP-309 is not fully depleted after 180 s (see Figure 4.6 (left)). When HPA was added CP-309 formation started earlier, 20 s after injection, proceeded at a faster rate, and yielded approximately 3 times more of the intermediate. Depletion of CP-309 occurred at

---

[78] B. D. Dickerson et al. *Appl. Phys. Lett.*, **86**: 171915, 2005.

similar times for all reactions. No significant dependence on the HPA concentration was observed, as all tested HPA concentrations lead to similar amounts of CP-309, on a similar timescale (see Figure 4.6 (right), blue, red, and black).

The increase of reaction rate and yield can be attributed both to the higher mobility and reactivity of short chain ligands, which makes more monomer available, as well as their reduced steric hindrance. Additionally, different solubilities of HPA and ODPA derivates contribute to the preference of CP-309 for short chain ligands, as well as solubilities of the intermediate species they terminate. The intermediate species terminated by the long chain ligand ODPA have a reduced solubility in TOPO compared to HPA-terminated intermediate species. Similar solubility differences have been documented for ODPA derivatives, compared to shorter chain phosphonates.[79] The reduced solubility of intermediates that are stabilized only by ODPA is apparent from the cloudiness of the reaction solution and the increased baseline intensity of the samples taken after 80 s, 100 s and 120 s in Figure 4.6 (left). As the reaction progresses and CP-309 is consumed the trend reverses, CP-309 is dissolved and the absorption spectra after 150 s and 180 s show no scattering.

These results match the observations of Kim et al. who performed a similar experiment in which they grew dual diameter nanorods in different PA ligand mixtures. They describe that in pure ODPA hardly any rod growth occurs, while an increasing fraction of HPA ligand leads to an increase in growth. They attributed this to slow monomer supply at the $(000\bar{1})$ facet if only ODPA ligands are present, because diffusion occurs less efficiently through longer than through shorter chain ligands.[69] Increasing the HPA fraction increases growth in [0001] direction, while the growth rate in $[000\bar{1}]$ direction remains constant. The growth rate at the (0001) facet is thus controlled by ODPA concentration, while the $(000\bar{1})$ facet has no such restrictions, as long as a low amount of HPA is present. This suggests different rate determining steps at the two facets: growth in [0001] direction appears to be diffusion controlled, while in the $[000\bar{1}]$ direction, it is independent of diffusion, and thus, reaction controlled. It is therefore a viable assumption that the formation of CP-309 directly influences the rate determining step, as the formed concentration of this species as visible in the UV/vis is also constant over all phosphonic acid mixtures that include at least a small fraction of HPA.

4.1.5 Influence of H_2O on CP-309 formation

To answer whether there is a causal relationship between the presence of CP-309 and fast 1D nanorod growth the reaction was repeated under conditions that suppress CP-309 formation. Kirkwood and Boldt have shown that addition of water to the reaction quantitatively prevents the formation of CdSe coordination polymers, likely due to breaking of anhydride bonds that bridge individual magic-size clusters.[38] The absence of CP-309 is expected to lead to a decrease in anisotropic growth and an increase in homogeneous nucleation, because the lack of an equilibrium between monomer and coordination polymer would result in a homogeneously distributed, high monomer concentration as opposed to an average, low monomer concentration with local hot-spots around the CP-309 fibrils.

UV/vis kinetic measurements in the absence of seed particles show that co-injection of 50 µL of water completely suppresses formation of CP-309 (see Figure 4.7 (left), blue traces), as opposed to the reaction under dry conditions (red traces). Under wet conditions NCs nucleate directly

---

[79] Emile Drijvers et al. *Chem. Mater.*, **28**: 7311–7323, 2016.

[38] Nicholas Kirkwood and Klaus Boldt. *Nanoscale*, **10**: 18238–18248, 2018.

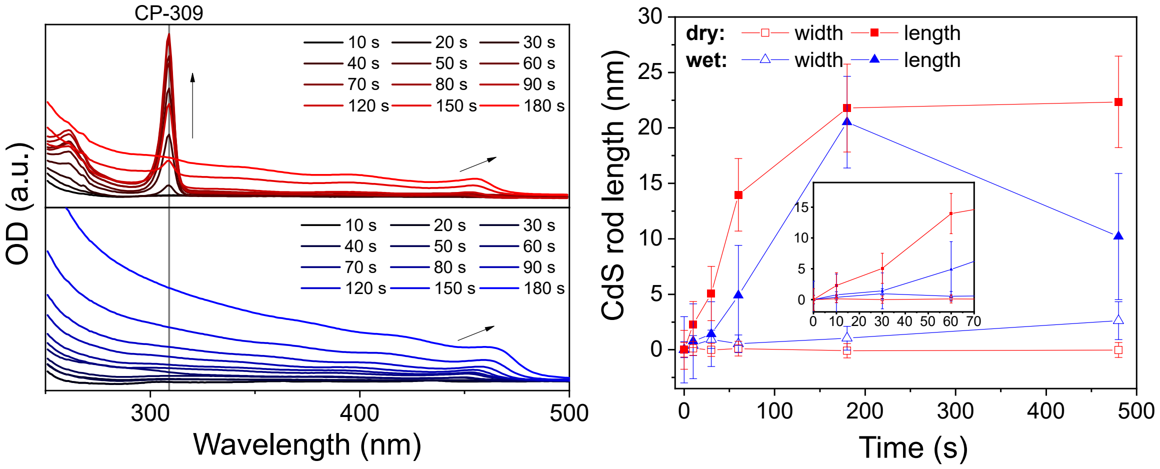

Figure 4.7: UV/vis spectra of the evolution of CP-309 (left) in dry conditions (red traces) and in the presence of 50 µL of water (blue traces). Length of CdS segment (right, full symbols) and width (hollow symbols) for dry conditions (red squares) and wet conditions (blue triangles).

after injection, 60 s earlier than in the presence of CP-309, and grow at a faster rate. It shows that water clearly affects the nanocrystal growth rate by increasing the oversaturation of the monomer solution. In literature water has been found to speed up TOP-S conversion,[80] act as a proton source that activates Cd-ODPA complexes,[37] and protonate phosphonates, which leads to their desorption from the particle surface.[81] All these effects can be expected to contribute to a faster reaction rate. Additionally, water might contribute to the fast formation of H_2S which has been suggested as the active chalcogen species in this type of nanoparticle synthesis.[82] Fast formation of large amounts of these agents will speed up the reaction while reducing control over particle shape and composition.

When CdS dual diameter nanorods were grown in the presence of 50 µL of water a significant loss of regioselectivity can be observed in the TEM. While the dry reaction, performed at the standard S-Cd ratio of 8-1, produces almost exclusively bottle-shaped nanorods with uniform lengths of the CdS part (see Figure 4.8, red boxes), under wet conditions particle size and shape have a much broader distribution (blue boxes). The circumference of the dual nanorods that form appear less regular and the CdSe seeds grow in thickness as well as in length (Figure 4.7 (right)). There is also a significant quantity of bi-, tri-, and tetrapods present, as well as nanorods that are narrower than the CdSe seed particles over their entire length. These are a likely product of homogeneous nucleation of pure CdS nanocrystals. The initial 1D growth rates were 13 nm/min under dry and 4.2 nm/min under wet conditions, as determined from TEM analysis (see Figure 4.7 (right)). Eventually, the nanorods reach similar lengths after 3 min under both conditions. In contrast to the dry reaction the nanorods decrease in length again if water is present and end up approximately

---

[80] Jonathan S. Owen et al. *J. Am. Chem. Soc.*, **132**: 18206–18213, 2010.

[37] Zhong Jie Jiang and David F. Kelley. *ACS Nano*, **4**: 1561–1572, 2010.

[81] Michaela Meyns et al. *Chem. Mater.*, **26**: 1813–1821, 2014.

[82] Leah C. Frenette and Todd D. Krauss. *Nat. Commun.*, **8**: 2082, 2017.

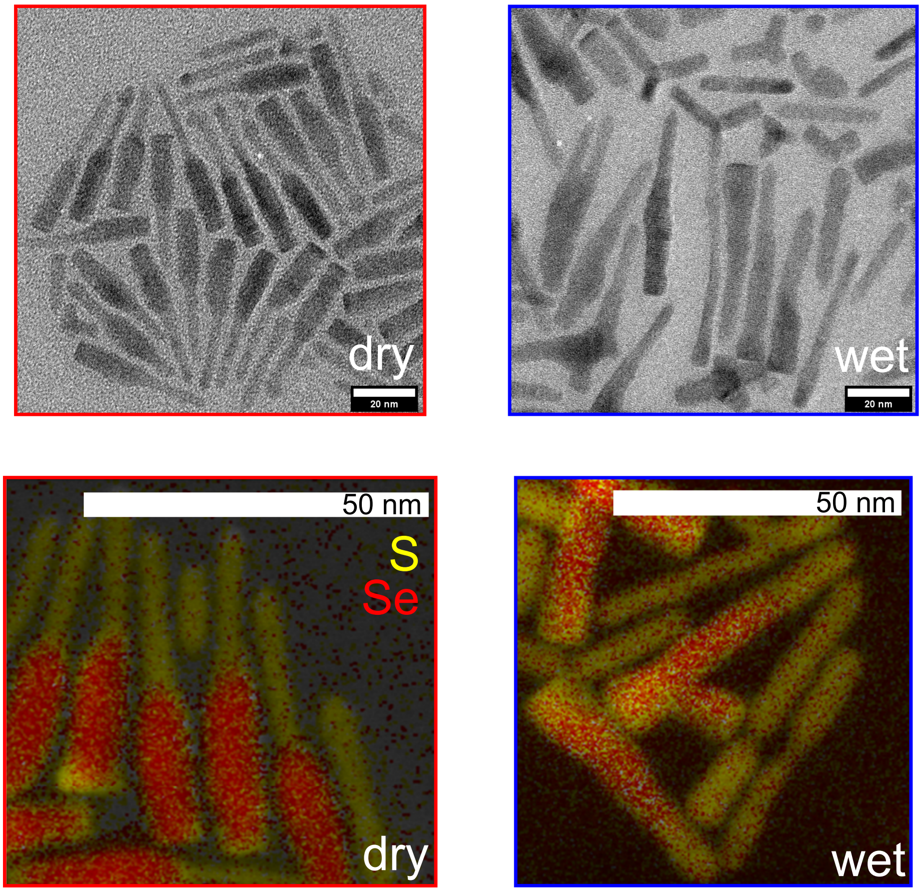

Figure 4.8: TEM micrographs (top) of reaction products after 480 s and EDX elemental maps (bottom) displaying the distribution of sulfur (yellow) and selenium (red) in the dual diameter rods made under dry (red box) and wet conditions (blue box).

15 nm shorter after 8 min. The irregular growth can be rationalized by increased Ostwald ripening and surface etching of the nanorods brought on by water and hydroxy ions.[83]

This is supported by elemental mapping using EDX spectroscopy: For the dry reaction (red box) it shows a clear separation of CdSe in the seed and CdS, which is found exclusively in the thin rods and, to a much lesser extent, at the opposite (0001) facet (see Figure 4.8). After reaction in the presence of water Se and S are found distributed over the whole structure. EDX mapping also reveals that a significant number of nanorods grown under wet conditions have a low Se content (blue box). This can only be explained by transfer of Se ions to homogeneously nucleated CdS rods *via* ripening. Apart from the much higher number of homogeneously nucleated nanorods the initial 1D growth rate is 3-fold slower under wet conditions. This is notable, because in the presence of water overall faster reaction kinetics were expected. Hence, the main effect from the addition of water in the early reaction stages is the suppression of CP-309, making it a feasible negative control. At later reaction stages, the side effects of water addition become apparent. As

---

[83] Nuri Oh and Moonsub Shim. *J. Am. Chem. Soc.*, **138**: 10444–10451, 2016.

temperature variations can be excluded the faster growth suggests that in the presence of CP-309 the monomer concentration available for 1D growth is actually higher than for a homogeneous reaction mixture. H_2O completely suppresses the formation of identifiable intermediates.

4.1.6 Effects of the 1D structure of CP-309

To fully test the hypothesis that CPs are essential intermediates for rod growth it is also necessary to show that the accumulation of the monomer into localized aggregates is required for rapid 1D growth. As the phosphonic acid-based synthesis always produces fibrillar intermediates, MSCs were grown in a separate step following the easily scalable synthesis by Nevers et al.[84] These MSCs were then injected into the dual rod growth reaction as single-source precursors. The MSCs are stabilized by oleic acid, which does not form an anhydride that can act as a bridging ligand. They have a characteristic, sharp absorption peak at 324 nm that does not shift over time, indicating the formation and dissolution of a distinct, metastable species. TEM analysis shows that this species forms individual clusters instead of fibrils or lamella. Absorption spectra and TEM micrographs are shown in Figure 4.9. EDX analysis (see Appendix B, Table 4.9) leads to a Cd:S ratio of 2:1, making MSC-324 the closest analogue to CP-309 that lacks the extended structure.

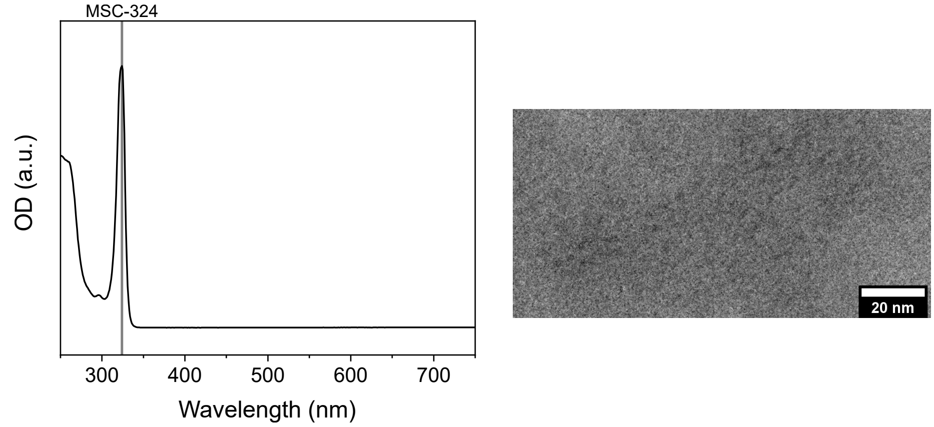

Figure 4.9: UV/vis spectra of MSC-324 (left) and corresponding TEM micrograph (right).

The shift from the phosphonic acid to fatty acid ligand system constitutes a significant difference between the intermediates. To compare the two a series of three experiments was performed in which the reaction conditions were gradually adjusted towards the CdSe/CdS dual rod synthesis: Experiment I consisted of injection of MSC-324 into pure TOPO, followed by adding the seed particles in TOP. This results in a twofold excess of Cd over S, and the absence of additional ligands. In Experiment II, TOP-S was injected before adding the seed particles and MSC solution to account for the 8-fold excess of sulfur employed in the standard reaction. So far no phosphonic acids were present to prevent a possible formation of CP-309 in-situ. Experiment III was therefore performed analogously to Experiment II, but in the presence of both ODPA and HPA to emulate the complete reaction conditions of dual diameter rod growth. For all three experiments the amount of MSCs

---

[84] Douglas R. Nevers et al. *Chem. Commun.*, **53**: 2866–2869, 2017.

was adjusted so that the amount of potential monomer was kept constant. The reactions were monitored by UV/vis and TEM.

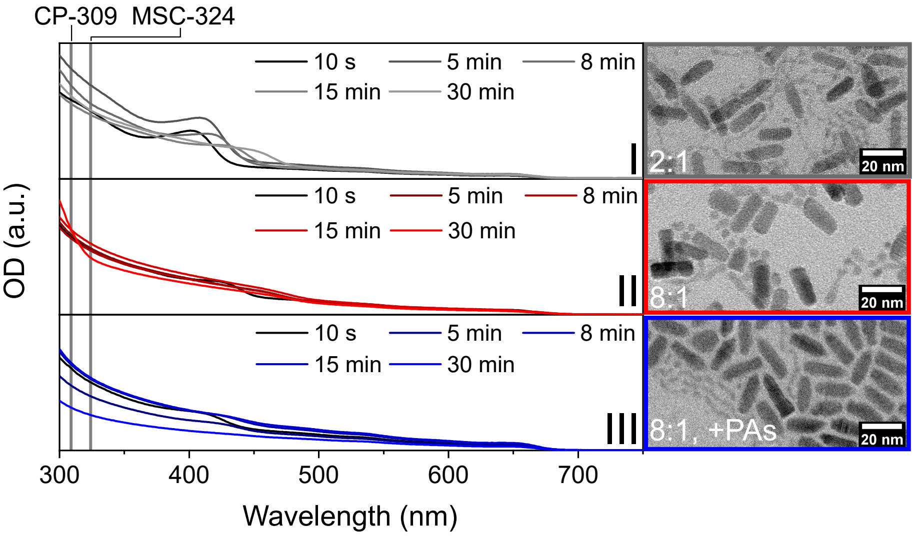

Figure 4.10: UV/vis spectra of dual diameter rod growth using MSC-324 a as single source precursor with a Cd:S ratio of 2:1 (Experiment I, top, gray traces), 1:8 (Experiment II, middle, red traces), and 1:8 in the presence of phosphonic acids (Experiment III, bottom, blue traces) with the corresponding TEM images of the sample taken after 8 min (right column).

UV/vis spectra of all samples in this series of experiments show the absorption of CdSe seed particles starting at 650 nm (see Figure 4.10 (left column)). The absorption peak of MSC-324 was not observed in any sample, indicating rapid decomposition upon injection. Instead, at 10 s a signal around 400 nm appears in Experiment I (gray traces) that shifts towards lower energies over the course of the reaction. After 15 min this signal broadens and shows less distinct features. The wavelength and the red-shift are indicative of nucleation and growth of CdS particles. The TEM image shown in Figure 4.10 (gray box) reveals that these particles nucleate homogeneously next to the seed particles, which retain their shape. No heterogeneous nucleation is observed.

In Experiments II and III the CdS absorption edge at 400 nm is noticeably less intense and shifted to lower energies by approximately 30 nm after 10 s (red and blue traces). These changes are attributed to the variation of injection order, different Cd:S ratio, and the lower amount of MSC-324 added to achieve a constant amount of monomer. If MSCs are injected after the addition of CdSe seeds instead of before a visible increase of thickness for the CdSe rods is apparent from the respective TEM micrograph (red box), indicating heterogeneous, isotropic shell growth. TEM analysis of Experiment III (blue box) shows a change in seed particle morphology: the $(000\bar{1})$ facet becomes pointed, while the opposing (0001) facet remains flat. It was not possible to determine whether this is due to site-selective etching or a minimal growth of a CdS rod, resembling the dual rod synthesis with a Cd:S ratio of 1:2. In all experiments significant homogeneous nucleation of CdS nanocrystals occurs, as evident from appearance of the CdS absorption at 450 nm, along with the TEM data.

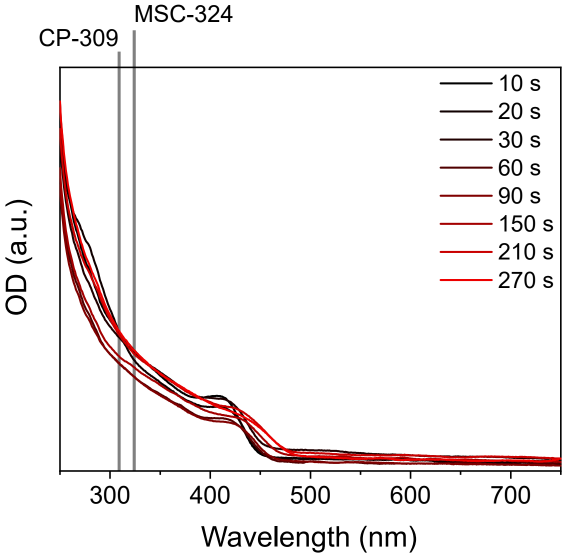

Figure 4.11: UV/vis kinetics of injection of MSC-324 and TOP-S into a TOPO/phosphonic acid mixture.

As conversion between intermediate species has been widely reported,[31,32,35,85] this possibility was investigated by performing Experiment III without seed particles present. UV/vis spectra of samples taken from the reaction are shown in Figure 4.11. No formation of CP-309 from MSC-324 is observed, but instead rapid nucleation of particles immediately after injection occurs. The sharpening of the $(000\bar{1})$ tip observed in Experiment III is therefore not a result of CP-309 formed from MSC-324, but can be attributed solely to the presence of phosphonic acids, which is consistent with the results of the previous experiments. MSC-324 itself does not contribute to anisotropic growth, but instead dissolves rapidly at reaction temperature, leading to a sudden release of homogeneously distributed monomer at high concentration and thus inducing homogeneous nucleation. These experiment emphasize the importance of the extended structure of CP-309 for reaction-controlled nanorod growth. It affects both the spatial distribution of the monomer and its release rate from the monomer reservoir.

Experiments with the MSC-324 precursor cannot be performed in the absence of fatty acids. However, their low relative concentration and the much larger binding affinity of phosphonate ligands makes a significant effect of the oleate ligands from the MSCs on the nucleation mechanism unlikely.[86,87]

---

[31] Patrick D. Cunningham et al. *ACS Nano*, **14**: 3847–3857, 2020.

[32] Stefan Kudera et al. *Adv. Mater.*, **19**: 548–552, 2007.

[35] Cristina Palencia, Kui Yu, and Klaus Boldt. *ACS Nano*, **14**: 1227–1235, 2020.

[85] Chaoran Luan et al. *J. Phys. Chem. Lett.*, **10**: 4345–4353, 2019.

[86] Adam J. Morris-Cohen et al. *J. Phys. Chem. C*, **114**: 897–906, 2009.

[87] Peter E. Chen et al. *J. Am. Chem. Soc.*, **139**: 3227–3236, 2017.

4.1.7 Proposed reaction mechanism

The formation of nanorods, independent of the occurrence of CP-309, reinforces the general results from the study by Kim et al.[69] However, the high thermal stability of CP-309 requires the assumption of an inhomogeneous distribution of the reactive species, which likely dissolves readily only at the end of the fibrils.[33] In the proximity of a seed particle an aggregate of CP-309 provides a steady feed of new material for a reaction-controlled growth reaction with pseudo-zero-order kinetics.

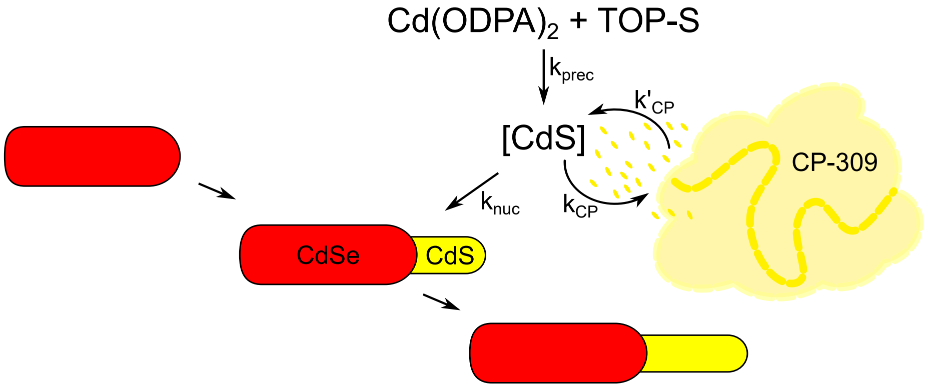

Scheme 4.3: Proposed mechanism: the CdS nucleation monomer [CdS] is in equilibrium with CdS bound in CP-309. At the seed surface the material is supplied to the reaction site, forming a new nanorod.

Based on the presented findings the rod growth mechanism shown in Scheme 4.3 is proposed. The cadmium and chalcogenide precursor react to form the active monomer species, which is in turn bound in form of CP-309 if the following conditions are fulfilled: (a) the reaction is carried out in the absence of protic additives, and (b) the reaction is given sufficient time to settle in the equilibrium that favors CP-309 formation over free monomer. If one of the two conditions is not met, CdS is directly formed from the monomer, either *via* homogeneous or heterogeneous nucleation, depending on the oversaturation and availability of seed particles. If CP-309 is present, it creates localized regions of high precursor concentration in the reaction solution. At the active $(000\bar{1})$ facet, CP-309 decomposes to monomer, is transferred to the seed particle and removed from the equilibrium by forming solid CdS. CdS nanorods grow at a constant rate that is limited by the decomposition of CP-309. The final particle length is correlated with the total amount of added precursor. Formation of CP-309 can be promoted by increasing the chalcogenide concentration, which lowers the solubility of free monomer.

These results must be regarded as an addition to the ongoing discussion in literature which remains focused largely around the direct impact of ligand chain lengths and their binding behavior rather than as a challenge to previous studies. The CP-309 based mechanism expands upon works focussed on these aspects rather than questions its validity. The two theories cannot be separated, as both are required to get a complete picture of the mechanisms of anisotropic growth.

4.2 Magic-size clusters as precursors for tipped rod growth

An expansion upon classical seeded rods is their anisotropic modification by growth of a heteromaterial tip. The first report on this class of structures covered the introduction of a metal-tip,[88] which introduces a Schottky barrier within the particle. These structures are attractive candidates for catalysis.[89–92] In 2005, semiconductor-tipped rods were first reported in the form of PbSe@CdE rods (E=Se, S),[93], followed in 2013 by CdSe@CdS rods that showed luminescence upconversion.[20] Unfortunately, the synthesis suffers from reproducibility issues, but was successfully modified by changing the tip material to CdTe.[23] With CdTe, up to 50 % of nanorods could be tipped in a highly reproducible synthesis, forming particles that can be used as a model system for photocatalytic water-splitting: the combination of the CdTe/CdS type II and the CdSe/CdS type $\mathrm{I}^{1/2}$ structure allows for long-lived charge separation of the hole and the electron, a prerequisite for this application.[24]

The question of different accessibility of tips of different materials was further investigated by Florian Enders in his PhD thesis.[68] He found that while tips can be grown from both CdTe and ZnTe, the same approach with CdSe yields not rods with a heteromaterial tip, but leads to significant side nucleation of separate CdSe particles. Without added seed particles, MSCs form as an intermediate before particles nucleate, while the usage of Se precursor leads to immediate nucleation of MSe particles. Florian Enders hypothesized that MSCs slow down homogeneous nucleation by decreasing the monomer concentration in the reaction, acting as a monomer reservoir.

In the previous Section 4.1 it was shown that CPs play such a role in nanorod growth: the reaction intermediate redissolves to locally provide monomer to the reaction site (Scheme 4.3). It was, however, also shown that MSCs do not act the same way during nanorod growth, as using them as a precursor mainly lead to side-nucleation (see Section 4.1.6). Rod growth did thus not occur directly from the magic-sized intermediates, but was unrelated to their structure. Whether this is the case as well in the growth of heteromaterial tips on preexisting rods will be investigated in this section: CdTe-based MSCs are used as precursors for the growth of CdTe tips on CdSe/CdS seeded rods. If the growth of tips is unrelated to the structure of MSCs, this should not lead to increased heterogeneous nucleation compared to the reaction from the molecular precursors. This would in turn suggest that the appearance of MSCs and the growth of heterotips on rods have a different connection.

4.2.1 Preparation of CdTe Magic Size Clusters

For the synthesis of CdTe MSCs a protocol by Zanella et al. was used. The reaction was monitored by UV/vis kinetics over the course of 60 min (see Figure 4.12). The first cluster species, which is identified by a sharp absorption peak at a fixed wavelength, appears at 445 nm after 8 min of reaction time. An additional signal appears after 10 min at 371 nm. This peak increases in intensity until 20 min in, after which time it can no longer be detected due to the high optical density of the

---

[88] Taleb Mokari et al. *Science*, **304**: 1787–1790, 2004.

[89] Sun Mi Kim et al. *Nano Lett.*, **13**: 1352–1358, 2013.

[90] Yifat Nakibli and Lilac Amirav. *Chem. Mater.*, **28**: 4524–4527, 2016.

[91] Yifat Nakibli et al. *Nano Lett.*, **18**: 357–364, 2018.

[92] Ji Yong Choi et al. *ACS Catal.*, **11**: 13303–13311, 2021.

[93] Stefan Kudera et al. *Nano Lett.*, **5**: 445–449, 2005.

[24] Maria Wächtler. *Nachr. Chem.*, **67**: 44–50, 2019.

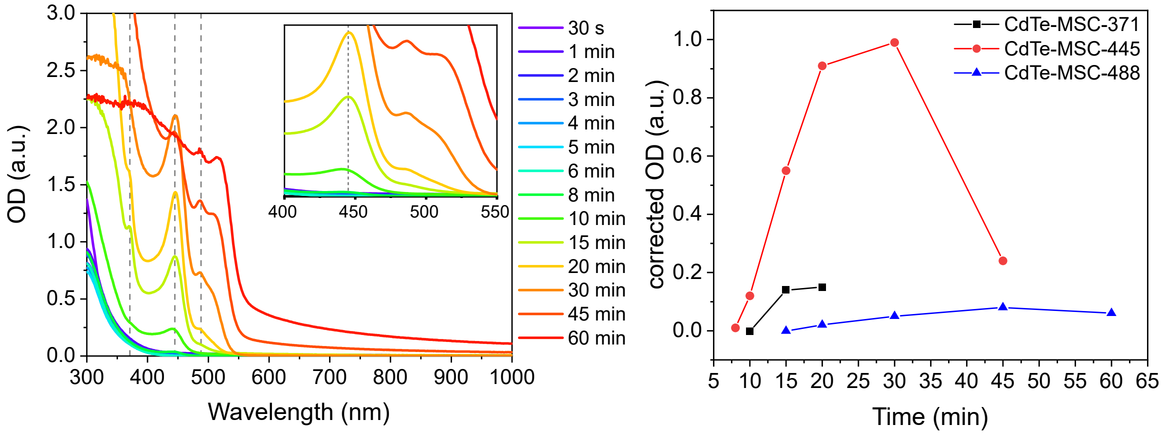

Figure 4.12: UV/vis kinetics of CdTe MSC growth following the synthesis by Zanella et al.[94] Three separate species show up at distinct wavelengths indicated by dashed lines (371 nm, 445 nm and 488 nm) (left). The inset shows a detailed view of the lower wavelength region. Their intensities over time reveal that the species show up after one another, with a time delay (right).

system which is a result of the nucleation of more and more material. While CdTe-MSC species were reported at this energy before,[95] MSC species usually appear in order of size (from smallest to largest). It is thus not completely clear whether this is in fact a cluster species or a secondary peak of the 445 nm species.

After 15 min of reaction time, a second cluster at 488 nm appears. The species at 445 nm arrives at its highest intensity after 30 min, after which the intensity sharply decreases. The population of the 488 nm species reaches its maximum at 45 min, after which it decreases as well. The decrease in population of the two species coincides with the appearance of a fourth signal at approximately 520 nm. Since this signal shifts towards higher wavelengths over time, it is attributed to the nucleation of CdTe particles that grow over time in favor of the depletion of the cluster species.

In order to only use MSCs and not pre-formed particles in the reaction, the reaction was stopped at a point in time at which MSCs was present, but no particles had nucleated yet. Stopping the reaction after 20 min yielded MSCs as an orange substance. Elemental analysis via EDX showed a content of 70 % mass percent CdTe MSCs and an 1:1 elemental ratio of Cd:Te (see Appendix B, Table B.3). It is mainly composed of a 445 nm and a 488 nm species, which are the same species that were observed during CdTe tip growth.[68]

4.2.2 MSCs as precursors: Reaction parameters

Reaction temperature, oleic acid, and Te^{2-} concentration were previously identified as parameters than influence the fraction of rods with CdTe tips.[68] At higher temperatures, the reaction rate of the monomer to material is increased, which leads to deposition of more material, and thus, a higher amount of rods with a tip. Oleic acid is hypothesized to stabilize the monomer, which in turn makes more monomer available, favoring growth of tips. The Te^{2-} concentration is especially interesting in this experiment, as the MSC solution contains equimolar amounts of Cd and Te. In

---

[95] D Gao et al. *Nat. Commun.*, **10**: , 2019.

the original synthesis, a two-fold excess of TOP-Te is employed, so the experiments that use only MSCs as a Te^{2-} source differ significantly from the original synthesis. If additional Te^{2-} is required to arrive at a high fraction of tipped rods it would indicate that the overall monomer concentration regulates heterogeneous nucleation of material, and not the structure of the reaction intermediate.

The fraction of tipped vs. untipped rods is the direct measure for the success of the reaction, but its determination is a point of contention. One possibility to arrive at this number is counting the tipped and untipped rods in a given number of particles from TEM micrographs. This approach has multiple sources of error, the first being the strong locality of the method, as only a small fraction of total particles can be counted. In order to keep this constant, the same number of particles is counted for every sample. The particles used here are wider than the ones used in Florian Enders' PhD thesis, which reduces the facet selectivity of the reaction, so the heteromaterial nucleated on the rods appear as thickened ends to the particles instead of the cane-like structures reported previously. However, thickened ends can occur in seeded rod samples unrelated to the growth of heteromaterial tips. They can be a result incomplete formation of tetrapods, e.g., if the used seed particles are in cubic sphalerite instead of wurtzite structure, or can be related to particle ripening. This limits the reliability of this method for determining the fraction of tipped rods.

An alternative measure of for the fraction of rods with heterotips uses spectroscopic analysis via PL. The CdTe/CdS heterojunction creates a type II interface. Electron and hole are localized at this interface, where depopulation of excited states via non-radiative pathways is strongly favored due to a combination of strain-induced band bending and Coulomb interaction.[23] This reduces the intensity of the emission signal, which makes the relative reduction in intensity a measure of the tipping degree. As a global method, this does not suffer from the same drawbacks as TEM evaluation. However, a reduction in PL lifetime can stem from a number of effects, among them the formation of trap-states within the band gap. These can be a result of the adsorption of anionic, lattice terminating ligands such as Te^{2-} and oleate,[96] or simply etching due to oleate addition.[83] Both analysis *via* PL and *via* TEM thus paint an incomplete picture and have to be considered together.

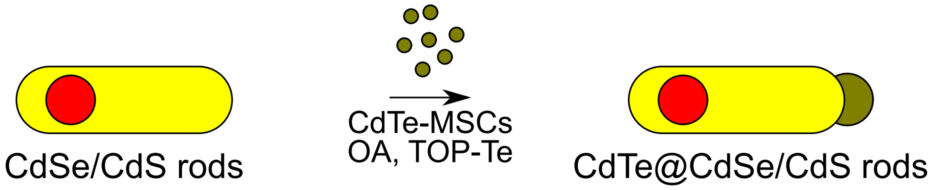

Scheme 4.4: Reaction scheme for CdTe tip growth on CdSe/CdS dual rods using MSCs as a precursor.

In the standard tip growth reaction, a TOP-Te solution is added to the reaction mixture of seed particles, TOPO, oleyl amine, and ODE at 200 °C, followed by the drop-wise addition of a cadmium oleate solution via a syringe pump. In the following experiments, the injection solutions are replaced by a MSC stock solution, as shown in Scheme 4.4. Variations include two reaction temperatures, 175 °C and 200 °C, and different concentrations of the additives oleic acid and TOP-Te. In the original reaction, free oleic acid is only present in trace amounts from the cadmium oleate solution, while here the amounts are 50 µL and 200 µL, respectively. Experiments are run

---

[96] Nicholas C. Anderson et al. *J. Am. Chem. Soc.*, **135**: 18536–18548, 2013.

with and without additional TOP-Te to compare the influence of a 1:1 to a 1:2 ratio of Cd:Te. Additionally, reference experiments are run without any CdTe monomer source to exclude effects related to prolonged heating.

Temperature dependence

A stock solution of MSCs was added via syringe pump to a solution of CdSe/CdS rods, oleic acid (200 µL), TOPO, and ODE. As the MSCs themselves are amine capped, no more oleyl amine was added. The reaction was performed at two temperatures, 175 °C and 200 °C, and the fraction of tipped rods was determined by both PL measurement and manual counting of thickened ends from TEM micrographs.

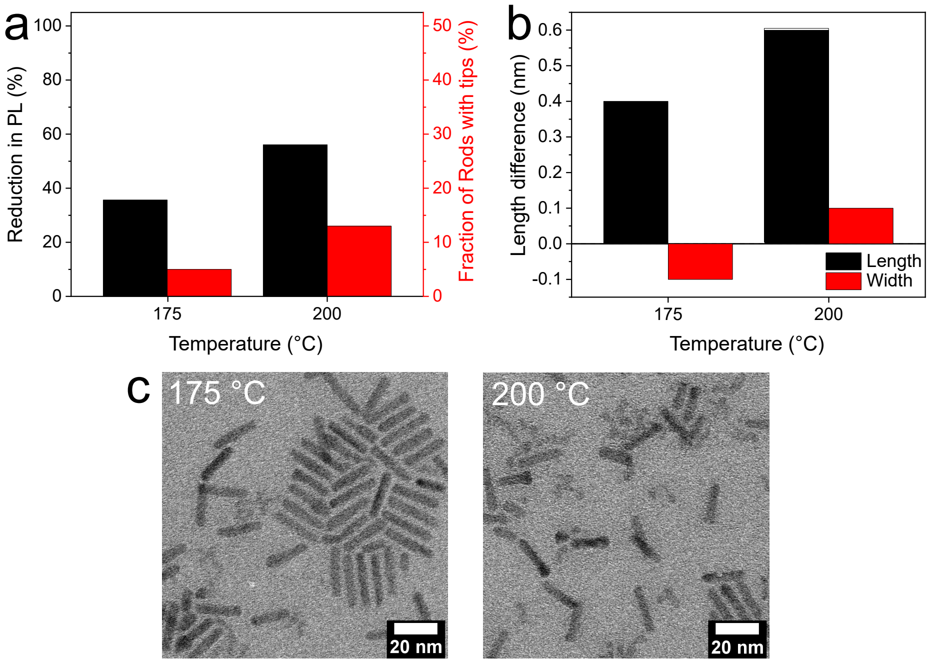

Figure 4.13: Temperature dependence of tip growth on seeded rods from CdTe MSCs. Fraction of rods with thickened ends and reduction in PL intensity plotted against the reaction temperature (a). Change in particle length (black) and width (red) depending on the reaction temperature (b). TEM micrographs of the samples (c).

Raising the temperature from 175 °C to 200 °C lead to an increase both in the fraction of rods with thickened ends from HR-TEM evaluation and the reduction in PL: they increased from 5 to 13 % and 36 to 56 %, respectively, as shown in Figure 4.13 (a). Since the PL intensity is not only affected by tip growth, but also by etching reactions which are favored at higher temperatures, the difference in particle length and width before and after the reaction was monitored (Figure 4.13 (b)). Etching would lead to a decrease in particle size,[83] while the deposition of material due to tip growth leads to an increase. The width remains largely the same (the observed change of 0.1 nm is within the margins of error), but the particle length increases by 0.4 nm at 175 °C and 0.6 nm at 200 °C. Consequently, etching can be disregarded at these temperatures.

A reduction in PL intensity can hint at growth of heteromaterial tips. As the reduction is stronger at the higher reaction temperature, that would suggest a higher amount of tips with increased temperature, which in turn would mean that overall, more material is deposited on the nanorods. The TEM micrographs (Figure 4.13 (c)) reveal that side nucleation can be observed at both temperatures. This does typically not occur in the reaction from the molecular precursors.[68] The fact that noticeable amounts of material go into side nucleation makes it likely that at least part of the thickened rod ends are not related to CdTe tips. Additionally, the fraction of rods with thickened ends from the micrograph is still only approximately half of the amount that would be expected in the synthesis from the molecular precursors. This leads to the conclusion that the reaction from the MSCs as shown here is notably less efficient at growing tips than the reaction directly from the molecular precursors.

Dependence on oleic acid and TOP-Te additives

The influence of oleic acid on the MSC based growth of heterotips was evaluated by repeating the experiment with 50 µL and 200 µL of added oleic acid. If excess oleic acid stabilizes monomer in the reaction, a higher amount of it would reduce side nucleation. All reactions were performed at 175 °C. As a purely MSC based reaction occurs at a Cd:Te ratio of 1:1, 1 equivalent of TOP-Te was added in order to achieve the 2-fold Te-excess of the original reaction conditions. The reaction was also performed without adding any precursor in order to check whether thickened ends that can be mistaken for CdTe tips occur independent of CdTe monomer supply. The results are shown in Figure 4.14.

Additional TOP-Te completely quenches photoluminescence and increases the fraction of rods with thickened ends from 8 %/5 % to 32 %/41 % for 50 µL/200 µL of oleic acid, see Figure 4.14 (a, c). This means that the quenched emission is at least in part the result of Te^{2-}-ligands on the surface, as not all rods have tips that would explain the complete quench of their photoluminescence. The reaction also yields noticeably more thickened ends at a Cd:Te ratio of 2:1 than at 1:1, which indicates that the monomer concentration has a significant impact on the reaction: In accordance with the law of mass action more Te^{2-} increases the oversaturation and leads to more nucleation. Between the different amounts of oleic acid, the fraction of particles with thickened ends varies by approximately a fourth. This seems significant, however, the margins of error associated with manual counting of rods with thickened ends are large as well. Additionally, the variation goes in both directions: In the MSC experiment, 50 µL of oleic acid leads to a higher amount, and in the 200 µL, the opposie is true, further indicating that these variations do not follow a system. Thus, additional experiments are required to determine whether the amount of oleic acid has an impact on the reaction.

To clarify this, the change of the particle widths and lengths was evaluated. The reference samples show significant reduced length upon heating by −4.1 nm (50 µL of oleic acid, see Figure 4.14 (b)) and −4.2 nm (200 µL of oleic acid, see Figure 4.14 (d)). No significant changes of the reference samples are observed with regard to particle width (−0.1 nm and −0.3 nm, respectively). Similar results were found in the experiments including MSCs or MSCs and TOP-Te each showed increases in particle length that were bigger, the more oleic acid and Te^{2-}-source was added: With only MSCs, particle length and width did not change beyond the confidence interval (0.1 nm and −0.1 nm) for both oleic acid concentrations. The length changed only by 0.4 nm, and only for the 200 µL oleic acid sample. With additional TOP-Te, particle width increased by 1 nm and 1.7 nm

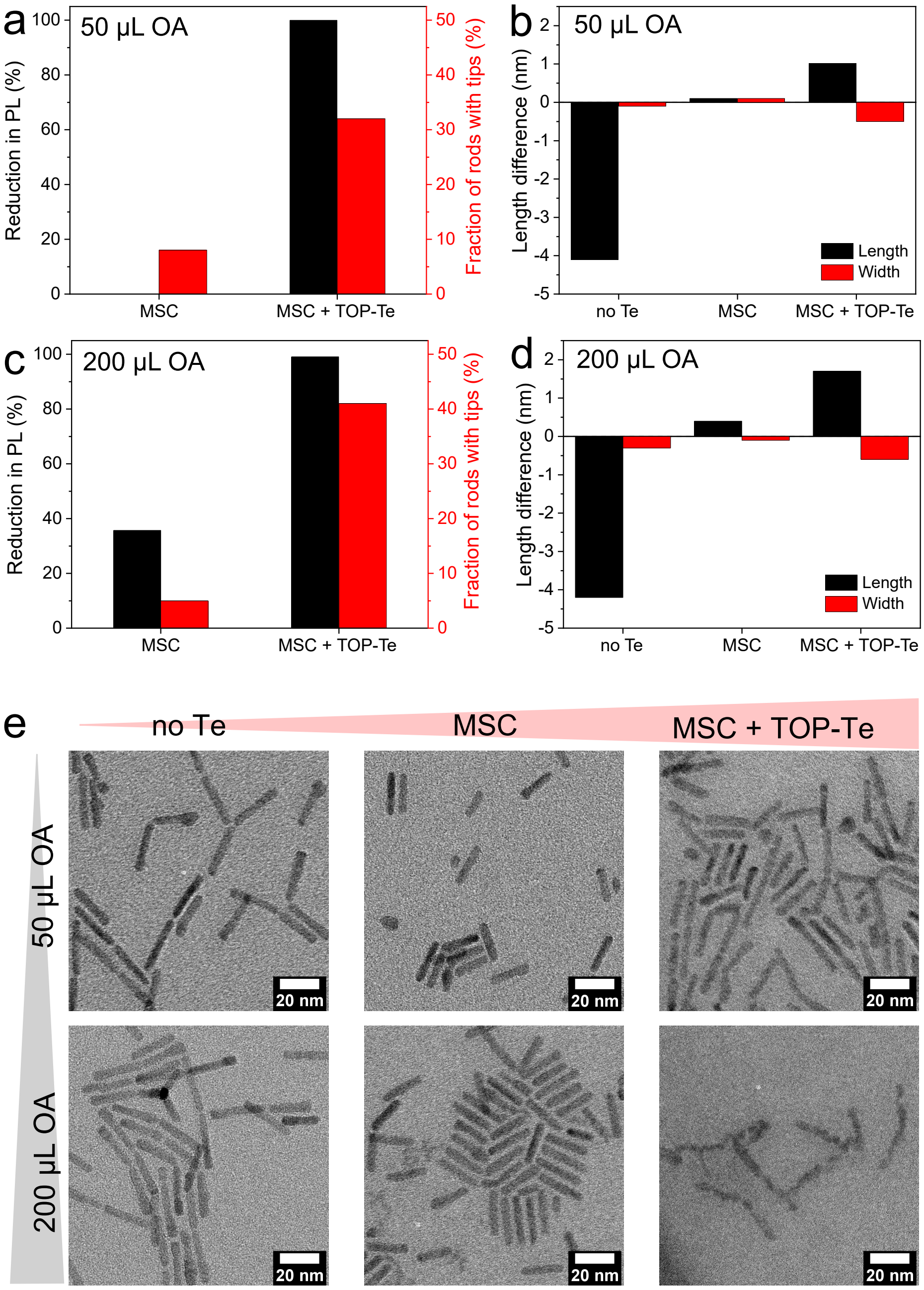

Figure 4.14: Dependence of tip growth from CdTe MSCs on oleic acid and telluride addition. Tip degree and reduction of PL intensity plotted against the reaction conditions with regard to Te addition with 50 µL (a) and 200 µL oleic acid added (c). Change in particle length (black) and width (red) is shown in the right column (b, d). TEM micrographs of the samples (e).

for 50 µL and 200 µL of oleic acid, respectively, and the width changed by −0.5 nm and −0.6 nm. Thus, changes in particle size are in the same range regardless of the added volume of oleic acid.

This is in accordance with literature, which reports that oleic acid does not lead to etching behavior, in contrast to oleate.[83] The effects observed in the TEM are thus likely caused by ripening. Additionally, the reference experiments show that a significant amount of the rods have thickened ends as well (Figure 4.14 (e), left column). These thickened ends could be misinterpreted as heteromaterial tips, if any monomer was added during the reaction. This sheds additional doubt on TEM analysis for determination of tip growth. At least for samples that contain thicker rods with less pronounced faceting, it is hard to distinguish actual rod growth from ripening effects or incomplete tetrapods. Locally resolved elemental mapping or methods that resolve the material contrast, such as high-angle annular dark-field (HAADF) TEM could provide further insight.

TEM analysis of the MSC and MSC + TOP-Te samples with 200 µL of oleic acid (Figure 4.14 (e), bottom row, middle and right) also show that side nucleation remains prevalent. This indicates that the addition of TOP-Te does not increase the selectivity of the reaction, but rather the overall amount of monomer, and thus, nucleation as a whole.

Generally, the fraction of rods with thickened ends was significantly lower over all experiments with MSCs as a precursor than with molecular precursors. The Cd:Te ratio had by far the biggest impact on the amount of thickened ends in the rods, which indicates that the solubility product of the monomer has a significant impact on the reaction. The MSCs appear to only act as a source of monomer without any shape-directing effect. MSCs also lead to more side nucleation, which rarely occurs in the reaction from the molecular precursors.

4.2.3 MSCs and tip growth: conclusion

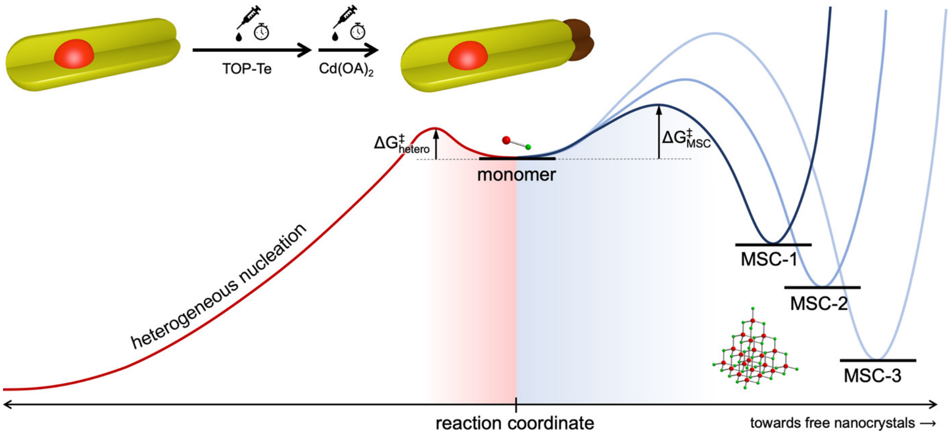

Scheme 4.5: Schematic of the proposed mechanism for tip growth and the relationship between MSCs and the formation of tips. Adapted from Enders et al.[14]

The growth of CdTe tips on CdS nanorods does not involve CdTe MSCs as essential reaction intermediates. They can be used as a precursor in this type of synthesis, but the synthesis is less efficient than if the molecular precursors are used; both in regard to the fraction of tipped rods, and in the suppression of unwanted side nucleation. MSCs thus play a different role than the CPs; they do not have an effect that favors anisotropic growth, but simply redissolve, which sets free monomer. Material then nucleates independent of whether it was previously bound in MSCs, similar to the experiment regarding MSCs during rod growth (Section 4.1.6).

This opens up the question of why MSCs were described in the context of successful growth of CdTe tips, but not in the context of CdSe tips, if they do not directly impact the tip growth reaction. Based on the findings presented in this chapter, further studies were conducted in the group,[14] which identified MSCs as predictors of tip growth rather than necessary intermediates. They form under similar conditions. For CdTe, the temperature window for nucleation of CdTe and formation of MSCs overlap. In the case of CdSe, MSCs and crystalline phase form at a much lower temperature of around 120 °C. At that temperature, the deposition of material on preformed nuclei is not activated as the ligands are not mobilized but remain at the particle surface, effectively capping it. This explains the reproducibility issues of CdSe tip growth and provides a good argument for the study of reaction intermediates in addition to their potential value as precursors.

4.3 Conclusion

This chapter showed that for a deeper understanding of anisotropic growth reactions, it is worth looking at reaction intermediates. Of the known classes of reaction intermediates, CPs and MSCs, only CPs have an influence on anisotropic growth. CPs are associated with selective rod growth, specifically in the $[000\bar{1}]$ direction. Their occurrence coincides with selective growth in one direction, and the suppression of their formation leads to a loss in selectivity, leading to the conclusion that they heavily and directly influence reaction kinetics. In contrast, MSCs do not provide a morphology directing effect, which emphasized the influence of CPs' 1D structure.

MSCs are not essential intermediates during growth of heteromaterial tips on nanorods. As precursors, they do not work as effectively as the molecular precursors. They act as a source of monomer, which emphasizes the differences in mechanism during rod and tip growth. Despite this fact, studying MSCs in the context of heterogeneous tip growth is valuable: as MSCs form under similar conditions as tips, they are predictors for conditions that favor tip growth. This simplifies the screening process for suitable tip materials and reaction conditions: if it is possible to grow MSCs, that is a good indicator that tips can be grown under similar reaction conditions.

Overall, the results of this chapter provide deeper insight into reaction intermediates as important factors for anisotropic growth, and why it is worth to study them. Especially CPs with their intrinsic tendency to provide monomer in an anisotropic fashion could provide a valuable tool for introduction of dopants. At the very least, they are a factor that has to be considered if direct, anisotropic introduction of dopant ions is the aim, and reaction conditions have to be adjusted so that they don't suppress their formation.

5 Introducing TM^{2+}-dopants: Domain Doping of Nanoheterostructures

While the first chapter dealt with the aspect of anisotropic growth, this chapter shifts the focus towards bivalent transition metal (TM^{2+}) doping of heterostructures. Literature offers a variety of approaches to achieve this goal, from brute force with pyrophoric compounds over the selective dissolution of doped clusters to simply adding dopant during the growth reaction. The aim of this chapter is to test the most promising approaches regarding selectively doping one material domain in a heterostructure, while the other domains remain undoped.

The possible approaches can be roughly categorized by the point in time during the reaction at which the dopant is introduced, as shown in Scheme 5.1: dopant introduction can occur before (I.), after (II.), or during heterojunction formation (III.). Each approach will be discussed separately. All the shown approaches can potentially allow selective introduction of dopant ions into one of the domains, keeping the other undoped. This is a first step towards control over the dopant locale, which is a necessary prerequisite to the overall aim of this thesis: The creation of a structure with a TM^{2+}-doped domain which is spatially separated from a reported domain, e.g., a seed within a seeded rod structure.

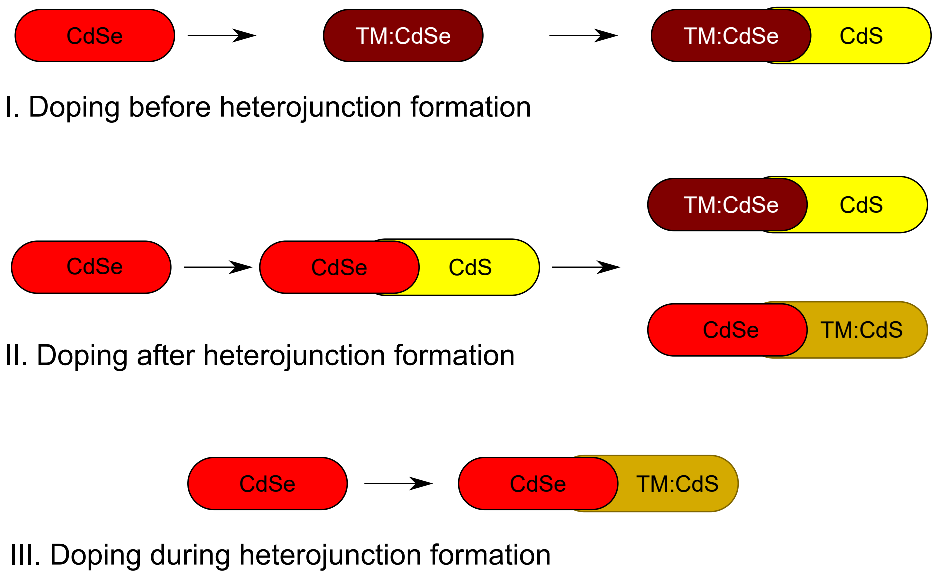

Scheme 5.1: Different points during heterostructure synthesis at which dopant can be introduced into a seeded rod.

5.1 Doping before heterojunction formation

Doping before heterojunction formation is the first approach towards nanoparticles with doped domains to be discussed. This involves a two-step process. First, doped particles are synthesized. Then, those doped particles are used to grow complex structures, i.e., as seeds in a seeded rods approach. The key challenge in this approach is suppressing self-purification effects caused by high reaction temperatures (typically 350 °C in the CdSe/CdS seeded rod synthesis) and keeping the dopant from diffusing out of the seed particle into the surrounding domains. First, a simple seeded rod synthesis with doped seeds is used to establish the relevance of these factors for the system at hand. Subsequently, a shell growth approach is tested to potentially improve dopant retention within a seed particle.

The diffusion doping approach by Vlaskin et al. was used,[51] in order to create the doped seed particle necessary for these approaches. This method has a variety of advantages over other doping methods, such as cluster decomposition and doping with pyrophoric reactants: Firstly, it is available for a wide range of dopant/host combinations including Mn^{2+} ions and CdSe in the wurtzite phase, which is notoriously hard to achieve. The low tendency of Mn to adsorb on wurtzite-CdSe surfaces and the poor interaction between the soft Se^{2-} and the intermediate to hard Mn^{2+} ions according to the hard and soft acids and bases (HSAB) principle make doping difficult. Apart from the synthetic challenge, Mn/CdSe is an attractive system due to being the most common II-VI semiconductor doped with the most commonly used magnetic ion, and the fact that the electronic structure is strongly dependent on the particle size: The position of the d-levels in Mn^{2+} can either be located within the band gap for CdSe dots with a diameter $d < 3.3\,\text{nm}$, or within the CB for particles with $d > 3.3\,\text{nm}$.[97] An additional synthetic advantage of diffusion doping is the high dopant level that can be achieved, with a cationic fraction of Mn of up to 0.4.[51] This can make up for potential dopant loss due to self-purification or cation exchange processes during the growth of another domain, e.g., a CdS rod. And lastly, the synthesis is relatively easy, highly reproducible, and does not require the use of pyrophoric chemicals that are both a safety and an environmental hazard.

5.1.1 Doped cores in a seeded growth approach

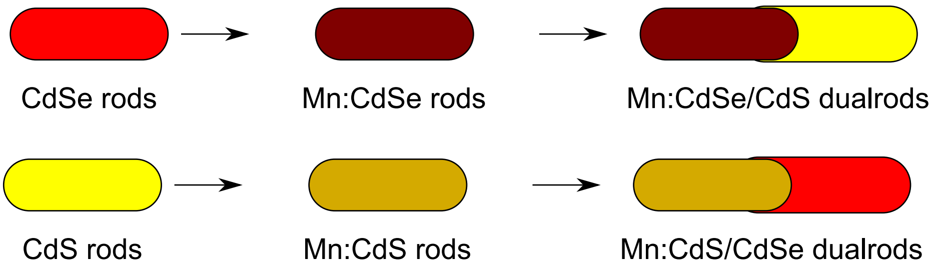

Scheme 5.2: Reaction scheme for dual rod growth with diffusion doped cores.

A first approach towards doping before heterojunction formation is the growth of dual rods from doped rods as seed particles. This offers the advantage of slightly bigger domains that have the

---

[51] Vladimir A. Vlaskin et al. *J. Am. Chem. Soc.*, **135**: 14380–14389, 2013.
[97] Rémi Beaulac et al. *Nano Lett.*, **8**: 1197–1201, 2008.

potential to more easily compensate for the strain induced by dopant introduction. Additionally, the bigger domains can simplify analytics, since a higher fraction of doped material in the sample makes it easier to detect the dopant. As shown in the previous Chapter 4.1, dual rod growth works well for CdS growth on CdSe. In order to achieve different structures, both Mn:CdSe/CdS dual rods and the inverse structure, Mn:CdS/CdSe dual rods, were synthesized. This experiment is a necessary step in order to better understand which approach is best suited to achieve the goal of anisotropic introduction of a dopant.

CdS and CdSe rods were synthesized in a seeded rod approach and subsequently doped *via* the diffusion doping approach.[11,51,70] This yielded Mn:CdS and Mn:CdSe rods with a cationic fraction of Mn $X_{\mathrm{Mn}} = c_{\mathrm{Mn}}/(c_{\mathrm{Mn}} + c_{\mathrm{Cd}})$ of 0.29 and 0.11, respectively, based on elemental analysis *via* ICP-OES (see Appendix B, Table B.4 for details). The obtained doped and undoped particles were then used as seeds in a dual rod approach at 320 °C, creating CdSe/CdS, Mn:CdSe/CdS, CdS/CdSe, and Mn:CdS/CdSe dual rods.[70] UV/vis analysis of the rod and dual rod samples (Figure 5.1 (a and b)) shows absorption peaks at 650 nm (CdSe, (a), black trace) and 480 nm (CdS, (b), black trace). The peak shape is typical for rod-shaped particles. Upon doping, no significant changes are observed (red trace). CdSe/CdS dual rod growth lead to the appearance an additional feature at 480 nm appears which is assigned to the CdS domain grown on the seed particle (Figure 5.1 (a), gray trace). This additional peak is more pronounced for Mn:CdSe/CdS dual rods (a, dark red trace) than for CdSe/CdS dual rods, which is attributed to a lower seed particle concentration of the doped seeds resulting from losses during particle purification after doping. This leads to a higher amount of available CdS monomer, and, consequently, material per seed particle for the doped dual rods.

In the HR-TEM micrographs (Figure 5.1 (c)), this is evident from the longer CdS rod domain for the doped sample, as well as the homogeneous nucleation of CdS rods without seeds, i.e., without the typical coke bottle/lollipop shape. For CdS/CdSe dual rods an additional absorption signal appears at 650 nm (Figure 5.1 (b), gray trace), indicating growth of a CdSe domain. For Mn:CdS/CdSe dual rods, the CdSe signal appears at lower wavelengths of 600 nm, which indicates that the grown domains are smaller in diameter than in the undoped case (b, dark red trace). This is supported by the HR-TEM micrographs which show significantly slimmer particles (Figure 5.1 (d)). Generally, CdS/CdSe dual rods do not show coke bottle morphology, but thickened domains with higher contrast at both the (0001) and the (000$\bar{1}$) ends, reminiscent of a barbell. This hints at a different growth mechanism with reduced facet selectivity compared to the CdSe/CdS dual rod mechanism presented in Section 4.1.7.

Due to their high number of unpaired electrons, the local magnetic environment of transition metal ions can be probed by electron paramagnetic resonance spectroscopy (EPR). For a Mn^{2+} -doped material, an EPR signal is expected that is characterized by hyperfine splitting: As a d^5 system, an isolated Mn^{2+} ion has five electrons whose magnetic spins couple with the spin of the Mn nucleus ($I = 5/2$), leading to spectra that split up into six equidistant signals, the hyperfine structure. If Mn^{2+} centers are close to each other the electron spins do not only interact with the nucleus to which they are bound, but also with nuclei that are further away. This interaction is distance dependent, and referred to as dipolar coupling. As each electron interacts with a number of nuclei in such a system, this results in multiple coupling signals that overlay, which leads to one

---

[11] Luigi Carbone et al. *Nano Lett.*, **7**: 2942–2950, 2007.

[70] Danja Fischli, Florian Enders, and Klaus Boldt. *J. Phys. Chem. C*, **124**: 12774–12783, 2020.

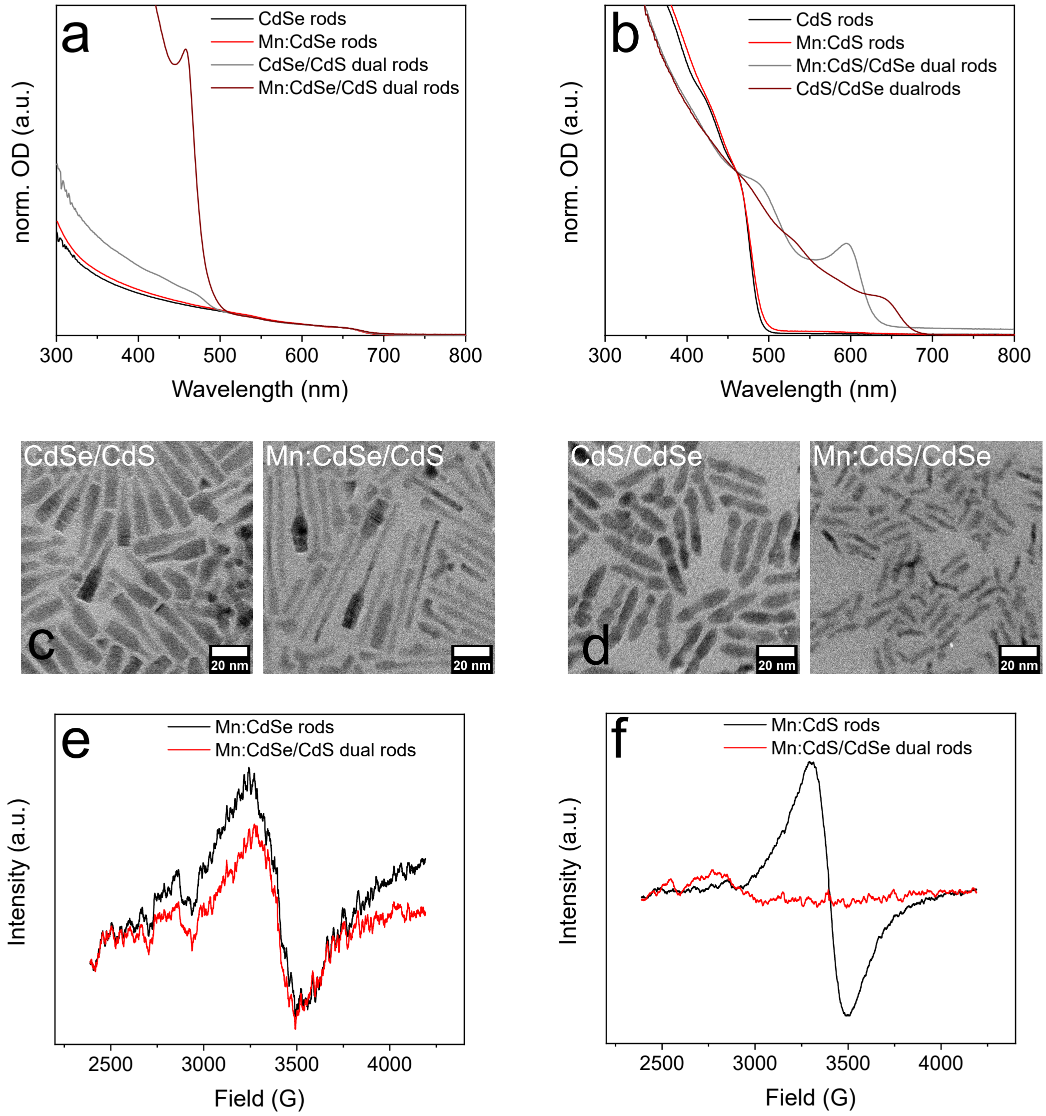

Figure 5.1: UV/vis absorption spectra (a) of CdSe rods (black), Mn:CdSe rods (red), CdSe/CdS dual rods (gray), and Mn:CdSe/CdS dual rods (dark red). UV/vis absorption spectra (b) of CdS rods (black), Mn:CdS rods (red), CdS/CdSe dual rods (gray), and Mn:CdS/CdSe dual rods (dark red). UV/vis spectra were normalized to the first excitonic peak of the original rod particles. HR-TEM micrographs of the dual rod samples (c and d). EPR spectra of Mn:CdSe rods (black) and Mn:CdSe/CdS dual rods (red, e), and Mn:CdS rods (black) and Mn:CdS/CdSe dual rods (red, f), acquired at −50 °C.

broad signal that masks the hyperfine structure. A singular, broad EPR signal of a Mn^{2+}-doped sample thus indicates Mn^{2+} centers that are close together, either due to high concentration, or due to the formation of clusters consisting of multiple Mn^{2+} ions.[98,99]

Such a broad signal is detected in EPR analysis of Mn:CdSe/CdS dual rods and Mn:CdSe rods (Figure 5.1 (e)). The EPR signals appear at the same field of approximately 3400 G, and have similar intensity. The single, broad signal indicates dipolar coupling and thus, that a significant amount of Mn^{2+} centers that are in proximity to each other. The Mn:CdS rod sample shows a similar signal as the Mn:CdSe rod sample (Figure 5.1 (f)). However, when the Mn:CdS/CdSe dual rod is grown, the signal disappears, indicating dopant loss due to self-purification of the system. This is consistent with elemental analysis, which shows that only 1.6 % of the initial dopant level is retained for Mn:CdS/CdSe dual rods, in contrast to 12 % for Mn:CdSe/CdS dual rods.

The HSAB principle (Hard and soft acids and bases) provides a possible explanation for this behavior. Archer, Santangelo, and Gamelin showed for Co^{2+} ions that dopants preferentially accumulate in a CdS domain rather than a CdSe domain.[45] This is attributed to better interactions between TM^{2+} and S^{2-} than between TM^{2+} and Se^{2-}. According to the HSAB principle, borderline and hard TM^{2+} Lewis acids cannot outcompete the softer Cd^{2+} for binding sites with the soft Se^{2-} base. This principle holds true for Mn^{2+} ions as well,[50] since their hardness is further increased due to the half-filled d-shell of the high-spin d^5 system.[48] This explains reports of fast self purification and dopant loss upon addition of Cd^{2+} ions to diffusion doped CdSe and CdS particles.[51]

Based on the literature reports, it is reasonable to assume that in the presented experiments, Mn^{2+} is excluded quickly as soon as dual rod growth starts, simply due to the fact that the softer Cd^{2+} ions are present. As S^{2-} is a harder base than Se^{2-} dopant loss should be less pronounced for Mn:CdS/CdSe rods than for Mn:CdSe/CdS rods, but the opposite is observed here. A possible explanation that could be verified by additional experiments is that Mn^{2+} dopants are first excluded for both types of dual rods, and then reabsorbed into a growing CdS domain, but not a CdSe domain, due to the better HSAB interactions. This would mean that instead of Mn:CdSe/CdS dual rods, CdSe/Mn:CdS dual rods are synthesized starting from Mn:CdSe rods. In order to prove this hypothesis, it would be key to verify whether the dopant ends up in the CdSe or the CdS domain. This is not possible *via* EPR for these strongly doped particles because the hyperfine splitting that would allow for conclusions with regard to the local environment is masked by dipolar coupling. Analysis with magnetic circular dichroism spectroscopy could answer this question,[55] but this method is highly specialized and not easily available.

These results show that TM^{2+}-doped seeds in a seeded rod synthesis have a strong tendency to undergo self-purification, with losses of 88 % and 98 % of dopant concentration during growth of Mn:CdSe/CdS and Mn:CdSe/CdS dual rods, respectively. For the retained dopant, it cannot be determined with commonly available methods whether it is located in only one domain of the particle, and if so, in which. Consequently, a simple seeded growth synthesis is not suitable to reliably retain control over which particle domain is doped.

---

[98] B. T. Allen and D. W. Nebert. *J. Chem. Phys.*, **41**: 1983–1985, 1964.

[99] Robert T. Ross. *J. Chem. Phys.*, **42**: 3919–3922, 1965.

[45] Paul I. Archer, Steven A. Santangelo, and Daniel R. Gamelin. *J. Am. Chem. Soc.*, **129**: 9808–9818, 2007.

[50] Raffaella Buonsanti and Delia J. Milliron. *Chem. Mater.*, **25**: 1305–1317, 2013.

[48] Ralph G. Pearson. *Inorg. Chem.*, **27**: 734–740, 1988.

[55] Charles J. Barrows, Vladimir A. Vlaskin, and Daniel R. Gamelin. *J. Phys. Chem. Lett.*, **6**: 3076–3081, 2015.

5.1.2 Trapping dopants inside the seed particle

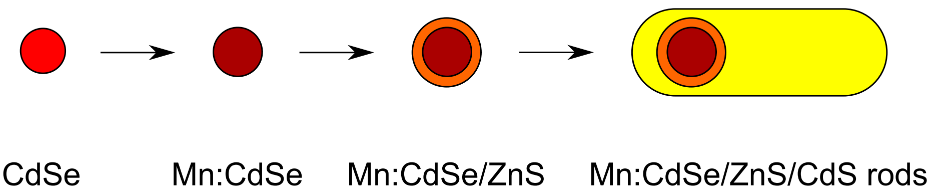

Scheme 5.3: Reaction scheme of dopant trapping by shell growth.

In order to suppress the tendency of Mn^{2+} to diffuse out of the doped seed particle, an approach by Hofman et al. offers a promising solution: The authors use a thin ZnS shell around the doped Mn:CdS core in order to trap the dopant at the ZnS/CdS interface, within the particle. The lattice mismatch of ZnS vs. CdS provides a barrier over which the dopant cannot diffuse.[59]

This approach was applied to the growth of Mn:CdSe/ZnS/CdS seeded rods. Briefly, CdSe seeds were grown and subsequently doped *via* the diffusion doping route at 300 °C. The obtained Mn:CdSe dots were then used directly in a seeded rod synthesis at 350 °C. In an additional experiment, a shell of 1 monolayer (ML) of ZnS was grown around the Mn:CdSe dots at 310 °C, which were then used as seeds in a CdSe/CdS seeded rod synthesis.[11] In order to monitor additional effects of the shell growth, undoped reference experiments were run in parallel.

Evaluation of the particle size (Figure 5.2 (a), black) shows that the seed particles grow both due to Mn diffusion doping and ZnS shell growth. Diffusion doping leads to a broadening of the size distribution as well as an increase in diameter by approximately 0.6 nm. This is a result of the doping mechanism which relies on the deposition of MnSe units on the particle surface. From the increase in diameter, an approximate cationic fraction $X_{\mathrm{Mn}} = c_{\mathrm{Mn}}/(c_{\mathrm{Mn}} + n_{\mathrm{Cd}}) = 0.39$ can be calculated, not accounting for changes in density due to mixing effects. This value is consistent with data from earlier studies,[51,100] and elemental analysis *via* ICP-OES, which gives the cationic fraction as 0.39, and a Mn/Se ratio of 1.2. The growth of the ZnS shell results in an increase in diameter by 0.8 nm for the undoped sample (CdSe and CdSe/ZnS dots) and 1.1 nm for the doped sample (Mn:CdSe and Mn:CdSe/ZnS dots). The lattice parameter of ZnS is $a = 0.3854$ nm, so the expected increase in diameter due to the growth of 1 ML is 0.77 nm, which matches the observed change in the undoped sample reasonably well. The doped sample increases by a higher amount (equivalent to approximately 1.42 ML of ZnS), which is likely a result of a lower amount of seeds in the synthesis. This is caused by a combination of losses during particle purification after the doping reaction, and the unreliability of sizing curves for doped particles. These sizing curves give a reasonable estimate of the dot size, size distribution, and concentration for undoped QDs. Dopant introduction, however, affects the absorption characteristics, as the introduction of Mn^{2+} dopants provides additional d-levels in the CB, leading to a shift of the absorption peak to higher energies. The seed concentration is thus easily overestimated, leading to a higher relative amount of ZnS in the shell growth reaction, and thus, growth of more monolayers per particle.

The same effect occurs during rod growth (Figure 5.2 (a), red). An underestimation of losses due to particle purification in previous steps leads to the overestimation of seed concentration, and thus,

---

[59] Elan Hofman et al. *J. Am. Chem. Soc.*, **139**: 8878–8885, 2017.

[100] Danja Fischli. *Lokalisierte Dotierung von Halbleiternanokristallen*. MA thesis. Konstanz: University of Konstanz, 2018.

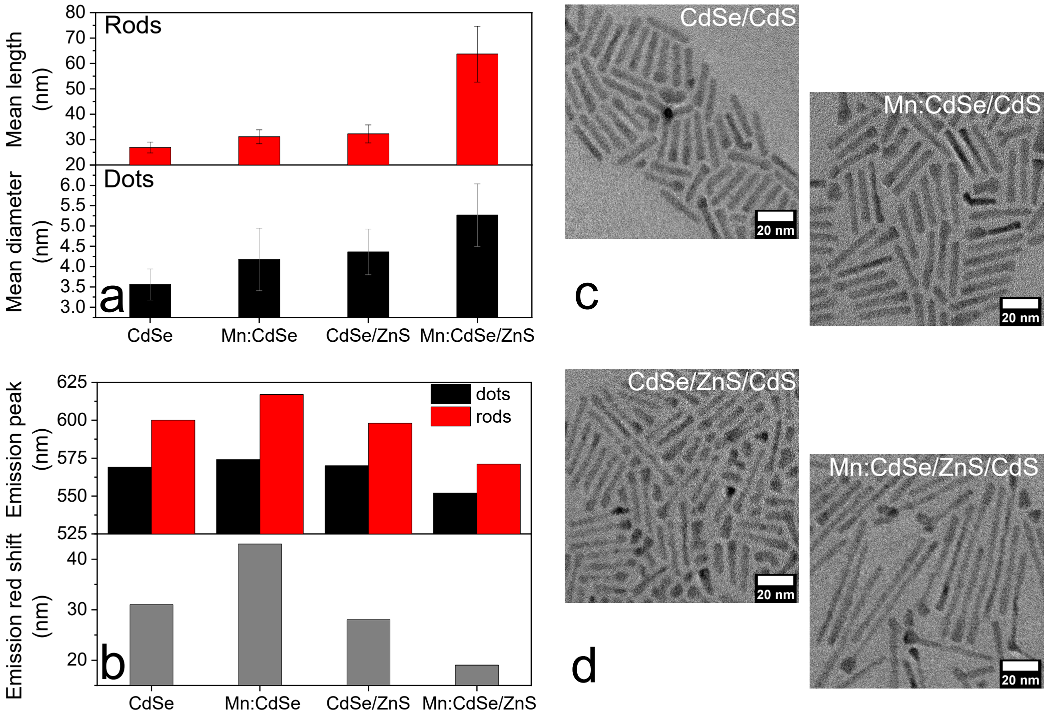

Figure 5.2: Particle sizes (a) of CdSe dots, Mn:CdSe doped dots, CdSe/1 ML ZnS dots, and Mn:CdSe/1 ML ZnS dots (black), as well as rods grown from these seeds (red). Emission peak position (b) of the same rod and dot samples (red and black, respectively, along with the emission red shift due to rod growth (gray). HR-TEM micrographs of the rod samples (c and d).

a lower amount of seeds in the reaction, resulting in longer rods. This is why the rods grown from undoped cores are the shortest with approximately (26.00 ± 2.11) nm, while Mn:CdSe/CdS and CdSe/ZnS/CdS rods are longer by approximately 5 nm ((31.12 ± 2.74) nm and (32.25 ± 3.55) nm, respectively). This effect is even more pronounced for the Mn:CdSe/ZnS/CdS rods, which are processed in a purification procedure twice, and reach (63.66 ± 11.01) nm in length.

In this multistep process, there are multiple factors that affect the optical properties of the nanoparticles. In diffusion doping, the particle growth caused by the deposition of material on the particles alone would lead to a decrease in band gap energy due to the inverse relationship between particle size and size of the band gap (quantum size effect). However, for CdSe QDs with a size of more than 3.3 nm the introduction of Mn^{2+} dopants leads to a shift to higher energies due to additional d-levels in the CB. In this case, the two effects balance out to an emission red shift of approximately 5 nm, from 569 nm for CdSe to 574 nm for Mn:CdSe QDs. A red shift of this size would indicate a size increase of only 0.2 nm in an undoped system.[8] Here, the particles grow by 0.6 nm, three times that value, so the red-shifting effect of the increasing size is significantly lowered by the opposing effects of dopant introduction.

Growth of a ZnS shell on CdSe creates a type I-structure, which typically leads to red-shifted

---

[8] Jacek Jasieniak et al. *J. Phys. Chem. C*, **113**: 19468–19474, 2009.

emission.[101] In the undoped samples, a red shift of only 1 nm, from 569 nm (CdSe) to 570 nm (CdSe/ZnS) is observed, which is on the lower side for the growth of 1 ML of ZnS on CdSe.[102] For the doped sample, a blue shift of 22 nm occurs instead, from 574 nm (Mn:CdSe) to 552 nm (Mn:CdSe/ZnS) (see Figure 5.2 (b), black). This is remarkable in so far that both doping and growth of a shell alone lead to red shifts in the other experiments, but the combination of the two caused the opposite. The effect must thus be due to the combination of the two.

Shifts to higher energy in heterostructures are typically a result of an increase in confinement. In this case this could be caused by alloying of the core with the shell material.[103] The fact that this was only observed in particles that do not only have a shell, but are also doped leads to the assumption that doping facilitates the formation of an alloy. Literature studies show that the lattice mismatch between MnS and a $Zn_xCd_{1-x}S$ alloy is 0 for $x = 0.5$, i.e., in an alloy of 50% CdS and 50% ZnS.[104] Here, a CdSe/ZnS system is studied, which has a strong lattice mismatch of 12 % of the two materials. The lattice constants of MnSe[105] and MnS[106] are located between those of ZnS[107] and CdSe[108], with lattice mismatches of 4 % (CdSe/MnSe), 6 % (MnSe/MnS), and 1 % (MnS/ZnS) (see Appendix A for details). Such an alloying effect requires mobility of the cations, which can reportedly be facilitated by added dopants.[109] It is thus possible that the highly mobile Mn^{2+} ions facilitate alloy formation between the CdSe core and the ZnS shell by mediating the lattice mismatch. Under the assumption that the core/shell structure of the seed particles remain largely intact that means a significant amount of Mn^{2+} dopants is located in or close to the core-shell interface.

Upon rod growth, a red shift is observed for all samples relative to the emission of the seed particles (Figure 5.2 (b), gray). This shift is due to the formation of a type $I^{1/2}$ structure (CdSe/CdS), which decreases confinement as the electron wave function can extend into the CdS shell. This red shift amounts to 30 nm for the undoped CdSe/CdS rod sample, and is slightly lower for the CdSe/ZnS/CdS sample (28 nm). A significant deviation is observed for the doped samples with red shifts of 43 nm for Mn:CdSe/CdS (1.5 times that of CdSe/CdS) and 19 nm for Mn:CdSe/ZnS/CdS (0.75 times that of CdSe/CdS). The higher red shift for Mn:CdSe/CdS is attributed to the fact that during diffusion doping, the seed particle size increased due to MnSe addition. This is not visible in spectroscopic analysis of the Mn:CdSe seeds, because the blue shift due to dopant incorporation partly compensated for this effect. Upon addition of Cd^{2+} ions during rod growth, fast self-purification occurs, where the Mn^{2+} dopants diffuse out of the seed particle and are exchanged for Cd^{2+}.[52] Mn^{2+} that accumulates in the CdS domain of the rod will not affect the emission properties at room temperature as exciton recombination occurs almost exclusively in the CdSe core. An energy transfer between the seed and the dopant would occur *via* the Dexter mechanism, which requires wave function overlap and scales with $exp1/R$. It is thus only effective for distances of less than 1 nm. Thus, the strong red shift reflects the increase in seed particle size due to doping. In

---

[101] Taleb Mokari and Uri Banin. *Chem. Mater.*, **15**: 3955–3960, 2003.

[102] Margaret A. Hines and Philippe Guyot-Sionnest. *J. Phys. Chem.*, **100**: 468–471, 1996.

[103] Klaus Boldt et al. *J. Phys. Chem. C*, **118**: 13276–13284, 2014.

[104] Angshuman Nag, S. Chakraborty, and D. D. Sarma. *J. Am. Chem. Soc.*, **130**: 10605–10611, 2008.

[105] The Materials Project *Materials Data on MnSe by Materials Project* July 2020 DOI: 10.17188/1199092

[106] The Materials Project *Materials Data on MnS by Materials Project* July 2020 DOI: 10.17188/1192718

[107] The Materials Project *Materials Data on ZnS by Materials Project* July 2020 DOI: 10.17188/1187297

[108] The Materials Project *Materials Data on CdSe by Materials Project* July 2020 DOI: 10.17188/1187302

[109] Urko Petralanda et al. *J. Phys. Chem. Lett.*, **9**: 4895–4900, 2018.

[52] Charles J. Barrows et al. *ACS Nano*, **10**: 910–918, 2016.

the case of Mn:CdSe/ZnS/CdS rods, the reduced red shift can be attributed to fact that the exciton remains strongly confined to the core already due to the described alloying. This reduces the effect of rod growth on the emission properties, as the alloy acts as a barrier towards the exciton.

For elemental analysis the Se concentration is chosen as a reference because it is a measure for the seed concentration and can be set as constant over all reaction steps. ICP-OES data shows that the Mn:CdSe/ZnS dots have a Mn/Se ratio of 0.95, which amounts to 80 % retention of dopant with regard to the original Mn:CdSe dots. Mn:CdSe/ZnS/CdS rod growth leads to a retention of 5 % of dopants in the shelled seed particles, leading to a final Mn/Se ratio of 0.05. Mn:CdSe/CdS rods retain 4 % of the original dopant level with a final Mn/Se ratio of 0.05. In both cases, the final dopant concentration is approximately the same, as most of the dopant is lost during rod growth. The formation of the ZnS shell has little impact on the final dopant concentration.

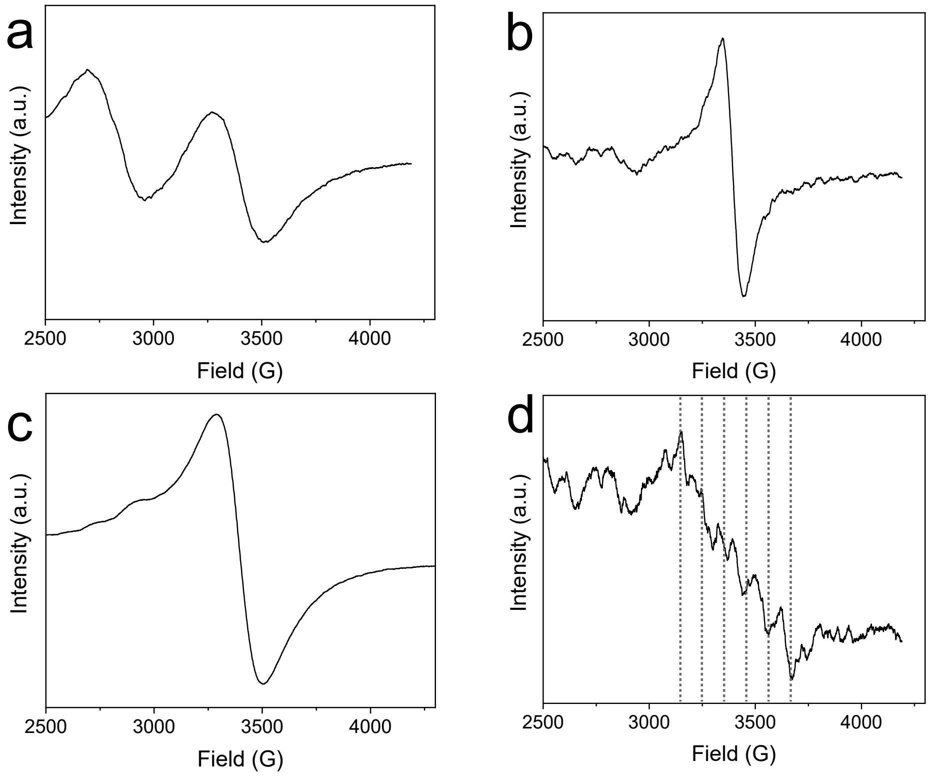

Figure 5.3: EPR spectra of the doped samples: Mn:CdSe dots (a), Mn:CdSe/CdS rods (b), Mn:CdSe/ZnS dots (c), and Mn:CdSe/ZnS/CdS rods (d). Vertical, dashed lines are equidistant and are guides to the eye for hyperfine splitting.

EPR measurements were performed in order to provide insight into the local distribution of the dopants within the particles (Figure 5.3). The broad, dipolar coupling observed for both Mn:CdSe and Mn:CdSe/ZnS dots (Figure 5.3, (a) and (c), respectively) matches the high dopant concentrations from elemental analysis. The dipolar interaction is distance dependent and indicates Mn^{2+} centers that are close together. This is typical for diffusion doped particles, as the dopant levels that are achieved *via* this route are very high compared to other methods.[51] The additional signal for Mn:CdSe with a center of 2800 G can be caused by either Mn^{4+} centers due to oxidation or by inhomogeneties in the magnetic field. The Mn:CdSe/ZnS sample shows a broad dipolar coupling that is similar to that of Mn:CdSe, though there is no additional signal visible (Figure 5.3, (c)).

A dipolar signal is visible in the EPR analysis of Mn:CdSe/CdS rods(Figure 5.3, (b)) as well, though it is less broad than that of Mn:CdSe. In contrast, the Mn:CdSe/ZnS/CdS rods show a very weak signal without dipolar coupling (Figure 5.3, (d)). The low signal to noise ratio does not allow for reliable conclusions, but an equidistant pattern similar to hyperfine splitting appears to be present. Remarkably, elemental analysis showed the same, low dopant level for both Mn:CdSe/CdS and Mn:CdSe/ZnS/CdS rod samples, but their EPR spectra differ significantly. As dopant concentration per particle is the same in both samples, Mn^{2+} centers must be in a different environment in the samples to account for these differences. Dipolar coupling in the Mn:CdSe/CdS rod sample indicates Mn^{2+} centers that are close together, but that is not necessarily related to a high overall Mn concentration. It can also be caused by clusters of two or more Mn^{2+} ions.[98,99] Hints of the existence of high local accumulations Mn^{2+} ions were reported previously.[100] In the case of Mn:CdSe/ZnS/CdS rods, the possible hyperfine splitting can be taken as a hint that the dopant is well distributed, e.g., radially in a CdSe/ZnS/CdS alloy. Accumulation of dopant is favored, as Mn^{2+} experiences minimal lattice strain in such an alloy.[104] This would indicate that while the biggest part of the dopant is excluded quickly, a small part is locally retained due to the ZnS shell within the alloyed interface.

Despite the success Hofman et al. had with the usage of shell growth as a means to trap dopants in Mn:CdS/ZnS/CdS core shell particles, the method does not prevent dopant loss in the Mn:CdSe/ZnS/CdS seeded rod system. It is reasonable to assume that an alloy forms at the core/shell interface, in which small amounts of dopant are retained. A number of factors inherent to the system favor the formation of an alloy, i.e., the high reaction temperatures necessary for rod growth (300 °C and up), the big lattice mismatch which leads to a higher tendency of the materials to interdiffuse in order to reduce pressure, and the high dopant concentration that directly results from the chosen method of diffusion doping. A possible solution to this problem would be lower reaction temperatures and the usage of less heavily doped seed particles, both of which require the usage of more reactive, pyrophoric precursors. However, the formation of an alloy is an interesting observation that should be further studied. EXAFS is a method ideally suited to probe the local coordination of an ion,[110] and could thus uncover the composition of the formed alloy. A appealing question that could be answered is whether the composition and kinetics of a dopant-mediated alloy formation differs from those made by other methods.

5.2 Doping after heterojunction formation

As previously shown, doped particles have a strong tendency towards self-purification. Under reaction conditions necessary for heterogeneous growth dopant is largely lost due to factors such as the addition of Cd precursors and high temperatures of up to 350 °C. It is thus a logical next step to try and add the dopant to the system after the heterojunction is formed. This was done by applying the diffusion doping approach to CdSe/CdS dual rods. They are attractive candidates for this approach, as they have large domains of both CdSe and CdS materials. CdSe/CdS dual

---

[110] Klaus Boldt et al. *Nano Lett.*, **20**: 1009–1017, 2020.

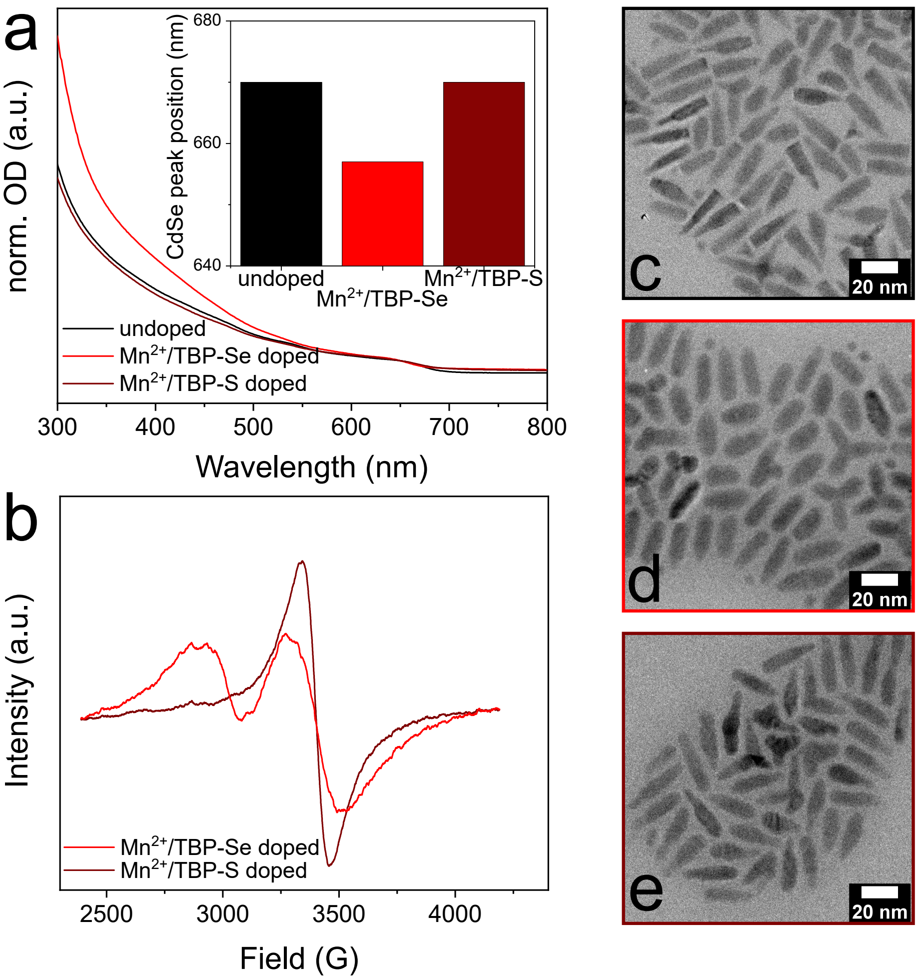

Figure 5.4: Diffusion doping of CdSe/CdS dual rods. UV/vis absorption spectra (a) of undoped particles (black), Mn^{2+}/TBP-Se doped particles, and Mn^{2+}/TBP-S doped particles (red and dark red, respectively). EPR spectra (b) of Mn^{2+}/TBP-Se and Mn^{2+}/TBP-S doped particles (red and dark red, respectively). HR-TEM micrographs of the samples (c-e).

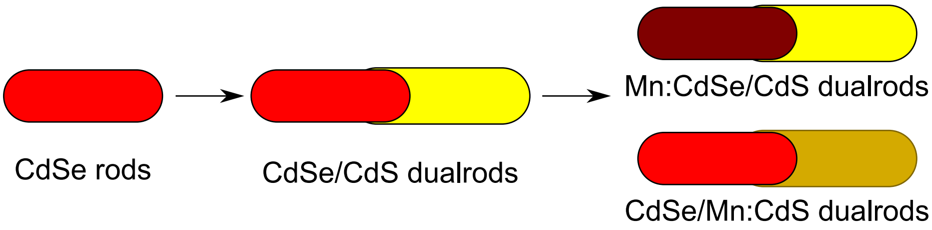

Scheme 5.4: Reaction scheme of diffusion doping of dual rods.

rods were prepared by growing a CdS rod on top of a CdSe seed at 320 °C. Samples of obtained particles were then submitted to a CdSe and a CdS diffusion doping procedure at 300 °C.

Both cdSe and CdS can be doped *via* diffusion doping, as shown in chapter 5.1.1. Typically, the difference between doping CdSe or CdS is the choice of chalgogenide, in the form of TBP-Se or TBP-S, that is added alongside the dopant during the procedure. An excess of chalcogenide lowers the chemical potential of Mn^{2+} in the lattice by eliminating the cation competition for chalcogenide anions. The usage of high concentration of Mn^{2+} ions in turn prevents Ostwald ripening by increasing the chemical potential for both Mn^{2+} and Cd^{2+} ions in the solution, and thus preventing dissolution of material.[51]

Hypothetically, an exposed CdSe domain could be targeted by doping with a Mn^{2+}/TBP-Se mixture, and a CdS domain with a Mn^{2+}/TBP-S mixture. However, the CdSe part of the dual rod likely has a shell of CdS material around it (see Section 4.1.2), which would lead to the CdSe domain not being exposed. In literature reports, no attempt was made so far to dope with a chalcogenide/dopant mixture that does not match the material presented at the surface. The experiment presented here can provide insight into whether the chalcogenide in solution must match the one at the surface in order to successfully introduce dopant, or if a doped shell can form that then diffuses into the particle anyway.

Figure 5.4 shows the results of the Mn^{2+}/TBP-Se and the Mn^{2+}/TBP-S dual rod doping experiments. In the absorption spectra (Figure 5.4 (a), Mn/Se doping leads to a blue shift of the absorption peak associated with the CdSe domain from 670 nm to 657 nm, which indicates successful incorporation of Mn^{2+} ions into the CdSe domain.[51] The signal around 450 nm, which is assigned to the CdS domain, changes in intensity. For Mn/S doping, the CdSe absorption peak is observed at the same wavelength as in the undoped sample, indicating that the CdSe domain remains undoped if S instead of Se is present in the reaction mixture. The CdS absorption region remains unchanged. Dopant incorporation into the CdS domain would not be visible in the absorption spectra, as the Mn^{2+} d-levels would be located in the band gap. Direct absorption into these levels is spin-forbidden, so these levels would only be visible in emission spectra at low temperatures.[111]

The EPR shows a broad, dipolar coupling signal for both the Mn^{2+}/TBP-Se and the Mn^{2+}/TBP-S doping experiments (Figure 5.4 (b)), indicating the successful incorporation of Mn^{2+} ions that are in close proximity to each other. As in previous experiments, an additional signal is observed at approximately 2800 G for Mn/Se doping that either stems from partial oxidation to Mn^{4+} or from inhomogeneties in the magnetic field. Elemental analysis reveals that doping with the Mn^{2+}/TBP-S mixture is more than twice as efficient than with Mn^{2+}/TBP-Se, as the former results in a Mn/Se

---

[111] Xiaoli Yang et al. *J. Am. Chem. Soc.*, , 2019.

ratio of 3.15, with only 1.42 for the latter. A possible reason for this is the better interaction of Mn^{2+} with S^{2-} compared to with Se^{2-} according to HSAB.

The HR-TEM micrographs in Figure 5.4 (c-e) show that for doping with the Mn/S mixture, particle morphology is largely retained, as the typical dual rod shape with the broader CdSe seed and a more narrow CdS tail is still clearly visible (c, e). For the doping experiment with the Mn/Se mixture, this is not the case (d). The CdS bottleneck cannot be distinguished from the CdSe part anymore, instead, broad rods are formed. This indicates that ripening effects take place if the Mn^{2+}/TBP-Se system is employed, but not with the Mn^{2+}/TBP-S system. A possible explanation for the selective occurrence of ripening processes is that the ions in solution do not match the ions on the particle surface. As ripening effects such as Ostwald ripening require the dissolution and re-nucleation of material,[15] they can be suppressed if the solubility of the monomer is lowered. When doping dual rods with Mn^{2+}/TBP-S, this is achieved by the addition of Mn^{2+} and S^{2-} ions, with the S^{-} anion matching the particle surface, lowering CdS solubility by means of increasing the solubility product. For Mn^{2+}/TBP-Se, Se^{2-} is less effective at suppressing ripening, as the CdSe domain is covered by a thin shell of CdS. The fact that dopant is still successfully incorporated using the Mn^{2+}/TBP-Se system leads to the conclusion that Mn-Se units are still deposited. It is possible that a doped shell is formed around the particle, from where dopant diffused into the particle.

Both the experiment with Mn^{2+}/TBP-Se addition, and with Mn^{2+}/TBP-S addition were successful in introducing dopants into the dual rod. During doping with Mn^{2+}/TBP-S, dopant is incorporated, as evident from elemental and EPR analysis, but does not lead to a blue shift of the CdSe peak in the absorption spectra. Data points towards selective incorporation into the CdS domain in this experiment. For the Mn^{2+}/TBP-Se system, incorporation into the CdSe domain is evident from absorption spectra. This coincides with ripening effects, leading to loss of particle morphology and thus, anisotropy. No definite conclusion can be drawn with regard to the selectivity in this reaction, as dopant incorporation into CdS cannot be excluded. Since the aim of the thesis is the anisotropic reduction of dopants, and the resulting structure loses its compositional anisotropy in the process, diffusion doping is not the method of choice towards this aim.

5.3 Doping during heterojunction formation

As neither diffusion doping before heterojunction formation nor after heterojunction formation proved to be successful in anisotropic introduction of dopants, the third approach, doping during heterojunction formation, was addressed. A wide array of doping methods are available under this category, among them brute force doping with pyrophoric dopants[41] and doped particle growth by cluster decomposition.[45] The most promising and simplest approach is the addition of dopants during seeded rod growth as first presented by Dehnel et al.[57] They were able to successfully introduce Mn^{2+} dopants into the CdS domain of CdSe/CdS seeded rods. The key factor to suppress self-purification was lowering the reaction temperature from 320 °C to 350 °Cto 290 °C. This approach will be covered in the following section.

---

[15] W. Ostwald. *Z. Phys. Chem.*, **34U**: 495–503, 1900.

[41] D. J. Norris et al. *Nano Lett.*, **1**: 3–7, 2001.

[57] Joanna Dehnel et al. *ACS Nano*, **14**: 13478–13490, 2020.

5.3.1 Coordination polymers and dopants

The role of coordination polymers for anisotropic particle growth was established in Chapter 4: species such as CP-309 act as monomer reservoirs that locally release monomer, enhancing the selectivity for growth in the $[000\bar{1}]$ over the $[0001]$ direction. Since the aim is to anisotropically introduce dopants at the particle tips, the question arises whether it is possible to grow CPs that contain dopants. If dopant ions are incorporated into the CP network that would mean that they can release a monomer species which already contains dopant-chalcogenide bonds at the location of the reaction. In that case, a single source precursor similar to the cluster decomposition doping methods could be created.

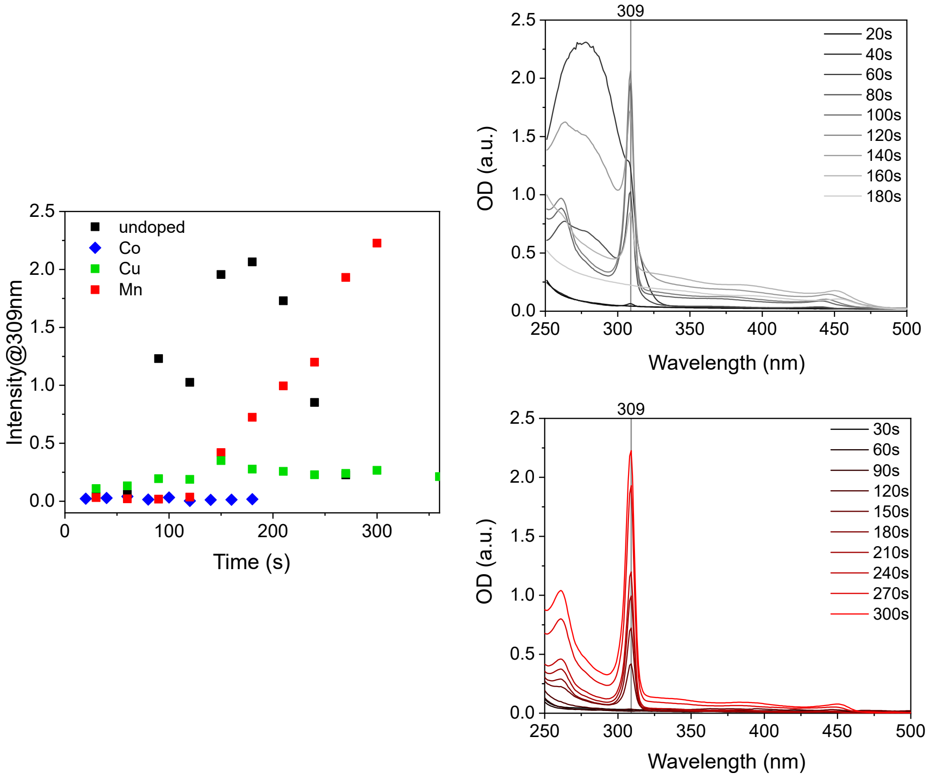

Figure 5.5: UV/vis absorption analysis of CP-309 formation without dopants (black symbols), and in the presence of Mn^{2+} (red symbols), Co^{2+} (blue symbols), and Cu^{2+} (green symbols) dopants. CP-309 signal evolution over time (left). UV/vis absorption spectra of the undoped (right side, gray) and Mn^{2+} doped experiments (right side, red).

CP-309 syntheses were performed with and without the addition of manganese(II) acetate, cobalt(II) acetate, and copper(II) acetate. Samples of equal volume were drawn at regular intervals and the intensity of the CP-309 absorption signal at 309 nm was evaluated. The results are shown in Figure 5.5).

In the undoped experiment, the CP-309 signal first appears after 40 s and increases until it reaches a maximum after 180 s, after which it decreases as particles are formed. This is indicated by the signal at approximately 450 nm that shifts over time towards lower energies. The signal at 260 nm is assigned to a molecular species that can be separated from CP-309 by size-selective precipitation,[76] but was only detected alongside the 309 nm species. It is thus assumed that they are at an equilibrium (cf. Section 4.1.2). The intense, broad signal between 250 nm and 300 nm in the undoped reaction is likely an artifact, as it not observed over all samples and too broad to belong to a reaction intermediate or a small particle species.

For Mn^{2+} addition, CP-309 appears in the absorption spectra at 120 s of reaction time, and increases to approximately the same intensity as the undoped sample, which is reached at 300 s, after which the observation frame ended. After 240 s, CdS particle formation can be observed. Mn^{2+} does thus not affect the formation of CP-309, but only slows down its rate. In the experiments with Co^{2+} (blue symbols) and Cu^{2+} (green symbols), neither CP-309 nor particle formation is observed, indicating that the addition of the acetic acid salts of these potential dopants prevent the formation of CP-309 on the observed timescale and in the used concentration.

This could be caused by crystal water that is added with the salts that acts as a protic additive and prevents CP formation (see Section 4.1.5). An alternative explanation is provided by the Irving-Williams series, which gives an empirical stability order for complexes of bivalent transition metal ions.[112] This order is $Cu^{2+} > Co^{2+} > Cd^{2+} > Mn^{2+}$ for the ions compared here. Cu^{2+} and Co^{2+} ions thus form complexes of higher stability and can outcompete Cd^{2+} ions for ligands, while Mn^{2+} cannot.

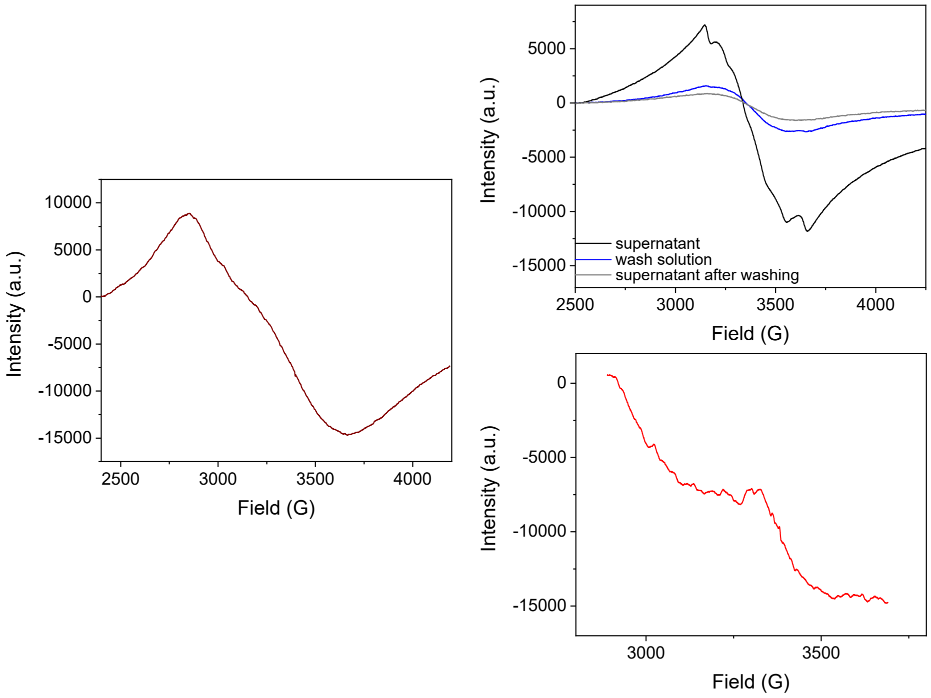

Figure 5.6: EPR analysis of Mn:CP-309 experiment. EPR spectra of Mn:CP-309 raw sample (left), supernatant, washing solution and supernatant after washing (top right), and Mn:CP-309 sample after washing (bottom right, red).

---

[76] Qiyu Yu and Chun-Yan Liu. *J. Phys. Chem. C*, **113**: 12766–12771, 2009.

[112] Harry Irving and Robert J. P. Williams. , **162**: 746–747, 1948.

As Mn(II) acetate is the only dopant source with which coordination polymer growth can still be observed, further experiments were conducted in order to verify if Mn^{2+} ions are incorporated into the polymer network. This would lead to the formation of a mixed precursor, similar to the one used in the cluster decomposition method.[45] The reaction was thus stopped at a point when particle formation has not yet started. CP-309 is then isolated and investigated via EPR. The EPR spectra (Figure 5.6 (left)) show a broad dipolar coupling with a shape that indicates multiple species. The coordination polymer was further purified by washing with hexanes, and the washing solution as well as the original supernatant and the supernatant after washing were similarly analyzed with EPR. High concentrations of Mn^{2+} are indicated by a broad dipolar coupling signal for all of the wash solution samples, while the final product shows little to no EPR signal. This indicates that even with Mn^{2+} doping, the dopant is not incorporated into the coordination polymer, but rather enclosed during the synthesis, and can be removed by washing.

This means that no CP species with preformed Mn-S bonds is formed. The fact that the synthesis by Dehnel et al. works anyway shows that it is in fact not necessary to the growth of a doped material domain to have these bonds formed in the precursors.[57] This is in accordance with studies by Archer, Santangelo, and Gamelin who showed that a cluster with a preformed dopant-chalcogenide bond does not perform better as a doping agent than a salt containing the dopant.[45] Doping during heterojunction formation must work via a different mechanism, possibly related to adsorption of dopant on reactive sites. Consequently, the fact that no CP was formed in the presence of Co^{2+} and Cu^{2+} dopants does not rule out that doping of seeded rods is possible during the formation of the heterojunction.

5.3.2 Direct doping of CdSe/CdS seeded rods

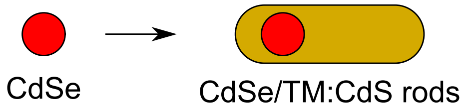

Scheme 5.5: Reaction scheme of direct doping during seeded rod growth.

While it was shown in the publication by Dehnel et al. that Mn^{2+} dopant can be incorporated by their approach, they did not extend their experiments to other dopants nor did they address possible effects on particle growth kinetics and morphology due to the addition of the dopant and acetate ligands. These open questions will be covered in the following section.

Particle growth experiments without and with Mn^{2+} and Co^{2+} dopants were conducted and monitored over a timeframe of 30 min. Co^{2+} was chosen as the second dopant as it is well established for doping CdS particles, and it acts as a photoluminescence (PL) quencher, simplifying the analytics required to verify dopant incorporation. As shown in Figure 5.7, particle growth occurs at similar speed as in the undoped reference for Mn^{2+} doping, but is slightly slower and results in shorter particles for Co^{2+} doping. The particle morphology is not affected for the doping experiments, as is visible in the HR-TEM micrographs (Figure 5.7, bottom row). Additionally, PL lifetimes of all samples were obtained and plotted against the particle length (see Appendix C, Table C.1). This x-axis was selected over the reaction time as the emerging formation of the CdSe/CdS type I$^{1/2}$

structure influences the lifetime as well. It is thus feasible to compare particles of similar length rather than particles that were grown for the same amount of time.

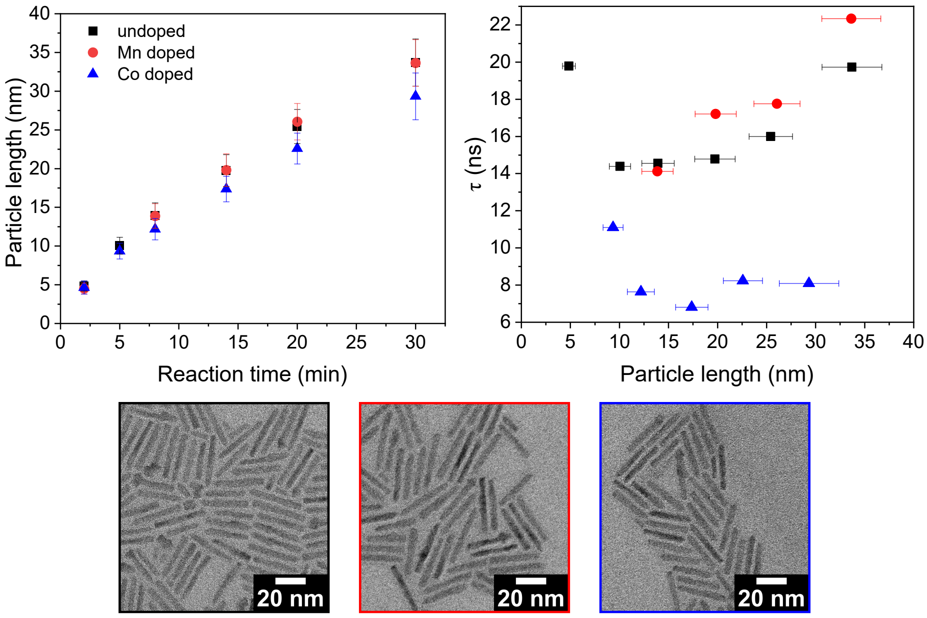

Figure 5.7: Direct doping of CdSe/CdS nanorods by dopant addition during the seeded rod synthesis. Particle length evolution over time (left), and PL lifetime in dependence of particle length (right) for Mn^{2+} doping (red symbols), Co^{2+} doping (blue symbols), and undoped reference experiment (black symbols). HR-TEM micrographs of 30 min samples of the experiments (bottom).

The lifetime τ decreases at the first stage of the undoped reaction from 19.74 ns to 14.38 ns. This is a result of the formation of a CdSe/CdS core-shell particle at the early stages of rod growth. The overcoating with CdS leads to enhanced quantum efficiency due to saturation of the increased coordination of unsaturated bonds at the surface, as well as increased confinement of the hole to the particle core. Over the course of the experiment, the lifetime then increases again, until it reaches 19.72 ns after 30 min. This is due to the fact that with increasing rod length, it is more likely that an exciton is excited along the rod as opposed to near the seed, in which recombination is detected. The exciton must then first travel to the recombination center. This process is characterized by the competition between 1D exciton diffusion along the rod to the seed and exciton trapping due to surface traps. The holes specifically are trapped on a picosecond timescale with an efficiency of >99 %.[113] They travel along the rod from surface trap to surface trap, which can be described by a 1D random walk model.[22] When the wave functions of the electron, which localizes fast in the CdSe seed, and the trapped hole overlap, recombination can occur. The PL lifetime thus scales with the number of traps in which a hole is bound as it travels along the rod, and thus, the rod length.

The Mn^{2+} doping experiment shows similar behavior to the undoped samples. The lifetimes vary from the reference by 2 ns at most, which is well within expected deviations due to fitting

---

[113] Kaifeng Wu et al. *J. Am. Chem. Soc.*, **137**: 10224–10230, 2015.

[22] James K. Utterback et al. *Nat. Chem.*, **8**: 1061–1066, 2016.

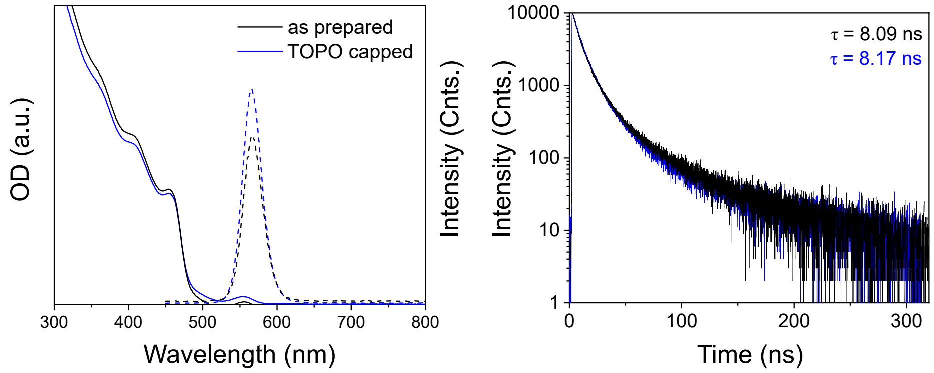

Figure 5.8: Effect of TOPO capping on CdSe/Co:CdS nanorods grown for 30 min. UV/vis absorption (solid lines) and emission spectra (dashed lines, left) and PL decay (right) before (black) and after TOPO treatment (blue).

and sample handling. In the Co^{2+} experiment, the lifetimes are consistently reduced relative to the reference, to the range of 6 ns to 11 ns. Co^{2+} ions act as PL quenchers, reducing the lifetimes. The lifetime reduction hence hints at successful incorporation of Co^{2+} dopants, while no definite conclusion can be drawn from the presented data regarding Mn^{2+} doping, as radiative recombination via the Mn^{2+} d-levels is possible, but cannot be observed at room temperature.[114]

The fact that the fluorescence is quenched only party, but not completely upon Co^{2+} incorporation indicates, that the dopant is selectively incorporated in the CdS rod domain, and does not diffuse in the CdSe core. If the core were doped, a complete quench of PL would be observed, as Archer, Santangelo, and Gamelin was able to prove. However, they also showed that Co^{2+} dopants can also be adsorbed to the particle surface, leading to false positives for doping.[45] This is not a factor in Mn^{2+} doping, as the binding energies of Mn^{2+} ions to wurtzite CdS are not sufficient for adsorption to the particle surface.[6] Ligand exchange with TOPO can remove these excess TM^{2+} dopants from particles surfaces.[45] In order to exclude the possibility of adsorbed Co^{2+} ions, the procedure was performed on CdSe/Co:CdS rods.

The results of this approach are shown in Figure 5.8. The UV/vis absorption and emission spectra show no significant change due to TOPO capping (left). Similarly, the PL decay curves are similar in shape, and only a slight increase in lifetime τ occurs within the margins of error. As the main changes due to removal of dopants are expected in the PL decay lifetimes, the fact that they remain stable is a good indicator that a significant amount of dopant is indeed incorporated into the particles instead of only adsorbed on their surface.

5.3.3 Direct detection of Mn^{2+} dopants

A consistent challenge throughout the described experiments so far has been the detection of Mn^{2+} dopants. A first method to solve this problem is elemental analytics such as ICP-OES which give a quantitative number of the dopant concentration in a given sample. This approach is a quantitative one, but cannot be viewed in isolation, as it gives very little qualitative information

---

[114] Vladimir A. Vlaskin et al. *Nano Lett.*, **10**: 3670–3674, 2010.

[6] Steven C. Erwin et al. *Nature*, **436**: 91, 2005.

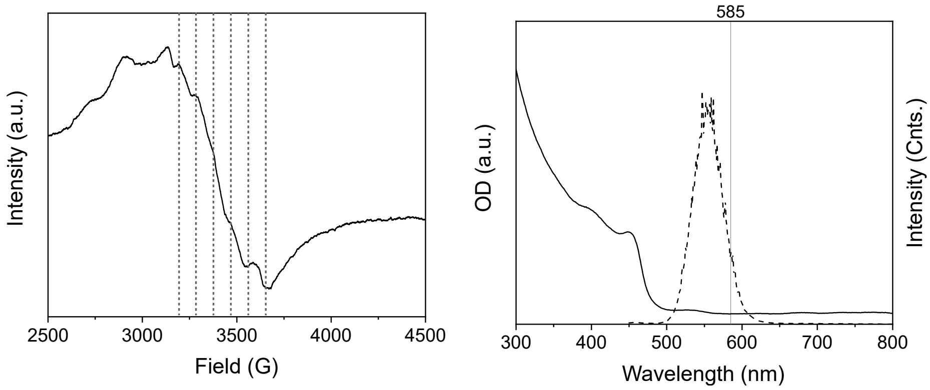

Figure 5.9: Direct doping of ZnSe/Mn:CdS nanorods. EPR spectra measured at −50 °C (left). Vertical, dashed lines are equidistant and are guides to the eye for hyperfine splitting. UV/vis absorption and emission spectra (room temperature) (right).

about the location of the dopants within the sample (in the particle, adsorbed to the surface, or simply in solution). EPR spectroscopy on the other hand gives only limited information on the concentration, especially for solutions of doped nanoparticles with varying particle concentrations over different reaction steps, but can provide insight into the specific location of the dopant. For instance, the signal of a Mn^{2+} dopant close to the particle surface can be distinguished from one closer to the center, if hyperfine splitting is observed.[115] This becomes more difficult if the dopant concentration, which is notoriously hard to control, is high enough that the distance dependent dipolar coupling that emerges from closely located Mn^{2+} centers overlays and masks this signal. A third option is the Mn^{2+} emission, which is the basis for a variety of applications of Mn^{2+}-doped nanoparticles, e.g., as probes for temperature[114] or lattice strain.[116]

This third option has its limits for systems consisting of seeded rods. In the CdSe/CdS system, excitons recombine almost exclusively in the CdSe core. This holds true for Mn^{2+}-doped CdSe/CdS systems as well, as the d-levels of Mn^{2+} are located within the CB of CdSe particles for typical particle sizes greater than 3.3 nm.[97] For particles with ZnSe cores, however, detection of the Mn^{2+} dopant emission is possible.

In order to verify the success of the direct doping approach with Mn^{2+} it was tested for the ZnSe/CdS system in addition to the CdSe/CdS system. The EPR and spectroscopic data is shown in Figure 5.9. In the EPR, the signal shows hints of hyperfine splitting underneath the dipolar signal, which indicates lower dopant concentrations than in previous experiments, or Mn^{2+} centers that are far apart. The absorption spectra shows the typical signature of the CdS rod at 480 nm, while the emission spectra shows a signal at 550 nm. The Mn^{2+} emission is expected at 585 nm. Such a signal cannot be observed beyond an ambiguous shoulder. Instead, the main recombination is still centered in the core. This could possibly be circumvented by measuring at lower temperatures, as the ratio of Mn^{2+} emission to ZnSe core emission is temperature dependent.[111]

As the detection of Mn^{2+} emission is not possible at room temperature due to the seed emission being strongly favored, seedless CdS and Mn:CdS rods were grown for an additional experiment

---

[115] W W Zheng et al. *J. Phys. Chem. C*, **115**: 23305–23314, 2011.

[116] Sandrine Ithurria et al. *Phys. Rev. Lett.*, **99**: 5–8, 2007.

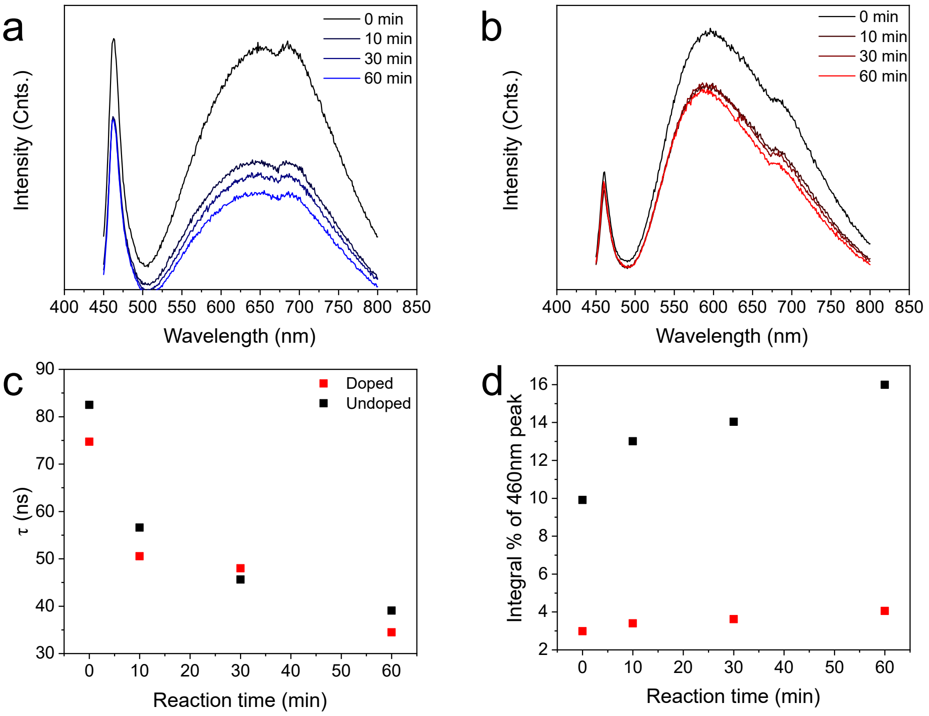

Figure 5.10: Photodegradation of surface trap states in Mn:CdS rods and pure CdS rods. Emission spectra kinetics of the photodegradation process of undoped (blue traces, a) and Mn^{2+}-doped CdS rods (red traces, b). Recovery over time of PL lifetime τ due to irradiation with blue light (c) and band gap emission intensity (d) of Mn:CdS (red symbols), and undoped CdS rods (black symbols).

that excludes this factor. Pure CdS rods show poor quantum yields due to surface defects, which mask a possible dopant emission. One factor contributing to these defects is H_2S that is produced during the synthesis and then adsorbed to the particle surface, creating deep-hole traps within the particle band gap.[117] These can be removed by photochemical degradation, e.g., by irradiation with blue light.

Both CdS and Mn:CdS rods show an emission peak at 460 nm, which is assigned to the band gap emission, and a broad trap emission between 500 nm 800 nm (Figure 5.10 (a, b)). Upon irradiation with blue light under nitrogen atmosphere, the spectra change, mainly in the trap emission area. Both the doped and undoped sample show recovery of the band gap emission lifetime τ from 75 ns and 83 ns to 35 ns and 40 ns, respectively (c). The total recovery is approximately the same for both samples. The relative integral of the band gap emission (d), however, recovers much faster for the undoped sample, from 10 % to 16 % after 60 min, while for the doped sample, values stay below 5 %. This indicates that for the doped sample, an additional component contributing to the non-bandgap emission is present, which is not affected by photodegradation, and thus not a result of traps due to adsorbed H_2S. The differing shapes of the trap emission point in the same direction.

This becomes more apparent if plotted together, as shown in Figure 5.11. The Mn^{2+} doped

---

[117] Chaodan Pu and Xiaogang Peng. *J. Am. Chem. Soc.*, **138**: 8134–8142, 2016.

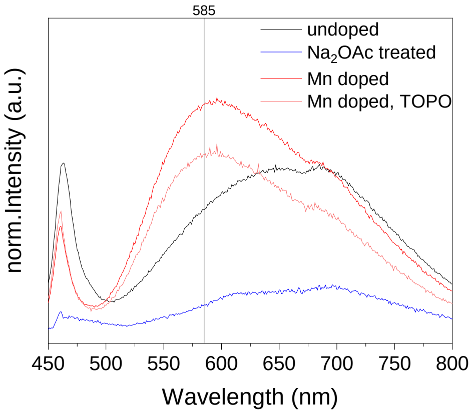

Figure 5.11: Emission spectra of CdS rods. Undoped (black), Mn^{2+}-doped before (red) and after TOPO capping (light red), Na_2OAc "doped" as a reference (black).

sample (red) shows an additional component centered around 585 nm, which is not present in the undoped sample (black). As this might be a result of etching due to acetate ligands, which are added during the reaction in the form of manganese(II) acetate, a reference experiment was conducted using disodium acetate (blue). This experiment results in significant quenching of the band gap emission, but not in a signal at 585 nm. In conclusion, the 585 nm emission is assigned to doped Mn^{2+} ions. As this signal is not significantly reduced upon TOPO capping neither (light red), the Mn^{2+} are incorporated. The direct doping approach is thus successful for both Mn^{2+} and Co^{2+} doping.

5.4 Postfunctionalization of doped nanorods: Tip growth on doped rods

The direct doping approach has proved to be an easy way to introduce both Co^{2+} and Mn^{2+} ions into pure CdS rods as well as seeded rods. Based on this doping method, experiments can now be conducted to establish whether postfunctionalization of domain doped nanorods is possible without dopants loss. Tip growth is an interesting option, as it is well established, works at relatively low temperatures (200 °C), and the possible outcome is promising: The combination of transition metal dopants with the possibility of recombination via the d-states could lead to the creation of a defined off state in tipped rods which is spectroscopically interesting.[68]

A typical tip growth reaction was performed on CdSe/Mn:CdS doped nanorods. At 200 °C, a TOP-Te stock solution was added to the rod-containing reaction mixture, followed by drop-wise addition of a cadmium oleate stock solution via a syringe pump, and an annealing period. The total reaction time was 40 min. EPR spectra of the particles were obtained before and after the reaction, shown in Figure 5.12 (left, black and blue traces). The initial signal of the doped particles is reduced for the tipped sample, which can indicate dopant loss over the course of the reaction.

In order to determine which reaction step leads to this outward-diffusion of dopant, the experi-

---

[68] Florian Enders. *Tailoring the Charge Carrier Relaxation in Colloidal Semiconductor Nano-Heterostructures*. PhD thesis. Konstanz: University of Konstanz, 2019.

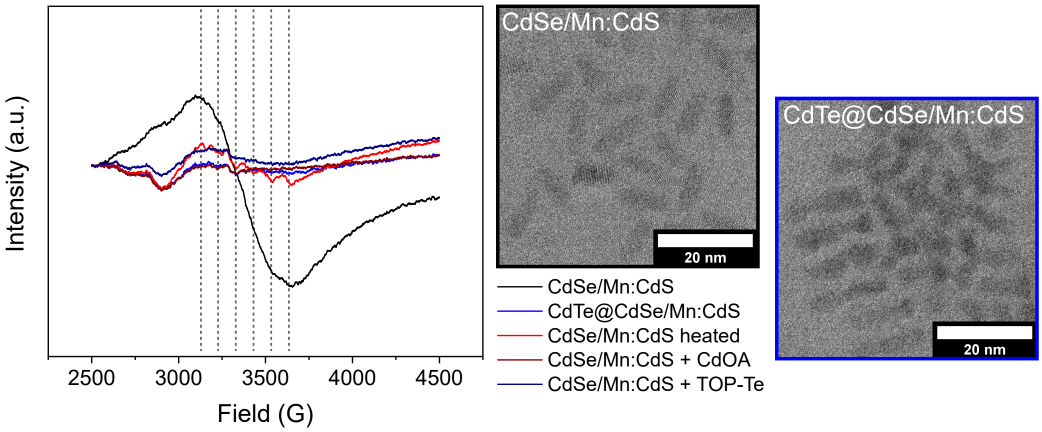

Figure 5.12: Tip growth experiments on CdSe/Mn:CdS nanorods. EPR analysis of the original CdSe/Mn:CdS rods (black), CdTe@CdSe/Mn:CdS rods (blue), and CdSe/Mn:CdS rods after treatment with TOP-Te (dark blue), Cd oleate (dark red), or only heat (red, left). Vertical, dashed lines are equidistant and are guides to the eye for hyperfine splitting in the heated rod sample. EPR spectra were obtained at −50 °C. TEM micrographs of the rods before and after tip growth (right).

ment was repeated with the addition of only TOP-Te (dark blue), and only cadmium oleate stock solution (dark red). EPR analysis of both of these experiments resulted in similar EPR spectra as the tip growth experiment. This indicates that the potential dopant loss is not due to a cation exchange process, as described for diffusion doping processes.[51,52] The total reaction time was kept the same for all the described reactions.

Elemental analysis shows a Mn/Se ratio of 3.15 for the initial CdSe/Mn:CdS rods. For the tipped growth sample, this value slightly drops to 2.66 (15 % reduction). For addition of only cadmium oleate, the final value is 0.49 and for only TOP-Te addition, it is 0.15 (85 and 96 % reduction). This indicates that the changes in the EPR spectra cannot be completely explained by purification effects, but that changes in sample concentration and solubility issues play a role.

In an additional experiment the particles were heated under tip growth conditions without the addition of chalcogenide or metal precursors. This resulted in particles with an EPR spectrum that shows equidistant signals that can be interpreted as hyperfine splitting (Figure 5.12, red trace). Hyperfine splitting would indicate that Mn^{2+} centers are further apart after heat treatment than before. According to elemental analysis, the cationic fraction is only slightly reduced (9.9 % vs. 8 % Mn cationic fraction), so this cannot be explained simply by dopant loss which would lead to a larger mean distance between the Mn^{2+} centers. A better explanation is provided by the clustering behavior, which was described before.[100] The theory assumes that Mn^{2+} ions form clusters in Mn:CdSe/CdS rods which lead to local recrystallization effects from the wurtzite phase to cubic α-MnS observed by TEM. Such a cluster could form during rod growth, leading to Mn^{2+} centers in proximity. Upon prolonged heating, the Mn^{2+} ions diffuse apart and are homogeneously distributed within the particle, leading to longer distances between the magnetic centers, which in turn can cause hyperfine splitting in the EPR. This would also indicate that the dopants are localized in clusters upon direct doping, and that this localization is disbanded upon heating.

In order to quantify the speed at which the suggested declustering process happens, the heating

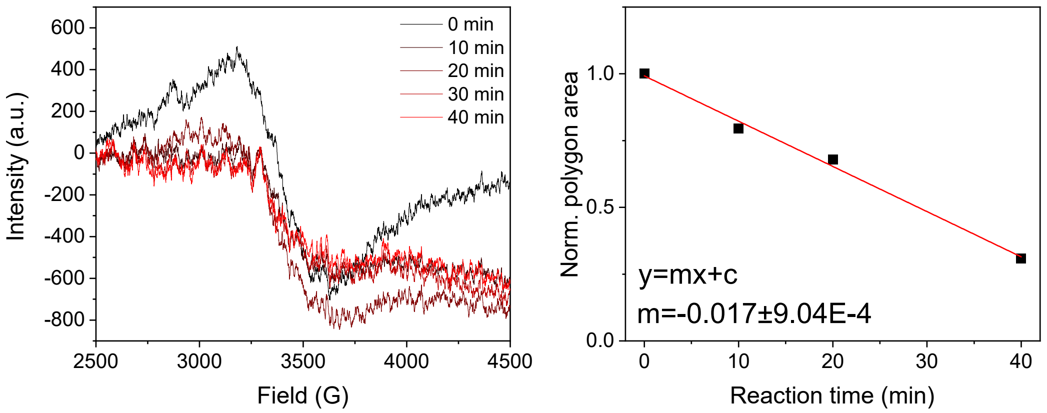

Figure 5.13: Quantification of dopant loss due to heating at 200 °C. EPR spectra of the drawn samples (left), and plot of the polygon area underneath the curve against the reaction time (right). EPR spectra were obtained at −50 °C.

experiment was repeated and monitored via EPR, as shown in Figure 5.13. Samples of a constant volume were drawn and measured without further purification, eliminating the possibility that changes in sample concentration affect the EPR spectra. Due to the poor signal-to-noise ratio, it cannot be determined whether hyperfine splitting occurs. The signal intensity represented by the polygon area underneath the EPR signals for each sample was calculated and plotted against the reaction time. Fitting this data yielded a linear fit with a slope of $m = (0.017 \pm 9.040) \times 10^{-4}$, which indicates a loss of 1.7 % of the original intensity per minute at the reaction temperature of 200 °C. This is not to be equated with the actual dopant loss, as the noise of the signal contributes to the polygon area as well. However, it gives an idea of the purification speed. For a reaction at 300 °C, purification would be close to instantaneous.

5.5 Conclusion

Multiple routes towards doping the entirety of a domain of a nanorod were investigated. Doping before heterojunction formation was first tested by growing Mn:CdSe/CdS dual rods and Mn:CdS/CdSe dual rods from diffusion doped seed particles. This approach was not successful, as the seed particles showed fast self-purification upon growth of a new domain, with up to 99 % of the initial dopant lost. With the available methods, it could not be distinguished whether the remaining dopant shows a tendency to remain preferentially in one specific material domain.

In a second approach, Mn:CdSe/ZnS nanoparticles were used as seeds in a seeded rod approach. The growth of a ZnS shell around a doped Mn:CdSe particle was successful and did not lead to significant dopant loss. Alloy formation was observed, probably furthered by doping, a behavior that has not yet been described and should be further investigated with regard to the intentional creation of graded shells. Growth of a seeded rod from the Mn:CdSe/ZnS particles did not lead to improved retention of dopant compared to growth from Mn:CdSe particles, but it affected their location: the retained dopant appeared to accumulated at the CdSe/ZnS/CdS alloy interface, while in the synthesis without the shell, dopant ions appeared to form clusters in the CdS rod domain.

Doping after heterojunction formation *via* diffusion doping of CdSe/CdS dual rods was performed both using a S^{2-} and a Se^{2-} containing precursor. This experiment showed, that doping with this route is possible regardless of whether the added chalcogenide matches the surface material. Even though the CdSe domain was covered by a CdS shell, it could be shown that with addition of Se^{2-}, it is possible to introduce dopant in this domain. One drawback was observed: doping of CdSe occured hand in hand with ripening processes that lead to a reduction in anisotropy.

Direct doping of seeded rods during rod growth, i.e., by adding the dopant during the reaction, appears to be the most promising approach for domain doping. While reaction intermediates play a large role for rod growth, they themselves do not need to be doped or even tolerate the specific dopant ion in order to make direct doping possible. Direct doping was shown to be successful for both Co^{2+} and Mn^{2+} dopants and will be the method of choice for localized doping in subsequent experiments in this thesis. Both the incorporation of Co^{2+} and Mn^{2+} dopants could be proven spectroscopically. The rod morphology was not affected.

Subsequently, doped particles were postfunctionalized by growing a CdTe tip on CdSe/Mn:CdS rods. This was successful and did not lead to immediate dopant loss. Results strongly hint that Mn^{2+} dopants cluster together within the particle during rod growth, and diffuse away from each other upon heating. This means that direct doping in itself leads to a certain degree of localized doping.

6 Introducing distance dependence: Localized Co^{2+} doping of CdSe/CdS seeded rods

So far, this thesis has dealt with the two aspects of localized doping, namely control over anisotropic growth and dopant introduction separately: In Chapter 4 the role of reaction intermediates for anisotropic growth was investigated in order to gain more insight into and control over rod growth kinetics. Chapter 5 dealt with finding the most suitable way to introduce TM^{2+} dopants into nanoheterorods while achieving control over the material domain in which the dopant is localized. In this chapter, the findings of both previous chapters are combined in order to find a way to selectively introduce TM^{2+} ions into only part of a material domain, creating a structure in which the dopant is located at a distance from a reporter structure, e.g., the seed. Essentially, distance dependence can be introduced that way.

So far, similar structures have mainly been synthesized from II-IV semiconductor nanocrystals by partial cation exchange, in which the bivalent host cation is first exchanged for monovalent cations, e.g., Ag^+ or Cu^+, before it is reexchanged for an alternative bivalent cation.[118] The anion sublattice is retained. Due to reactivity differences, this exchange is facet sensitive, and occurs from the rod ends, allowing for the creation of segmented nanorods.[119] While for starting materials such as roxbyite the introduction of up to 6 domains into a single particle is possible,[63] for the more thermodynamically stable II-IV semiconductors the available material combinations are limited due to solubility and mixing effects, and require care with regard to the specific reaction conditions.[64] Additionally, achieving doped structures instead of heterostructures with separated material domains via this route poses an additional challenge.

This chapter aims to find an easier solution to the challenge of local TM^{2+} doping, which will enable the facile synthesis of an interesting model system with a tunable distance between TM^{2+} dopant and a seed particle, while providing further insight into anisotropic growth mechanisms.

Parts of this chapter have been previously published in the following publication:

Danja Fischli, Luisa Rieger, and Klaus Boldt. Localized Co^{2+} Doping of CdSe/CdS Seeded Nanorods. *The Journal of Physical Chemistry C*, **126**: 12150–12158, 2022. DOI: `10.1021/acs.jpcc.2c02081`

---

[118] Karol Miszta et al. *ACS Nano*, **5**: 7176–7183, 2011.

[119] Patrick Adel et al. *Chem. Mater.*, **26**: 3121–3127, 2014.

[63] Benjamin C. Steimle, Julie L. Fenton, and Raymond E. Schaak. *Science*, **367**: 418–424, 2020.

[64] Luca De Trizio and Liberato Manna. *Chem. Rev.*, **116**: 10852–10887, 2016.

6.1 Direct doping during dual rod growth

In the previous chapter the most straightforward and promising doping route was identified to be direct doping during heterojunction formation. This means that the dopant is present during the heterogeneous growth phase of, e.g., a seeded rod synthesis. In the original form that was presented by Dehnel et al. that means that a dopant salt is dissolved in TOP and injected during the early stages of the synthesis, leading to incorporation of dopant ions which are statistically distributed over the particles.[57] In Section 5.3.2 it could be shown that this approach can be used to introduce Co^{2+} as well as Mn^{2+} ions which simplifies analytics via optical spectroscopy methods. Due to the Co^{2+} ions' tendency to quench photoluminescence (PL), dopant incorporation can be confirmed by optical spectroscopy, i.e., room temperature PL and lifetime measurements. Mn^{2+} ions on the other hand are more difficult to detect in nanoparticles, since they require low temperature PL spectroscopy or well resolved EPR analysis (see Section 5.3.3 for details). Since the doping mechanism was shown to work well for both ions, Co^{2+}-doped nanorods are an attractive model system that could later be expanded to other ions, and will be the system on which this chapter will concentrate.

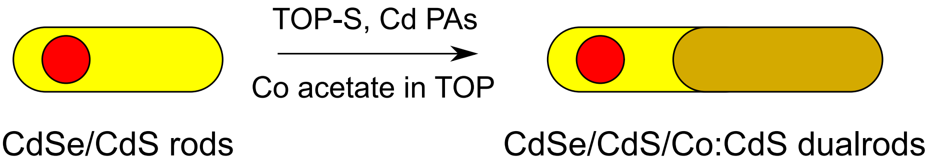

Scheme 6.1: Reaction scheme for direct doping during dual rod growth.

In order to get from uniformly doped to locally doped nanorods, the original procedure presented in Section 5.3.2 has to be modified. A simple way to do this is the adaption of a dual rod reaction scheme in order to grow a doped domain on top of an undoped one. Theoretically, this should enable the growth of a doped CdS domain on a previously formed CdSe/CdS nanorod. The preformed, undoped CdS domain of the original rod would then provide the spatial separation of the CdSe seed and the dopant in the newly grown doped domain. Varying the length of the rods that are used as seeds can then be used to vary this distance. This procedure is summed up in Scheme 6.1.

Doped rod and dual rod growth was performed repeatedly with different seed lengths to get statistically relevant results and check for reproducibility. Additional reference experiments include direct doping during seeded rod growth (as opposed to dual rod growth) and undoped experiments. Samples were drawn at regular intervals during the synthesis and investigated using PL spectroscopy, and their lifetimes τ were obtained in order to determine the effects of dopant introduction.

Generally, shorter PL lifetimes τ are expected for Co^{2+} doped nanorods as relative the to undoped samples. Co^{2+} dopants in the tetrahedral ligand field of the CdS host matrix provide spin-allowed, non-radiative relaxation pathways for the exciton via Förster or Dexter-type energy transfer to the $^4A_2 \rightarrow ^4T_1(P)$ ligand field transition.[121] The d-d transitions of the Co^{2+} dopants have an energy of 725 nm and lie within the CdS band gap, efficiently quenching the band edge luminescence of

---

[57] Joanna Dehnel et al. *ACS Nano*, **14**: 13478–13490, 2020.

[121] Victor I Klimov. *Nanocrystal quantum dots*. CRC press, 2017.

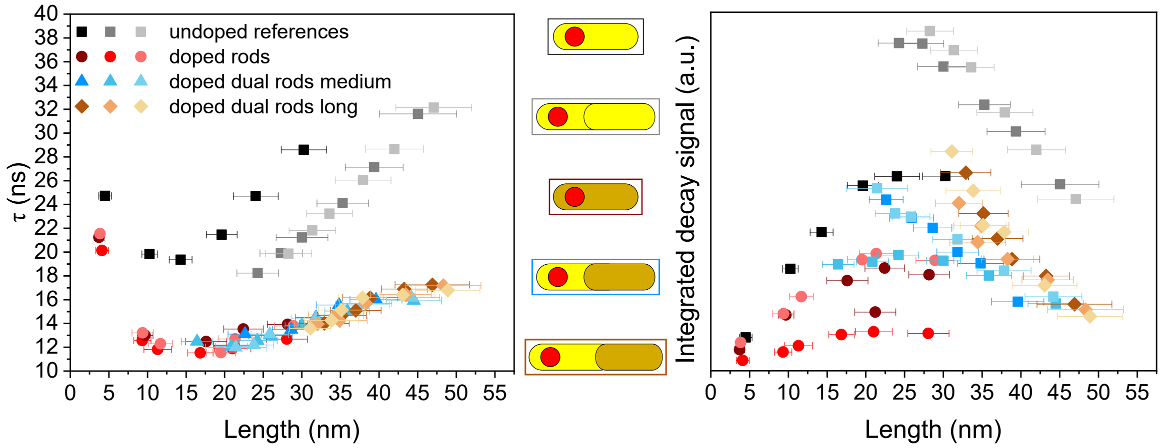

Figure 6.1: PL analysis of CdSe/CdS/Co^{2+}:CdS dual rods. Photoluminescence lifetime kinetics τ in dependence of total rod length (left). Integrated decay signal as a measure of quantum yield in dependence of total rod length (right). Undoped reference experiments of rods (black symbols) and dual rods (gray symbols, two experiments), doped rods (red symbols, three experiments), doped dual rods of medium and long seed lengths (blue and yellow symbols, three experiments each). Data was recorded at the PL maximum of the CdSe seed.

these semiconductor nanocrystals. Therefore, shorter lifetimes in CdSe/CdS/Co^{2+}:CdS dual rods should arise from a direct competition between radiative recombination in the CdSe seed and quenching of the exciton in the doped domain.[45]

As the data presented in Figure 6.1 (left) shows, the proposed correlation is confirmed by the obtained experimental data: τ of the doped samples (colored symbols) are systematically lower by 8 ns to 10 ns than those of the undoped reference samples (black/gray). The introduction of the non-radiative relaxation also leads to an overall decrease in signal intensity which is shown in Figure 6.1 (right) in terms of the integrated decay signal: Doped rods (red) and dual rods (blue and yellow) show systematically lower integrals than their undoped counterparts (black and gray, respectively). Differences are observed between the undoped rods and the undoped dual rods as well: The rods shower longer lifetimes and lower integrated decay signals, i.e., quantum yields. The changes in lifetime could be caused by the fact that dual rod seeds went through a purification procedure. This can affect the ligand concentration at the surface, which can, in turn, affect the number of surface traps.[96] However, such a process does not simultaneously explain the differences in QY, as this quantity should decrease with increasing amount of trap states, and thus, reduced lifetime. The QY increase in the context of reduces lifetime might be attributed to changes in the experiment, i.e., in laser intensity during measurement, or different particle concentrations in the samples.

Hypothetically, the reduced lifetime could also be a result of the added acetate ligands of the cobalt source. Acetate can affect the PL behavior of CdS rods, as shown in Section 5.3.3. This was excluded by growing nanorods with the addition of cadmium acetate at 290 °C as a control experiment. After 15 min, a sample was drawn, and then, a solution of cadmium(II) acetate

---

[45] Paul I. Archer, Steven A. Santangelo, and Daniel R. Gamelin. *J. Am. Chem. Soc.*, **129**: 9808–9818, 2007.

[96] Nicholas C. Anderson et al. *J. Am. Chem. Soc.*, **135**: 18536–18548, 2013.

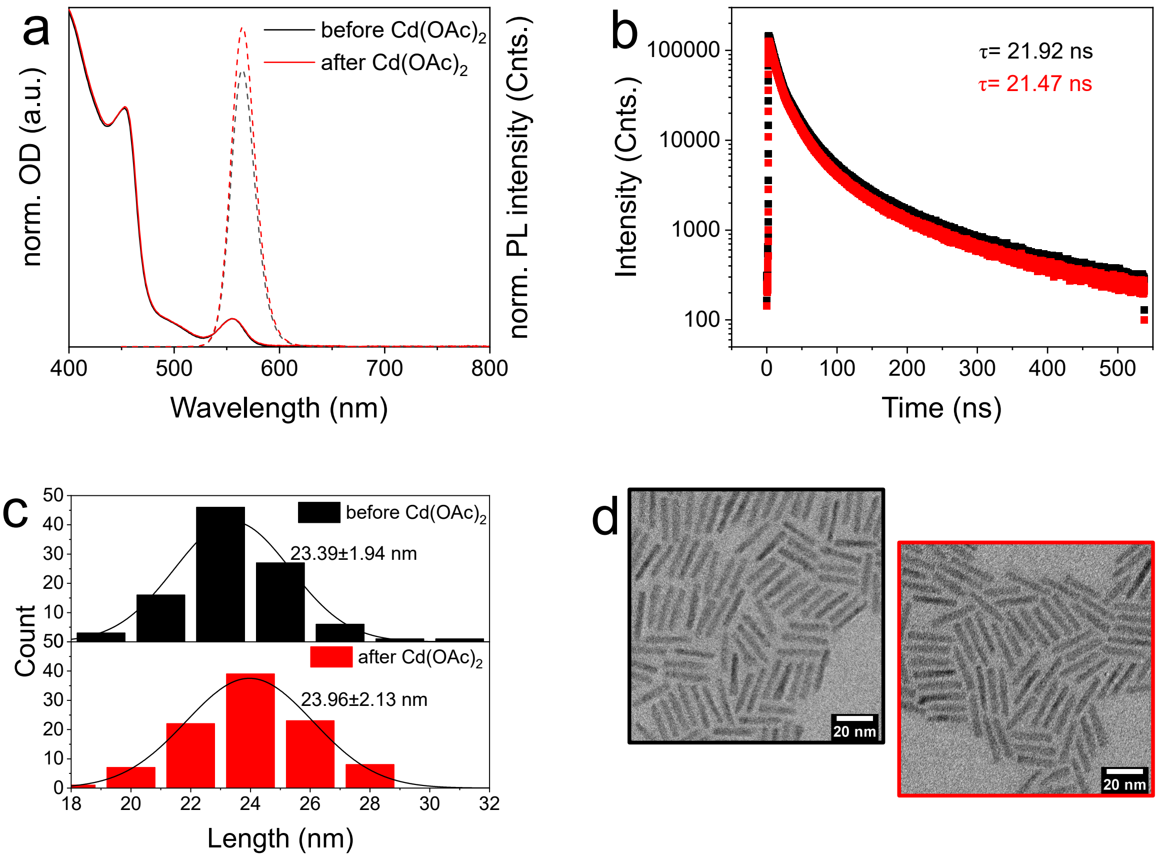

Figure 6.2: Absorption (solid lines) and emission spectra (dashed lines) of CdSe/CdS seeded rods, before (black) and after (red) the addition of Cd acetate in TOP (a). Photoluminescence lifetime decay (b), histograms (c) and TEM micrographs (d) of the same samples.

was added. The sample before and after the addition of cadmium(II) acetate are compared in Figure 6.2. If the changes in PL behavior in doped rods were caused by acetate ligands, PL lifetimes should be reduced here just like in experiments in which cobalt(II) acetate is used. Instead, only minor changes in emission intensity are observed (Figure 6.2 (a)), while PL lifetime remains the same (b). The rod morphology is not altered (Figure 6.2 (c, d)). The reduced PL lifetimes in the doping experiments can thus be attributed to dopant incorporation as opposed to etching or ligand exchange effects due to acetate addition.

For locally restricted introduction of Co^{2+} dopants, a dependence of the lifetime on the length of the undoped part of the rod is expected. An exciton can be created at any position within the rod. In an undoped particle, it would travel along the rod to the CdSe seed, where it can minimize its energy before radiative recombination. In a doped particle, the Co^{2+} dopant acts as an efficient trap for the exciton. Since the transfer to these trap states are fast and efficient, they reduce the amount of excitons that reach the seed, reducing the intensity of the emission peak, and decreasing the lifetime, because only excitons that do not encounter the trap state are detected, which are usually the ones excited close to the seed. A longer original rod increases the distance between

CdSe core and dopant, reducing the efficiency of the energy transfer between the two and thus, the influence of the dopant trap states on CdSe seed emission.

This is not reflected in the data. The evolution of τ is not noticeably different between directly doped rods and dual rods (red symbols and blue/yellow symbols, respectively). The datasets of the doped samples form an overall trend that is dependent on the total rod length and is consistent over all doped samples, regardless of the length of the original rods. Similar behavior is observed for the integrated decay signal.

This indicates that the dual rod approach does not lead to the growth of a doped domain on top of an undoped seed particle, i.e., not to localized doping. Instead, the dopant appears to be statistically distributed over the entire particle indicating dopant diffusion within the CdS domain. The fact that Co^{2+} diffusion in CdS nanomaterials is so fast is an interesting observation in itself and warrants further study of these processes, as there is no literature data available for this system. These processes have to be minimized t o achieve local control over the dopant introduction.

Diffusion is favored by long reaction times and high temperatures. As precursor reactivity requires a certain temperature window for the reaction to happen with sufficient control over particle size, monodispersity, and overall reaction kinetics, reaction time is the parameter that should be focused on in order to achieve control over the dopant locale. Thus, reducing the time that a doped particle is kept at elevated temperatures is the logical next step.

6.2 Distance dependent doping of CdSe/Co:CdS nanorods

6.2.1 Localized introduction of Co^{2+} into semiconductor nanorods

In order to selectively introduce Co^{2+} dopants to the nanoparticle tips, the established protocol for uniformly doped CdSe/Mn:CdS seeded rods presented in Section 5.3.2 was further modified to reduce the time doped particles were kept at high temperatures.[57] The Co^{2+} source was added during the nanorod growth reaction after the desired length of the undoped region was reached, in this case after 15 min. Three samples were drawn during the reaction: The first one right before dopant addition (15 min of reaction time), the second one 1 min after dopant addition (16 min of reaction time), and the third one 15 min after dopant addition, at which point the reaction was stopped after a total of 30 min of reaction time. It should be noted that at typical rod growth reactions at 350 °C, the reaction solution would already be depleted of monomer after 15 min of reaction time. In this case, at 290 °C, the reaction is significantly slower, so growth is still active (see Figure 5.7). Thus, doped material can be deposited, while at 350 °C, the dopant would be added to completely formed rods already in the ripening stage.

The absorption spectra shown in Figure 6.3 (a) show the typical absorption behavior of CdSe/CdS seeded rods with a local absorption maximum at approximately 550 nm that is associated with the CdSe core and the CdS absorption at around 450 nm. An additional, broad signal in the range of 600 nm to 650 nm is present in the doped samples, which can be attributed to the absorption of a range of d-d transitions of Co^{2+}.[122] The emission spectra exhibit a sharp decrease in quantum yield for both doped samples (red), compared to the undoped sample (black). PL lifetime measurements (Figure 6.3 (b)) reveal that PL lifetimes of doped nanorods decrease compared to the undoped sample, by 8 ns and 10 ns in the doped samples taken at 1 min (red) and 15 min (dark red),

---

[122] Pavle V. Radovanovic and Daniel R. Gamelin. *J. Am. Chem. Soc.*, **123**: 12207–12214, 2001.

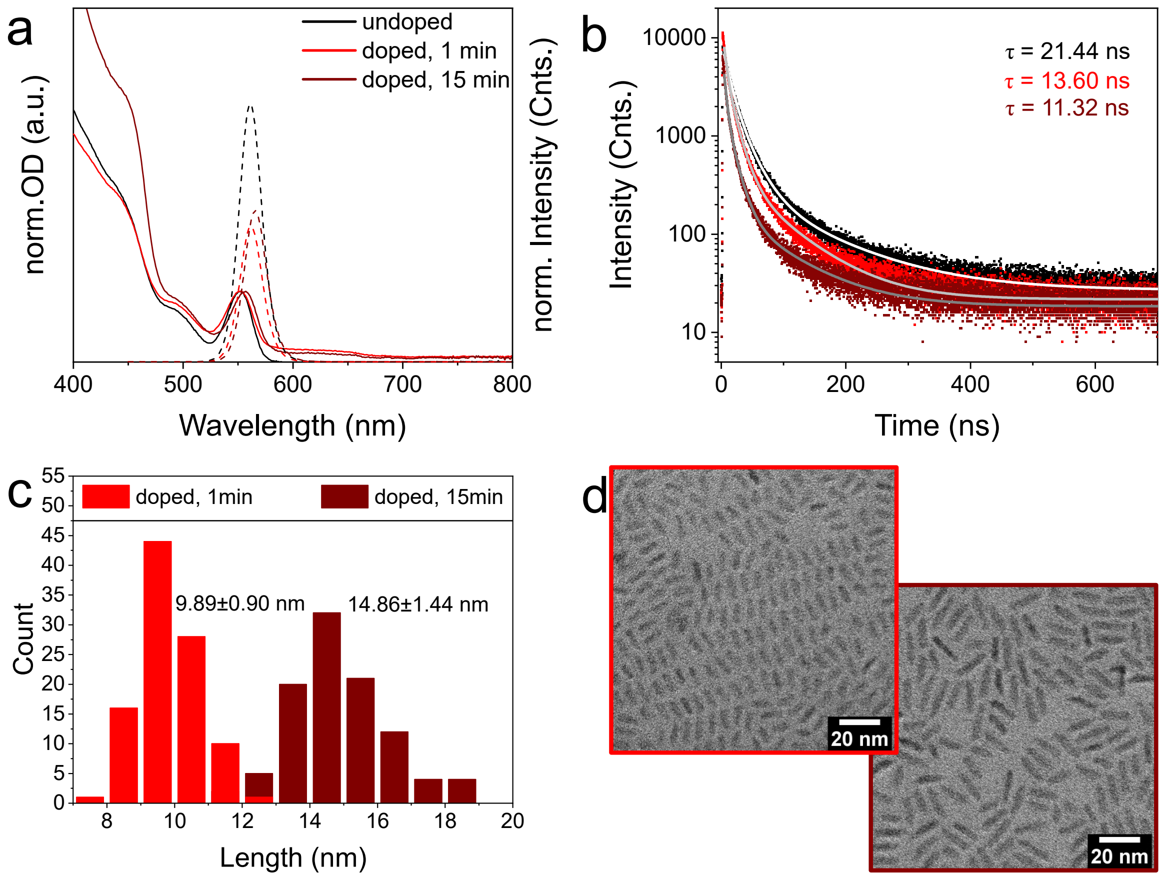

Figure 6.3: Absorption (solid lines) and emission spectra (dashed lines) of CdSe/CdS/Co^{2+}:CdS rods before (black, 15 min of reaction time), 1 min (red, 16 min of reaction time) and 15 min (dark red, total reaction time 30 min) after dopant addition (a). Photoluminescence decay of the same samples (b). histograms (c) and TEM micrographs of the doped samples (d).

respectively. This is attributed to the introduction of Co^{2+} dopants into the particle, and within the range that was observed in the dual rods experiment shown in Section 6.1.

PL quenching is stronger in the sample taken after 15 min than after 1 min. While the rods grow by (4.97 ± 2.34) nm (see Figure 6.3 (c)), a further reduction in lifetime is observed. No change would be expected for the growth of conventional nanorods in this size range, as quantum confinement is not affected. Consequently, this has to be a result of doping. Interestingly though, ICP-OES measurements show a decrease in Co content relative to Se (and thus per particle) from $X_{\mathrm{Co/Se}}(1\,\mathrm{min}) = 2.3$ to $X_{\mathrm{Co/Se}}(15\,\mathrm{min}) = 0.7$, which corresponds to 387 and 12 dopant atoms per particle, respectively (see Appendix B, Table B.5 for elemental analysis data). That means that the quenching efficiency of the dopant increases while the dopant content decreases.

The opposite would be expected for statistical distribution of dopant over the particle: In that case, the higher dopant content increases the chances of an exciton encountering a dopant trap state before it can recombine in the seed, reducing the lifetime τ. Instead, the system parameters change from a higher dopant content, but reduced influence of the dopant on exciton recombination in the seed, to a lower dopant content, but with increased influence on exciton recombination. This strongly suggests mobility of the guest ions in the CdS lattice, which matches the results presented in Section 6.1. Additionally, this hints at a significant influence of the dopant location on the optical properties: At this reaction stage, particle growth occurs mainly in one dimension, along the c-axis, so the doped material will deposit at the particle ends. With increasing reaction time, diffusion processes lead to exclusion of most of the dopants,[123] while the remaining dopants delocalize over the particle volume, reducing the mean distance between the seed as the main center of recombination and the dopant as a quencher. This further confirms the interpretation of the directly doped dual rod experiments presented in Section 6.1. Consequently, localized doping is only achieved in the early stages after adding the cobalt source, and a deeper understanding of the diffusion processes that work against dopant localization is necessary.

6.2.2 Dependence of optical characteristics on the dopant location

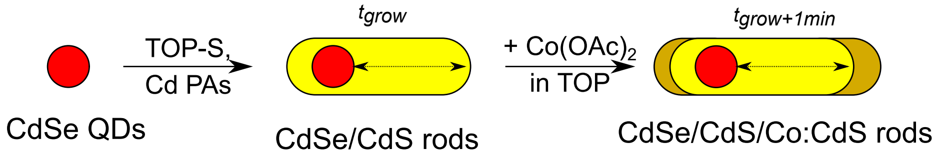

Scheme 6.2: Reaction scheme for direct localized doping during rod growth.

Scheme 6.2 shows the optimized reaction scheme. In order to suppress dopant diffusion and achieve localized doping, the time that the doped particles are heated was kept as short as possible. The reaction was stopped one minute after dopant addition, minimizing the time that diffusion is kinetically possible. PL lifetime measurements were performed on samples taken right before and 60 s after dopant addition. This experiment was performed for different reaction times t_{grow} from 2 min to 45 min of particle growth before dopant addition, at which point a sample was drawn, dopant was added, and the reaction was stopped 1 min later. This yielded doped seeded rods with total lengths of 4 nm to 22 nm.

Figure 6.4 (a) shows a plot of $\Delta\tau$ and the values of τ_{undoped} and τ_{doped} against the nanorod length. In order to facilitate comparison of the different samples, the changes of the PL lifetimes is also summarized with the net lifetime reduction $\Delta\tau = \tau_{\text{undoped}} - \tau_{\text{doped}}$ as a measure of the influence of dopant addition on the PL behavior. The biggest $\Delta\tau = 14$ ns is observed after 2 min of reaction time, at 3 nm of particle size. $\Delta\tau$ decreases significantly with increasing particle length, reaching 3 ns for particles of 22 nm length.

This effect can be explained as follows: The exciton is excited at a random position along the length of the nanorod and diffuses along the c-axis, while it is delocalized in the (a,b)-plane. Assuming efficient trapping by either the CdSe seed or a Co^{2+} dopant at the tip, the probability of non-radiative deactivation via the dopant is directly proportional to the rod's length.[22,124]

$\Delta\tau$ was thus approximated as a linear function of the particle length (Pearson's $r = -0.912$). Variation from the linear fit occurs mainly for the first three data points, after 2 min, 5 min and

---

[123] Dingan Chen et al. *J. Am. Chem. Soc.*, **131**: 9333–9339, 2009.

[22] James K. Utterback et al. *Nat. Chem.*, **8**: 1061–1066, 2016.

[124] Kaifeng Wu et al. *ACS Nano*, **9**: 4591–4599, 2015.

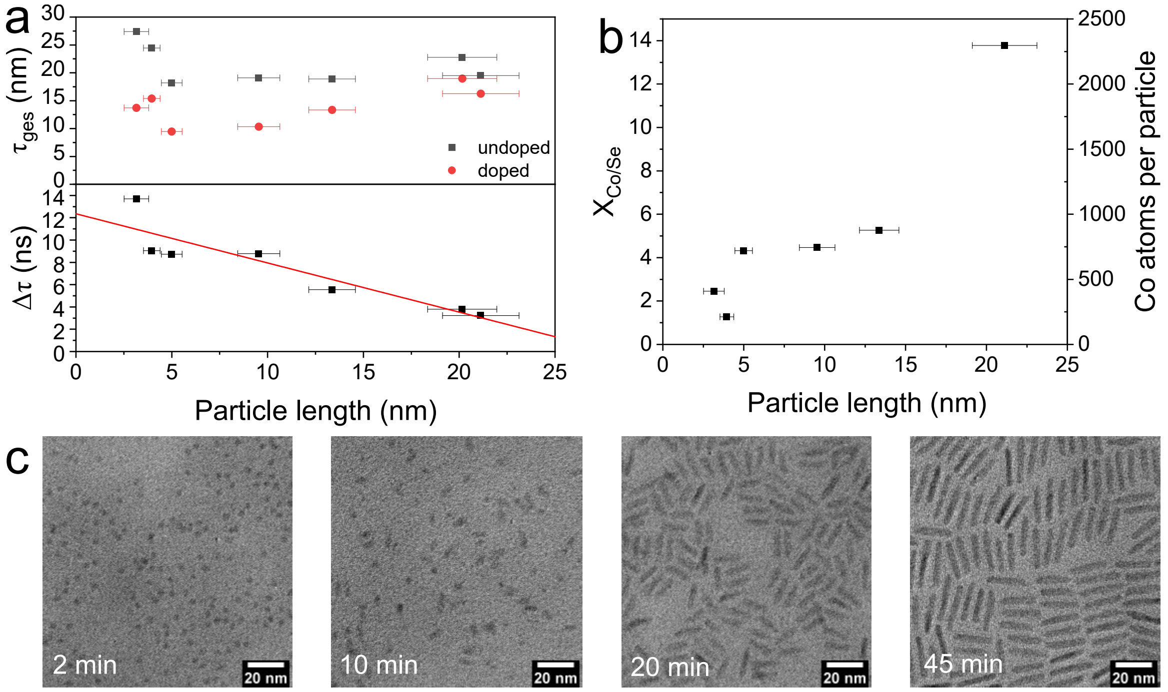

Figure 6.4: Total lifetimes τ for doped (red) as well as undoped samples (gray), and doping-induced reduction of photoluminescence lifetime $\Delta\tau = \tau_{undoped} - \tau_{doped}$ in dependence on the particle length (a). Relative Co content $X_{\mathrm{Co/Se}} = c_{Co}/c_{Se}$ vs. particle length (b). TEM micrographs of representative samples grown for different reaction times before dopant addition (c).

10 min of growth. Deviation from a near-spherical core/shell particle does not occur until approximately 10 min after Cd and S precursor addition (see Figure 6.4 (c)).[70] Therefore, the average distance between dopants and seed particle is significantly smaller, and consequently, the influence of the dopant induced recombination pathway is bigger than for samples grown 10 min or more before dopant addition. As stated before, this is not an effect of increased Co content in the particle: as the ICP-OES data in Figure 6.4 (b) shows, the sample with the smallest $\Delta\tau$ is the one with the highest dopant content per particle. Also, even samples with similar dopant level, e.g., those with rod lengths of approximately 10 nm and 15 nm, show significantly different values for $\Delta\tau$, from 9 ns and 5 ns.

6.2.3 Quantification of Diffusion Kinetics

Since diffusion is the main process limiting dopant localization in the system, the underlying kinetics were further investigated and quantified. Purified, locally doped particles that were grown for 45 min before dopant addition ((22.00 ± 1.99) nm in length) were dried and heated in TOPO at temperatures ranging from 125 °C to 250 °C. The diffusion rate was monitored by PL lifetime measurements: A statistical distribution of dopant within the particle due to diffusion is expected to decrease the mean distance between dopant and seed, increasing the likelihood of fast, non-

---

[70] Danja Fischli, Florian Enders, and Klaus Boldt. *J. Phys. Chem. C*, **124**: 12774–12783, 2020.

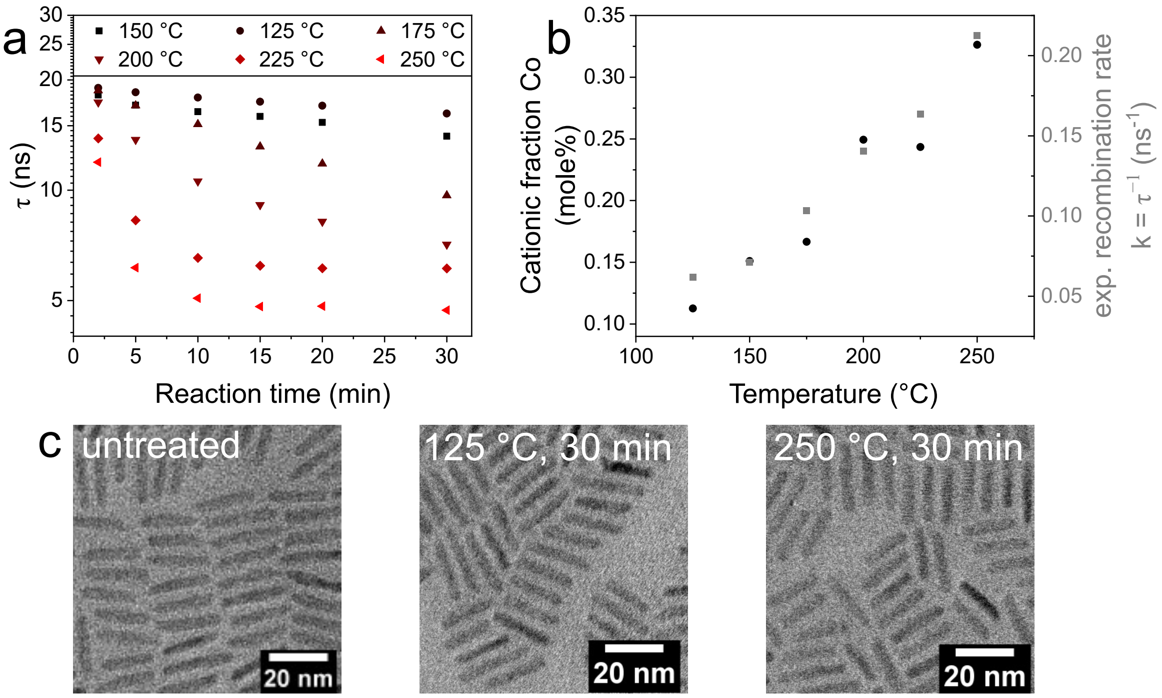

Figure 6.5: Photoluminescence lifetimes τ vs. reaction time for CdSe/CdSe/Co^{2+}:CdS nanorods heated at different temperatures to promote dopant diffusion (a). Relative Co content after 30 min of heating at varying temperatures (b). TEM micrographs of representative rod samples before and after heating (c).

radiative decay. In accordance with the proposed theory, lifetimes decrease over time at elevated temperatures, as shown in Figure 6.5 (a). This process becomes faster with increasing temperature.

In principle, several processes might occur here, i.e., cation exchange, etching/particle degradation, or diffusion processes. Additionally, TOPO has in the past been used to remove excess dopants that are adsorbed to the particle surface.[45] As shown previously (see Section 5.3.2, Figure 5.8) this process does not affect PL lifetimes and, hence, complexation of Co^{2+} by TOPO can be discounted in this experiment. Etching or Ostwald ripening processes that could release Cd ions into the solution can be excluded as well, since these would be visible in the TEM as a change of particle morphology, such as broadening and shortening of the nanorods, visible degradation, or second phase growth.[125]

Representative TEM micrographs show that the particles retain their shape, even upon 30 min of treatment at 250 °C (see Figure 6.5 (c)). Also, particle degradation would change the Cd/Se ratio as the CdS shell is etched, which is not the case (see Appendix B). This, in turn, also excludes the possibility of cation exchange processes, as there are no additional cations present that could be exchanged. This leaves dopant diffusion processes as the remaining possible cause for the changes in τ.

ICP-OES analysis of the samples before and after 30 min of heat treatment suggests a significant loss of Co dopant from 18 % cationic fraction (2315 dopant atoms per particle) to below 0.5 % (between 4 and 14 dopants per particle, see Figure 6.5 (b)). This indicates a self-purification

---

[125] Nuri Oh and Moonsub Shim. *J. Am. Chem. Soc.*, **138**: 10444–10451, 2016.

process that leads to exclusion of the dopant from the particle. Comparing the final Co contents after treatment at different temperatures reveals that the higher the temperature, the more dopant is retained. If self-purification was the only process that occurred, the opposite would be expected, as self-purification occurs faster at higher temperature.[123] Instead, the data can be explained through the solubility limit of Co in CdS at the respective temperature, which determines the final Co content: The bulk solubility of CoS in CdS is 4 mole-% at 500 °C.[126] At the reaction temperatures employed here, it will be lowered, which means that the initial Co content of the doped particles of 18 % far exceeds the thermodynamic solubility limit.

For the introduction of heteroions, i.e., dopants, into a host matrix, a range of configurations is possible. On one end of the spectrum there is the case of maximum enthalpy: The dopants cluster together, forming a distinct phase within the host material. On the other, there is the system with maximum entropy: Dopants are distributed uniformly over the entire host matrix. Localized doping is located between the two extremes, as it aims for dopant accumulating in certain regions of a particle without them forming a distinct phase. Consequently, localized doping is thermodynamically unfavorable, as a system will run towards maximum entropy, i.e., uniform distribution of dopant rather than significant differences in local concentration.

In order to achieve dopant localization, the reaction must thus be stopped and "frozen" at a point when it has not yet reached thermodynamic stability. For the method utilized here, this can be described as follows: Due to the sudden addition of metal precursor in the form of cobalt(II) acetate in TOP to a reaction mixture with an 8-fold chalcogenide excess, doped material, or, due to the large excess of Co and S precursor, possibly a distinct Co_xS_y phase, nucleates on the particles. The rapid quenching of the reaction by cooling freezes the system in this metastable state. Further heating, either by letting the reaction run longer, as shown in Section 6.2.1 as well as in the direct doping of dual rods (Section 6.1), or tempering at different temperatures, allows the system to equilibrate and reach the solubility of CoS in CdS at the given temperature. This will also affect the PL behavior, since a higher amount of Co in the particle will lead to a smaller mean distance between dopant and core, statistically speaking. The conclusion is drawn that the diffusion process monitored here by lifetime measurements is the diffusion of Co within the particle.

Additionally, the experiments, especially at higher temperatures (225 °C and 250 °C), reveal that after a certain reaction time, an equilibrium is reached and τ remains constant at a value that differs depending on the temperature (with 4 ns at 250 °C compared to 7 ns at 200 °C), as shown in Figure 6.5 (a). Plotting the experimental recombination rate at equilibrium $k = \tau^{-1}$ (see Figure 6.5 (b)), a linear correlation with the temperature is apparent, which is similar to the relationship between temperature and final dopant content. This provides additional evidence for the fact that the photoluminescent properties at thermal equilibrium are dependent on the final dopant content and thus, the mean distance between the recombination center in the CdSe seed and the dopant.

In order to quantify the activation energy, the PL lifetimes presented in Figure 6.5 were used as a measure of the change of dopant localization and entered into the Arrhenius plot shown in Figure 6.6. To achieve this, the PL decay data of each data point was fitted with a triexponential fit, yielding τ for each time point within a temperature series. Then, a monoexponential fit was applied to each time series in order to calculate the reaction coefficient k for the diffusion at the respective

---

[126] W. Becker and H.D. Lutz. *Mater. Res. Bull.*, **13**: 907–911, 1978.

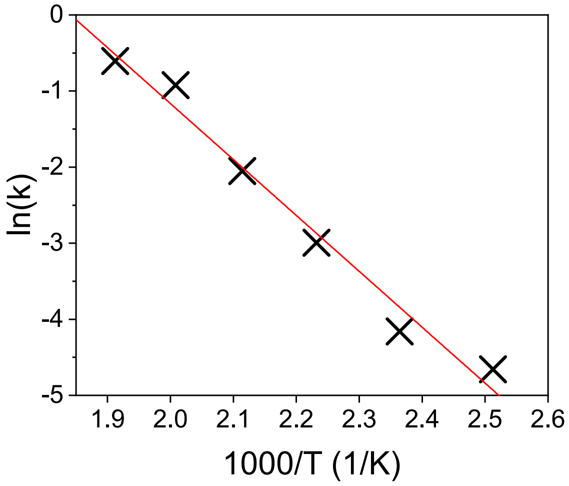

Figure 6.6: Arrhenius plot of Co^{2+} diffusion kinetics within CdSe/CdSe/Co^{2+}:CdS nanorods.

temperature. Plotting $\ln(k)$ against $\frac{1000}{T}$, the Arrhenius plot is obtained, which is subsequently fitted linearly. The general Arrhenius equation

$$\ln(k) = \ln(k_0) + \frac{1}{T} \cdot \frac{E_a}{RT}$$

with the activation energy E_a, the molar gas constant R, and the absolute temperature T, corresponds to the linear fit equation

$$y = y_0 + x \cdot m$$

The fit yields

$$\ln(k_0) = y_0 = 13.534\,65$$

and

$$m = -7.34994$$

. The activation energy is given as

$$E_a = -R \cdot m = 61.11\,\mathrm{kJ\,mol^{-1}} = 0.633\,\mathrm{eV}$$

.

Judging from this value for the activation energy the Co^{2+} ions likely occupy interstitial sites, as the activation energy of diffusion *via* a vacancy mechanism, e.g., the self-diffusion of Cd in CdS, would be significantly higher, typically in the range of $150\,\mathrm{kJ\,mol^{-1}}$ to $300\,\mathrm{kJ\,mol^{-1}}$.[127] Literature data reports the diffusion data for Co in CdTe as $D_0 = 3.8 \times 10^{-8}\,\mathrm{cm^2\,s^{-1}}$ and $E_a = 0.75\,\mathrm{eV}$.[128] The activation energy matches the obtained data reasonably well, considering that CdTe crystallizes in the cubic sphalerite structure instead of wurtzite, and the anion differs from the system presented

---

[127] J Zmija. *Acta Phys. Pol. Ser. A*, 345–355, 1973.

[128] L. Shcherbak et al. *J. Phase Equilibria Diffus.*, **36**: 99–109, 2015.

here. This report is the only literature data for Co diffusion in II-VI semiconductors,[129] which constitutes a significant gap in literature, as diffusion data is necessary to understand and evaluate doped nanomaterials not only on the nanoscale, but also in the bulk.

In order to estimate the accuracy of the obtained value for the activation energy, other systems have to be consulted (see Table 6.1).

System	E_a (kJ mol^{-1})	D_0 (cm^2 s^{-1})	Source
Co in CdS	61.11	–	this study
Co in CdTe	72.36	3.8×10^{-8}	Shcherbak et al.[128]
Ni in CdS	105	6.75×10^{-3}	Łukaszewicz[130]
Cu in CdS	92.5	2.1×10^{-3}	Sullivan[131]
Cu in CdS	69.37	8×10^{-5}	Lepley et al.[132]
Mn in ZnS	237	2.3×10^{3}	Williams[133]
Cu in ZnS	61.66	4.3×10^{-4}	Korsun and Nemchenk[134]

Table 6.1: Reference data for diffusion of TM in II-IV semiconductors.

The parameters for Cu in CdS and ZnS are the best match for the data obtained from the Arrhenius plot. This can be attributed to the fact that Co^{2+} (high spin) and Cu^{2+} have similar ionic radii and charge densities. Overall, the parameters that were found for diffusion of Co in CdS appear within a reasonable range for diffusion of TM ions in II-IV semiconductors.

It is important to emphasize that dopant diffusion is largely dependent on the employed conditions. Activation energy of self-diffusion of Cd in CdSe for example varies between $E_a = 120.44\,\text{kJ}\,\text{mol}^{-1}$ and $210.04\,\text{kJ}\,\text{mol}^{-1}$, depending on whether diffusion occurs under Cd or Se saturation.[127] Additionally, the concentration gradient within the system plays a significant role,[135,136] especially for doped nanoparticles, as the small reservoir of dopant will be depleted faster than in model systems comprised of bulk materials. Also, variations will arise due to the fact that nanoparticles are studied here as compared to bulk semiconductors in reference data. The fact that the value for dopant diffusion in nanoparticles matches the bulk values reasonably well hints at the possibility that bulk diffusion data can be used to predict gradients on the nanoscale. Since properties can differ significantly between bulk and nanomaterial further research should be conducted on the basis of this observation.[137]

Using literature data for the diffusion coefficient for Co in CdTe[128] along with the evaluation of the activation energy, it is possible to approximate the diffusion speed at room temperature, which allows an estimate of the stability of the system. The diffusion coefficient at 20 °C equals $D_{\text{RT}} = 4.8 \times 10^{-19}\,\text{cm}^2\,\text{s}^{-1}$. Using the lattice parameter $c = 6.843 \times 10^{-10}$ m for w-CdS[138] in the

---

[129] Avijit Saha et al. *Nanoscale*, **9**: 2806–2813, 2017.

[128] L. Shcherbak et al. *J. Phase Equilibria Diffus.*, **36**: 99–109, 2015.

[130] T. Łukaszewicz. *Phys. Status Solidi*, **73**: 611–616, 1982.

[131] George A Sullivan. *Phys. Rev.*, **184**: 796–805, 1969.

[132] B Lepley et al. *J. Phys. D. Appl. Phys.*, **12**: 1917–1928, 1979.

[133] V. A. Williams. *J. Mater. Sci.*, **7**: 807–812, 1972.

[134] V M Korsun and A M Nemchenk. *Sov. Phys. Solid State, USSR*, **8**: 2988, 1967.

[135] Adolf Fick. , **170**: 59–86, 1855.

[136] John R. Manning. , **124**: 470–482, 1961.

[137] Dan Guo, Guoxin Xie, and Jianbin Luo. *J. Phys. D: Appl. Phys.*, **47**: 013001, 2013.

[138] The Materials Project *Materials Data on CdS by Materials Project* July 2020 DOI: `10.17188/1272700`

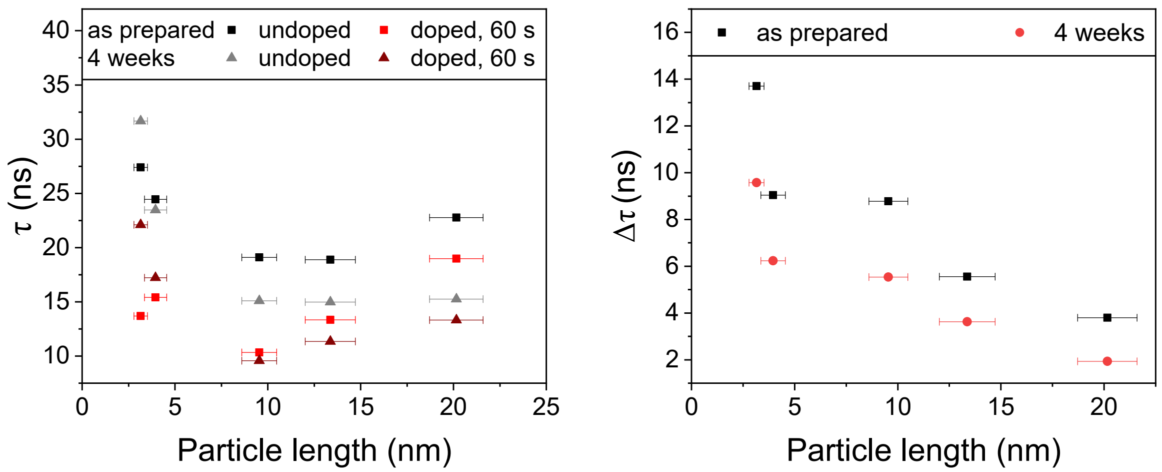

Figure 6.7: Photoluminescence lifetime data vs. particle length right after the synthesis and after 4 weeks of storage at room temperature. PL lifetime τ vs. particle length (left). PL lifetime reduction $\Delta\tau = \tau_{\text{undoped}} - \tau_{\text{doped}}$ due to doping right after synthesis and after 4 weeks of storage (right).

Einstein-Smoluchowski equation to calculate the time for one jump $\tau_{\text{jump}} = \frac{c^2}{2D}$,[139] the time in which one dopant atom travels one lattice parameter c further along the c-axis is obtained. With the resulting value of $\tau_{\text{jump}} = 4830\,\text{s}$ it can be concluded that a dopant atom will make that jump approximately every 90 min.

While this is a fairly rough estimate, considering the different host matrix, and likely a lower limit for the rate of diffusion of Co in CdS, it emphasizes the need to store locally doped particles in a cool environment, as diffusion can still occur at room temperature. This is also evident from comparison of τ_{doped}, τ_{undoped}, and $\Delta\tau$ of freshly prepared particles compared to after 4 weeks of storage (see Figure 6.7). Both for doped and undoped particles, extended storage reduces the PL lifetime, indicating etching and, for the doped samples, diffusion processes. Dopant influence is reduced upon extended particle storage, indicating a reduced dopant influence due to self-purification processes. $\Delta\tau$ as well as τ values are significantly lower after storage at room temperature compared to right after preparation. This indicates active diffusion processes within the particles.

From these experiments it can be concluded that Co^{2+} diffusion within the particle is very fast. In order to retain control over the dopant locale, it is thus essential to minimize the time that particles are heated when the dopant is already introduced. This extends to sample storage as well: Low storage temperatures will further slow down dopant diffusion and help retain localization.

6.2.4 Evaluation of dopant location

While the dependence of $\Delta\tau$ on the particle length is apparent, this result does not answer the question of the specific location of the dopant within the particles. CdSe/CdS seeded rod growth consists of growth in three directions: Growth in [0001] direction on the cadmium rich (0001) facets, growth in $[000\bar{1}]$ direction, on the sulfur rich $(000\bar{1})$ facet, and growth in particle width,

---

[139] A. Einstein. *Ann. Phys.*, **322**: 549–560, 1905.

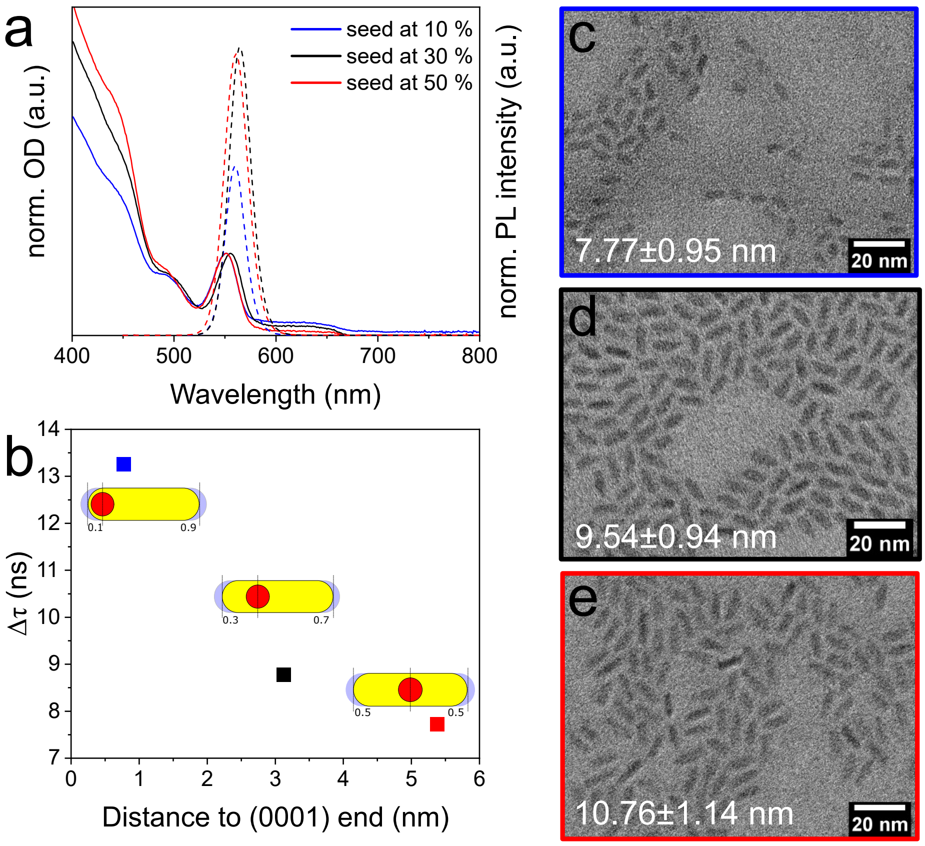

Figure 6.8: (A) Absorption (solid lines) and emission spectra (dashed lines) of doped rod samples with different seed positions. Spectra are normalized with regard to the absorption signal of the seed. TEM micrographs of doped rod samples with the seed at 10 % (top right), at 30 % (middle right), and at 50 % of the rod length (bottom right). Doping-induced reduction of photoluminescence lifetime $\Delta\tau$ in dependence on seed distance from the (0001) end of the particle (bottom left).

i.e., on the non-polar facets. This means that in principle, there are also three possible locations where the dopant can be deposited: on the (0001) end, the $(000\bar{1})$ end, and/or along the particle width.

Kim et al. showed the dependence of the reaction speed in the different growth directions on the concentration of short and long-chain phosphonic acid ligands.[69] Varying this ratio enables the synthesis of particles with different seed positions within the rod, and thus, different distances towards the (0001) and the $(000\bar{1})$ ends, respectively. Using this approach, doped seeded rods were synthesized where the seed is located at approximately 10 %, 30 %, and 50 % of the particle length from the (0001) end.

The absorption spectra shown in Figure 6.8 (a) show a lower intensity for the CdS signal at approximately 450 nm for the rods with the seeds at 10 % of the particle length, while for seed positions at 30 % and 50 % the intensities are comparable. This can be explained by the fact that moving the seed further towards the (0001) end is a result of lowering the growth rate at

---

[69] Dahin Kim et al. *ACS Nano*, **11**: 12461–12472, 2016.

the respective end, leading to an overall reduced particle length. This is supported by TEM data (Figure 6.8 (c-e)) that reveal the particle length to be (7.77 ± 0.95) nm, (9.54 ± 0.94) nm, and (10.76 ± 1.14) nm, respectively, meaning that the rods with seeds at 10 % of the particle length are approximately 2 nm shorter than those with seeds at 30 %. The quantum yield of the rod sample with the seed positioned at 10 % of the rod length is significantly reduced as well, partly due to the overall smaller size to the shell, but also due to the fact that the small size of the rod in (0001) direction gives the particle the character of a core-shell particle rather than a seeded rod.

Figure 6.8 (b) shows the reduction in PL lifetime $\Delta\tau = \tau_{undoped} - \tau_{doped}$ due to doping plotted against the seed distance from the (0001) end of the particle. This distance takes into account the assumed seed position within the rod, as well as the varying rod length. The 10 % sample shows the largest lifetime reduction $\Delta\tau = 13$ ns, which is comparable to the 2 min sample shown in Figure 6.4 (top left). The 30 % and the 50 % sample show significantly lower lifetime reductions with $\Delta\tau = 8.5$ ns and 7.5 ns, respectively. An inverse relationship between the distance to the (0001) end and the lifetime reduction can be observed.

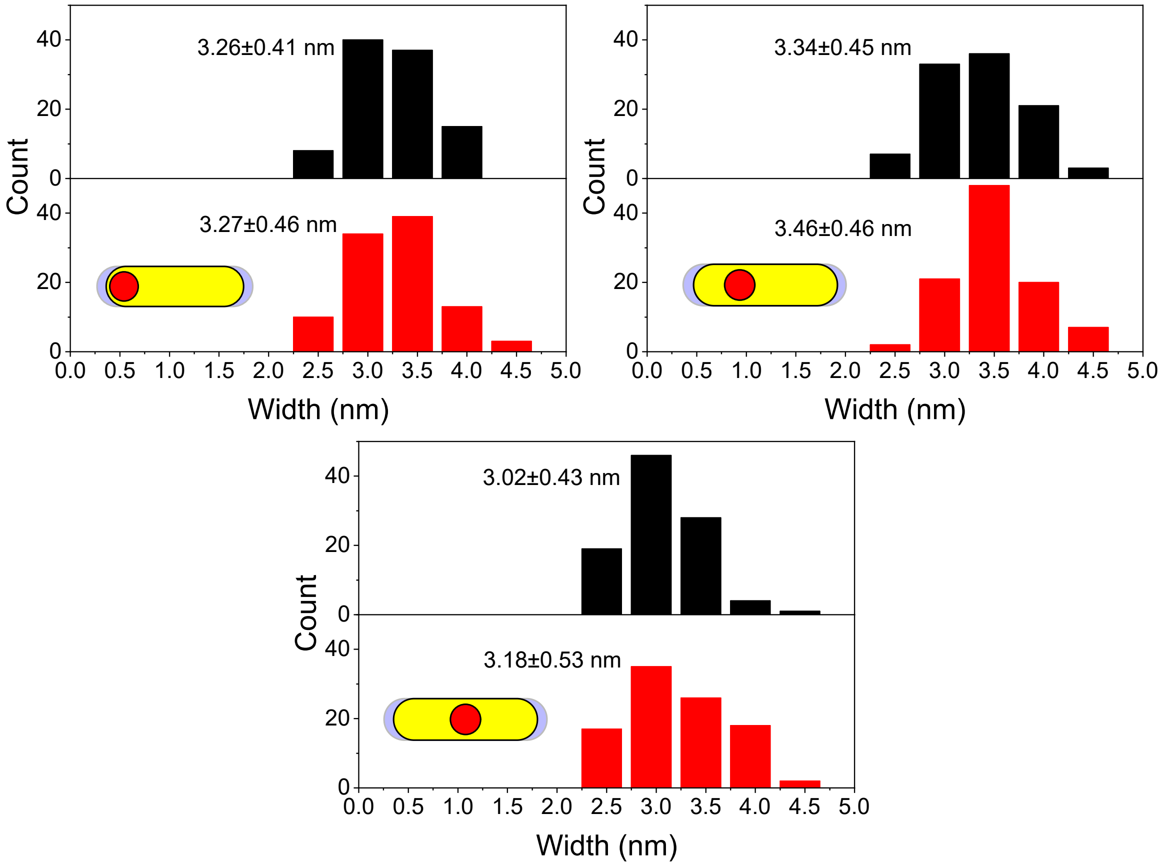

Figure 6.9: Particle width histograms before and 1 min after dopant addition. All samples were grown for 15 min before dopant addition. Seeds at 10 % of particle length (top left), seeds at 30 % of particle length (top right), and seeds at 50 % of particle length (bottom).

This means that the possibility of dopants located around the width of the particle can be excluded and localized doping at the nanorod tips was achieved. If dopants were deposited on the particle sides, the mean distance between the dopant and the seed would be approximately the same over all samples, and no relationship with the particle length would be found. Also, a change in particle width would be expected if significant amounts of material were deposited, which is not the case. Figure 6.9 shows that changes in particle width are within the margins of error, and lower than 0.4 nm, which would be equal to the growth of half a monolayer of CdS.[138] Furthermore, the PL quenching effect is weaker, the further away the CdSe seed is from the (0001) end of the particle, with the 10 % sample behaving largely like a core shell particle with dopant deposited on the outside. While this does not allow for definite conclusions regarding growth on the $(000\bar{1})$ end, deposition of dopant at the (0001) end definitely occurs.

Unfortunately, direct imaging of the dopant distribution in the nanorods using electron microscopy is difficult: due to the spectral overlap of the Co $M_{2,3}$ with the Cd $N_{2,3}$-edge in the EELS spectrum, the signals of these elements could not be clearly separated, as shown in Figure 6.10(b, c). However, bright spots at both tips of the nanorods in the EFTEM image measured at the Co edge are in accordance with a concentration of dopant ions in these regions, as concluded from the spectroscopic data above (Figure 6.10 (a)). Spectral and microscopy data combined imply that the length correlation in Figure 6.4 (top left) is actually a correlation with the distance to the (0001) end, which is the shorter distance between seed and tip. This is in accordance with previous results, which show that particle growth is not completely anisotropic, but occurs at both ends.[69,70] Hence, a clear distance dependence can be observed, in accordance with rapid deposition of material along the c-axis only.

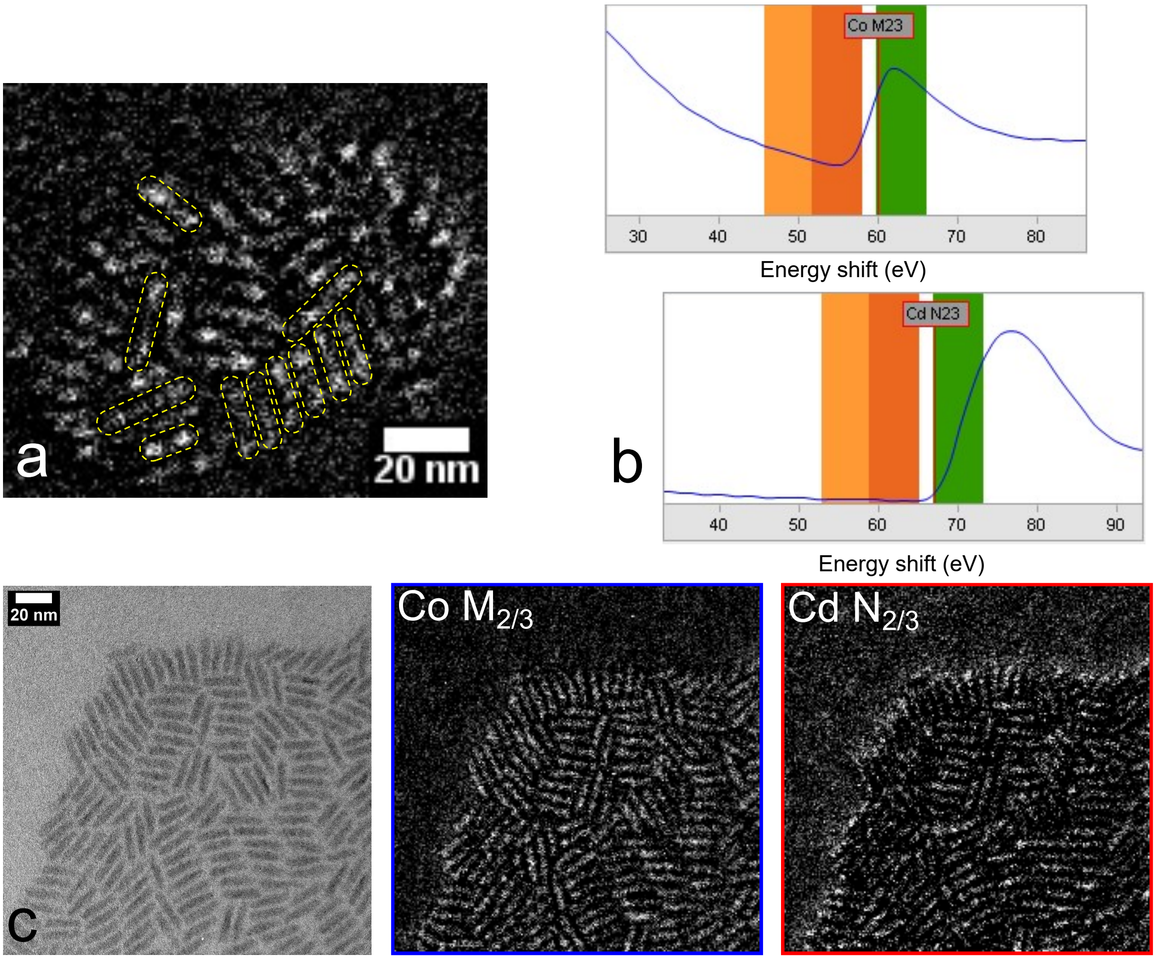

Figure 6.10: EFTEM elemental mapping. EFTEM micrograph (a) taken at the Co M-edge (60 eV) with rod outlines (yellow) as a guide to the eye. Energetically close position (b) of the Co M-edge and the Cd N-edge (67 eV, screenshots taken from the Gatan Digital Micrograph acquisition software). Orange mark the pre-edge and green the post-edge measuring positions. Unfiltered, Co M edge and Cd N edge EFTEM micrographs (c) of a CdSe/Co^{2+}:CdS rod sample.

6.3 Conclusion

Localized introduction of Co^{2+}-dopants was achieved. The suppression of diffusion processes was identified to be the main requirement for localized doping. That entails both minimizing the time doped particles are kept at reaction temperature and sample storage at low temperatures. Localization was confirmed utilizing the inherent characteristics of Co^{2+}-ions as PL quenchers. It could be shown that the position of the dopant within the particle has a bigger effect than the doping level, paving the way towards the study of distance dependent interactions within nanorods.

The results show that dopant that is added at the beginning of a seeded rod or dual rod synthesis diffuses over the entire particle, and enters previously undoped domains as well as newly grown ones. The key to localized doping is adding the dopant at a later stage, during the synthesis, which leads to deposition at the rod tips. It could be directly confirmed that doped material forms at the (0001) end, while for the $[000\bar{1}]$ direction further studies are necessary. For instance, direct imaging via an appropriate elemental mapping method could clear this up, which poses a challenge due to the energetic closeness of the relevant Cd and Co EELS edges and the low dopant levels.

The diffusion process of Co^{2+} in CdS was further investigated and its activation energy quantified. The obtained value is in the range of literature values for other TM/semiconductor systems, and is the first report of this specific system. This is especially noteworthy since that means that diffusion processes on the nanoscale have a similar activation energy as in bulk materials.

In conclusion, this chapter showed the successful introduction of distance dependence into nanoheterorods, which will pave the way for further studies on the topic of exciton dynamics and can serve as a tool to gain a deeper understanding into fundamental processes on the nanoscale.

7 Summary

The aim of this thesis was to create nanoparticles in which distance-dependent interactions can be studied. To achieve this, a method to locally introduce TM^{2+} ions as dopants into nanoheterorods had to be established. This required a good understanding of anisotropic growth mechanisms as well as doping methods, and combining the two areas of expertise in order to accomplish this synthetic goal.

The first chapter was dedicated to gaining a better understanding of a so far rarely discussed factor in anisotropic growth: Reaction intermediates. The coordination polymer CP-309 was identified to play a key role in CdS seeded rod growth, as it contributes to 1D particle growth. A delayed injection approach, which allows time for CP-309 to form before seeds are added, further favors CP-309 formation, speeding up the anisotropic rod growth reaction. CP-309 was isolated, characterized, and found to be an analogue of the previously reported Cd/Se-based CP-350 species.

Reaction parameters that contribute to the formation were identified. A high excess of sulfur precursor lead to a bigger supply of CP-309, speeding up the growth rate and increasing the final rod length despite a constant amount of monomer, which was controlled by the amount of Cd precursor. The ratio of short to long chain ligands affected the formation and solubility of the reaction intermediate. With 100% long chain precursor, solubility was reduced, hindering CP-309 formation. Small amounts (18 %) of short chain ligand mitigated that effect. As long to short chain ligand ratio is often discussed as a main factor for anisotropic growth kinetics, this discovery is a valuable puzzle piece towards the big picture of understanding anisotropic growth.

Protic additives such as water suppress the formation of coordination polymers by breaking up anhydride bonds within the network. If CP-309 formation is suppressed by water addition, the 1D growth rate is reduced. Additionally, ripening processes set in at an early stage of the reaction, which influences particle morphology and distribution of CdSe and CdS material within the particles: A severe lack of control over the reaction is the consequence.

The role of the 1D fibrillar structure of CPs became apparent in a control experiment in which MSCs were used as a precursor. These MSCs don't convert to CPs, but also act as a monomer reservoir. Even if reaction conditions are similar to those of a typical rod growth reaction, homogeneous side nucleation occurs instead of heterogeneous seeded rod growth.

These results were then summarized to formulate a proposed reaction mechanism. CPs reversibly bind the active monomer species, keeping the overall concentration beneath the threshold of homogeneous nucleation. Due to the 1D structure, CP-309 can provide a steady feed of monomer to the reactive, energy-rich facets of the seed particle, and provide the conditions necessary for a reaction instead of a diffusion controlled regime.

The role of MSCs for growth of heteromaterial tips on nanorods was subsequently covered. From previous studies a link between the success of the reaction and the occurence of MSCs was known, but the nature of the relationship wasn't.[68] Since MSCs do not show any shape directing

---

[68] Florian Enders. *Tailoring the Charge Carrier Relaxation in Colloidal Semiconductor Nano-Heterostructures*. PhD thesis. Konstanz: University of Konstanz, 2019.

properties in CdS rod growth, it was investigated whether that fact holds true in this type of anisotropic reaction as well. CdTe MSCs were synthesized and their potential as precursors for tip growth was studied. It could be shown that while it is possible to use them for that purpose, the outcome was overall worse, leading to more side nucleation and a less efficient reaction compared to the molecular precursors. From these observations followed the conclusion that MSCs are not necessary intermediates in the reaction, but rather form under similar conditions. This makes them a predictor of suitable reaction conditions, allowing for easy screening.

The second chapter shifted the focus towards dopant introduction and aimed to find a suitable reaction route for anisotropic dopant introduction. To that end, different doping methods were checked for their potential for specifically doping a domain of a heterostructure, i.e., the seed or the CdS domain of a seeded rod. The evaluated methods were categorized by the point at which the dopant is introduced: before, after, or during heterojunction formation. Additionally, it was checked whether the doping is retained in a further reactions such as tip growth.

For doping before heterojunction formation, CdSe and CdS rods were doped *via* the established diffusion doping approach and used as seeds in a dual rod synthesis. Up to 99 % of the initial dopant concentration was lost during dual rod growth, indicating that self-purification is strongly favored under these conditions. With the available methods, it was not possible to distinguish whether the dopant preferentially resides in one domain.

To trap the dopant inside the seed, a shelling approach was employed. A ZnS shell of 1 ML was grown on Mn:CdSe QD seeds and used in a seeded rod synthesis. Results indicate that a similar ratio of dopant is retained with and without the shell. However, differences in the EPR spectra show that the shell growth does indeed lead to localization of the dopant at the CdSe/ZnS/CdS interface, while without the shell, dopant ions cluster together in the CdS domain of the particle. Spectroscopic results also hint that the Mn:CdSe/ZnS/CdS system show a significant amount of alloying that is facilitated by the dopant. As alloying is interesting for the synthesis of graded shell particles for lasing applications, this side effect of doping should be further investigated. Overall, doping before heterojunction formation is not a feasible way to specifically dope only one particle domain, as outward diffusion and self-purification prevent dopant retention in one domain during subsequent reaction steps.

Doping after heterojunction formation was performed on CdSe/CdS dual rods using the diffusion doping approach. It could be shown that despite the fact that the CdSe domain is covered by a thin CdS shell due to the morphology of the dual rod, it could be successfully doped using a mixture containing Se^{2-} and Mn^{2+} ions. This indicates that the chalcogenide in solution does not need to match the one on the surface. However, ripening effects occurred when the chalcogenides did not match, leading to a loss of anisotropy. In contrast, if S^{2-} was used instead, dopants were selectively incorporated into the CdS domain, while the particle shape was retained. Matching the chalcogenides can thus induce selective doping of one domain over the other.

As a third option, doping during heterojunction formation was performed by addition of dopant during a typical seeded rod synthesis. It could be shown that dopants do not have to be incorporated into potential reaction intermediates in order for doping to be successful. Thus, incorporation of both Co^{2+} and Mn^{2+} into CdSe/CdS seeded rods was successful without drawbacks with regard to growth anisotropy. Thus, this is the method of choice for the aim of this thesis.

CdSe/Mn:CdS rods were subsequently employed in a tipped rod synthesis in order to check for dopant retention upon postfunctionalization. These experiments revealed that simply heating the particles to reaction temperature leads to both a partial dopant loss, and changes in the local environment of the dopant over time: When Mn^{2+} is incorporated into CdSe/CdS rods, the dopants are close together forming clusters. Upon heating, they first decluster, then diffuse outwards. This emphasizes the relevance of diffusion processes as the main antagonists for doping.

In the third chapter, doping and anisotropic growth were combined to achieve localized introduction of dopants. Direct doping with Co^{2+} ions during CdSe/CdS/CdS dual rod growth did not yield the desired structure of CdSe/CdS/Co:CdS dual rods, with an undoped CdS domain that acts as a spacer between the CdSe seed as a reporter and a doped Co:CdS domain. Instead, the dopant diffused all over the particle due to the high reaction temperatures.

Localized doping was successful if the doped particles' time at reaction temperature was minimized. The dopant was only added towards the end of the desired reaction time, so only small doped domains were grown at the rod tips. Quenching the reaction shortly after lead to a system in which the distance between seed and doped domain could be varied by the amount of time for which the particles were allowed to grow before dopant addition. With this approach it could be shown that the dopant location, i.e., the distance to the seed, has a higher impact on the optoelectronic properties than the total amount of dopants per particle.

The diffusion process opposing dopant localization was investigated and the necessary activation energy quantified. This allowed an estimate of the diffusion speed at different temperatures, which was verified in experiments: diffusion is sufficiently fast so that dopant localization cannot be maintained over long periods of storage at room temperature, emphasizing the need for low storage temperatures.

Lastly it could be shown that the doped domain grows on the (0001) facet, while growth on the $(000\bar{1})$ facet could not be definitely proved. This was achieved by changing the position of the CdSe seed in the CdS rod, and investigating the changes in optical properties. The influence of the dopant on exciton recombination in the seed increases with reduced distance of the seed to the (0001) end. As in the classic seeded rod synthesis the seed is located at 1/3 of the particle length, that means that the distance on which the interaction between dopant and seed depends is actually the shorter distance to the (0001) end. With the results of the third chapter, the overall aim of localized doping and introducing distance dependent was achieved. This constitutes an unprecedented level of power over the local composition of nanorods, and a significant increase in control over particle anisotropy.

From the results presented here, various opportunities that warrant further research arise. CPs can be used to enhance anisotropic rod growth, and further studies are necessary to understand their composition and structure. Using MSCs as predictors for tip growth will prove a valuable tool to expand the synthesis to more materials, which is especially interesting for catalysis.

The experiments on shelling as a means to trap dopant uncovered a so far not reported function of dopant introduction: it can facilitate alloying. This topic requires further study and might prove efficient at creating core/shell structures with alloyed interfaces without the need for long annealing times. This process could be studied by methods like EXAFS and provide insight into ion mobility and the factors that contribute to it.

Whether dopant is only deposited on the (0001) end of the particle, or also on the $(000\bar{1})$ end could not be answered, but warrants further studies. High resolution elemental mapping might be able to uncover the answer. Alternatively, a seeded growth approach that moves the CdSe seed closer to the $(000\bar{1})$ end is a possibility. A third option is a partial cation exchange reaction, which occurs from the $(000\bar{1})$ end: A release of dopant ions would indicate dopant located near that end.

A key finding of this thesis was the fact that the dopant location within the particle can matter more than the dopant concentration. This is a fundamental fact that changes the view on previous studies in the field.

The possibility of localized doping was only shown for Co^{2+} dopants in this thesis. Achieving the same with Mn^{2+} dopants will provide access to a complex system with two radiative relaxation pathways. As Mn^{2+}-doped systems have proven to be versatile sensors, e.g., for pressure and temperature, locally doped structures present the possibility to study the influence of these factors on relaxation kinetics and exciton mobility.

The localized introduction of transition metal dopants adds another tool to tune the electronic structure of nanoparticles to the nanoscientists' tool box. Along with size and shape control, as well as the opportunity to combine different materials, this will make it possible to create elaborate heterostuctures that can be tailored to fit specific applications and experiments. It would be possible, for instance, to create a tip@TM:rod structure, in which the exciton energy is stored in the dopant d-levels, before releasing it upon heating.

Introducing magnetic ions into only one end of a nanorod could make it possible to use magnetic fields to create self-assemblies of excitonic nanostructures. That way, it could be studied in how far the alignment in the magnetic field, the field strength, and the magnetic gradient of the dopants within the particle impacts the emissive properties of the particles. An interesting experiment would be if the dopant ions can be kept localized at one particle end by such a field, or if the location of the dopants can be changed, i.e., to the longitudinal edge of a nanorod. This could make it possible to study the mobility of the exciton around the particle, which is so far spectroscopically unavailable.

It was previously shown that electrical light emitting devices containing an active layer of isotropically doped nanoparticles can be fabricated, in which magnetic polarons can be induced.[140] Using anisotropically doped nanorods instead can potentially provide an even more versatile system for spintronics applications, e.g., by using the aforementioned additional possibilities to form assembled films.

---

[140] Franziska Muckel et al. *Nano Lett.*, **17**: 4768–4773, 2017.

Zusammenfassung

Das Ziel diese Arbeit war es, Nanopartikel herzustellen, in denen abstandsabhängige Wechselwirkungen untersucht werden können. Dazu musste eine Methode zur lokalen Dotierung von Nanoheterostäbchen mit bivalenten Übergangsmetallionen gefunden werden. Dieses Ziel erfordert ein gutes Verständnis anisotroper Wachstumsmechanismen und Dotiermethoden, sowie die Kombination dieser beiden Gebiete.

Im ersten Kapitel sollte ein besseres Verständnis eines bisher vernachlässigten Einflussfaktors auf anisotropes Wachstum erlangt werden, nämlich der Bildung von Reaktionsintermediaten. Dem Koordinationspolymer CP-309 kommt eine Schlüsselrolle im Wachstum von CdS-Stäbchen aus einem Kernpartikel zu, da es 1D-Wachstum fördert. Ein Reaktionsansatz mit verzögerter Zugabe, in dem CP-309 gebildet werden kann bevor die Kernpartikel zugegeben werden, begünstigte die Bildung von CP-309 und beschleunigte damit das anisotrope Partikelwachstum. CP-309 wurde isoliert, charakterisiert, und als Analogon der literaturbekannten, Cd/Se-basierten CP-350-Spezies identifiziert.

Reaktionsbedingungen, die die Bildung des Koordinationspolymers begünstigen, wurden gefunden. Ein großer Überschuss der Schwefelvorstufe führte zu einem größeren Vorrat an CP-309, was die Wachstumsrate und die endgültige Partikellänge fördert, trotz konstanter, durch den Cadmiumvorläufer kontrollierter, Monomermenge in der Reaktion.

Das Verhältnis lang- zu kurzkettiger Liganden beeinflusste die Bildung und Löslichkeit des Reaktionsintermediates. Wurden zu 100 % langkettige Liganden eingesetzt, so war die Löslichkeit herabgesetzt und die Bildung von CP-309 erschwert. Schon kleine Mengen (18 %) eines kurzkettigen Liganden konnten diesen Effekt ausgleichen. Da das Verhältnis lang- zu kurzkettiger Liganden häufig als Hauptfaktor für die Kinetik anisotroper Wachstumsprozesse diskutiert wird, stellt diese Erkenntnis ein wertvolles Puzzlestück zum Verständnis anisotropen Wachstums dar.

Protische Additive wie Wasser unterdrücken die Bildung der Koordinationspolymere, indem Anhydridbrücken innerhalb des Netzwerks aufgebrochen werden. Wurde die Bildung von CP-309 durch Zugabe von Wasser unterdrückt, so war die Geschwindigkeit des 1D-Wachstums reduziert. Zusätzlich traten bereits in einer frühen Phase der Reaktion Partikelreifungsprozesse auf, die die Partikelmorphologie, sowie die Verteilung des CdSe- und CdS-Materials innerhalb des Partikels beeinflussen: ein signifikanter Verlust der Kontrolle über die Reaktion war die Folge.

Die Rolle der fibrillären 1D Struktur der Koordinationspolymere wurde deutlich in einem Kontrollexperiment, in dem Cluster mit magischen Größen (MSCs) als Vorläufer eingesetzt wurden. Diese MSCs wandeln sich nicht in Koordinationspolymere um, können aber Monomer bereitstellen. Selbst wenn die Reaktionsbedingungen so gewählt wurden, dass sie einer typischen Stäbchensynthese ähnlich kamen, trat homogene Nebennukleation anstelle heterogenem Wachstum eines Stäbchens auf den Kernpartikel auf.

Auf Grundlage diese Ergebnisse wurde ein Reaktionsmechanismus vorgeschlagen. Koordinationspolymere binden die aktive Monomerspezies reversibel, und halten dadurch die Monomerkonzentration unterhalb der homogenen Nukleationsschwelle. Aufgrund der 1D-Struktur kann

CP-309 einen kontinuierlichen Vorrat an Monomer an den reaktiven, energetisch ungünstigen Facetten des Kenpartikels sicherstellen, und die notwendigen Bedingungen für einen reaktions- statt diffusionskontrollierten Reaktionsweg gewährleisten.

Im Folgenden wurde die Rolle der MSCs für das Spitzenwachstum auf Nanostäbchen untersucht. Vorhergegangene Untersuchungen hatten einen Zusammenhang zwischen dem Auftreten von MSCs und dem Erfolg der Synthese hergestellt, der Mechanismus dahinter war jedoch unklar.[68] Da MSCs im Gegensatz zu CPs bisher keinerlei formdirigierende Eigenschaften während des Wachstums von CdS Nanostäbchen gezeigt hatten, wurde untersucht, ob diese Tatsache sich auch für diese Form von anisotropem Wachstum bewahrheitet. Dazu wurden CdTe-basierte MSCs hergestellt und ihre Eignung als Vorläufer für das Spitzenwachstum untersucht. Es konnte gezeigt werden, dass sie sich zwar tatsächlich dazu eignen, die Ergebnisse jedoch deutlich schlechter waren, als in der auf Cadmium- und Tellurvorläufern basierende Synthese. Es trat mehr Nebennukleation auf, und der Anteil der Stäbchen mit Spitzen war reduziert. Aus diesen Beobachtungen kann abgeleitet werden, dass MSCs keine notwendigen Reaktionsintermediate für Spitenwachstum sind, sondern unter ähnlichen Bedingungen entstehen. Das macht sie zu einem Indikator für geeignete Reaktionsbedingungen, was deren Einstellung erleichtert.

Im zweiten Kapitel lag der Schwerpunkt auf der Einbringung der Dotierionen mit dem Ziel, Reaktionsbedingungen für anisotrope Dotierung zu finden. Dazu wurden verschiedene Dotiermethoden auf ihre Eignung untersucht, eine spezifische Domäne einer Heterostuktur zu dotieren, d.h. den Kern oder die CdS-Domäne eines Stäbchens. Die untersuchten Methoden wurden unterteilt nach dem Zeitpunkt, zu dem das Dotierion eingebracht wird: Bevor, nach oder während der Bildung des Heteroübergangs. Zusätzlich wurde überprüft,ob die Dotierung auch über weitere Reaktionsschritte, z.B. das Aufwachsen einer Spitze, erhalten bleibt.

Zur Dotierung vor der Bildung des Heteroübergangs wurden zunächst CdSe und CdS Stäbchen mittels der bekannten Diffusionsdotierung dotiert und als Kernpartikel in einer Doppelstäbchensynthese verwendet. Die Menge an Dotierionen pro Partikel sank während des Wachstums der Doppelstäbchen um bis zu 99 %, was darauf hinweist, dass Selbstreinigungseffekte unter den Reaktionsbedingungn eine nennenswerte Rolle spielen. Mit den zur Verfügung stehenden Methoden konnte nicht festgestellt werden, ob die übrigen Dotierionen bevorzugt in einer Domäne lokalisiert sind.

Mittels Schalenwachstum wurde versucht, die Dotierionen innerhalb des Kernpartikels einzuschließen. Mn:CdSe Quantenpunkte wurden mit einer ZnS-Schale von 1 ML Dicke versehen und die resultierenden Partikel als Kern in einer Stäbchensynthese eingesetzt. Die Ergebnisse zeigten, dass eine ähnlich große Menge an Dotierionen erhalten blieb, egal ob der Kernpartikel eine Schale aufwies oder nicht. Trotzdem traten Unterschiede in den EPR-Spektren auf, die auf unterschiedliche Umgebungen der Dotierionen schließen lassen: durch Schalenwachstum sind die Dotierionen in der CdSe/ZnS/CdS-Grenzfläche verteilt, während die Dotierionen in der Synthese ohne Schale Cluster innerhalb der CdS-Domäne bilden. Die Ergebnisse der spektroskopischen Untersuchungen wiesen außerdem darauf hin, dass das Kern/Schale/Stäbchen-System zur Bildung einer Mischphase in der Grenzschicht neigten, was durch die Dotierionen verstärkt wird. Da diese Mischphasen an der Grenzschicht interessant sind für die Herstellung von Partikeln mit gradierten Schalen für Lasing-Anwendungen sollte dieser Nebeneffekt der Dotierung weiter untersucht werden. Generell

---

[68] Florian Enders. *Tailoring the Charge Carrier Relaxation in Colloidal Semiconductor Nano-Heterostructures*. Diss. Konstanz: University of Konstanz, 2019.

erscheint die Dotierung vor der Bildung des Heteroübergangs als nicht geeignet, um nur eine Domäne eines Partikels zu dotieren, da Diffusion aus dem Partikel heraus, sowie Selbstreinigungprozesse den Erhalt der Dotierung in einer Domäne über mehrere Reaktionsschritte hinweg verhindern.

Dotierung nach der Bildung des Heteroübergangs wurde anhand der Diffusionsdotierung von CdSe/CdS Doppelstäbchen untersucht. Es wurde gezeigt, dass die CdSe-Domäne erfolgreich dotiert werden kann, obwohl sie aufgrund der Doppelstäbchen-Morphologie von einer dünnen CdS-Schicht bedeckt war. Dazu wurde eine Reaktionsmischung verwendet, die sowohl Se^{2-}- als auch Mn^{2+}-Ionen enthält. Dies weist darauf hin, dass das Chalkogenid in Lösung nicht notwenidgerweise dem Chalkogenid an der Partikeloberfläche entsprechen muss, damit die Dotierung erfolgreich sein kann. Wenn die Chalkogenide einander nicht entsprechen, kommt es allerdings zu Reifungprozessen, die die Anisotropie der Partikel reduzieren. Wurden dagegen S^{2-}-Ionen eingesetzt, so wurden die Dotierionen selektiv in die CdS Domäne eingebracht, wobei die Partikelform erhalten blieb. Wird das Chalkogenid in Lösung also auf das Chalkogenid an der Partikeloberfläche abgestimmt, so kann selektive Dotierung einer Domäne erreicht werden.

Als dritte Methode wurde die Dotierung während der Bildung des Heteroübergangs durch Zugabe der Dotierionen während einer typischen Stäbchensynthese mit sphärischen Kernen untersucht. Es wurde gezeigt, dass die Dotierionen nicht in potentielle Reaktionintermediate eingebaut werden müssen, damit Dotierung möglich ist. Sowohl die Dotierung der CdSe/CdS-Stäbchen mit Co^{2+}-, als auch die mit Mn^{2+}-Ionen war erfolgreich, ohne dass Nachteile im Bereich des anisotropen Wachstums entstanden. Daher wurde die direkte Dotierung als Methode der Wahl zur Erreichung des Ziels dieser Arbeit identifiziert.

CdSe/Mn:CdS Stäbchen wurden anschließend in einer Spitzenwachstumsreaktion eingesetzt, um den Erhalt der Dotierung bei der Postfunktionalisierung zu überprüfen. Diese Experimente zeigten, dass bereits das Heizen der Partikel sowohl zum partiellen Verlust der Dotierung, als auch zu einer Änderung der lokalen Umgebung der Dotierionen über einen längeren Zeitraum führten: Wird Mn^{2+} in in CdSe/CdS Stäbchen eingebracht, so sind die Dotierionen zunächst nahe beeinander und bilden Cluster. Durch Temperatureinwirkung diffundieren die Ionen zunächst auseinander, dann aus dem Partikel heraus. Dies unterstreicht die Bedeutung der Diffusionsprozesse als Hauptgegenspieler der Dotierung.

Im dritten Kapitel wurden Dotierung und anisotropes Wachstum kombiniert, um Dotierionen lokalisiert in die Partikel einzubringen. Direkte Dotierung mit Co^{2+}-Ionen während dem CdSe/CdS/CdS Doppelstäbchenwachstum führte nicht zur gewünschten Struktur der CdSe/CdS/Co:CdS-Doppelstäbchen, in der eine undotierte CdS-Domäne als Abstandshalter zwischen dem CdSe-Kern als Hauptrekombinationszentrum und der dotierten Co:CdS-Domäne vorliegt. Stattdessen diffundierten die Dotierionen aufgrund der hohen Reaktionstemperatur über den ganzen Partikel hinweg.

Es war möglich, lokalisiert zu dotieren, wenn die dotierten Partikel so kurz wie möglich auf der Reaktionstemperatur gehalten wurden. Dazu wurden die Dotierionen erst am Ende der gewünschten Reaktionszeit zugegeben, sodass lediglich lokal begrenzte, dotierte Domänen an den Spitzen der Partikel aufwuchsen. Die Reaktion wurde kurz darauf gestoppt, was zu einem System führte, in dem der Abstand zwischen dem Kern und der dotierten Domäne durch Veränderung der Reaktionszeit vor der Dotierionenzugabe eingestellt werden kann. Durch diesen Ansatz konnte gezeigt werden, dass der Ort der Dotierung, d.h. der Abstand vom Kern, einen größeren Einfluss hat als die Gesamtmenge an Dotierion pro Partikel.

Der der Lokalisierung entgegenwirkenden Diffusionsprozess wurde untersucht und seine Aktivierungsenergie bestimmt. Dies erlaubte eine Abschätzung der Diffusionsgeschwindigkeit bei unterschiedlichen Temperaturen, die mittels Experimente überprüft wurden: Die Diffusion ist so schnell, dass Lokalisierung der Dotierionen nicht über längere Zeit bei Raumtemperatur erhalten bleibt. Dies unterstreicht, dass die Proben bei niedrigen Temperaturen gelagert werden sollten.

Zuletzt konnte gezeigt werden, dass die dotierten Domänen am (0001)-Ende des Partikels aufwachsen, während Wachstum am $(000\bar{1})$-Ende nicht endgültig nachgewiesen oder widerlegt werden konnte. Dies war möglich, indem Stäbchen mit unterschiedlicher relativer Position des CdSe-Kerns hergestellt, und die daraus Änderung der optischen Eigenschaften untersucht wurden. Der Einfluss der Dotierionen auf die Rekombination des Exzitons im Kern war stärker, je näher der Kern am (0001)-Ende war. Da der Kern in der klassischen Stäbchensynthese etwa bei 1/3 der Stäbchenlänge lokalisiert ist, bedeutet das, dass die kritische Dimension, von der die Wechselwirkung zwischen Dotierion und Kern abhängt, der kürzere Abstand zum (0001)-Ende ist.

Mit den Ergebnissen des dritten Kapitels lässt sich festhalten, dass das Ziel der lokalisierten Dotierung und der Einbringung einer Abstandsabhängigkeit erfolgreich war. Dies stellt ein bisher unerreichtes Maß an Einfluss auf die lokale Zusammensetzung von Nanostäbchen dar, sowie einen signifikanten Fortschritt in der Kontrolle über Partikelanisotropie.

Ausgehend von den hier präsentieren Ergebnissen ergeben sich verschiedene Fragestellungen, die weiterer Forschung bedürfen. Koordinationspolymere können verwendet werden, um anisotropes Wachstum weiter zu verstärken. Weitere Untersuchungen sind notwendig, um ihre Zusammensetzung und Struktur aufzuklären. Die Verwendung von MSCs als Indikator für erfolgreiches Spitzenwachstum wird sich als wertvolles Hilfsmittel erweisen, um die bestehende Syntheseroute auf weitere Materialien zu erweitern, was insbesondere für Katalyseanwendungen interessant ist.

Die Experimente im Bereich des Schalenwachstums als Mittel zur Einschließung von Dotierionen zeigten einen bisher unbekannten Nebeneffekt der Dotierung: Sie kann die Bildung von Mischphasen erleichtern. Dieser Bereich sollte weiter erforscht werden, da Dotierung damit ein interessantes Mittel zur Synthese von Kern/Schale-Strukturen mit gradierten Schalen sein kann, ohne dass lange Alterungszeiten notwendig sind. Dieser Prozess könnte beispielsweise mittels EXAFS weiter untersucht werden, und Erkenntnisse im Bereich der Ionenmobilität und den dazu beitragenden Faktoren liefern.

Eine ungeklärte Frage, die weiterer Experimente bedarf, ist, ob Dotierionen sich nur am (0001)-Ende des Partikels, oder auch am $(000\bar{1})$-Ende anlagern. Hochauflösende lokale Elementaranalyse könnte dies beantworten. Alternativ könnte eine Stäbchensynthese, bei der der CdSe-Kern weiter zum $(000\bar{1})$-Ende verschoben ist, weitere Erkenntnisse bringen. Als dritte Möglichkeit kommt ein partieller Kationenaustausch in Frage, da diese Reaktionen am $(000\bar{1})$-Ende beginnen: Werden dabei Dotierionen freigesetzt, würde das auf Dotierung nahe an diesem Ende hinweisen.

Ein zentrales Erkenntnis dieser Arbeit ist, dass der Ort der Dotierung eine größere Rolle spielen kann als die Dotierionenkonzentration. Dies ändert den Blickwinkel auf frühere Arbeiten in diesem Feld.

Die Möglichkeit der lokalisierten Dotierung wurde im Rahmen dieser Arbeit lediglich für Co^{2+}-Ionen gezeigt. Die gleiche Struktur mit Mn^{2+}-Dotierung würde ein komplexes System mit zwei strahlenden Relaxationswegen zugänglich machen. Das Potential der Mn^{2+}-dotierten Systeme als breit einsetzbare Sensoren, z.B. für Druck und Temperatur ist bereits bekannt. Lokalisiert dotierte Strukturen würden es daher erlauben, den Einfluss dieser Faktoren auf die Relaxationskinetik und Exzitonbeweglichkeit zu untersuchen.

Mit der lokalisierte Dotierung mit Übergangsmetallionen steht der Nanowissenschaft ein weiteres

Werkzeug zur Verfügung, mit dem die elektronische Struktur von Nanopartikeln beeinflusst werden kann. Zusammen mit Größen- und Formkontrolle, sowie der Option, verschiedene Materialien zu kombinieren, ist es möglich, aufwendige Heterostrukturen aufzubauen, die auf spezifische Anwendungen und Experimente zugeschnitten werden können. Es wäre beispielsweise möglich, dotierte Stäbchen mit einer Spitze aus einem Heteromaterial herzustellen, in der die Energie eines Exzitons zunächst in den d-Zuständen des Dotierions gespeichert wird, bevor sie temperaturgesteuert freigesetzt werden kann.

Die Einbringung magnetischer Ionen in ein Ende eines Nanostäbchens könnte es ermöglichen, magnetische Felder zu nutzen, um Selbstassemblierung zu induzieren. Dabei könnte untersucht werden, inwieweit die Ausrichtung im Magnetfeld, sowie die Feldstärke und der Gradient der Dotierionen innerhalb des Partikels die Emissionseigenschaften der Partikelüberstrukturen beeinflusst. Weitere interessante Experimente könnten zeigen, ob es möglich ist, mittels eines Magnetfelds die Dotierionen an einem Ende des Partikels zu halten, oder ihre Position an die Längskante eines Stäbchens zu ändern. Dadurch könnte die spektroskopisch normalerweise nicht zugängliche Bewegung des Exzitons um das Stäbchen herum untersucht werden.

In der Literatur wurde bereits gezeigt, dass licht-emittierende Geräte mit isotrop dotierten Partikeln in der aktiven Schicht hergestellt werden können, in dem magnetische Polaronen entstehen.[140] Mit den oben beschriebenen Assemblierungen aus anisotrop dotierten Nanostäbchen sind potentiell noch variablere Systeme für spintronische Anwendungen möglich.

---

[140] Franziska Muckel u. a. *Nano Lett.*, **17**: 4768–4773, 2017.

8 Experimental Details

8.1 Methods and instruments

8.1.1 Steady state absorption spectroscopy

Steady-state UV/vis absorption spectra were acquired in solution using an Agilent Cary 60 spectrophotometer with a spectral range of 190 nm to 1100 nm. The samples were measured in Hellma quartz cuvettes with an optical path length of 10 mm and a wavelength range of 200 nm to 2500 nm. In UV/vis spectroscopy the sample's wavelength dependent extinction of ultraviolet and visible light is detected. Typically, this is the electronic transition between the highest occupied and the lowest unoccupied electronic state. As a photon of sufficient energy to bridge this energy gap is absorbed, the electron is excited to the higher state. The absorbance A is described by the Lambert-Beer law:

$$A = \log \frac{I_0}{I} = \epsilon \cdot c \cdot d$$

The absorbance depends upon the extinction coefficient ϵ of the material at the specific energy, the concentration c of the analyte, and the optical path length l. It describes the correlation of the initial intensity of the light I_0, and the final intensity after passing though the sample I at a given wavelength. In order to obtain an absorption spectrum, the intensity is measured continuously by scanning though the desired energy range with a monochromator.

8.1.2 Time-resolved photoluminescence spectroscopy

Photoluminescence spectra and fluorescence decays using time-correlated single photon counting (TCSPC) were obtained using a PicoQuant FluoTime-300 spectrophotometer equipped with a pulsed 405 nm excitation laser with a <50 ps pulse width. The samples were measured in Hellma quartz cuvettes with an optical path length of 10 mm and a wavelength range of 200 nm to 2500 nm. Excited electronic states have a limited lifetime, after which they decay to their ground state, which leads to release of the energy difference, e.g., in the shape of a photon. This process is the basis of photoluminescence emission spectroscopy: A sample is excited at a fixed wavelength. The photons that are then emitted upon relaxation are then detected at a 90° angle to the excitation light source in order to prevent detection of the excitation beam. Using a monochromator before the detector steady state emission spectra can be measured.

In order to obtain values for the lifetime of states time-resolved measurements can be performed by time-correlated single photon counting (TCSP). This allows the measurement of the time that passes between the excitation laser pulse and the detection of the photon due to relaxation. Repeated measurements allow the application of statistics in order to get a histogram of the time between excitation and relaxation, which take the form of a decay curve that can then be fitted to calculate the fluorescence lifetime.

8.1.3 High-resolution transmission electron microscopy (HR-TEM)

High-resolution TEM micrographs were obtained using a Jeol JEM 2200FS transmission electron microscope operated at 200 kV. Samples were prepared by dropcasting 10 µL of dilute sample solution in toluene onto a carbon-coated copper grid (Quantifoil) held with tweezers. After 30 s the excess solution is removed with a piece of filter paper.
Transmission electron microscopy uses the interaction of electrons with a sample in order to get an image of the sample. While in principle comparable to light microscopy electron microscopy has much higher resolution. The resolution is limited by the wavelength of the incident beam: The structure with which the incident radiation interacts has to be bigger than the wavelength of the incident radiation. Electrons can be accelerated to much higher wavelengths than photons, leading to a higher possible resolution. For instance, electrons accelerated at 200 kV have a de Broglie wavelength of 2.5 pm which allows a resolution of below 0.1 nm
In a TEM, the electrons are generated and accelerated in a cathode. The electron beam is then focused using a system of electromagnetic lenses electrostatic plates. The specimen stage is inserted into the beam, and below it, the detector, which typically is a CCD chip. The entire system is operated under vacuum in order to minimize interaction of the electron beam with molecules that are not the sample. The electron beam is focussed on the sample, and a picture is taken by detecting the electrons after passing though the specimen. The electrons interact with the sample atoms which determines the contrast of the picture. In an area of high mass or thickness, the electrons are scattered and blocked from reaching the detector. Areas of high mass thus appear dark in typical TEM pictures. In complementary methods that detect scattered electrons instead, e.g., dark field TEM, an inverted picture where high mass areas are lighter can be obtained.
One of these methods is Energy-filtered TEM (EFTEM). Electrons interact with the sample and excite valence electrons of sample atoms into higher energy states, which leads to energy loss in of the incident electron that is characteristic for the transition it excited. An image of these elastically scattered electrons can be detected, which allows for imaging areas in which specific elements are present. This process is most efficient for elements with a mass number z lower than 20. Additionally, EDX measurements can be performed on a TEM. The mechanisms of this technique are described in Section 8.1.4.

8.1.4 Energy dispersive X-Ray spectroscopy (EDX)

Quantitative EDX measurements were performed on a Hitachi TM3000 Tabletop SEM with a Bruker Quantax EDX Detector for the EDX measurements. The purified samples were dropcast on silicon wafers and dried. This was repeated until a sufficient amount of sample was deposited.
EDX analysis is an elemental analysis technique that relies on the interaction of a sample with the electron beam in an electron microscope. The electrons are accelerated in the cathode, reaching uniform energy determined by the applied acceleration voltage. When the electrons hit the sample, they interact with the atoms at the surface, exciting valence electrons into higher states which leaves a hole. This hole can be filled with an electron from a higher energy state. The energy difference between the two states is then emitted as X-ray radiation, which is characteristic for the specific element and transition. This allows qualitative and quantitative analysis of the local composition of a sample, as well as mapping the distribution of the elements within the sample.
As the electron beam has limited penetration depth, depending on its energy only surface atoms

up to a certain depth are analyzed. EDX is best suited for analysis of heavier atoms with an atomic number z of 20 or higher.

8.1.5 Inductively coupled plasma optical emission spectrometry (ICP-OES)

ICP-OES measurements were performed on an Agilent 5800 ICP-OES equipped with an autosampler. The samples were digested in nitric acid and hydrogen peroxide according to a published procedure.[141] Briefly, a small amount of sample was dried in a falcon tube. The resulting pellet was digested in 0.5 mL of concentrated nitric acid for 15 min, followed by the addition of 0.5 mL of hydrogen peroxide (30%), while taking care to keep the lid closed whenever possible to prevent escape of H_2S and H_2Se that forms during sample digestion. As soon as the sample material is completely dissolved, the sample solution is diluted to a volume of 10 mL with 1% nitric acid in Milli-Q water. All employed chemicals were trace analysis grade.

For calibration, a serial dilution of a commercially available standard was used to cover the samples' concentration range via three-point-calibration. Additionally, a blank sample that underwent the same digestion procedure as the samples was measured as a fourth calibration point.

ICP-OES is a technique for quantitative elemental analysis with a lower threshold in the ppb range. A high frequency field in a coil is used to induce an Argon plasma in the torch. Free electrons are accelerated and collide with atomic rumps, heating up the plasma. The sample is introduced into the sample chamber as an aerosol, where it is heated by the plasma to temperatures of up to 10 000 K. The contained analytes are excited and show optical emission of characteristic wavelengths, the intensities of which are detected by a CCD chip. Usage of a polychromator allows the simultaneous detection of up to 70 elements.

8.1.6 Electron paramagnetic resonance spectroscopy (EPR)

EPR spectra were recorded on a table-top X-band spectrometer MiniScope MS 400 (MagneTech) equipped with a temperature controller H03 (Magnetech).

EPR uses the interaction of the magnetic moment of unpaired electrons with an external magnetic field to detect their local environment. Electrons have a magnetic moment and spin quantum number of $s = 1/2$. When an external magnetic field B_0 is applied the magnetic moment aligns either parallel ($m_s = +1/2$) or antiparallel ($m_s = -1/2$) to the external field. According to the Zeeman effect an energy separation between the lower and upper state is induced:

$$\Delta E = g_e \cdot \mu_B \cdot B_0$$

g_e is the electron g-factor and the μ_B Bohr magneton. The splitting between the levels is thus proportional to the magnetic field strength. An unpaired electron can witch between the states by absorption or emission of a photon of sufficient energy $E = h\nu$. For an EPR experiment, the excitation wavelength is fixed in the microwave range (typically 9 GHz), and the magnetic field is varied. The change in absorption at different field strengths is measured and yields the EPR spectrum. Only unpaired electrons can be detected, which makes this method well suited for transition metal ions with unpaired electrons.

---

[141] Calynn Morrison et al. *Chem. Mater.*, **32**: 1760–1768, 2020.

8.1.7 Infrared spectroscopy (IR)

Infrared spectra were acquired using a Perkin Elmer Spectrum 100 FT-IR spectrometer with ATR detection.

IR radiation is absorbed by the sample and excites vibrational modes of molecular bonds. The observed frequencies are characteristic for the respective bonds, which makes IR spectroscopy an efficient tool for the identification of functional groups within a sample. Vibrational modes are IR active if they have an induced or dynamic dipole moment.

IT can be measured in reflection, e.g., in attenuated total reflectance (ATR). A solid sample is pressed to the surface of a light conductor. The light is then reflected by the opposing side of the conductor, in total reflection, and can then be reflected into the sample again. This can be done repeatedly which enhances the interaction of the sample with the radiation, improving the signal-to-noise ratio.

8.2 Materials

Cadmium acetate (99.995 %), cadmium oxide (CdO, >99.5 %), diethyl zinc (≥52 wt. % Zn basis), n-hexane (95 %), n-hexylphosphonic acid (HPA, 95 %), methanol, 1-octadecene (ODE, 90 %), octane, 1-octanethiol (>98.5 %), oleic acid (OA, >99 %), oleyl alcohol (85 %), sulfur flakes (>99.99 %), tributylphosphine (TBP, 97 %), tri-n-octylphosphine (TOP, 97 %), tri-n-octylphosphine oxide (TOPO, 99 %), and zinc acetate (99.99 %) were purchased from Sigma-Aldrich. n-Octadecylphosphonic acid (ODPA, >99 %) was purchased from PCI Synthesis. Chloroform (99.9 %) and oleylamine (OlAm, >80-90 % C18) were acquired from Acros. Selenium shot (99.999 %), cobalt(II) acetate (anhydrous, ≥98+ %), and manganese(II) acetate (anhydrous ,≥98+ %) were purchased from Alfa Aesar, and tellurium shot (99.9999 %) were purchased from ABCR, acetone (> 99 %) and methanol (>99.8 %) from VWR and toluene (>99.5 %) from Carl Roth. Hydrogen peroxide (30 %, trace metal grade), nitric acid (69%, trace metal grade), and multielement standards for elemental analysis were purchased from Merck. All chemicals were used as received without further purification.

8.3 Synthesis protocols

8.3.1 Precursor compounds

TOP-Se (1.7 M) A solution of selenium in TOP was prepared by mixing 2.686 g of Se shot with 20 ml of TOP and stirring the mixture at 150 °C in a glove box until the solution was clear.

TOP-S (2.0 M) A solution of sulfur in TOP was prepared by mixing 1.334 g of S flakes with 20 mL of TOP and stirring the mixture at 150 °C in a glove box until the solution was clear.

TOP-Te (0.5 M) A solution of tellurium in TOP was prepared by mixing 1.276 g of crushed Te shot with 20 mL of TOP and stirring the mixture at 150 °C in a glove box until the solution was clear. Lower concentrations were obtained by diluting the stock solution with TOP.

Cd oleate (0.1 M) Cadmium oleate was prepared by stirring 0.231 g of cadmium acetate in 0.631 mL of oleic acid and 8.9 mL of octadecene at 250 °C in a glove box until it was dissolved. The temperature was reduced to 100 °C and 0.658 mL of oleylamine were added before the mixture was allowed to cool to room temperature.

Zn oleate (0.2 M) Zinc oleate was prepared by stirring 0.367 g of zinc acetate in 0.631 mL of oleic acid and 8.9 mL of octadecene at 250 °C in a glove box until it was dissolved. The temperature was reduced to 100 °C and 0.658 mL of oleylamine were added before the mixture was allowed to cool to room temperature.

Mn oleate Manganese(II) oleate stock solution for diffusion doping was prepared by stirring 0.12 g of manganese(II) acetate hydrate, 60.8 mL of octadecene, and 2.24 mL of oleic acid at 90 °C under reduced pressure until dissolved.

8.3.2 CdSe quantum dots

CdSe nanoparticles were synthesized following a hot-injection protocol reported by Carbone et al.[11] 3.0 g of TOPO, 0.280 g of ODPA, and 0.060 g of CdO were loaded into a 25 mL three-neck flask and degassed for 1 h at 120 °C under reduced pressure. The mixture was then heated to 350 °C under nitrogen until clear, cooled to 120 °C and again degassed under reduced pressure for 30 min to remove water formed during the formation of cadmium phosphonates. The reaction was then heated to 370 °C under nitrogen. 1.8 mL of TOP were added, and then 433 µL of TOP-Se (1.7 M) were swiftly injected. A color change was observed from colorless to deep red, and the reaction was stopped after 30 s by injection of 5 mL of oleyl alcohol and cooling to room temperature with compressed air. After the temperature fell below 130 °C, a 5 mL portion of toluene was added to the reaction mixture. The particles were washed three times by precipitation with methanol and redispersing in toluene. The nanocrystal solution was stored under ambient conditions for further use.

8.3.3 CdSe nanorods

CdSe nanorods were synthesized following a modified hot-injection protocol reported by Carbone et al.[11] 6.0 g of TOPO, 1.16 g of ODPA, 0.16 g of HPA, and 0.172 g of CdO were loaded into a 25 mL three-neck flask equipped with a thermocouple, septum and condenser, and degassed under reduced pressure at 120 °C for 1 h. Then, under nitrogen flow, the mixture was heated to 350 °C until it turned clear. 3 mL of TOP were added, and the flask was cooled down to 120 °C. At this temperature the reaction mixture was degassed under reduced pressure for 30 min to remove the water that was released during the formation of Cd phosphonates. 160 nmol of spherical CdSe nanocrystals were dried and dissolved in 4.4 mL of TOP-Se (1.7 M) and 0.4 mL of TOP. The solution was loaded into a syringe equipped with a 2.0 mm (14 G) cannula and injected swiftly into the reaction mixture at 320 °C. After 10 min the reaction was quenched by removal of the heating mantle and subsequent cooling by blowing pressurized air over the flask. At 130 °C, 8 mL of toluene were added to prevent solidification. The particles were precipitated using 30 mL of methanol,

---

[11] Luigi Carbone et al. *Nano Lett.*, **7**: 2942–2950, 2007.

centrifuged at 3650 × rcf for 5 min and the supernatant was decanted. The precipitate was dried and redispersed in 2 mL of toluene. These purification steps were repeated twice. The nanorods were stored in toluene.

8.3.4 CdS nanorods

CdS nanorods were synthesized following a modified hot-injection protocol reported by Carbone et al.[11] 3.0 g of TOPO, 0.290 g of ODPA, 0.080 g HPA, and 0.060 g CdO were loaded into a 25 mL three-neck flask equipped with a thermocouple, septum, and condenser, and degassed at 120 °C for 1 h under reduced pressure. Then, under nitrogen flow, the mixture was heated to 350 °C until it turned clear. 1.8 mL of TOP were added, and the flask was cooled down to 120 °C. At this temperature the reaction mixture was degassed under reduced pressure for 30 min to remove the water that was released during the formation of Cd phosphonates. 1.8 mL of TOP-S were loaded into a syringe equipped with a 2.0 mm (14 G) cannula and injected swiftly into the reaction mixture at 350 °C (290 °C for a doping batch) under nitrogen. After the desired reaction time, typically 8 min, the reaction was quenched by removing the heating mantle and subsequent cooling by blowing pressurized air over the flask. At 130 °C, 3 mL of toluene were added to prevent solidification. The particles were precipitated using 20 mL of methanol, centrifuged at 3650 × rcf for 5 min and the supernatant was decanted. The precipitate was dried and redispersed in 1 mL of toluene. These purification steps were repeated twice. The nanorods were redispersed and stored in toluene.

8.3.5 ZnSe quantum dots

ZnSe quantum dots were synthesized following a modified hot-injection protocol reported by Cozzoli et al.[142] A 25 mL three-neck flask equipped with a condenser, thermocouple and septum was loaded with 8.6 mL oleyl amine and degassed under reduced pressure at 80 °C for 1 h, and subsequently heated to 300 °C under inert atmosphere. In a nitrogen glove box 11.60 mL, 2.68 mL TOP-Se and 0.37 mL diethyl zinc were mixed to form the precursor. 3.2 mL of this mixture were swiftly added to the reaction flask *via* a syringe equipped with a (2 mm) (14 G) cannula and the temperature was lowered to 265 °C. After 30 min of reaction time, 1 mL precursor was added drop wise to the reaction over the course of 8 min. This step was repeated two more times. After another 30 min of reaction time after the last precursor addition the reaction was stopped and the reaction mixture transferred to a centrifuge vial under inert conditions. The particles were precipitated with acetone and centrifuged at 3650 × rcf for 10 min, which yielded a yellow oil that was frozen in liquid nitrogen to form a white precipitate that was separated by centrifugation and redispersed in chloroform. The purification steps were repeated twice. The final product was redispersed in chloroform and stored under nitrogen atmosphere.

In order to exchange the amine ligands on the particle surface, a ligand exchange procedure was performed. A 25 ml three-neck flask equipped with a condenser, thermocouple and septum was loaded with 3.0 mL oleylamine and 3.0 mL octadecene, and degassed under reduced pressure at 80 °C for 1 h. The flask was then flooded with nitrogen and the ZnSe cores were added. The temperature was increased to 120 °C and the mixture was degassed for 1 h under reduced pressure. After flooding with nitrogen, 2 mL of Zn oleate stock solution (0.2 M) were added and the reaction was kept at 120 °C for 1 h. The light yellow reaction mixture was cooled to room temperature

---

[142] P. Davide Cozzoli et al. *Chem. Mater.*, **17**: 1296–1306, 2005.

and transferred to a centrifuge tube under inert conditions. After precipitation with acetone, the mixture was centrifuged and the supernatant discarded. The precipitate was redispersed in 3 mL of chloroform. The purification step was repeated once. The resulting precipitate was redispersed in 2 mL of chloroform and stored under nitrogen.

8.3.6 CdE/CdS dual rods (E=Se, S)

Dual rods were synthesized following a modified hot-injection protocol reported by Carbone et al.[11] 2.5 g of TOPO, 0.241 g of ODPA, 0.060 g of HPA, and 0.048 g of CdO were loaded into a 25 mL three-neck flask equipped with a thermocouple, condenser, and septum and degassed under reduced pressure at 120 °C for 1 h. Then the mixture was heated to 350 °C under nitrogen flow until it turned clear. 0.8 mL of TOP were added, the flask was cooled down to 120 °C and degassed under reduced pressure for 30 min. For simultaneous injection 50 nmol of seed nanorods were dried and dissolved in 1.6 mL of TOP-S (2.0 M) and 0.8 mL of TOP inside a nitrogen glove box. The solution was loaded into a syringe equipped with a 2.0 mm(14 G) cannula and swiftly injected into the reaction mixture at 360 °C. For delayed injection 50 nmol CdSe rods in 0.8 mL TOP and 1.6 mL of TOP-S were loaded into separate syringes. TOP-S was swiftly injected into the reaction mixture at 360 °C, followed by the seed solution after a delay of approximately 30 s. Due to the injected volume the temperature in the flask drops to the intended growth temperature of 320 °C. After 8 min the reaction was stopped by removing the heating mantle and cooling using pressurized air. At 130 °C, 5 mL of toluene were added. Purification was done according to the procedure described above.

Variations of this reaction scheme include different amounts of TOP-S (0.37 mL, 1.6 mL, 2.25 mL and 3.7 mL), different molar ratios of phosphonic acids ($f_{\mathrm{ODPA}} = 1.0,\ 0.82,\ 0.64$ and 0.46), and the addition of 50 µL of water to the TOP-S injection solution.

8.3.7 Dual rod synthesis using a MSC precursor

CdS magic-size clusters (MSC-324) were prepared according to a published procedure.[84] In a 50 mL three-neck flask equipped with a thermocouple, condenser, and septum, 2.56 g of CdO and 20 mL of oleic acid were degassed at 50 °C under reduced pressure for 15 min, before the mixture was heated at 160 °C under nitrogen until it turned clear. The temperature was lowered to 100 °C, and the solution was degassed again for 1 h under reduced pressure. After flushing with nitrogen a solution of 0.32 g of sulfur in TOP (4 mL) was added to the flask at 50 °C, and the reaction was heated to 140 °C, where it was kept for 1 h. Ethyl acetate (24 mL) was added to the resulting viscous solution and the mixture was centrifuged at 3650 × rcf for 10 min. The supernatant was discarded, and the precipitate was redissolved in hexane. The purification step is repeated once, and the resulting precipitate is dried under reduced pressure. The elemental composition was analyzed by EDX.

MSC-324 was then dissolved in *n*-hexane to form a 0.1 M solution. For Experiment I, 1.8 g of TOPO were loaded into a 25 mL three-neck flask equipped with a thermocouple, condenser, and septum and degassed under reduced pressure at 120 °C for 1 h. 0.8 mL of TOP were added under nitrogen, and the reaction mixture was heated to 360 °C. 1.6 mL of MSC-324 stock solution, then 50 nmol of CdSe rods in 0.8 mL of TOP were added using syringes equipped with a 2.0 mm

---

[84] Douglas R. Nevers et al. *Chem. Commun.*, **53**: 2866–2869, 2017.

(14 G) cannula. The temperature dropped by approximately 40 °C and was set to 320 °C for particle growth. Experiment II reflects the 8-fold sulfur excess employed in the CdSe/CdS dual rod synthesis while keeping the rest of the parameters unchanged. Here, 0.998 mL of 2 M TOP-S and 0.84 mL of the MSC-324 stock solution were injected, followed by 50 nmol of CdSe rods in 0.8 mL of TOP. For Experiment III, 0.043 g of HPA and 0.174 g of ODPA are added to the flask before degassing. The injections were performed as in Experiment II.

8.3.8 CP-309 synthesis

CP-309 was synthesized following a protocol reported by Wurmbrand et al.[33] 0.205 g of CdO, 1.07 g of ODPA and 2.93 g of TOPO were loaded into a 50 mL three-neck flask equipped with a thermocouple, condenser, and septum, and degassed under reduced pressure at 120 °C for 1 h. The flask was flushed with nitrogen and heated to 320 °C until it turned clear. The temperature was subsequently lowered to 150 °C and the mixture was degassed under reduced pressure for 1 h to remove water produced during the formation of Cd phosphonates. After flushing with nitrogen 2.32 mL of TBP-S (0.343 M, 0.11 g S per 10 mL of TBP) were swiftly injected through a 2.0 mm (14 G) cannula at 330 °C. The temperature was reduced to 300 °C immediately after injection. After 15 min the reaction was quenched by removal of the heating mantle and rapid cooling in a stream of pressurized air. At 130 °C 5 mL of toluene were added to prevent solidification. The solution was centrifuged at 3650 × rcf. The supernatant was discarded, and the colorless precipitate was washed three times with 0.5 mL of hexane. The pellet was dissolved in 10 mL of hexane by gentle heating to approximately 50 °C. The solution was again centrifuged and the precipitate containing excess CdO was discarded. The solution of CP-309 in hexane was stored under nitrogen atmosphere at room temperature where it slowly formed a colorless gel.

8.3.9 MSe/CdS seeded nanorods (M=Cd, Zn)

Seeded nanorods were synthesized following a hot-injection protocol reported by Carbone et al.[11] 3 g TOPO, 0.290 g ODPA, 0.080 g HPA and 0.086 g CdO were loaded into a 25 mL three-neck flask equipped with a thermocouple, condenser, and septum and degassed for 1 h at 150 °C under reduced pressure. The mixture was then heated to 350 °C under nitrogen until clear, cooled to 100 °C and again degassed under reduced pressure for 30 min to remove water formed during the formation of cadmium phosphonate. 1.8 mL TOP was added, and the reaction was then heated to 350 °C under nitrogen. A portion of 80 nmol seed dots was dissolved in 1.88 mL of TOP-S (2.0 M) and 0.2 mL of TOP. This solution was swiftly injected into the reaction mixture and the nanorods were allowed to grow for 8 min after which the heating mantle was removed, and the flask was cooled to room temperature with compressed air. After the temperature fell below 130 °C, a 5 mL portion of toluene was added to the reaction mixture and the particles were washed three times by precipitation with methanol and dispersing in toluene. The washed nanocrystal solution was stored under ambient conditions for further use.

---

[33] Daniel Wurmbrand et al. *Chem. Commun.*, **54**: 7358–7361, 2018.

8.3.10 CdTe@CdSe/CdS tipped nanorods

Growth of CdTe tips on CdSe/CdS nanorods was performed following a protocol by Enders et al.[23] A 25 mL three-neck flask equipped with a condenser, thermocouple and septum was loaded with 1.44 g TOPO, 1.6 mL octadecene and 1.6 mL oleylamine and the mixture was degassed under reduced pressure at 80 °C for 1 h. The flask was then flooded with nitrogen and 0.8 mL (16 nmol) of a dispersion of CdSe/CdS seeded nanorods in TOP were added under inert gas conditions. The reaction mixture was heated to 200 °C, 0.48 mL of Te in TOP (0.1 M) were added, and the solution was stirred for 10 min. This was followed by the addition of 0.24 mL of Cd oleate in octadecene (0.1 M) over 30 min via a syringe pump. The color of the solution turned from bright orange to green/brown, depending on the size of the initial rods. After the addition was complete, the particles were annealed for 10 min at 200 °C. The reaction mixture was then cooled to 80 °C and 5 mL dry $CHCl_3$ were added. The particles were transferred into a centrifuge vial under inert gas conditions and precipitated using dry acetone, centrifuged, and redispersed in dry chloroform. This purification procedure was repeated once. The resultant dispersion was stored in a glove box.
For MSC-based synthesis, CdTe MSCs were prepared according to a procedure by Zanella et al.[94] 5.541 g of CdO and 2.2 mL of nonanoic acid were added to a 25 mL three-neck flask equipped with a condenser, thermocouple, and septum. The flask was heated to 100 °C under reduced pressure for 15 min. Subsequently, it was flooded with nitrogen and heated to 200 °C until the mixture turned clear and colorless. At 100 °C, 2.5 mL of decylamine was added, and the mixture was kept under reduced pressure for 15 min to remove water that formed during complexation. After flooding with nitrogen, 6 mL of TOP-Te (0.3 M) was added with a syringe equipped with a 2 mm (14 G) cannula at 90 °C. After a defined growth time at 120 °C the reaction was stopped by adding 2 mL of toluene. The mixture was precipitated by adding 20 mL of methanol and centrifuged at 3650 × rcf for 10 min. The precipitate was redissolved in 1 mL of chloroform. The purification step was repeated twice. The obtained orange product was redispersed in toluene and stored in the glove box until further use.
0.287 mmol of MSC (Elemental analysis by EDX) were dissolved in 5.15 mL of octadecene and 0.5 mL of oleylamine. 0.96 mL of this stock solution (0.05 M) was added via syringe pump over 1 h instead of the Cd oleate solution. Variations include the amount of oleic acid (0 µL, 50 µL and 200 µL), the reaction temperature (157 °C and 200 °C), as well as whether TOP-Te was added.

8.3.11 Diffusion doping

Diffusion doping was performed according to a procedure by Vlaskin et al.[51] 8.6 mL of Mn oleate stock solution and 0.68 mL of oleylamine were loaded into a 25 mL three-neck flask equipped with a condenser, thermocouple, and septum and degassed for 1 h at 90 °C under reduced pressure. The flask was flooded with nitrogen, heated to 300 °C, and CdSe or CdS particles (65 mmol with regard to CdE units) and 0.17 g selenium shot (or 0.07 g sulfur flakes) dissolved in 0.5 mL of octadecene and 0.5 mL of tributylphosphine were injected. After 1 h of reaction time the flask was cooled to room temperature and the solution was transferred to a centrifuge vial. The particles were precipitated by addition of 20 mL of acetone, centrifuged at 3650 × rcf for 5 min, and the

---

[23] Florian Enders et al. *Nanoscale*, **10**: 22362–22373, 2018.

[94] Marco Zanella et al. *J. Phys. Chem. C*, **114**: 6205–6215, 2010.

[51] Vladimir A. Vlaskin et al. *J. Am. Chem. Soc.*, **135**: 14380–14389, 2013.

supernatant was removed. The precipitate was dried and redispersed in 1 mL of toluene. The purification step was repeated twice. The purified nanocrystals were stored in toluene under inert conditions.

8.3.12 ZnS shell growth

ZnS shell growth was performed according to a procedure by Boldt et al.[13] CdSe QDs (100 mmol in terms of CdSe units) were dissolved in 3.0 mL oleylamine and 3.0 mL of octadecene in a 25 mL three-neck flask equipped with a condenser, thermocouple, and septum and degassed for 1 mL at 120 °C under reduced pressure. The flask was flooded with nitrogen and heated to 310 °C. Starting at a temperature of 230 °C 0.48 mL of zink oleate (0.2 M) and 0.03 mL octanethiol in 2.47 mL octadecene were added by syringe pump ($2\,\mathrm{mL\,h^{-1}}$, 2 mL total injection volume). When the addition was complete, the mixture was kept at 310 °C for 5 min before the reaction was cooled to room temperature. The solution was transferred to a centrifuge vial, precipitated with 20 mL of acetone, and centrifuged at 3650 × rcf for 5 min. The supernatant was discarded and the precipitate redispersed in chloroform. This purification procedure was repeated twice. The resulting particles were stored in chloroform under inert conditions.

8.3.13 TM^{2+}:CP-309 experiments

2.5 g of TOPO, 0.241 g of ODPA, 0.06 g of HPA, 0.048 g of CdO, and 0.045 g manganese acetate(or 0.045 g cobalt(II) acetate, or 0.036 g copper(II) acetate) were loaded into a 25 mL three-neck flask equipped with a thermocouple, condenser, and septum and degassed under reduced pressure at 120 °C for 1 h. Then the mixture was heated to 350 °C under nitrogen flow until it turned clear. 0.8 mL of TOP were added, the flask was cooled down to 120 °C and degassed under reduced pressure for 30 min to remove water formed during formation of cadmium phosphonates. The temperature was set to 320 °C and 1.6 mL of TOP-S (2.0 M) were injected with a syringe equipped with a 2.0 mm (14G) cannula. After an appropriate reaction time, e.g., when yellow color indicated the formation of CdS nanoparticles, the reaction was stopped by removal of the heating mantle. The flask was cooled to room temperature. At 100 °C, 5 mL of toluene were added to prevent solidification. The gel was washed three times by precipitation with methanol and dispersing in hexane. The washed nanocrystal solution was stored under ambient conditions for further use.

8.3.14 Direct TM^{2+} doping during heterojunction formation

Direct doping during rod growth was performed according to a method by Dehnel et al.,[57] and the previously described procedures for dual rod and seeded rod growth (Sections 8.3.6 and 8.3.9, respectively) with the following modifications: The reaction temperature was set to 290 °C, and a solution of dopant in TOP was added instead of pure TOP. This solution was prepared by adding 10 mg of cobalt(II) acetate or maganese(II) acetate (anhydrous) to 1.8 mL of TOP and heating it to 150 °C in a nitrogen glove box. If necessary, the mixture was sonicated before addition to the reaction mixture.

---

[13] Klaus Boldt et al. *Chem. Mater.*, **25**: 4731–4738, 2013.

[57] Joanna Dehnel et al. *ACS Nano*, **14**: 13478–13490, 2020.

8.3.15 Locally Co^{2+} doped CdSe/CdS nanorods

The synthesis for locally doped nanorods was modified from published protocols.[11,57] 3.0 g of TOPO, 0.290 g of ODPA, 0.06 g of HPA and 0.08 g of CdO were loaded into a 25 mL three-neck flask equipped with a thermocouple, septum and condenser, and degassed under reduced pressure at 120 °C for 1 h. Then, under nitrogen flow, the mixture was heated to 350 °C until it turned clear. The flask was cooled down to 120 °C. At this temperature the reaction mixture was degassed under reduced pressure for 30 min to remove the water that was released during the formation of Cd phosphonates, followed by the addition of 0.9 mL of TOP. 80 nmol of spherical CdSe nanocrystals prepared according to a published protocol[11] were dried and dissolved in 1.8 mL of TOP-S (2.0 M). The solution was loaded into a syringe equipped with a 2.0 mm (14 G) cannula and injected swiftly into the reaction mixture at 290 °C. After the appropriate reaction time for the desired particle length, 10 mg of cobalt(II) acetate dissolved in 0.9 mL of TOP were added under nitrogen. After an additional 60 s, the reaction was stopped by removal of the heating mantle and subsequent cooling by blowing pressurized air over the flask. At 130 °C, 5 mL of toluene were added. The particles were precipitated using 30 mL of methanol, centrifuged at 3650 × rcf for 5 min, and the supernatant was decanted. The precipitate was dried and redispersed in 1 mL of toluene. These purification steps were repeated twice. The nanorods were redispersed and stored in toluene.

8.3.16 Diffusion experiments

10 nmol of CdSe/Co:CdS locally doped nanorods were dried, combined with 1 g of TOPO, placed in a preheated aluminum block, and heated under nitrogen atmosphere at temperatures of 125 °C to 250 °C for a total of 30 min. The reaction was quenched by a rapid drop of temperature. Samples were drawn at appropriate intervals and investigated via UV/vis and PL spectroscopy without further purification. After 30 min, 1 mL of Toluene was added to prevent solidification. The particles were purified once by precipitation with methanol, centrifugation, and subsequent redispersion in toluene, before performing TEM and elemental analysis via ICP-OES.

Appendix A

Material lattice constants

Table A.1: Lattice constants for selected materials as published in The Materials Project.[143]

Material	Space Group	a (Å)	b (Å)	c (Å)	α (°)	β (°)	γ (°)	Source
CdS	$P6_3mc$	4.21	4.21	6.84	90	90	120	[138]
CdSe	$P6_3mc$	4.39	4.39	7.17	90	90	120	[108]
MnS	$F\bar{4}3m$	5.53	5.53	5.53	90	90	90	[106]
MnSe	$F\bar{4}3m$	5.95	5.95	5.95	90	90	90	[105]
ZnS	$F\bar{4}3m$	5.45	5.45	5.45	90	90	90	[107]

---

[143] Anubhav Jain et al. *APL Mater.*, **1**: 011002, 2013.

Appendix B

Elemental analysis

B.1 EDX analysis

Table B.1: EDX analysis of CP-309. The values are based on the detection of Cd, S, P, C, and O. Three separate regions of the sample were scanned and averaged.

Element	1	2	3	average
S (at%)	0.95	0.58	1.05	0.86
Cd (at%)	2.34	1.28	3.11	2.24
S:Cd ratio	1:2.46	1:2.20	1:2.96	1:2.54

Table B.2: EDX analysis of MSC-324. The values are based on the detection of Cd, S, C, and O. Four separate regions of the sample were scanned and averaged.

Element	1	2	3	4	average
S (at%)	3.79	2.67	2.00	3.25	2.92
Cd (at%)	8.25	5.77	4.08	6.75	6.21
S:Cd ratio	1:2.17	1:2.16	1:2.04	1:2.08	1:2.11

Table B.3: EDX analysis of CdTe MSCs. The values are based on the detection of Cd, Te, C, and P. Three separate regions of the sample were scanned and averaged.

Element	1	2	3	average
Te (at%)	9.26	10.67	8.65	9.53
Cd (at%)	10.19	10.73	9.99	10.30
Te:Cd ratio	1:0.91	1:0.99	1:0.87	1:0.92

B.2 ICP-OES analysis

Different measures of dopant concentration were used in this thesis, namely the cationic fraction, the ratio of Mn to Se concentration, and the number of dopants per particle. The cationic fraction of a dopant X_{TM} is calculated from the concentrations c from ICP-OES analysis according to the following equation:

$$X_{\mathrm{TM}} = \frac{c_{\mathrm{TM}}}{c_{\mathrm{TM}} + c_{\mathrm{Cd}}}$$

In order to be able to better compare the doping levels over a series of seeded growth reactions, the Se concentration was used as an internal standard. The amount of Se per particle, which stems from the CdSe seed particle, is assumed to be constant over the reaction steps.

$$c_{\mathrm{TM/Se}} = \frac{c_{\mathrm{TM}}}{c_{\mathrm{Se}}}$$

For Chapter 6, the number of dopant atoms per particle $n_{\mathrm{TM/particle}}$ was calculated. To do so, the number of Se atoms $n_{\mathrm{Se/particle}}$ per CdSe seed particle was used as a reference. This quantity was calculated according to the following equation using the particle radius $V = 4/3 \cdot \pi \cdot r^3$ with $d = 2r = 2.6\,\mathrm{nm}$, which was determined from the sizing curve.[8] The density of CdSe is $\rho_{\mathrm{CdSe}} = 5.82\,\mathrm{g\,cm^{-3}}$, the molar mass is $M_{\mathrm{CdSe}} = 191.37\,\mathrm{g\,mol^{-1}}$

$$n_{\mathrm{Se/Particle}} = \frac{\rho_{\mathrm{CdSe}} \cdot V_{\mathrm{Particle}}}{M_{\mathrm{CdSe}}}$$

The number of dopants per particle was then calculated from the concentrations according to ICP-OES analysis with the following equation:

$$n_{\mathrm{TM/particle}} = \frac{c_{\mathrm{TM}}}{c_{\mathrm{Se}}/n_{\mathrm{Se/particle}}}$$

---

[8] Jacek Jasieniak et al. *J. Phys. Chem. C*, **113**: 19468–19474, 2009.

Table B.4: ICP-OES analysis of the samples discussed in Chapter 5.

Sample	c_{Cd}(mol L^{-1})	c_{Mn} (mol L^{-1})	c_{Se} (mol L^{-1})	Mn/Se ratio	Cd/Se ratio	Mn cationic fraction
Mn:CdSe rods	1.57×10^{-4}	1.89×10^{-5}	8.02×10^{-5}	0.24	1.96	0.11
Mn:CdS rods	1.49×10^{-4}	6.17×10^{-5}	0.00	-	-	0.29
Mn:CdSe/CdS dual rods	2.10×10^{-3}	1.64×10^{-6}	5.75×10^{-5}	0.03	36.46	0.00
Mn:CdS/CdSe dual rods	1.49×10^{-4}	7.28×10^{-7}	4.17×10^{-5}	0.02	3.58	0.00
Mn:CdSe dots	1.38×10^{-4}	9.03×10^{-5}	7.47×10^{-5}	1.21	1.85	0.40
Mn:CdSe/CdS seeded rods	3.25×10^{-4}	3.64×10^{-7}	7.47×10^{-6}	0.05	43.46	0.00
Mn:CdSe/ZnS dots	1.88×10^{-4}	7.46×10^{-5}	7.80×10^{-5}	0.96	2.41	0.28
Mn:CdSe/ZnS/CdS rods	2.83×10^{-4}	3.64×10^{-7}	7.35×10^{-6}	0.05	38.55	0.00
Mn:CdSe/CdS dual rods	1.17×10^{-4}	8.65×10^{-5}	6.08×10^{-5}	1.42	1.93	0.42
CdSe/Mn:CdS dual rods	1.20×10^{-4}	6.02×10^{-5}	1.91×10^{-5}	3.15	6.30	0.33
CdSe/Mn:CdS rods	3.63×10^{-5}	4.00×10^{-6}	1.39×10^{-6}	2.87	26.07	0.10
CdTe@CdSe/Mn:CdS rods	3.60×10^{-4}	1.38×10^{-5}	5.19×10^{-6}	2.66	69.25	0.04
CdSe/Mn:CdS rods + heat	2.26×10^{-4}	1.97×10^{-5}	5.95×10^{-6}	3.30	38.00	0.08
CdSe/Mn:CdS rods + CdOA	1.13×10^{-4}	1.64×10^{-6}	3.29×10^{-6}	0.50	34.42	0.01
CdSe/Mn:CdS rods + TOP-Te	1.21×10^{-4}	5.46×10^{-7}	3.55×10^{-6}	0.15	34.17	0.00

Table B.5: ICP-OES analysis of the samples discussed in Chapter 6.

Sample	c_{Cd} (mol L^{-1})	c_{Co} (mol L^{-1})	c_{Se} (mol L^{-1})	Co/Se ratio	Cd/Se ratio	Co cationic fraction
Doping 15 min	9.60×10^{-5}	1.14×10^{-5}	4.94×10^{-6}	2.30	19.43	0.11
Doping 15 min+15	6.78×10^{-5}	3.39×10^{-7}	4.69×10^{-6}	0.07	14.47	0.00
CdSe/CdSCoCdS 2 min	9.22×10^{-5}	1.83×10^{-5}	7.47×10^{-6}	2.45	12.33	0.17
CdSe/CdSCoCdS 5 min	5.84×10^{-5}	6.45×10^{-6}	5.07×10^{-6}	1.27	11.54	0.10
CdSe/CdSCoCdS 10 min	1.38×10^{-4}	3.39×10^{-5}	7.85×10^{-6}	4.32	17.55	0.20
CdSe/CdSCoCdS 15 min	6.40×10^{-5}	1.19×10^{-5}	2.66×10^{-6}	4.47	24.05	0.16
CdSe/CdSCoCdS 20 min	1.62×10^{-4}	2.80×10^{-5}	5.32×10^{-6}	5.26	30.47	0.15
CdSe/CdSCoCdS 30 min	7.97×10^{-5}	3.73×10^{-6}	3.04×10^{-6}	1.23	26.22	0.04
CdSe/CdSCoCdS 45 min	5.54×10^{-5}	1.22×10^{-5}	8.87×10^{-7}	13.78	62.52	0.18
Diffusion 125 °C	1.51×10^{-4}	1.70×10^{-7}	6.71×10^{-6}	0.03	22.42	0.00
Diffusion 150 °C	1.12×10^{-4}	1.70×10^{-7}	4.81×10^{-6}	0.04	23.31	0.00
Diffusion 175 °C	1.02×10^{-4}	1.70×10^{-7}	4.31×10^{-6}	0.04	23.61	0.00
Diffusion 200 °C	1.36×10^{-4}	3.39×10^{-7}	5.95×10^{-6}	0.06	22.81	0.00
Diffusion 225 °C	1.39×10^{-4}	3.39×10^{-7}	4.69×10^{-6}	0.07	29.67	0.00
Diffusion 250 °C	1.56×10^{-4}	5.09×10^{-7}	6.21×10^{-6}	0.08	25.06	0.00
seed 10 %	1.25×10^{-5}	1.70×10^{-7}	2.66×10^{-6}	0.06	4.68	0.01
seed 30 %	6.40×10^{-5}	1.19×10^{-5}	2.66×10^{-6}	4.47	24.05	0.16
seed 50 %	1.13×10^{-4}	1.02×10^{-6}	1.13×10^{-5}	0.09	9.99	0.01

Appendix C

Exponential decay fits

C.1 Domain doping

The PL decay data was fitted to a triexponential model and the overall lifetime τ was obtained by calculating the weighted mean of the three components.

$$\tau = t_1 \frac{A_1}{A_1 + A_2 + A_3} + t_2 \frac{A_2}{A_1 + A_2 + A_3} + t_3 \frac{A_3}{A_1 + A_2 + A_3}$$

In the direct doping experiment, the data for the undoped and the Mn^{2+}-doped particles was fitted to a biexponential model.

Table C.1: Photoluminescence fit data for the direct doping experiment shown in Figure 5.7.

	Time (min)	A_1	t_1 (ns)	A_2	t_2 (ns)	A_3	t_3 (ns)	τ (ns)
undoped	2	10 359	16.07	1348	48.35			19.78
	5	11 192	12.42	1312	31.17			14.39
	8	11 548	12.71	982	36.24			14.55
	14	10 952	12.42	1210	36.24			14.79
	20	11 918	13.42	986	47.18			16.00
	30	11 655	15.67	973	68.24			19.72
Mn doped	2	–	–	–	–			–
	5	–	–	–	–			–
	8	10 485	11.14	1711	32.40			14.12
	14	10 531	13.66	1100	51.18			17.21
	20	11 588	14.47	1021	55.03			17.76
	30	11 542	17.46	1016	77.78			22.36
Co doped	2	–	–	–	–		–	–
	5	5786	5.82	6818	15.57	411	62.40	11.10
	8	8416	4.55	5155	12.67	473	44.64	7.63
	14	9632	4.02	5263	11.92	426	47.34	6.81
	20	8040	4.81	6095	12.74	533	47.98	8.23
	30	9591	5.10	4847	14.02	365	63.70	8.09

Table C.2: Photoluminescence fit data for the TOPO capping experiment shown in Figure 5.8.

	A_1	t_1 (ns)	A_2	t_2 (ns)	A_3	t_3 (ns)	τ (ns)
as prepared	9591	5.10	4847	14.02	365	63.70	8.09
TOPO capped	9228	5.01	6004	13.03	338	57.40	8.17

C.2 Localized doping

Table C.3: Photoluminescence fit data for the experiment shown in Figure 5.10.

	Time (min)	A_1	t_1 (ns)	A_2	t_2 (ns)	A_3	t_3 (ns)	τ (ns)
Doped	0	405	5.97	102	44.66	34	301.28	31.82
	10	300	6.2	72	52.38	15	427.01	31.10
	30	454	5.63	102	44.18	22	346.66	25.41
	60	473	5.86	96	52.84	15	542.34	27.36
Undoped	0	427	6.66	111	58.71	45	402.73	47.14
	10	545	6.04	134	50.41	40	354.65	33.70
	30	624	5.54	142	47.65	34	372.99	28.72
	60	572	5.77	136	43.7	34	305.85	26.48

Table C.4: Photoluminescence fit data for the experiment shown in Figure 6.1, undoped references (black and gray traces).

	Time (min)	A_1	t_1 (ns)	A_2	t_2 (ns)	A_3	t_3 (ns)	τ (ns)
rods (black)	2	1374	4.68	2891	20.42	285	91.72	20.13
	5	5319	4.02	5969	14.21	616	70.41	12.57
	8	8124	4.18	7997	13.85	808	68.46	11.82
	14	12 977	4.34	11 090	14.06	1072	72.22	11.52
	20	14 409	4.6	10 942	14.7	1142	76.73	11.88
	30	9125	15.86	13 871	4.68	1116	86.15	12.68
dual rods medium (gray)	2	102 064	8.9	54 938	28.11	3743	127.77	18.23
	5	93 025	9.4	52 150	29.52	4251	132.28	19.92
	8	81 217	9.96	46 578	30.34	4415	131.96	21.21
	14	60 618	10.99	37 867	31.48	4933	128.85	24.11
	20	47 911	11.77	30 756	33.01	5220	133.52	27.13
	30	31 448	13.11	21 332	34.5	4818	139.66	31.62
dual rods long (dark gray)	2	97 675	9.31	53 857	29.89	4425	131.01	19.87
	5	82 662	9.89	48 029	30.95	5109	129.14	21.82
	8	71 612	10.28	44 239	31.39	5239	131.36	23.23
	14	54 236	11.17	34 922	32.64	5329	134.07	26.04
	20	40 802	11.81	28 526	32.98	5265	135.8	28.66
	30	26 879	12.8	20 385	33.27	4755	136.63	32.14

Table C.5: Photoluminescence fit data for the experiment shown in Figure 6.1, doped seeded rods (red traces).

	Time (min)	A_1	t_1 (ns)	A_2	t_2 (ns)	A_3	t_3 (ns)	τ (ns)
red	2	1374	4.68	2891	20.42	285	91.72	20.13
	5	5319	4.02	5969	14.21	616	70.41	12.57
	8	8124	4.18	7997	13.85	808	68.46	11.82
	14	12 977	4.34	11 090	14.06	1072	72.22	11.52
	20	14 409	4.6	10 942	14.7	1142	76.73	11.88
	30	9125	15.86	13 871	4.68	1116	86.15	12.68
dark red	2	2424	4.82	5875	20.76	653	86.49	21.24
	5	15 870	4.61	17 403	15.09	1739	68.71	13.00
	8	18 517	4.62	18 799	14.55	1747	66.57	12.17
	14	31 559	5.18	25 107	15.87	2375	73.5	12.47
	20	37 213	5.83	24 017	18.26	2338	87.54	13.53
	30	32 681	3.93	18 633	21.81	1911	108.09	13.93
light red	2	3411	5.67	7372	21.42	761	93.93	21.55
	5	16 608	4.64	17 140	15.49	1796	70.7	13.21
	8	23 972	4.63	22 386	14.83	2305	67.18	12.28
	14	41 755	4.98	19 187	15.84	3105	73.23	11.54
	20	44 078	5.16	28 304	16.8	3226	79.57	12.69
	30	41 769	5.6	22 548	18.84	2857	93.48	13.78

Table C.6: Photoluminescence fit data for the experiment shown in Figure 6.1, doped dual rods medium length (blue traces).

	Time (min)	A_1	t_1 (ns)	A_2	t_2 (ns)	A_3	t_3 (ns)	τ (ns)
dark blue	2	67 251	5.99	37 650	19.13	3212	91.28	13.10
	5	61 436	5.79	33 168	18.88	3081	93.69	13.01
	8	55 687	5.95	30 212	19.35	2999	94.39	13.49
	14	43 158	6.28	23 769	20.21	2640	98.01	14.52
	20	36 735	6.31	20 575	20.85	2566	105.41	15.55
	30	23 060	6.2	12 918	20.56	1807	108.17	15.99
medium blue	2	37 027	5.18	29 515	15.95	2805	72.15	12.47
	5	41 767	5.14	28 467	16.15	2655	76.87	12.05
	8	44 592	5.4	28 135	17.09	2821	80.75	12.57
	14	39 787	5.77	24 085	18.5	2817	88.18	13.85
	20	32 180	5.96	19 388	19.58	2513	96.41	15.05
	30	22 118	6	12 891	20.08	1856	105	15.91
light blue	2	77 757	5.64	41 789	18.24	3210	84.23	11.98
	5	66 163	5.64	35 548	18	3206	83.13	12.20
	8	63 254	5.99	32 004	19.62	2884	96	13.08
	14	49 075	6.31	25 316	20.64	2887	98.36	14.44
	20	35 133	6.35	18 328	21.05	2505	104.59	15.56
	30	25 981	6.57	12 604	21.8	1864	111.99	16.17

Table C.7: Photoluminescence fit data for the experiment shown in Figure 6.1, doped dual rods long (yellow traces).

	Time (min)	A_1	t_1 (ns)	A_2	t_2 (ns)	A_3	t_3 (ns)	τ (ns)
brown	2	79 160	6.58	37638	21.85	3149	106.93	14.01
	5	58 501	6.4	29 606	21.23	3184	105.46	14.66
	8	25 376	20.9	46 658	6.55	2990	99.16	15.09
	14	37 667	6.79	20 605	21.91	2523	109.33	16.17
	20	30 297	6.79	19 434	21.78	2255	110.34	16.89
	30	20 405	6.56	12 009	21.41	1733	114.23	17.25
light brown	2	65 687	6.31	32 833	20.79	3055	104.98	13.96
	5	55 436	6.27	28 098	20.61	2916	104.28	14.24
	8	47 222	6.45	25 018	20.85	2632	104.71	14.72
	14	38 288	6.66	21 044	21.51	2361	110.29	15.69
	20	29 491	6.73	17 033	21.41	2237	106.53	16.44
	30	18 764	6.48	11 285	21.2	1609	113.75	17.18
yellow	2	92 397	6.25	39 766	21.87	3751	106.38	13.58
	5	71 242	6.38	32 751	21.65	3497	105.53	14.26
	8	53 916	6.65	26 439	22.04	2919	109.25	15.13
	14	48 264	6.76	23 867	22.79	2999	114.8	16.17
	20	28 389	6.56	15 619	21.41	2168	109.06	16.40
	30	9438	20.98	18 158	6.24	1475	119.76	16.79

Table C.8: Photoluminescence fit data for the experiment shown in Figure 6.3.

	A_1	t_1 (ns)	A_2	t_2 (ns)	A_3	t_3 (ns)	τ (ns)
undoped	3776	11.04	2674	25.72	297	115.05	21.44
doped	3374	4.72	4073	14.89	413	73.51	13.60
doped + 15 min	2291	4.16	1719	14.19	161	82.57	11.32

Table C.9: Photoluminescence fit data for the length dependence experiment shown in Figure 6.4.

Time (min)		A_1	t_1 (ns)	A_2	t_2 (ns)	A_3	t_3 (ns)	τ (ns)
2	undoped	73	3.35	450	22.81	83	73.44	27.40
	doped	104	1.73	229	10.90	66	42.26	13.70
5	undoped	996	8.38	3397	22.74	303	96.34	24.44
	doped	911	4.27	1411	17.36	114	80.09	15.40
10	undoped	4274	10.23	5946	19.92	354	85.18	18.19
	doped	3829	3.68	3703	12.38	203	64.87	9.45
15	undoped	7265	10.26	7137	21.65	590	97.15	19.10
	doped	3865	3.81	4881	11.83	390	56.07	10.33
20	undoped	2341	10.43	1788	22.78	162	98.23	18.89
	doped	1327	5.25	2073	14.15	191	60.62	13.33
30	undoped	8275	11.02	5876	26.38	864	110.78	22.77
	doped	7394	8.73	5168	23.29	600	108.04	18.97
45	undoped	19 595	12.31	6435	30.41	688	121.86	19.49
	doped	14 537	9.07	9097	21.30	715	98.27	16.26

Table C.10: Photoluminescence fit data for the dopant diffusion experiment shown in Figure 6.5.

Temperature	Time (min)	A_1	t_1 (ns)	A_2	t_2 (ns)	A_3	t_3 (ns)	τ (ns)
125 °C	2	16 758	8.81	10 686	23.89	1237	115.16	19.02
	5	12 542	8.34	9032	22.22	1055	107.22	18.49
	10	10 553	8.05	7688	21.51	900	102.31	17.89
	15	9632	7.75	7588	20.69	812	101.83	17.43
	20	9604	7.72	7281	20.46	776	99.41	17.00
	30	8117	7.01	7927	18.31	764	91.58	16.18
150 °C	2	18 643	8.56	12 579	22.63	1378	107.9	18.19
	5	11 634	7.95	9245	20.46	914	98.8	17.07
	10	10 881	8.2	6987	21.02	670	100.85	16.38
	15	12 358	7.65	9003	19.77	821	97.65	15.90
	20	12 709	7.12	10 604	18.4	942	91.04	15.31
	30	10 246	6.56	9147	16.97	703	84.83	14.04
175 °C	2	10 624	8.16	8076	22.05	976	105.96	18.71
	5	9652	7.69	7403	20.25	858	94.22	17.03
	10	9228	6.64	8285	17.66	779	88.98	15.14
	15	8600	5.74	8331	15.39	700	77.72	13.16
	20	9450	5.17	8840	14.24	689	72.04	11.82
	30	8057	4.01	9494	11.32	623	58.01	9.68
200 °C	2	8924	7.66	7488	20.15	850	95.1	17.38
	5	9358	6.27	8347	16.42	715	80.3	13.74
	10	7846	4.34	9919	12.05	703	59.6	10.58
	15	8375	3.84	9644	10.86	611	54.22	9.13
	20	7635	3.63	8244	9.92	549	46.24	8.21
	30	7256	3.17	6848	9.07	389	46.15	7.11
225 °C	2	14 188	5.81	15 467	15.63	1340	78.53	13.85
	5	12 663	3.64	17 634	9.71	875	46.68	8.28
	10	10 850	3.16	11 921	8.22	471	41.83	6.54
	15	9955	3.07	10 908	7.83	398	41.35	6.23
	20	10 297	3.1	10 623	7.79	404	39.6	6.13
	30	10 998	3.28	9423	8.12	337	42.69	6.12
250 °C	2	16 926	5.28	18 407	14	1229	72.28	11.92
	5	12 779	2.98	10 906	8.25	471	43.47	6.15
	10	8604	2.52	6546	6.84	315	38.26	5.08
	15	7622	2.28	6484	6.27	342	33.82	4.82
	20	7418	2.47	5083	6.72	245	36.89	4.83
	30	6052	2.26	5226	6.15	261	32.61	4.71

Table C.11: Photoluminescence fit data for the seed position dependence experimental data shown in Figure 6.8.

Seed position		A_1	t_1 (ns)	A_2	t_2 (ns)	A_3	t_3 (ns)	τ (ns)
10 %	undoped	2133	11.68	1554	29.26	168	144.07	24.54
	doped	1772	3.75	1520	13.98	142	76.48	11.29
30 %	undoped	7265	10.26	7137	21.65	590	97.15	19.10
	doped	3865	3.81	4881	11.83	390	56.07	10.33
50 %	undoped	6135	10.32	4761	26.1	593	120.13	22.53
	doped	2839	5.05	3538	15.95	350	82.29	14.80

Table C.12: Photoluminescence fit data for the undoped reference experiment shown in Figure 6.2.

	A_1	t_1 (ns)	A_2	t_2 (ns)	A_3	t_3 (ns)	τ (ns)
undoped	78 443	9.15	42 146	30.74	6914	113	21.92
doped	69 679	9.48	37 045	29.94	5712	112.8	21.47

Table C.13: Photoluminescence fit data for the length dependence experiment after 4 weeks of storage shown in Figure 6.7.

Time (min)		A_1	t_1 (ns)	A_2	t_2 (ns)	A_3	t_3 (ns)	τ (ns)
2	undoped	431	11.6	1039	30.61	111	119.65	31.68
	doped	345	6.19	527	25.01	24	187.2	22.11
5	undoped	1667	10.45	4359	23.12	341	91.45	23.46
	doped	1954	5.02	5408	18.07	338	74.29	17.23
15	undoped	14 263	11.32	7248	20.33	206	93.26	15.10
	doped	4981	4.01	7823	11.47	406	40.97	9.56
20	undoped	12 992	10.82	5941	20.59	286	87.32	14.98
	doped	6420	5.54	10 423	13.16	381	59.75	11.35
30	undoped	31 011	11.63	6779	26.42	378	112.7	15.26
	doped	14 989	8.59	10 270	17.32	429	83.25	13.33

Bibliography

[1] Gordon E MOORE. Cramming More Components Onto Integrated Circuits. *Proceedings of the IEEE*, **86**: 82–85, 1965. DOI: `10.1109/jproc.1998.658762`

[2] MENGWU4 *aunps-stephmitchell* https://sustainable-nano.com/2019/11/12/gold-nanoparticles-color/ accessed Sep 02, 2022 Nov. 2019

[3] EUROPEAN FOOD SAFETY AUTHORITY *Titanium dioxide: E171 no longer considered safe when used as a food additive* https://www.efsa.europa.eu/de/news/titanium-dioxide-e171-https://www.efsa.europa.eu/en/news/titanium-dioxide-e171-no-longer-considered-safe-when-used-food-additive Accessed Sep 20, 2022 May 2021

[4] Daniel JOSELL, Sywert H. BRONGERSMA, and Zsolt TŐKEI. Size-Dependent Resistivity in Nanoscale Interconnects. *Annual Review of Materials Research*, **39**: 231–254, 2009. DOI: `10.1146/annurev-matsci-082908-145415`

[5] Sebastiaan VAN DIJKEN, Xin JIANG, and Stuart S. P. PARKIN. Room temperature operation of a high output current magnetic tunnel transistor. *Applied Physics Letters*, **80**: 3364–3366, 2002. DOI: `10.1063/1.1474610`

[6] Steven C. ERWIN, Lijun J. ZU, Michael I. HAFTEL, Alexander L. EFROS, Thomas A. KENNEDY, and David J. NORRIS. Doping semiconductor nanocrystals. *Nature*, **436**: 91, 2005. DOI: `10.1038/nature03832`

[7] Louis E. BRUS. Electron Electron and Electron-Hole Interactions in Small Semiconductor Crystallites - the Size Dependence of the Lowest Excited Electronic State. *Journal of Chemical Physics*, **80**: 4403–4409, 1984. DOI: `10.1063/1.447218`

[8] Jacek JASIENIAK, Lisa SMITH, Joel VAN EMBDEN, Paul MULVANEY, and Marco CALIFANO. Re-examination of the Size-Dependent Absorption Properties of CdSe Quantum Dots. *Journal of Physical Chemistry C*, **113**: 19468–19474, 2009. DOI: `10.1021/jp906827m`

[9] Victor K. LAMER and Robert H. DINEGAR. Theory, Production and Mechanism of Formation of Monodispersed Hydrosols. *J Am Chem Soc*, **72**: 4847–4854, 1950. DOI: `10.1021/ja01167a001`

[10] C. B. MURRAY, D. J. NORRIS, and M. G. BAWENDI. Synthesis and Characterization of Nearly Monodisperse Cde (E = S, Se, Te) Semiconductor Nanocrystallites. *Journal of The American Chemical Society*, **115**: 8706–8715, 1993. DOI: `10.1021/ja00072a025`

[11] Luigi CARBONE, Concetta NOBILE, Milena DE GIORGI, Fabio DELLA SALA, Giovanni MORELLO, Pierpaolo POMPA, Martin HYTCH, Etienne SNOECK, Angela FIORE, Isabella R. FRANCHINI, Monica NADASAN, Albert F. SILVESTRE, Letizia CHIODO, Stefan KUDERA, Roberto CINGOLANI, Roman KRAHNE, and Liberato MANNA. Synthesis and micrometer-scale assembly of colloidal CdSe/CdS nanorods prepared by a seeded growth approach. *Nano Lett.*, **7**: 2942–2950, 2007. DOI: `10.1021/nl0717661`

[12] Simon M. FAIRCLOUGH, Edward J. TYRRELL, Darren M. GRAHAM, Patrick J. B. LUNT, Samantha J. O. HARDMAN, Annette PIETZSCH, Franz HENNIES, Jonathan MOGHAL, Wendy R. FLAVELL, Andrew A. R. WATT, and Jason M. SMITH. Growth and characterization of strained and alloyed type-II ZnTe/ZnSe core-shell nanocrystals. *Journal of Physical Chemistry C*, **116**: 26898–26907, 2012. DOI: `10.1021/jp3087804`

[13] Klaus BOLDT, Nicholas KIRKWOOD, Gary A. BEANE, and Paul MULVANEY. Synthesis of Highly Luminescent and Photo-Stable, Graded Shell CdSe/$Cd_xZn_{1-x}S$ Nanoparticles by In Situ Alloying. *Chemistry of Materials*, **25**: 4731–4738, 2013. DOI: `10.1021/cm402645r`

[14] Florian ENDERS, Sebastian SUTTER, Danja FISCHLI, Rebecca KÖSER, Samuel MONTER, Simon CARDINAL, and Klaus BOLDT. Regioselective Growth Mechanism of Single Semiconductor Tips on CdS Nanorods. *Chemistry of Materials*, **32**: 10566–10574, 2020. DOI: `10.1021/acs.chemmater.0c03636`

[15] W. OSTWALD. Über die vermeintliche Isomerie des roten und gelben Quecksilberoxyds und die Oberflächenspannung fester Körper. *Zeitschrift für Physikalische Chemie*, **34U**: 495–503, 1900. DOI: `10.1515/zpch-1900-3431`

[16] Jin JOO, Hyon Bin NA, Taekyung YU, Jung Ho YU, Young Woon KIM, Fanxin WU, Jin Z. ZHANG, and Taeghwan HYEON. Generalized and facile synthesis of semiconducting metal sulfide nanocrystals. *Journal of The American Chemical Society*, **125**: 11100–11105, 2003. DOI: `10.1021/ja0357902`

[17] Z. Adam PENG and Xiaogang PENG. Nearly monodisperse and shape-controlled CdSe nanocrystals via alternative routes: Nucleation and growth. *Journal of The American Chemical Society*, **124**: 3343–3353, 2002. DOI: `10.1021/ja0173167`

[18] Felice SHIEH, Aaron E SAUNDERS, and Brian A KORGEL. General Shape Control of Colloidal CdS, CdSe, CdTe Quantum Rods and Quantum Rod Heterostructures. *Journal of Physical Chemistry B*, **109**: 8538–8542, 2005.

[19] Sandrine ITHURRIA and Benoit DUBERTRET. Quasi 2D Colloidal CdSe Platelets with Thicknesses Controlled at the Atomic Level. *Journal of The American Chemical Society*, **130**: 16504–16505, 2008. DOI: `10.1021/ja807724e`

[20] Zvicka DEUTSCH, Lior NEEMAN, and Dan ORON. Luminescence Upconversion in Colloidal Double Quantum Dots. *Nature Nanotechnology*, **8**: 649–653, 2013. DOI: `10.1038/nnano.2013.146`

[21] Dmitri V. TALAPIN, James H. NELSON, Elena V. SHEVCHENKO, Shaul ALONI, Bryce SADTLER, and A. Paul ALIVISATOS. Seeded Growth of Highly Luminescent CdSe/CdS Nanoheterostructures with Rod and Tetrapod Morphologies. *Nano Letters*, **7**: 2951–2959, 2007. DOI: `10.1021/nl072003g`

[22] James K. Utterback, Amanda N. Grennell, Molly B. Wilker, Orion M. Pearce, Joel D. Eaves, and Gordana Dukovic. Observation of trapped-hole diffusion on the surfaces of CdS nanorods. *Nat. Chem.*, **8**: 1061–1066, 2016. doi: `10.1038/Nchem.2566`

[23] Florian Enders, Arne Budweg, Peng Zeng, Jannika Lauth, Trevor A. Smith, Daniele Brida, and Klaus Boldt. Switchable dissociation of excitons bound at strained CdTe/CdS interfaces. *Nanoscale*, **10**: 22362–22373, 2018. doi: `10.1039/C8NR07973K`

[24] Maria Wächtler. Trendbericht Physikalische Chemie. *Nachrichten Aus Der Chemie*, **67**: 44–50, 2019. doi: `10.1002/nadc.20194084954`

[25] Guichuan Xing, Yile Liao, Xiangyang Wu, Sabyasachi Chakrabortty, Xinfeng Liu, Edwin K. L. Yeow, Yinthai Chan, and Tze Chien Sum. Ultralow-Threshold Two-Photon Pumped Amplified Spontaneous Emission and Lasing from Seeded CdSe/CdS Nanorod Heterostructures. *ACS Nano*, **6**: 10835–10844, 2012. doi: `10.1021/nn304200a`

[26] Andrei Mitrofanov, Anatol Prudnikau, Francesco Di Stasio, Nelli Weiss, René Hübner, Anna Maria Dominic, Konstantin B. L. Borchert, Vladimir Lesnyak, and Alexander Eychmüller. Near-Infrared-Emitting $Cd_xHg_{1-x}Se$-Based Core/Shell Nanoplatelets. *Chemistry of Materials*, **33**: 7693–7702, 2021. doi: `10.1021/acs.chemmater.1c01682`

[27] Florian D. Ott, Andreas Riedinger, David R. Ochsenbein, Philippe N. Knüsel, Steven C. Erwin, Marco Mazzotti, and David J. Norris. Ripening of Semiconductor Nanoplatelets. *Nano Letters*, **17**: 6870–6877, 2017. doi: `10.1021/acs.nanolett.7b03191`

[28] Ye Jiang, Wilfried-Solo Ojo, Benoit Mahler, Xiangzhen Xu, Benjamin Abécassis, and Benoit Dubertret. Synthesis of CdSe Nanoplatelets without Short-Chain Ligands: Implication for Their Growth Mechanisms. *ACS Omega*, **3**: 6199–6205, 2018. doi: `10.1021/acsomega.8b01006`

[29] Nicolo Castro, Cécile Bouet, Sandrine Ithurria, Nicolas Lequeux, Doru Constantin, Pierre Levitz, Diego Pontoni, and Benjamin Abécassis. Insights into the Formation Mechanism of CdSe Nanoplatelets Using in Situ X-ray Scattering. *Nano Letters*, **19**: 6466–6474, 2019. doi: `10.1021/acs.nanolett.9b02687`

[30] Chenqi Zhu, Dongdong Chen, Weicheng Cao, Runchen Lai, Chaodan Pu, Jiongzhao Li, Xueqian Kong, and Xiaogang Peng. Facet-Dependent On-Surface Reactions in the Growth of CdSe Nanoplatelets. *Angewandte Chemie International Edition*, **58**: 17764–17770, 2019. doi: `10.1002/anie.201909576`

[31] Patrick D. Cunningham, Igor Coropceanu, Kavan Mulloy, Wooje Cho, and Dmitri V. Talapin. Quantized Reaction Pathways for Solution Synthesis of Colloidal ZnSe Nanostructures: A Connection between Clusters, Nanowires, and Two-Dimensional Nanoplatelets. *ACS Nano*, **14**: 3847–3857, 2020. doi: `10.1021/acsnano.9b09051`

[32] Stefan Kudera, Marco Zanella, Cinzia Giannini, Aurora Rizzo, Yanqin Li, Giuseppe Gigli, Roberto Cingolani, Giuseppe Ciccarella, Werner Spahl, Wolfgang J. Parak, and Liberato Manna. Sequential growth of magic-size CdSe nanocrystals. *Advanced Materials*, **19**: 548–552, 2007. doi: `10.1002/adma.200601015`

[33] Daniel WURMBRAND, Jörg Wolfram Anselm FISCHER, Rose ROSENBERG, and Klaus BOLDT. Morphogenesis of anisotropic nanoparticles: self-templating via non-classical, fibrillar Cd2Se intermediates. *Chemical Communications*, **54**: 7358–7361, 2018. DOI: `10.1039/C8CC02058B`

[34] Denis GEBAUER, Antje VÖLKEL, and Helmut CÖLFEN. Stable Prenucleation Calcium Carbonate Clusters. *Science*, **322**: 1819–1822, 2008. DOI: `10.1126/science.1164271`

[35] Cristina PALENCIA, Kui YU, and Klaus BOLDT. The Future of Colloidal Semiconductor Magic-Size Clusters. *ACS Nano*, **14**: 1227–1235, 2020. DOI: `10.1021/acsnano.0c00040`

[36] Christopher M. EVANS, Alyssa M. LOVE, and Emily A. WEISS. Surfactant-Controlled Polymerization of Semiconductor Clusters to Quantum Dots through Competing Step-Growth and Living Chain-Growth Mechanisms. *Journal of The American Chemical Society*, **134**: 17298–17305, 2012. DOI: `10.1021/ja3079576`

[37] Zhong Jie JIANG and David F. KELLEY. Role of magic-sized clusters in the synthesis of CdSe nanorods. *ACS Nano*, **4**: 1561–1572, 2010. DOI: `10.1021/nn100076f`

[38] Nicholas KIRKWOOD and Klaus BOLDT. Protic additives determine the pathway of CdSe nanocrystal growth. *Nanoscale*, **10**: 18238–18248, 2018. DOI: `10.1039/c8nr06635c`

[39] L. LEVY, J. F. HOCHEPIED, and M. P. PILENI. Control of the Size and Composition of Three Dimensionally Diluted Magnetic Semiconductor Clusters. *The Journal of Physical Chemistry*, **100**: 18322–18326, 1996. DOI: `10.1021/jp960824w`

[40] J. F. SUYVER, S. F. WUISTER, J. J. KELLY, and A. MEIJERINK. Luminescence of nanocrystalline ZnSe:Mn^{2+}. *Physical Chemistry Chemical Physics*, **2**: 5445–5448, 2000. DOI: `10.1039/B006950G`

[41] D. J. NORRIS, Nan YAO, F. T. CHARNOCK, and T. A. KENNEDY. High-Quality Manganese-Doped ZnSe Nanocrystals. *Nano Letters*, **1**: 3–7, 2001. DOI: `10.1021/nl005503h`

[42] Dana A. SCHWARTZ, Nick S. NORBERG, Quyen P. NGUYEN, Jason M. PARKER, and Daniel R. GAMELIN. Magnetic Quantum Dots: Synthesis, Spectroscopy, and Magnetism of Co^{2+}- and Ni^{2+}-Doped ZnO Nanocrystals. *Journal of The American Chemical Society*, **125**: 13205–13218, 2003. DOI: `10.1021/ja036811v`

[43] Nick S. NORBERG, Gregory L. PARKS, G. Mackay SALLEY, and Daniel R. GAMELIN. Giant excitonic Zeeman splittings in colloidal Co^{2+}-doped ZnSe quantum dots. *Journal of The American Chemical Society*, **128**: 13195–13203, 2006. DOI: `10.1021/ja063425f`

[44] Gustavo M. DALPIAN and James R. CHELIKOWSKY. Self-Purification in Semiconductor Nanocrystals. *Physical Review Letters*, **96**: 226802, 2006. DOI: `10.1103/PhysRevLett.96.226802`

[45] Paul I. ARCHER, Steven A. SANTANGELO, and Daniel R. GAMELIN. Inorganic Cluster Syntheses of TM^{2+} -Doped Quantum Dots (CdSe, CdS, CdSe/CdS): Physical Property Dependence on Dopant Locale. *Journal of The American Chemical Society*, **129**: 9808–9818, 2007. DOI: `10.1021/ja0724361`

[46] Khalid M. HANIF, Robert W. MEULENBERG, and Geoffrey F. STROUSE. Magnetic ordering in doped $Cd_{1-x}Co_xSe$ diluted magnetic quantum dots. *Journal of The American Chemical Society*, **124**: 11495–11502, 2002. DOI: `10.1021/ja0262840`

[47] Ralph G. PEARSON. Hard and Soft Acids and Bases. *Journal of The American Chemical Society*, **85**: 3533–3539, 1963. DOI: `10.1021/ja00905a001`

[48] Ralph G. PEARSON. Absolute electronegativity and hardness: application to inorganic chemistry. *Inorganic Chemistry*, **27**: 734–740, 1988. DOI: `10.1021/ic00277a030`

[49] Ralph G. PEARSON. The HSAB Principle — more quantitative aspects. *Inorganica Chimica Acta*, **240**: 93–98, 1995. DOI: `https://doi.org/10.1016/0020-1693(95)04648-8`

[50] Raffaella BUONSANTI and Delia J. MILLIRON. Chemistry of Doped Colloidal Nanocrystals. *Chem. Mater.*, **25**: 1305–1317, 2013. DOI: `10.1021/cm304104m`

[51] Vladimir A. VLASKIN, Charles J. BARROWS, Christian S. ERICKSON, and Daniel R. GAMELIN. Nanocrystal Diffusion Doping. *Journal of The American Chemical Society*, **135**: 14380–14389, 2013. DOI: `10.1021/ja4072207`

[52] Charles J. BARROWS, Pradip CHAKRABORTY, Lindsey M. KORNOWSKE, and Daniel R. GAMELIN. Tuning Equilibrium Compositions in Colloidal $Cd_{1-x}Mn_xSe$ Nanocrystals Using Diffusion Doping and Cation Exchange. *ACS Nano*, **10**: 910–918, 2016. DOI: `10.1021/acsnano.5b07389`

[53] Payel MONDAL, Sowmeya SATHIYAMANI, Kushagra GAHLOT, and Ranjani VISWANATHA. Is the Lack of Orange Emission Infallible Proof of Unsuccessful Doping of Mn in Quantum Dots? *Journal of Physical Chemistry C*, **125**: 11007–11013, 2021. DOI: `10.1021/acs.jpcc.1c00359`

[54] Huijuan ZHOU, Detlev M. HOFMANN, Helder R. ALVES, and Bruno K. MEYER. Correlation of Mn local structure and photoluminescence from CdS:Mn nanoparticles. *Journal of Applied Physics*, **99**: 2006. DOI: `10.1063/1.2199267`

[55] Charles J. BARROWS, Vladimir A. VLASKIN, and Daniel R. GAMELIN. Absorption and Magnetic Circular Dichroism Analyses of Giant Zeeman Splittings in Diffusion-Doped Colloidal Cd1-xMnxSe Quantum Dots. *The Journal of Physical Chemistry Letters*, **6**: 3076–3081, 2015. DOI: `10.1021/acs.jpclett.5b01137`

[56] Rachel FAINBLAT, Charles J. BARROWS, Eric HOPMANN, Simon SIEBENEICHER, Vladmir A. VLASKIN, Daniel R. GAMELIN, and Gerd BACHER. Giant Excitonic Exchange Splittings at Zero Field in Single Colloidal CdSe Quantum Dots Doped with Individual Mn^{2+} Impurities. *Nano Letters*, **16**: 6371–6377, 2016. DOI: `10.1021/acs.nanolett.6b02775`

[57] Joanna DEHNEL, Yahel BARAK, Itay MEIR, Adam K. BUDNIAK, Anjani P. NAGVENKAR, Daniel R. GAMELIN, and Efrat LIFSHITZ. Insight into the Spin Properties in Undoped and Mn-Doped CdSe/CdS-Seeded Nanorods by Optically Detected Magnetic Resonance. *ACS Nano*, **14**: 13478–13490, 2020. DOI: `10.1021/acsnano.0c05454`

[58] Yongan YANG, Ou CHEN, Alexander ANGERHOFER, and Y. Charles CAO. Radial-Position-Controlled Doping of CdS/ZnS Core/Shell Nanocrystals: Surface Effects and Position-Dependent Properties. *Chemistry - A European Journal*, **15**: 3186–3197, 2009. DOI: `10.1002/chem.200802295`

[59] Elan HOFMAN, Richard John ROBINSON, Zhi-Jun LI, Boris DZIKOVSKI, and Weiwei ZHENG. Controlled Dopant Migration in CdS/ZnS Core/Shell Quantum Dots. *Journal of The American Chemical Society*, **139**: 8878–8885, 2017. DOI: `10.1021/jacs.7b02320`

[60] J YANG, R FAINBLAT, S G KWON, F MUCKEL, J H YU, H TERLINDEN, B H KIM, D IAVARONE, M K CHOI, I Y KIM, I PARK, H K HONG, J LEE, J S SON, Z LEE, K KANG, S J HWANG, G BACHER, and T HYEON. Route to the Smallest Doped Semiconductor: Mn^{2+}-Doped $(CdSe)_{13}$ Clusters. *J. Am. Chem. Soc.*, **137**: 12776–12779, 2015. DOI: `10.1021/jacs.5b07888`

[61] Jiwoong YANG, Franziska MUCKEL, Back Kyu CHOI, Severin LORENZ, In Young KIM, Julia ACKERMANN, Hogeun CHANG, Tamara CZERNEY, Vinayak S. KALE, Seong Ju HWANG, Gerd BACHER, and Taeghwan HYEON. Co^{2+}-Doping of Magic-Sized CdSe Clusters: Structural Insights via Ligand Field Transitions. *Nano Letters*, **18**: 7350–7357, 2018. DOI: `10.1021/acs.nanolett.8b03627`

[62] Fumitoshi KATO and Kevin R. KITTILSTVED. Site-Specific Doping of Mn^{2+} in a CdS-Based Molecular Cluster. *Chemistry of Materials*, **30**: 4720–4727, 2018. DOI: `10.1021/acs.chemmater.8b01482`

[63] Benjamin C. STEIMLE, Julie L. FENTON, and Raymond E. SCHAAK. Rational construction of a scalable heterostructured nanorod megalibrary. *Science*, **367**: 418–424, 2020. DOI: `10.1126/science.aaz1172`

[64] Luca DE TRIZIO and Liberato MANNA. Forging Colloidal Nanostructures via Cation Exchange Reactions. *Chemical Reviews*, **116**: 10852–10887, 2016. DOI: `10.1021/acs.chemrev.5b00739`

[65] Shinjita ACHARYA and Narayan PRADHAN. Insertion/Ejection of Dopant Ions in Composition Tunable Semiconductor Nanocrystals. *The Journal of Physical Chemistry C*, **115**: 19513–19519, 2011. DOI: `10.1021/jp2052147`

[66] Ayaskanta SAHU, Moon Sung KANG, Alexander KOMPCH, Christian NOTTHOFF, Andrew W. WILLS, Donna DENG, Markus WINTERER, C. Daniel FRISBIE, and David J. NORRIS. Electronic impurity doping in CdSe nanocrystals. *Nano Letters*, **12**: 2587–2594, 2012. DOI: `10.1021/nl300880g`

[67] Joren EILERS, Esther GROENEVELD, Celso DE MELLO DONEGÁ, and Andries MEIJERINK. Optical Properties of Mn-Doped ZnTe Magic Size Nanocrystals. *Journal of Physical Chemistry Letters*, **3**: 1663–1667, 2012. DOI: `10.1021/jz300300g`

[68] Florian ENDERS. *Tailoring the Charge Carrier Relaxation in Colloidal Semiconductor Nano-Heterostructures*. PhD thesis. Konstanz: University of Konstanz, 2019.

[69] Dahin KIM, Young Kuk LEE, Dongkyu LEE, Whi Dong KIM, Wan Ki BAE, and Doh C. LEE. Colloidal Dual-Diameter and Core-Position-Controlled Core/Shell Cadmium Chalcogenide Nanorods. *ACS Nano*, **11**: 12461–12472, 2016. DOI: `10.1021/acsnano.7b06542`

[70] Danja FISCHLI, Florian ENDERS, and Klaus BOLDT. Kinetically Driven Cadmium Chalcogenide Nanorod Growth Fed by Local Cluster Aggregates. *Journal of Physical Chemistry C*, **124**: 12774–12783, 2020. DOI: `10.1021/acs.jpcc.0c02730`

[71] Giovanni BERTONI, Vincenzo GRILLO, Rosaria BRESCIA, Xiaoxing KE, Sara BALS, Alessandra CATELLANI, Hongbo LI, and Liberato MANNA. Direct Determination of Polarity, Faceting, and Core Location in Colloidal Core/Shell Wurtzite Semiconductor Nanocrystals. *ACS Nano*, **6**: 6453–6461, 2012. DOI: `10.1021/nn302085t`

[72] Liang-Shi LI and A. Paul ALIVISATOS. Origin and Scaling of the Permanent Dipole Moment in CdSe Nanorods. *Physical Review Letters*, **90**: 097402, 2003. DOI: `10.1103/physrevlett.90.097402`

[73] Dirk DORFS, Asaf SALANT, Inna POPOV, and Uri BANIN. ZnSe Quantum Dots Within CdS Nanorods: A Seeded-Growth Type-II System. *Small*, **4**: 1319–1323, 2008. DOI: `10.1002/smll.200800084`

[74] Jing HUANG, Maksym V. KOVALENKO, and Dmitri V. TALAPIN. Alkyl Chains of Surface Ligands Affect Polytypism of CdSe Nanocrystals and Play an Important Role in the Synthesis of Anisotropic Nanoheterostructures. *Journal of The American Chemical Society*, **132**: 15866–15868, 2010. DOI: `10.1021/ja105132u`

[75] Chenghui XIA, Naomi WINCKELMANS, P. Tim PRINS, Sara BALS, Hans C. GERRITSEN, and Celso DE MELLO DONEGÁ. Near-Infrared-Emitting CuInS2/ZnS Dot-in-Rod Colloidal Heteronanorods by Seeded Growth. *Journal of The American Chemical Society*, **140**: 5755–5763, 2018. DOI: `10.1021/jacs.8b01412`

[76] Qiyu YU and Chun-Yan LIU. Study of Magic-Size-Cluster Mediated Formation of CdS Nanocrystals: Properties of the Magic-Size Clusters and Mechanism Implication. *Journal of Physical Chemistry C*, **113**: 12766–12771, 2009. DOI: `10.1021/jp903199y`

[77] Guang CAO, Vincent M. LYNCH, and Leonard N. YACULLO. Synthesis, Structural Characterization, and Intercalation Chemistry of Two Layered Cadmium Organophosphonates. *Chem. Mater.*, **5**: 1000–1006, 1993. DOI: `10.1021/cm00031a021`

[78] B. D. DICKERSON, D. M. IRVING, E. HERZ, R. O. CLAUS, W. B. SPILLMAN Jr., and K. E. MEISSNER. Synthesis Kinetics of CdSe Quantum Dots in Trioctylphosphine Oxide and in Stearic Acid. *Applied Physics Letters*, **86**: 171915, 2005. DOI: `10.1063/1.1921347`

[79] Emile DRIJVERS, Jonathan DE ROO, Pieter GEIREGAT, Krisztina FEHÉR, Zeger HENS, and Tangi AUBERT. Revisited Wurtzite CdSe Synthesis: A Gateway for the Versatile Flash Synthesis of Multishell Quantum Dots and Rods. *Chemistry of Materials*, **28**: 7311–7323, 2016. DOI: `10.1021/acs.chemmater.6b02666`

[80] Jonathan S. OWEN, Emory M. CHAN, Haitao LIU, and A. Paul ALIVISATOS. Precursor Conversion Kinetics and the Nucleation of Cadmium Selenide Nanocrystals. *J. Am. Chem. Soc.*, **132**: 18206–18213, 2010. DOI: `10.1021/ja106777j`

[81] Michaela MEYNS, Fabiola IACONO, Cristina PALENCIA, Jan GEWEKE, Mauricio D. CODERCH, Ursula E. A. FITTSCHEN, José M. GALLEGO, Roberto OTERO, Beatriz H. JUÁREZ, and Christian KLINKE. Shape Evolution of CdSe Nanoparticles Controlled by Halogen Compounds. *Chemistry of Materials*, **26**: 1813–1821, 2014. DOI: `10.1021/cm4037082`

[82] Leah C. FRENETTE and Todd D. KRAUSS. Uncovering Active Precursors in Colloidal Quantum Dot Synthesis. *Nature Communications*, **8**: 2082, 2017. DOI: `10.1038/s41467-017-01936-z`

[83] Nuri OH and Moonsub SHIM. Metal Oleate Induced Etching and Growth of Semiconductor Nanocrystals, Nanorods, and Their Heterostructures. *Journal of The American Chemical Society*, **138**: 10444–10451, 2016.

[84] Douglas R. NEVERS, Curtis B. WILLIAMSON, Tobias HANRATH, and Richard D. ROBINSON. Surface Chemistry of Cadmium Sulfide Magic-sized Clusters: a Window into Ligand-Nanoparticle Interactions. *Chemical Communications*, **53**: 2866–2869, 2017. DOI: `10.1039/c6cc09549f`

[85] Chaoran LUAN, Junbin TANG, Nelson ROWELL, Meng ZHANG, Wen HUANG, Hongsong FAN, and Kui YU. Four Types of CdTe Magic-Size Clusters from One Prenucleation Stage Sample at Room Temperature. *Journal of Physical Chemistry Letters*, **10**: 4345–4353, 2019. DOI: `10.1021/acs.jpclett.9b01601`

[86] Adam J. MORRIS-COHEN, Martin D. DONAKOWSKI, Kathryn E. KNOWLES, and Emily A. WEISS. The Effect of a Common Purification Procedure on the Chemical Composition of the Surfaces of CdSe Quantum Dots Synthesized with Trioctylphosphine Oxide. *The Journal of Physical Chemistry C*, **114**: 897–906, 2009. DOI: `10.1021/jp909492w`

[87] Peter E. CHEN, Nicholas C. ANDERSON, Zachariah M. NORMAN, and Jonathan S. OWEN. Tight Binding of Carboxylate, Phosphonate, and Carbamate Anions to Stoichiometric CdSe Nanocrystals. *Journal of The American Chemical Society*, **139**: 3227–3236, 2017. DOI: `10.1021/jacs.6b13234`

[88] Taleb MOKARI, Eli ROTHENBERG, Inna POPOV, Ronny COSTI, and Uri BANIN. Selective Growth of Metal Tips onto Semiconductor Quantum Rods and Tetrapods. *Science*, **304**: 1787–1790, 2004. DOI: `10.1126/science.1097830`

[89] Sun Mi KIM, Seon Joo LEE, Seung Hyun KIM, Sangku KWON, Ki Ju YEE, Hyunjoon SONG, Gabor A. SOMORJAI, and Jeong Young PARK. Hot Carrier-Driven Catalytic Reactions on Pt–CdSe–Pt Nanodumbbells and Pt/GaN under Light Irradiation. *Nano Lett.*, **13**: 1352–1358, 2013. DOI: `10.1021/nl400367m`

[90] Yifat NAKIBLI and Lilac AMIRAV. Selective Growth of Ni Tips on Nanorod Photocatalysts. *Chemistry of Materials*, **28**: 4524–4527, 2016. DOI: `10.1021/acs.chemmater.6b01482`

[91] Yifat NAKIBLI, Yair MAZAL, Yonatan DUBI, Maria WÄCHTLER, and Lilac AMIRAV. Size Matters: Cocatalyst Size Effect on Charge Transfer and Photocatalytic Activity. *Nano Letters*, **18**: 357–364, 2018. DOI: `10.1021/acs.nanolett.7b04210`

[92] Ji Yong CHOI, Won-Woo PARK, Bumjin PARK, Soohwan SUL, Oh-Hoon KWON, and Hyunjoon SONG. Optimal Length of Hybrid Metal–Semiconductor Nanorods for Photocatalytic Hydrogen Generation. *ACS Catalysis*, **11**: 13303–13311, 2021. DOI: `10.1021/acscatal.1c03754`

[93] Stefan KUDERA, Luigi CARBONE, Maria Francesca CASULA, Roberto CINGOLANI, Andrea FALQUI, Etienne SNOECK, Wolfgang J. PARAK, and Liberato MANNA. Selective Growth of PbSe on One or Both Tips of Colloidal Semiconductor Nanorods. *Nano Lett.*, **5**: 445–449, 2005. DOI: `10.1021/nl048060g`

[94] Marco Zanella, Azhar Z. Abbasi, Andreas K. Schaper, and Wolfgang J. Parak. Discontinuous Growth of II-VI Semiconductor Nanocrystals from Different Materials. *Journal of Physical Chemistry C*, **114**: 6205–6215, 2010. doi: `10.1021/jp906812t`

[95] D Gao, X Y Hao, N Rowell, T Kreouzis, D J Lockwood, S Han, H S Fan, H Zhang, C C Zhang, Y N Jiang, J R Zeng, M Zhang, and K Yu. Formation of colloidal alloy semiconductor CdTeSe magic-size clusters at room temperature. *Nature Communications*, **10**: 2019. doi: `10.1038/s41467-019-09705-w`

[96] Nicholas C. Anderson, Mark P. Hendricks, Joshua J. Choi, and Jonathan S. Owen. Ligand exchange and the stoichiometry of metal chalcogenide nanocrystals: Spectroscopic observation of facile metal-carboxylate displacement and binding. *Journal of The American Chemical Society*, **135**: 18536–18548, 2013. doi: `10.1021/ja4086758`

[97] Rémi Beaulac, Paul I. Archer, Xinyu Liu, Sanghoon Lee, G. Mackay Salley, Margaret Dobrowolska, Jacek K. Furdyna, and Daniel R. Gamelin. Spin-polarizable excitonic luminescence in colloidal Mn^{2+}-doped CdSe quantum dots. *Nano Letters*, **8**: 1197–1201, 2008. doi: `10.1021/nl080195p`

[98] B. T. Allen and D. W. Nebert. Hyperfine Structure in the EPR Spectrum of the Manganous Ion in Frozen Solutions. *Journal of Chemical Physics*, **41**: 1983–1985, 1964. doi: `10.1063/1.1726191`

[99] Robert T. Ross. Dipolar Broadening of EPR Spectra Due to Solute Segregation in Frozen Aqueous Solutions. *Journal of Chemical Physics*, **42**: 3919–3922, 1965. doi: `10.1063/1.1695859`

[100] Danja Fischli. *Lokalisierte Dotierung von Halbleiternanokristallen*. MA thesis. Konstanz: University of Konstanz, 2018.

[101] Taleb Mokari and Uri Banin. Synthesis and Properties of CdSe/ZnS Core/Shell Nanorods. *Chemistry of Materials*, **15**: 3955–3960, 2003. doi: `10.1021/cm034173+`

[102] Margaret A. Hines and Philippe Guyot-Sionnest. Synthesis and Characterization of Strongly Luminescing ZnS-Capped CdSe Nanocrystals. *The Journal of Physical Chemistry*, **100**: 468–471, 1996. doi: `10.1021/jp9530562`

[103] Klaus Boldt, Kyra N. Schwarz, Nicholas Kirkwood, Trevor A. Smith, and Paul Mulvaney. Electronic Structure Engineering in ZnSe/CdS Type-II Nanoparticles by Interface Alloying. *Journal of Physical Chemistry C*, **118**: 13276–13284, 2014. doi: `10.1021/jp503609f`

[104] Angshuman Nag, S. Chakraborty, and D. D. Sarma. To Dope Mn^{2+} in a Semiconducting Nanocrystal. *Journal of The American Chemical Society*, **130**: 10605–10611, 2008. doi: `10.1021/ja801249z`

[105] The Materials Project *Materials Data on MnSe by Materials Project* July 2020 doi: `10.17188/1199092`

[106] The Materials Project *Materials Data on MnS by Materials Project* July 2020 doi: `10.17188/1192718`

[107] The Materials Project *Materials Data on ZnS by Materials Project* July 2020 doi: `10.17188/1187297`

[108] THE MATERIALS PROJECT *Materials Data on CdSe by Materials Project* July 2020 DOI: `10.17188/1187302`

[109] Urko PETRALANDA, Luca DE TRIZIO, Graziella GARIANO, Roberto CINGOLANI, Liberato MANNA, and Sergey ARTYUKHIN. Triggering Cation Exchange Reactions by Doping. *Journal of Physical Chemistry Letters*, **9**: 4895–4900, 2018. DOI: `10.1021/acs.jpclett.8b02083`

[110] Klaus BOLDT, Stuart BARTLETT, Nicholas KIRKWOOD, and Bernt JOHANNESSEN. Quantification of Material Gradients in Core/Shell Nanocrystals Using EXAFS Spectroscopy. *Nano Letters*, **20**: 1009–1017, 2020. DOI: `10.1021/acs.nanolett.9b04143`

[111] Xiaoli YANG, Chaodan PU, Haiyan QIN, Shaojie LIU, Zhuan XU, and Xiaogang PENG. Temperature- and Mn^{2+} concentration-dependent emission properties of Mn^{2+}-doped ZnSe nanocrystals. *Journal of The American Chemical Society*, 2019. DOI: `10.1021/jacs.8b08480`

[112] Harry IRVING and Robert J. P. WILLIAMS. Order of Stability of Metal Complexes. *Nature*, **162**: 746–747, 1948. DOI: `https://doi.org/10.1038/162746a0`

[113] Kaifeng WU, Yongling DU, Hua TANG, Zheyuan CHEN, and Tianquan LIAN. Efficient Extraction of Trapped Holes from Colloidal CdS Nanorods. *Journal of The American Chemical Society*, **137**: 10224–10230, 2015. DOI: `10.1021/jacs.5b04564`

[114] Vladimir A. VLASKIN, Nils JANSSEN, Jos VAN RIJSSEL, Rémi BEAULAC, and Daniel R. GAMELIN. Tunable Dual Emission in Doped Semiconductor Nanocrystals. *Nano Letters*, **10**: 3670–3674, 2010. DOI: `10.1021/nl102135k`

[115] W W ZHENG, Z X WANG, J WRIGHT, B GOUNDIE, N S DALAL, R W MEULENBERG, and G F STROUSE. Probing the Local Site Environments in Mn:CdSe Quantum Dots. *Journal of Physical Chemistry C*, **115**: 23305–23314, 2011. DOI: `10.1021/jp2082215`

[116] Sandrine ITHURRIA, Philippe GUYOT-SIONNEST, Benoit MAHLER, and Benoit DUBERTRET. Mn^{2+} as a radial pressure gauge in colloidal core/shell nanocrystals. *Physical Review Letters*, **99**: 5–8, 2007. DOI: `10.1103/PhysRevLett.99.265501`

[117] Chaodan PU and Xiaogang PENG. To Battle Surface Traps on CdSe/CdS Core/Shell Nanocrystals: Shell Isolation versus Surface Treatment. *Journal of The American Chemical Society*, **138**: 8134–8142, 2016. DOI: `10.1021/jacs.6b02909`

[118] Karol MISZTA, Dirk DORFS, Alessandro GENOVESE, Mee Rahn KIM, and Liberato MANNA. Cation Exchange Reactions in Colloidal Branched Nanocrystals. *ACS Nano*, **5**: 7176–7183, 2011. DOI: `10.1021/nn201988w`

[119] Patrick ADEL, Andreas WOLF, Torben KODANEK, and Dirk DORFS. Segmented CdSe@CdS/ZnS Nanorods Synthesized via a Partial Ion Exchange Sequence. *Chemistry of Materials*, **26**: 3121–3127, 2014. DOI: `10.1021/cm500431m`

[120] Danja FISCHLI, Luisa RIEGER, and Klaus BOLDT. Localized Co^{2+} Doping of CdSe/CdS Seeded Nanorods. *The Journal of Physical Chemistry C*, **126**: 12150–12158, 2022. DOI: `10.1021/acs.jpcc.2c02081`

[121] Victor I KLIMOV. *Nanocrystal quantum dots*. CRC press, 2017.

[122] Pavle V. Radovanovic and Daniel R. Gamelin. Electronic Absorption Spectroscopy of Cobalt Ions in Diluted Magnetic Semiconductor Quantum Dots: Demonstration of an Isocrystalline Core/Shell Synthetic Method. *Journal of The American Chemical Society*, **123**: 12207–12214, 2001. doi: `10.1021/ja0115215`

[123] Dingan Chen, Ranjani Viswanatha, Grace L. Ong, Renguo Xie, Mahalingam Balasubramaninan, and Xiaogang Peng. Temperature dependence of "elementary processes" in doping semiconductor nanocrystals. *Journal of The American Chemical Society*, **131**: 9333–9339, 2009. doi: `10.1021/ja9018644`

[124] Kaifeng Wu, Lawrence J. Hill, Jinquan Chen, James R. McBride, Nicholas G. Pavlopolous, Nathaniel E. Richey, Jeffrey Pyun, and Tianquan Lian. Universal Length Dependence of Rod-to-Seed Exciton Localization Efficiency in Type I and Quasi-Type II CdSe@CdS Nanorods. *ACS Nano*, **9**: 4591–4599, 2015. doi: `10.1021/acsnano.5b01245`

[125] Nuri Oh and Moonsub Shim. Metal Oleate Induced Etching and Growth of Semiconductor Nanocrystals, Nanorods, and Their Heterostructures. *J. Am. Chem. Soc.*, **138**: 10444–10451, 2016. doi: `10.1021/jacs.6b03834`

[126] W. Becker and H.D. Lutz. Phase Studies in the Systems CoS-MnS, CoS-ZnS, and CoS-CdS. *Materials Research Bulletin*, **13**: 907–911, 1978. doi: `10.1016/0025-5408(78)90102-2`

[127] J Zmija. Investigation of Self-Diffusion of Cadmium and Selenium in CdSe Single Crystals. *Acta Phys. Pol. Ser. A*, 345–355, 1973.

[128] L. Shcherbak, O. Kopach, P. Fochuk, A. E. Bolotnikov, and R. B. James. Empirical Correlations Between the Arrhenius' Parameters of Impurities' Diffusion Coefficients in CdTe Crystals. *J. Phase Equilibria Diffus.*, **36**: 99–109, 2015. doi: `10.1007/s11669-015-0364-8`

[129] Avijit Saha, Mahima Makkar, Amitha Shetty, Kushagra Gahlot, A. R. Pavan, and Ranjani Viswanatha. Diffusion Doping in Quantum Dots: Bond Strength and Diffusivity. *Nanoscale*, **9**: 2806–2813, 2017. doi: `10.1039/c6nr09839h`

[130] T. Łukaszewicz. Studies on the Diffusion of Impurities in II–VI Compounds Based on the Two-Sample Luminescence Method. *Phys. Status Solidi*, **73**: 611–616, 1982. doi: `10.1002/pssa.2210730240`

[131] George A Sullivan. Diffusion and Solubility of Cu in CdS Single Crystals. *Physical Review*, **184**: 796–805, 1969. doi: `10.1103/PhysRev.184.796`

[132] B Lepley, P H Nguyen, C Boutrit, and S Ravelet. Copper Diffusion and Photovoltaic Mechanisms at Cu-CdS Contact. *J. Phys. D. Appl. Phys.*, **12**: 1917–1928, 1979. doi: `10.1088/0022-3727/12/11/020`

[133] V. A. Williams. Diffusion of Some Impurities in Zinc Sulphide Single Crystals. *Journal of Materials Science*, **7**: 807–812, 1972. doi: `10.1007/BF00549909`

[134] V M Korsun and A M Nemchenk. Electroluminescence in the Case of Cu Diffusion in ZnS Crystals. *Sov. Phys. Solid State, USSR*, **8**: 2988, 1967.

[135] Adolf Fick. Ueber Diffusion. *Annalen der Physik*, **170**: 59–86, 1855. doi: `https://doi.org/10.1002/andp.18551700105`

[136] John R. MANNING. Diffusion in a Chemical Concentration Gradient. *Phys. Rev.*, **124**: 470–482, 1961. DOI: `10.1103/PhysRev.124.470`

[137] Dan GUO, Guoxin XIE, and Jianbin LUO. Mechanical properties of nanoparticles: basics and applications. *Journal of Physics D: Applied Physics*, **47**: 013001, 2013. DOI: `10.1088/0022-3727/47/1/013001`

[138] THE MATERIALS PROJECT *Materials Data on CdS by Materials Project* July 2020 DOI: `10.17188/1272700`

[139] A. EINSTEIN. Ueber die von der molekularkinetischen Theorie der Waerme geforderte Bewegung von in ruhenden Fluessigkeiten suspendierten Teilchen. *Annalen der Physik*, **322**: 549–560, 1905. DOI: `https://doi.org/10.1002/andp.19053220806`

[140] Franziska MUCKEL, Charles J. BARROWS, Arthur GRAF, Alexander SCHMITZ, Christian S. ERICKSON, Daniel R. GAMELIN, and Gerd BACHER. Current-Induced Magnetic Polarons in a Colloidal Quantum-Dot Device. *Nano Lett.*, **17**: 4768–4773, 2017. DOI: `10.1021/acs.nanolett.7b01496`

[141] Calynn MORRISON, Haochen SUN, Yuewei YAO, Richard A. LOOMIS, and William E. BUHRO. Methods for the ICP-OES Analysis of Semiconductor Materials. *Chemistry of Materials*, **32**: 1760–1768, 2020. DOI: `10.1021/acs.chemmater.0c00255`

[142] P. Davide COZZOLI, Liberato MANNA, M. Lucia CURRI, Stefan KUDERA, Cinzia GIANNINI, Marinella STRICCOLI, and Angela AGOSTIANO. Shape and Phase Control of Colloidal ZnSe Nanocrystals. *Chemistry of Materials*, **17**: 1296–1306, 2005. DOI: `10.1021/cm047874v`

[143] Anubhav JAIN, Shyue Ping ONG, Geoffroy HAUTIER, Wei CHEN, William Davidson RICHARDS, Stephen DACEK, Shreyas CHOLIA, Dan GUNTER, David SKINNER, Gerbrand CEDER, and Kristin A. PERSSON. Commentary: The Materials Project: A materials genome approach to accelerating materials innovation. *APL Materials*, **1**: 011002, 2013. DOI: `10.1063/1.4812323`